

PSFC RR-83-30

Aspects of the Structural Effects of
Plasma Disruptions on Tokamaks

Aspects of the Structural Effects of Plasma Disruptions on Tokamaks

by
M. S. Tillack
M. S. Kazimi
L. M. Lidsky

Abstract

A scoping investigation was made into the structural effects of major plasma disruptions in tokamaks. Methods were developed for numerically analyzing the induced eddy currents, pressure loading, and distributed stresses and strains. A small simulation experiment was performed to measure strains induced by current transients in a cylindrical test apparatus.

The numerical routines developed include a set of efficient codes which give estimates for pressures and stresses in axisymmetric toroidal shells. These codes were used to examine the difference in response between central and shifted current transients, the effects of an electromagnetic shield, and the disruption effects in a high field compact design. For the base case, modeled with STARFIRE-like parameters, the peak strain is 5×10^{-4} in the poloidal direction and the peak bending stress is 0.7 MPa. The variations made to this case showed differences of only about a factor of two, indicating that for uniform loading in uniform structures the danger of structural failure is small.

In order to examine the effects of nonuniformities, a 3-D eddy current code was developed using a circuit network model. The code was extensively benchmarked with 2-D and axisymmetric test cases and then used to analyze the experimental part of the work. Analytic and numerical methods were applied to the structural analysis. It is observed that while structural irregularities cause only minor, local perturbations in the induced pressures, these irregularities produce larger effects on the stresses. Stress concentrations of 1-2 orders of magnitude in reactor structures can cause damage with a single disruption.

In addition, a small scale simulation experiment was performed. The experiment consisted of a copper shell 63.5 mm in radius with filaments running through the center to simulate plasma currents. Sinusoidal strains were measured with semiconductor strain gauges using synchronous detection. Peak induced current levels were ~ 1000 amps RMS, and peak measured strains were $\sim 10^{-7}$. The successful measurement of strains has demonstrated that synchronous detection is a viable technique that may be applied to tokamak experiments in the future.

An important result of the tests was the observation of widespread resonant behavior. This behavior was verified both analytically and numerically. The strains at resonances were as much as an order of magnitude larger than the strains off resonance. These observations support the conclusion that the strain level is dominated by the structural characteristics and not the induced pressure loading.

Acknowledgements

The authors gratefully acknowledge the financial support from DOE and the fusion safety group at EG&G Idaho which made this work possible.

We would also like to thank several people for their technical assistance:

Thanks to Pete Roemer for sharing his knowledge, time, and experience in electronics and system software.

Thanks to John Aspinall and Joe Johnson for their support and frequent technical advice, especially with numerical methods and programming.

Thanks to Ken Rettman for helping to build the experiment, and, equally important, for his invaluable ideas and intuition on how to build an experiment.

Thanks finally to MIT and the PFC for the use of their facilities and computers.

This report is based on a thesis submitted by the first author to the MIT Department of Nuclear Engineering in partial fulfillment of the requirements for the Degree of Doctor of Philosophy.

PUBLICATIONS UNDER CONTRACT #K-1702
ON FUSION SAFETY

A. General Safety and Risk Assessment

1. M. S. Kazimi et al., "Aspects of Environmental Safety Analysis of Fusion Reactors," MITNE-212, Dept. of Nuclear Engineering, M.I.T. October 1977.
2. R. W. Sawdye, J. A. Sefcik, M. S. Kazimi, "Reliability Requirements for Admissible Radiological Hazards from Fusion Reactors," Trans. Am. Nucl. Soc. 27, 65-66, November 1977.
3. R. W. Sawdye and M. S. Kazimi, "Application of Probabilistic Consequence Analysis to the Assessment of Potential Radiological Hazards of Fusion Reactors," MITNE-220, Dept. of Nuclear Engineering, M.I.T., July 1978.
4. R. W. Sawdye and M. S. Kazimi, "Fusion Reactor Reliability Requirements Determined by Consideration of Radiological Hazards," Trans. Am. Nucl. Soc. 32, 66, June 1979.
5. M. S. Kazimi and R. W. Sawdye, "Radiological Aspects of Fusion Reactor Safety: Risk Constraints in Severe Accidents," J. of Fusion Energy, Vol. 1, No. 1, pp. 87-101, January 1981.
6. S. J. Piet, M. S. Kazimi and L. M. Lidsky, "Potential Consequences of Tokamak Fusion Reactor Accidents: The Materials Impact," PFC/RR-82-19, Plasma Fusion Center, M.I.T., June 1982.
7. S. J. Piet, V. J. Gilberti, "FUSECRAC: Modifications of CRAC for Fusion Application," Nuclear Eng. Dept. and Plasma Fusion Center, M.I.T., PFC/RR-82-20, June 1982.
8. M. S. Kazimi, "Safety and Risk Targets for Fusion Energy," Societe Francaise de Radioprotection 10th Annual Congres, Avignon, France, Oct. 18-22, 1982.
9. M. S. Kazimi, "Safety Methodology and Risk Targets," in Proc. of 1982 IAEA Workshop on Fusion Safety, IAEA-TECDOC-277, 1983.
10. M. S. Kazimi, "Risk Considerations for Fusion Energy," Nuclear Technology/Fusion, Vol. 4, No. 2, Part 2, pp. 527-532, Sept. 1983.
11. S. J. Piet, M. S. Kazimi and L. M. Lidsky, "Relative Public Health Effects from Accidental Release of Fusion Structural Radioactivity," Nuclear Technology/Fusion, Vol. 4, No. 2, Part 2, pp. 533-538, Sept. 1983.

Publications under Contract #K-1702 (continued)

12. S. J. Piet, M. S. Kazimi and L. M. Lidsky, "Modeling of Fusion Activation Product Release and Reactor Damage from Rapid Structural Oxidation," Nuclear Technology/Fusion, Vol. 4, No. 2, Part 3, pp. 1115-1120, Sept. 1983.

B. Lithium Reactions

1. D. A. Dube, M. S. Kazimi and L. M. Lidsky, "Thermal Response of Fusion Reactor Containment to Lithium Fire," 3rd Top. Meeting on Fusion Reactor Technology, May 1978.
2. D. A. Dube and M. S. Kazimi, "Analysis of Design Strategies for Mitigating the Consequences of Lithium Fire within Containment of Controlled Thermonuclear Reactors, MITNE-219, Dept. of Nuclear Engineering, M.I.T., July 1978.
3. M. S. Tillack and M. S. Kazimi, "Development and Verification of the LITFIRE Code for Predicting the Effects of Lithium Spills in Fusion Reactor Containments," PFC/RR-80-11, Plasma Fusion Center, M.I.T., July 1980.
4. P. J. Krane and M. S. Kazimi, "An Evaluation of Accidental Water-Reactions with Lithium Compounds in Fusion Reactor Blankets," PFC/RR-81-26,, Plasma Fusion Center, M.I.T., July 1981.
5. M. S. Tillack and M. S. Kazimi, "Modelling of Lithium Fires," Nuclear Technology/Fusion, Vol. 2, No. 2, pp. 233-245, April 1982.
6. V. J. Gilberti and M. S. Kazimi, "Modeling of Lithium and Lithium-Lead Reactions in Air Using LITFIRE," PFC/RR-82-08, Plasma Fusion Center, M.I.T., January 1983.
7. E. Yachimiak, V. Gilberti, and M. S. Tillack, "LITFIRE User's Guide," Nuclear Eng. Dept. and Plasma Fusion Center, M.I.T., PFC/RR-82-11, June 1983.

C. Tritium

1. S. J. Piet and M. S. Kazimi, "Uncertainties in Modeling of Consequences of Tritium Release from Fusion Reactors," PFC/TR-79-5, Plasma Fusion Center and Nucl. Eng. Dept., M.I.T., July 1979.
2. M. J. Young and S. J. Piet, "Revisions to AIRDOS-II," PFC/TR-79-8, Plasma Fusion Center and Nucl. Eng. Dept., M.I.T., August 1979.
3. S. J. Piet and M. S. Kazimi, "Implications of Uncertainties in Modeling of Tritium Releases from Fusion Reactors," Proc. Tritium Technology in Fission, Fusion and Isotopic Applications, April 1980.

Publications under Contract #K-1702 (continued)

4. D. R. Hanchar and M. S. Kazimi, "Tritium Permeation Modelling of a Conceptual Fusion Reactor Design," PFC/RR-81-27, Plasma Fusion Center, M.I.T., July 1981.
5. D. R. Hanchar and M. S. Kazimi, "Transient Tritium Transport in a Solid Breeder Blanket," Nuclear Technology/Fusion, Vol. 4, No. 2, Part 2, pp. 395-400, Sept. 1983.

D. Electromagnetic Consideration

1. R. W. Green and M. S. Kazimi, "Safety Considerations in the Design of Tokamak Toroidal Magnet Systems," Trans. ANS 32, 69, June 1979.
2. R. W. Green and M. S. Kazimi, "Aspects of Tokamak Toroidal Magnet Protection," PFC/TR-79-6, Plasma Fusion Center, M.I.T., July 1979.
3. M. S. Tillack, "A Study of Structural Responses to Plasma Disruptions in Toroidal Shells," Dept. of Nucl. Eng. and Plasma Fusion Center, M.I.T., PFC/RR-83-16, June 1983.
4. M. S. Tillack, M. S. Kazimi and L. M. Lidsky, "Aspects of the Structural Effects of Plasma Disruptions on Tokamaks," Dept. of Nuclear Eng. and Plasma Fusion Center, M.I.T., PFC/RR-83-30.

E. Others

1. M. S. Kazimi, "IAEA Workshop on Fusion Safety March 23-27, 1981, Vienna, Austria," J. of Fusion Energy, Vol. 1, No. 3, pp. 241-243, 1981.

Contents

Abstract.....	i
Acknowledgments	ii
List of Publications	1
Table of Contents	4
List of Figures	7
List of Tables	11
Nomenclature	12
Chapter I Introduction	14
1. Motivation	14
2. Overview	16
3. Conclusions	19
Chapter II Background	21
1. Physics of Plasma Disruptions	22
1. Overview	22
2. Basic MHD Theory	23
3. Stabilization of Tearing Modes	25
2. Tokamak Experiments	27
1. Overview	27
2. Diagnostics Used	28
3. Some Results	28
3. Engineering Analysis	29
References	31
Chapter III Mechanical Strain Test	34
1. Purposes	34
2. Strain Gauge and Circuit Theory	35
1. Semiconductor Strain Gauges	35
2. Gauge Circuits	35
3. Performance of Gauges and Circuits	38
4. Rosette Calculations	39
3. Lock-in Amplifier Theory and Technique	39

4.	Other Techniques in Small Strain Measurement	41
5.	Experiments and Results	41
1.	Description of Experiments	41
2.	Fabry-Perot Experiment	43
3.	Electromagnet Calibration	49
4.	Small Strain Tests	52
5.	Conclusions	52
	References	56
Chapter IV	Electromagnetic Strain Test Design	58
1.	Overview	58
2.	Test Piece and Return Current Path	62
3.	Filament and Power Supply Design	67
1.	Filament Geometry	67
2.	Amplifier Design	69
3.	Transformer Design	73
4.	Magnet and Magnet Power Supply	75
5.	Detection Circuitry	75
1.	Gauges and Lead Wire Configuration	78
2.	Self-Compensating Wheatstone Bridge	81
3.	Signal Filtering	84
4.	Reference Channel Driver Circuit	86
	References	86
Chapter V	Electromagnetic Strain Test Results	90
1.	Operation of the Experiment	90
1.	Sources of Error	90
2.	Selection of Operating Frequencies	92
3.	Circuit Sensitivity and Data Conversion	93
4.	Resonant Behavior	95
5.	Data Taking Procedure	105
2.	Results for the Continuous Cylinder	105
1.	Self-Interactions	105
2.	External Field Interaction	114
3.	Results for the Cylinder with a Hole	114
	References	119
Chapter VI	Axisymmetric Calculations of Currents and Strains	123
1.	Introduction	123
1.	Overview of Pressures	123
2.	Overview of Stresses	127
2.	Description of Computational Method	129
1.	The Eddy Current Problem	129
2.	The Structural Problem	131
3.	Results	136
	References	146
Chapter VII	3-D Calculation of Currents and Strains	150
1.	Introduction	150
2.	Eddy Current Codes and FASTEDDY	150
1.	Methods for Eddy Current Problems	150

2.	Special Features of FASTEDDY	152
3.	Benchmarking FASTEDDY	154
1.	2-D Disk Benchmark	154
2.	2-D Torus Benchmark	162
3.	3-D Sample Run	168
3.	Structural Codes	168
4.	Analysis	170
1.	Estimates for a Uniform Axial Current	170
2.	Comparison with the Shell with a Hole	174
1.	Description of FASTEDDY Results	175
2.	Analytic Theory and Comparison with Data	185
3.	Comparison with the Continuous Shell	192
1.	Description of FASTEDDY Results	192
2.	PAFEC Results and Comparison with Data	196
	References	204
Chapter VIII	Conclusions	205
1.	Experimental Results	206
2.	Numerical Results	206
3.	Recommendations	207
Appendix A	Analytic Methods in Cylindrical Geometry	208
1.	Scalar Potential Harmonic Expansion	208
2.	Green's Function and Vector Methods	210
	References	213
Appendix B	Description of FASTEDDY	214
1.	Overview	214
2.	FASTMESH	216
1.	Mesh Relaxation	217
2.	Sample Input Deck	219
3.	FASTCOFF	223
1.	Evaluating the Inductance Matrix and its Inverse	223
2.	Treatment of Special Loops	225
3.	Description of Selected Subroutines	225
4.	FASTTIME	226
5.	FASTPLOT	227
6.	Problems and Recommendations	228
	References	229

List of Figures

Fig. 2.1	Fields from a Current Sheet Before and After Tearing	24
Fig. 2.2	Flux Surfaces in a Torus	26
Fig. 3.1	Potentiometer Circuit	37
Fig. 3.2	Wheatstone Bridge Circuit	37
Fig. 3.3	45° Rosette Pattern	40
Fig. 3.4	Lock-in Amplifier Block Diagram	40
Fig. 3.5	Strain Gauge Test Stand	44
Fig. 3.6	Scale Drawing of Test Cylinder	45
Fig. 3.7	Fabry-Perot Experiment Block Diagram	46
Fig. 3.8	Low Signal Experiment Block Diagram	47
Fig. 3.9	Bridge Circuit Schematic	48
Fig. 3.10	Gauge Output vs. Fabry-Perot Peak Number	50
Fig. 3.11	DC Electromagnet Calibration	51
Fig. 3.12	AC Electromagnet Calibration	53
Fig. 3.13	Lock-in Response at 29Hz . High Strain Range	54
Fig. 3.14	Lock-in Response at 29Hz . Low Strain Range	55
Fig. 4.1	Electromagnetic Strain Test Functional Block Diagram	60
Fig. 4.2	Diagram of Test Section	63
Fig. 4.3	Cross Section of Filaments and Shell	64
Fig. 4.4	Strains for a Symmetric Axial Current	68
Fig. 4.5	Filament Configuration	71
Fig. 4.6	Push-Pull Power Amplifier Schematic	72
Fig. 4.7	Base Drive Circuit Diagram	74
Fig. 4.8	Iron Core Transformer Dimensions	76
Fig. 4.9	EST Detection Electronics Block Diagram	79

Fig. 4.10	Strain Gauge Positions	80
Fig. 4.11	Gauge Locations Around the Hole	82
Fig. 4.12	Self-Compensating Wheatstone Bridge Circuit	83
Fig. 4.13	VCVS Active Filter Schematic	85
Fig. 4.14	6th Order Band Pass Filter Analytic Response	87
Fig. 4.15	6th Order Band Pass Filter Measured Response	88
Fig. 4.16	Lock-in Reference Channel Driver	89

Fig. 5.1	Strain Resonances from Self-Interactions	96
Fig. 5.2	Strain Resonances from External Field Interactions	97
Fig. 5.3	Filament Frequency Scan Near 240 Hz	99
Fig. 5.4	Mechanical Strain Resonance Data	100
Fig. 5.5	Modal Resonances of the Cylinder	104
Fig. 5.6	Fitted Data for Center Gauge, Self Interactions	110
Fig. 5.7	Fitted Data for Upper Gauge, Self Interactions	111
Fig. 5.8	State of Stress for Center Gauge, Self Interactions	112
Fig. 5.9	State of Stress for Upper Gauge, Self Interactions	113
Fig. 5.10	Fitted Data for Center Gauge, External Field Interactions	115
Fig. 5.11	Fitted Data for Upper Gauge, External Field Interactions	116
Fig. 5.12	State of Stress for Center Gauge, External Field Interactions	117
Fig. 5.13	State of Stress for Upper Gauge, External Field Interactions	118

Fig. 6.1	Definition of Coordinates	125
Fig. 6.2	Contours of Constant B from a Current Loop	126
Fig. 6.3	B-Lines and Equipotentials from a Current Loop	126
Fig. 6.4	Pressurized Torus Displacements	128
Fig. 6.5	Pressurized Torus Moments	128
Fig. 6.6	B-Spline Basis Functions and Derivatives	135
Fig. 6.7	Base Case Current Histories	138
Fig. 6.8	Base Case Pressure Histories	138

Fig. 6.9	Current Profiles	139
Fig. 6.10	Radial Pressure Profiles	139
Fig. 6.11	Circumferential Pressure Profiles	140
Fig. 6.12	Base Case Displacements	142
Fig. 6.13	Base Case Structural Response at 20 msec	143
Fig. 6.14	Radial Pressure with Plasma Shift	144
Fig. 6.15	Radial Pressure with EM Shield	144
Fig. 6.16	Structural Response at 20 msec with Plasma Shift	145
Fig. 6.17	Structural Response at 20 msec with EM Shield	147
Fig. 6.18	Radial Pressure for High Field Example	148
Fig. 6.19	Structural Response at 20 ms for High Field Example	149
Fig. 7.1	Location of Circulating Loops in FASTEDDY	153
Fig. 7.2	6x6 Mesh for the Disk Benchmark	157
Fig. 7.3	12x12 Mesh for the Disk Benchmark	157
Fig. 7.4	Initial Current Density for Disk Benchmark	158
Fig. 7.5	Disk Current Comparison at 1 msec	159
Fig. 7.6	Disk Current Comparison at 5 msec	159
Fig. 7.7	Disk Current Comparison at 10 msec	160
Fig. 7.8	5-Loop Disk Comparison at 1 msec	160
Fig. 7.9	Error in the Calculated Current for the Disk Benchmark	161
Fig. 7.10	16x16 Toroidal Mesh Generated by FASTEDDY	163
Fig. 7.11	Instantaneous Response of the Toroidal Benchmark	164
Fig. 7.12	Toroidal Benchmark - Power vs. Time	165
Fig. 7.13	Toroidal Benchmark Current Profile at 6 msec	166
Fig. 7.14	Toroidal Benchmark Current Profile at 50 msec	166
Fig. 7.15	Toroidal Benchmark Current Profile at 100 msec	167
Fig. 7.16	Current Streamlines at $t = 0$ for the Torus with a Poloidal Break	167
Fig. 7.17	Shell-Filament Equivalent Circuit	173
Fig. 7.18	Cross Section of Shell-Filament Circuit	173
Fig. 7.19	FASTEDDY 12x18 Mesh of the Cylinder with Hole	176
Fig. 7.20	FASTEDDY Logical Mesh	177
Fig. 7.21	Source Current History	178
Fig. 7.22	Total Resistive Power	178

Fig. 7.23	Current Streamlines with the Hole Present	179
Fig. 7.24	Induced Current Magnitude with the Hole Present	180
Fig. 7.25	Radial Magnetic Field – Self Interactions with the Hole Present	181
Fig. 7.26	Toroidal Magnetic Field – Self Interactions with the Hole Present	181
Fig. 7.27	Radial Pressure – Self Interactions with the Hole Present	182
Fig. 7.28	Axial Pressure – Self Interactions with the Hole Present	182
Fig. 7.29	Axial Field from the External Field Coil	183
Fig. 7.30	Radial Field from the External Field Coil	183
Fig. 7.31	Toroidal Pressure – External Field with Hole Present	184
Fig. 7.32	Stresses in the Shell - Pressure (Van Dyke)	187
Fig. 7.33	Stresses in the Shell - Torsion (Van Dyke)	188
Fig. 7.34	Membrane Stress at the Hole - Torsion (Van Dyke)	189
Fig. 7.35	Illustration of Helical Filaments	193
Fig. 7.36	Illustration of Continuous Cylinder with Filaments	194
Fig. 7.37	Current Streamlines for the Continuous Cylinder Test	195
Fig. 7.38	Current Magnitude for the Continuous Cylinder Test	197
Fig. 7.39	Radial Pressure – External Field Interaction	197
Fig. 7.40	Axial Pressure – External Field Interaction	198
Fig. 7.41	Toroidal Pressure – External Field Interaction	198
Fig. 7.42	PAFEC Displacements – Side View	199
Fig. 7.43	PAFEC Displacements – Top View	200
Fig. 7.44	PAFEC Principal Stresses at 6 inches	202
Fig. 7.45	PAFEC Principal Stresses at 9 inches	203

List of Tables

Table 1.1	Summary of Contents	18
Table 3.1	Purposes of the Mechanical Strain Test	36
Table 3.2	Techniques in Small Strain Measurement	42
Table 3.3	Summary of Measurements Taken for MST	42
Table 3.4	Major Problems Encountered with the MST	57
Table 4.1	Purposes of the EST	59
Table 4.2	Summary of Filament Design Parameters	70
Table 4.3	Filter Parameters	85
Table 5.1	Bridge Circuit Sensitivity Data	94
Table 5.2	Measured Mechanical Resonances	101
Table 5.3	Test Conditions for the Continuous Shell Tests	107
Table 5.4	Fourier Decomposition of the Data	108
Table 5.5	Harmonic Loading of the Shell	109
Table 5.6	Test Conditions with the Hole Present	120
Table 5.7	Data for the Cylinder with a Hole	121
Table 6.1	Reactor Data for STARFIRE Analysis	137
Table 7.1	Disk Benchmark Description	156
Table 7.2	Features of a Desirable FEM Code	169
Table 7.3	Summary of Cases Analyzed	171
Table 7.4	Data for the Cylinder with a Hole	190

Nomenclature:

a	minor radius
AC	alternating current, i.e. sinusoidal
A	magnetic vector potential
B_p	poloidal magnetic field (Tesla)
B_t	toroidal magnetic field (Tesla)
B_v	equilibrium vertical magnetic field
c	speed of sound
dB	decibels
DC	direct current, i.e. constant
D	flexural rigidity
E	modulus of elasticity or electric field
$E(k)$	complete elliptic integral of the second kind
f	frequency, hz
FEM	finite element method
G	shear modulus
GMD	geometric mean distance
h	shell thickness
i or I	current (amps)
j or J	current density (amps/m ²)
k	spring constant, N/m
K	surface current density (amps/m) or bending rigidity
$K(k)$	complete elliptic integral of the first kind
L	self inductance
m	axial mode number
M	general mutual inductance
M_o	mutual inductance with the source current
M_θ	toroidal moment (Nm/m)
M_ϕ	poloidal moment (Nm/m)
$M_{\phi\theta}$	twist (Nm/m)
n	circumferential mode number
N_θ	toroidal stress resultant (N/m)
N_ϕ	poloidal stress resultant (N/m)
p_a	radial pressure in toroidal coordinate system
p_r	radial pressure in cylindrical coordinates
p_ϕ	poloidal pressure
P_g	gauge power ($I^2 R$)
q_a	quality factor at a
Q_ϕ	poloidal shear (N/m)
r	resistance ratio for bridge circuit
r	distance from axis of symmetry
RMS	root mean squared, = $\sqrt{2}$ times the peak value
S_a	gauge sensitivity
S_c	gauge circuit sensitivity
S_g	gauge sensitivity

Nomenclature, continued

T	torque
R	resistance
R_g	gauge resistance
w	radial displacement
v	poloidal displacement
V	voltage
W	reactor total power output
$\langle \beta_t \rangle$	average toroidal beta
$\langle \beta_p \rangle$	average poloidal beta
γ	shear strain
ϵ	strain
ϵ_θ	toroidal strain
ϵ_ϕ	poloidal strain
$\epsilon_{\phi\theta}$	shear strain
η	resistivity (ohm-m)
θ	toroidal angle coordinate
b	rotational transform
μ_0	permeability of free space
ν	Poisson's ratio
ρ	electrical resistivity
ρ	material density
σ	stress
σ_b	bending stress
τ	shear stress, or time constant
ϕ_c	poloidal angle coordinate used in eddy current analysis
ϕ_s	poloidal angle coordinate used in structural analysis
χ_θ	theta curvature
χ_ϕ	phi curvature
ω	frequency, rad/sec
Ω	dimensionless frequency or Ohms
$()'$	$d()/d\phi$

Introduction

1.1. Motivation

The Nature of the Problem

For years tokamak experiments throughout the world have experienced the well-known phenomenon of plasma disruption. A disruption is a plasma instability which is driven by the magnetic energy of the large plasma currents characteristic of the tokamak design. In its worst manifestation, called a major disruption, the kinetic and magnetic energy of the plasma can all be deposited in the surrounding structures in a fraction of a second.

The disruptive instability defines a fairly reproducible upper limit on the normal range of operating parameters of experimental plasmas. It is possible to avoid disruptions with some degree of success by limiting the device to an operating regime below the threshold for disruptions. However, there are two reasons why the problem remains. First, tokamak operation is still somewhat of an inexact art, and the absence of disruptions cannot be guaranteed. Second, there are other system and plasma malfunctions which can trigger disruptions even within the stable operating regime. It then remains to be shown what the frequency of disruptions is likely to be, what the consequences are, and how to design a structure which can withstand their effects.

Because of the quantity of energy involved – several hundreds of megajoules – the implications of plasma disruptions for large power reactors may be serious. The energy in the plasma (all of which is released in a major disruption) is approximately equally split between plasma kinetic and poloidal magnetic energy. The kinetic energy is deposited in a fairly thin region of the first wall and/or limiter. The wall temperature can rise several hundreds of degrees, causing partial melting or vaporization. The large temperature gradients will result in large thermal strains. In addition, high energy particles striking the wall can sputter material directly.

In contrast, the magnetic energy need not necessarily be dumped entirely at the surface in closest proximity to the plasma. The large plasma current transient results in large induced voltages

in the nearby structures. Conducting materials will then develop eddy currents which in turn result in eddy current heating and the generation of $J \times B$ forces. If no closed conducting paths are present, then the voltages can become extremely large and arcing may occur across gaps between conductors.

With both thermal and magnetic energy sources, it is important to have some knowledge of the time scale and spatial concentration of their release into the structures. The limiting constraint on machine design for protection against disruptions will be at the point where effects are at a maximum.

Goals of This Work

The effects of disruptions can present difficult problems for the design of tokamak reactors. Designs such as STARFIRE, INTOR, and ETF have begun to address these problems, but only in incomplete and uncoordinated efforts. Usually this involves approximations of uniformity and axisymmetry. The primary goal of this thesis is to begin the development of more detailed and comprehensive techniques for studying the effects of disruptions in reactor structures, both computationally and experimentally. In particular, simple nonuniform source currents and structures are studied in an attempt to develop techniques and estimate effects in less idealized situations. The scope of this work is limited to only the effects of the plasma current transient, including induced eddy currents, pressure loading, stresses and strains.

The most important quantities in describing the effects of the current transient are stresses and eddy current heating. In order to solve for these, several computational steps are involved. First, a source current distribution is assumed. Then the induced eddy currents, J , formed by the current transient are solved, which results in $J \times B$ forces and ηJ^2 resistive heating. The forces can then be used to compute whole body effects such as net torques, or a structural problem can be solved to obtain the distributed stresses.

In reality, the various parts of the problem solution are all interrelated. The eddy current response produces feedback on the plasma, thus altering the source currents. The structural response can result in displacements which cause the eddy current pattern to be altered. For a general problem, the coupling of the plasma physics, induced eddy currents, and structural response is highly impractical. This is not to say that the coupling effects are not important, but only that for the first attempts it is wise to treat each part of the problem individually, at least until a reasonable understanding of the physical processes is obtained.

In this work, measurements of strain were made on a small simulation experiment using strain gauges. The direct measurement of induced currents would be extremely useful, but was avoided due to the difficulty and expense involved.

Related Work

Some of the elements required for a numerical description of the effects of plasma disruptions already exist or are under development. The area of eddy current codes is in a state of rapid transition. Until recently there has been little work in this field, but today it is an active area of research. Several methods have been studied and the circuit network integral method was chosen for analyzing eddy currents.

Structural codes are more commonly available than eddy current codes. A restricted survey of available codes included PAFEC, NASTRAN, and SAP4 – all available on the national fusion computer network MFENET. The application to toroidal shells with distributed loading presented a problem due to the sophistication of the elements, however the PAFEC code was identified as adequate for limited use.

There is less precedent for experimental work in the effects of disruptions. Plasma physics experiments clearly document the plasma physics aspects of the disruption and certain groups have gone as far as to measure heat loads on limiters. However, experiments specifically designed to measure electromagnetic effects are almost nonexistent. One recent exception is the FELIX experiment at Argonne National Laboratory.

1.2. Overview

This report examines the problem of induced eddy currents, stresses and strains in reactor structures due to plasma disruptions, focusing in particular on the effects of introducing nonuniformities in the source currents and in the structures. The work is approximately equally split between a computational effort and a small simulation experiment. For the numerical description of disruptions, eddy current and structural codes were developed to predict the behavior of shells subjected to current and field transients. An axisymmetric set of codes was written to give gross estimates of effects, including currents, pressures, stresses and strains. A 3-D integral method eddy current code was written and coupled to both analytic theory and a commercially available structural code to examine more detailed effects, including structural irregularities, complex plasma current distributions, structural resonant behavior, etc.

In addition to the computational work, a small simulation experiment was performed. The experiment consists of a small cylinder with copper filaments passing through the center and a coaxial magnetic field coil outside the structure. Strains are measured with semiconductor strain gauges and the results are then compared with numerical and analytic predictions. The experimental data is also valuable in identifying unexpected areas of concern that a purely computational approach might miss.

Chapter 2 contains background information for those unfamiliar with the field of plasma disruptions. This includes a survey of theoretical and experimental research, a brief discussion of the physics of disruptions, and an overview of engineering analysis which has been done.

Chapters 3-5 describe the experimental effort to simulate the structural effects of disruptions. The most critical concept for the success of the experiments is the application of semiconductor strain gauges at very low strains ($\epsilon < 10^{-8}$) and in an electromagnetically noisy environment. The Mechanical Strain Test, documented in Chapter 3, is intended to operate at very low strains, but in a relatively noise-free environment. It consists of a thin cylinder stressed axially by an electromagnet. The strains are driven sinusoidally so that synchronous detection can be used to detect the small signal in a noise background. This experiment served primarily as a testbed for some of the techniques used in the final experiment.

The Electromagnetic Strain Test, described in Chapter 4, operates at slightly higher strains, but in large noise fields. Copper filaments simulate plasma currents as they pass through a copper cylinder. Strains are measured both with and without an external applied field. Two experiments were performed. The first consisted of a continuous shell with helical, poloidally varying currents. The second experiment measured strains around a hole in the shell which were caused by an axial, symmetric current distribution. Chapter 5 contains the results of the Electromagnetic Strain Test.

Chapter 6 begins the computational part of the thesis by describing a simplified approach to compute pressures, stresses, and strains numerically in an axisymmetric toroidal geometry. This $1\frac{1}{2}$ -D work is simpler than the 3-D method developed in Chapter 7, giving rapid order of magnitude results for a variety of reactor sizes. An analytic description was attempted, but proved to be very cumbersome and unable to model any but the simplest problems. Appendix A contains a derivation in cylindrical geometry for induced currents which provides a way to predict induced currents for helically symmetric systems.

Chapter 7 describes the 3-D numerical work including the eddy current code FASTEDDY which was developed as a part of the thesis and the structural analysis done both analytically and with the commercially available code PAFEC. FASTEDDY is a special purpose code which treats curved shells with the possibility of reconnection as in a torus. The fields and currents are 3-D with the restriction that the current remains in the shell. An integral approach is used where the structure is broken into loops which are assigned averaged electrical properties. The solution is carried out as in an electrical network problem. Appendix B contains a user's guide which gives details into the operation of the code.

Table 1.1 Summary of Contents

Chapter 1	Introduction
Chapter 2	Background on Physics, Experiments, and Analysis
Chapter 3	Mechanical Strain Test
Chapter 4	Design of the Electromagnetic Strain Test
Chapter 5	Results from the Electromagnetic Strain Test
Chapter 6	Axisymmetric Method for Computing Structural Responses in Tori
Chapter 7	3-D Numerical Work, Eddy Current and Structural Codes
Chapter 8	Conclusions
Appendix A	Analytic Harmonic Solution of Induced Currents in a Cylinder
Appendix B	FASTEDDY User's Guide

1.3. Conclusions

The experimental effort has demonstrated the feasibility of measuring small strains in an electromagnetically noisy environment. Strains as low as 10^{-9} have been observed with mechanical loading and as low as 10^{-8} with electrical loading.

The principal experiment consists of a small cylinder driven by ~ 1 k amp sinusoidal currents, with strains detected through a Wheatstone bridge circuit using semiconductor strain gauges and synchronous detection techniques. The two experiments performed include one with a continuous shell and nonuniform source currents, and the second with uniform axial source currents inducing currents in a cylinder with a small hole.

One of the more important results of the experiment was the identification of structural resonant behavior. In this experiment, resonances dominate the behavior in the range of frequencies studied. After identifying the problem, resonant behavior in the experiment was examined with both analytic and numerical computations. A large number of resonances were identified, including larger narrow ones, and broader ones which create a continuum over some frequency ranges.

Another important experimental result was the appearance of spatial detail greater than originally expected. When the source currents possess spatial variation, both the induced currents and the fields possess similar variation. But since the pressures generated are caused by the product of the currents and fields, they contain mixing terms with more spatial detail than either the currents or the fields. With the addition of structural irregularities and restraints, the solution for strains becomes extremely complicated. In general, experience with the experiment has shown that the strains are more sensitive to variations in the structural parameters as opposed to variations in the pressure loading.

In the computational area, three approaches were examined: fully analytic, axisymmetric numerical, and 3-D numerical. Progress with a fully analytic treatment is difficult, especially with nonuniformities of any type. Certain eddy current problems can be solved in systems with helical symmetry and uniform structures. An approximate analytic solution for the structural analysis of eddy current loaded structures was possible for the experiment with a hole in the cylinder due to the special circumstances which prevail there. After numerically solving for the eddy current pressure loading, it was observed that to a good approximation the pressures were uniform.

An axisymmetric set of codes was developed and applied to the analysis of a shifted plasma, an electromagnetic shield, and a high field reactor. For scoping general effects and making order

of magnitude estimates, this method proved to be quite efficient. The currents are 1-D toroidally directed and the fields are 2-D in the (R,θ) plane. The structure is approximated with loops whose field and mutual inductances are known exactly. A lumped parameter circuit matrix equation is solved and the results are presented to a 1-D finite element method (FEM) special purpose structural code. The application to a STARFIRE test case showed peak poloidal strains of 5×10^{-4} and peak bending stresses of 0.7 MPa with a central current. A 25% outward shift caused a peak bending stress of 10 MPa and peak strain of 6×10^{-4} in the toroidal, rather than poloidal direction. In general, for the cases studied, the effects varied from the base case by less than a factor of two. This leads to the conclusion that stresses in uniform symmetric systems are not likely to damage the structures.

A 3-D shell eddy current code was developed, extensively benchmarked, and combined with a commercial finite element structural analysis code to analyze the Electromagnetic Strain Test. The eddy current code uses a discrete element electrical network analog to model the continuous structure of a torus. The main feature distinguishing this code from others is its ability to treat connected shells in a simple way. In order to do this, a vector potential formulation was used for mutual inductance calculations. Analysis of the experimental test with the hole indicated that whereas the perturbation to the pressures as a result of the presence of the hole were small and localized, the resulting strains were changed by over an order of magnitude. This indicates that for this situation, an accurate structural analysis is more critical than an accurate eddy current analysis. Analysis of the test with a continuous cylinder showed no surprises. The level of stress was consistent with a simple uniform current calculation and the spatial variation of the stresses closely follows the spatial variation of the source currents. The combined influence of resonant behavior, stress concentrations, and nonuniform restraints can easily raise the expected stress to the level at which failure could occur due to a single disruption.

Background

As an introduction to the field of plasma disruptions, this chapter contains a summary of the related published work. The description is very general; it is intended to introduce the unfamiliar reader to the current state of our understanding, and hopefully explain the context in which the remainder of the thesis is set. For the reader with an interest in more detail, an extensive bibliography is included at the end of the chapter. Due to the complexity of the phenomenon, our understanding of plasma disruptions today is still incomplete in both their evolution in the plasma and the effects they cause in the structures. This fact is as important to understand as the detailed theories which have been developed.

Research pertaining to disruptions has been broken into three categories: experiments, physics theory, and engineering analysis. Probably the most published aspect is experimental. The problem of plasma disruptions was identified through experimentation, and nearly every tokamak has documented disruptions to some extent. The experiments investigate almost exclusively the physics aspects of disruptions as compared to the nature of their effects on structures. Even further, these investigations tend to emphasize conditions prior to disruption as opposed to the behavior of the plasma *during* the disruption. One notable exception is temperature measurements on limiters which have been documented in a number of cases.

In second place is the theoretical analysis, which has been published in this country by primarily two groups — Oak Ridge and Princeton. The cause of major disruptions is generally believed to result from a resistive tearing instability. In order to appreciate the nature of the source term in the equations used to analyze the effects of disruptions, it is important to review the basic plasma physics. For the computational part of this thesis, the evolution of the plasma current was assumed as a starting point in all of the calculations. For the experimental part, the apparatus was designed to be able to reproduce some of the characteristics of a real disruption, which requires a gross understanding of the true evolution of current during a disruption.

The least studied aspect of disruptions is engineering analysis. Since there is almost no

experimental data existing on effects in structures, this is not surprising. Most of the published work has been done in connection with complete reactor designs. These designs contain many interrelated concerns in addition to disruptions, so their treatment of the specific problem of disruptions in general, and particularly electromagnetic loads, is understandably simplified. A summary is given below for work done on TNS, FED/INTOR, DEMO and STARFIRE.

2.1. Physics of Plasma Disruptions

2.1.1. Overview

The methods developed in this thesis apply equally well to plasma current disturbances of any kind or even an external field transient. Included in this list may be: internal disruptions, major disruptions, power transients, start-up and shut-down, system failures, and others. In this section, we review only the type of transient labeled "major plasma disruption". Since a major plasma disruption occurs very quickly and dumps all of the plasma energy, it is the most severe case to study.

A very detailed theory has evolved to explain the mechanisms of disruptions using a set of non-linear resistive MHD equations which are solved with computer simulations. At the forefront of the theoretical and computational effort are the ORNL group — including Hicks, Carreras, Wadell, Lynch, and Lee ^(2.1–2.5) — and the Princeton group — including Montecello, White, and Rosenbluth. ^(2.6–2.7) Numerous other authors have contributed to our understanding of tearing and resistive MHD. ^(2.8–2.17) Briefly, resistive MHD theory predicts the growth of unstable regions of the plasma. In certain cases, these regions can grow to such an extent that large parts of the plasma lose their confining properties. At this point plasma is lost, impurities enter the plasma rapidly, the current channel shrinks, and the overall balance of forces is lost. The entire process takes on the order of $100\mu\text{sec}$ in typical experiments, and is estimated to take tens of milliseconds in larger reactor-sized devices.

It is important to maintain a perspective on the status of our understanding of these events. The detail with which the literature describes disruptions conceals a fundamental inability to adequately describe the plasma and plasma current during disruption in a real machine. Whereas on the one hand there is compelling evidence that the theory correctly interprets the mechanisms of plasma disruption, on the other hand experiments show a degree of unpredictability which warrants caution. In addition, as stated earlier, these are but one of a class of plasma disturbances all of which are capable of serious effects on the reactor.

2.1.2. Basic MHD Theory

In ideal MHD theory, it can be shown that the plasma is stable to the class of current-driven instabilities called kink modes provided there is a sufficient rotational transform, or $q > 1$, where q is the safety factor. ^(2.18–2.19) This is the so-called Kruskal-Shafranov limit, where

$$q(r) = \frac{1}{2\pi} \int_0^{2\pi} \frac{r B_t(r, \theta) d\theta}{R(r, \theta) B_p(r, \theta)} \quad (2.1)$$

When q is locally less than 1, a phenomenon related to major disruptions is experimentally observed, called internal disruptions, or “sawtoothing”. An explanation for sawteeth is that the central current density builds up due to an increase in conductivity until q is less than one, at which time a rapid reorganization of the plasma core causes a flattening of the temperature and current density profiles. q returns to a value greater than one and the process repeats itself. This type of instability is classified as internal, since the affected region is within the $q = 1$ flux surface. Since internal disruptions result in current perturbations, they also induce eddy currents.

By controlling the plasma current profile, the Kruskal-Shafranov limit can be avoided. However, a different instability is observed to occur even when $q > 1$ throughout the entire plasma. This instability is predicted by resistive MHD theory which includes effects of finite plasma resistivity. Tokamak plasmas are normally stabilized by the nested structure of their magnetic flux surfaces. In a plasma with zero resistivity, magnetic field lines are unable to move across flux surfaces since Faraday’s law requires an electric field to form in that case:

$$\oint \mathbf{E} \cdot d\mathbf{l} = -\frac{d\Phi}{dt} \quad (2.2)$$

Particles in a plasma tend to remain attached to field lines, therefore if the flux surfaces remain well-behaved then the particles tend to be confined. With the inclusion of finite resistivity, a mechanism is introduced whereby field lines can cross one another and the stable, uniform magnetic field topology can be destroyed.

Fig. 2.1 shows a simplified drawing of a linear current sheet before and after tearing. The current starts out uniform with nested flux surfaces. Currents flowing in the same direction tend to attract, resulting in a compressive force on the current sheet. Given the constraints on a real plasma, the current cannot shrink to the center of the current distribution, but rather it tends to break into a small number of filaments which have a lower net magnetic energy.

The breaking of the current into smaller filamentary structures gives rise to “islands” in the flux surface topology – unconnected regions with the same value of the scalar flux function. The energy to drive the instability is supplied by the perpendicular magnetic field. The rate at which the island structures form is determined by resistive diffusion of the field lines at the location of

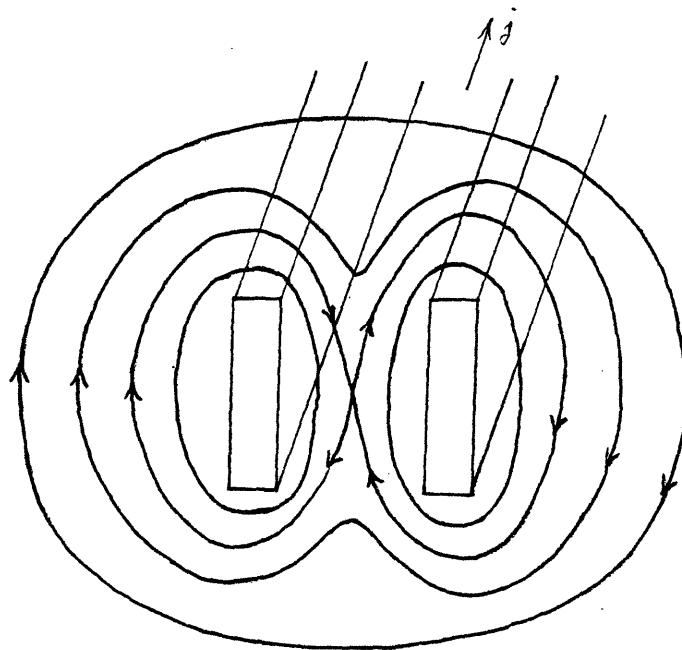
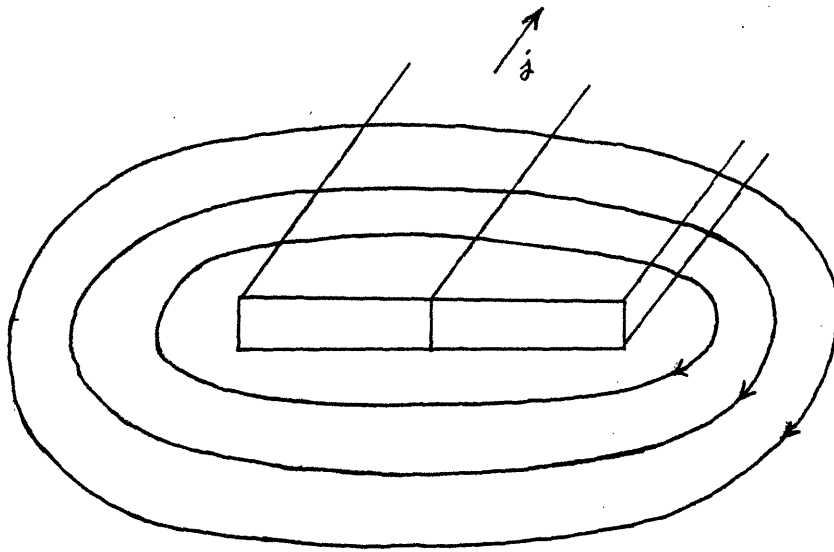


Figure 2.1 Fields from a Current Sheet Before and After Tearing

tearing and reconnecting field lines. This kind of fragmentation of plasma currents and formation of separate island structures is a simple picture of the mechanism suspected to result in major plasma disruptions.

The growth of island structures is seen both in theory and in experiment. Fig. 2.2 shows an example of the magnetic flux surfaces similar to the one above but in a toroidal geometry. Plasma currents flow toroidally in clumps, resulting in island structures. In the figure, the first two plots are for the $m = 2$ tearing mode with perturbed field amplitudes $b_r/B_0 = 2\%$ and 8% . The other plots are $m = 3$ with amplitudes 1% and 4% . The islands tend to form at mode rational surfaces where radial field perturbations tend not to cancel. Field lines which travel an integral number of times toroidally for each poloidal excursion compose what are called rational surfaces. Mode numbers m/n indicate that a field line travels m times toroidally for every n times poloidally before reconnecting. Particles travelling in orbits along these field lines may be excited resonantly by perturbations, which explains why instabilities tend to grow at these radial locations.

All plasmas have some level of island formation, but in a stable plasma the growth stops at some low level when the local fields relax sufficiently that the magnetic energy is insufficient to drive the modes further. The lower m number modes are more strongly unstable and are most likely to continue growing. It is postulated that a typical disruption will originate at the $2/1$ and $3/2$ surfaces. If the islands continue to grow without saturating, then the perturbed currents and fields can destabilize the plasma at other surfaces. If the islands grow finally to the point where they physically overlap, then rapid radial transport can occur via motion parallel to the field lines. When many modes are excited and ergodic regions formed, it is possible that a new equilibrium could be found in which case the discharge continues, slowly heating up to regain the energy lost during the disruption. However, it is more likely that the distorted currents and magnetic fields will interact in such a way as to release the plasma, resulting in a major plasma disruption.

Another possible sequence resulting in termination occurs if field lines intersect the first wall or limiter during the island growth phase. The growth of a single helical mode could result in this type of disruption. In this case, the entire plasma can dump itself locally in a matter of milliseconds. Wall and limiter related disruptions are observed experimentally in some devices. They can be a special concern due to their tendency for localized deposition of the plasma.

2.1.3. Stabilization of Tearing Modes

Several techniques have been considered for stabilizing tokamaks against disruptions. It is not clear whether or not these methods will be dependable enough such that protection requirements on the structure will be lessened. Most reactor designs do not assume the existence of a reliable scheme for eliminating disruptions.

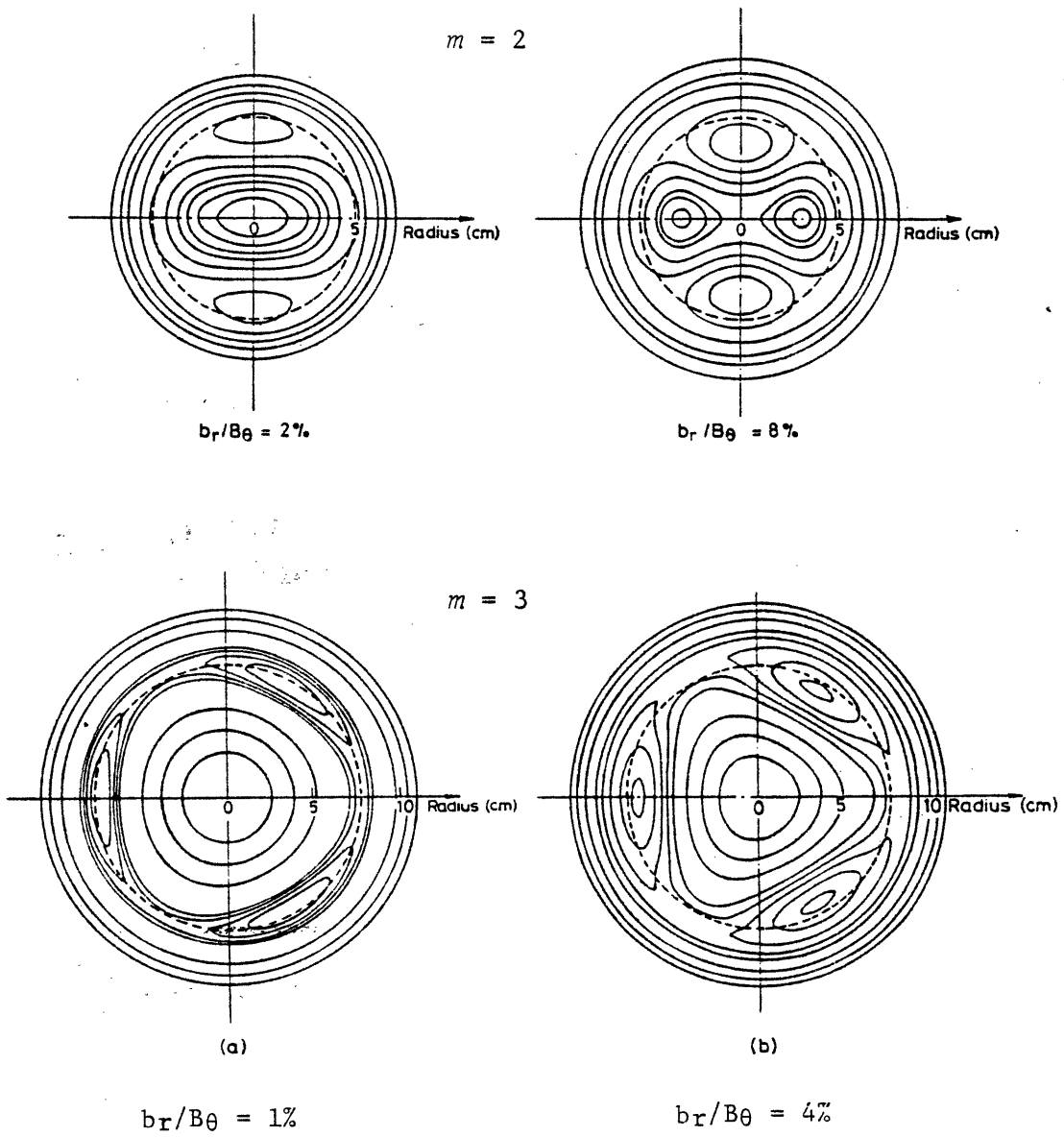


Figure 2.2 Flux Surfaces in a Torus (Ref. 2.22)

Except for discharges with very low q , most plasmas should exhibit a linearly unstable $m = 2/n = 1$ perturbation. The propensity for disruption depends upon the saturation width of the islands. This in turn is linked closely with a parameter Δ'_{mn} which represents the discontinuity in the derivative of the flux function at the singular surface.

$$\Delta'_{mn} = \frac{\lim_{\delta \rightarrow 0} \left(\left. \frac{d\psi_{mn}}{dr} \right|_{r_+} - \left. \frac{d\psi_{mn}}{dr} \right|_{r_-} \right)}{\psi_{mn}(r_{mn})} \quad (2.3)$$

where r_{mn} is the radial position of the singular surface, $q(r_{mn}) = m/n$, and $r_{\pm} = r_{mn} \pm \delta$. In linear tearing mode theory, the potential energy δW of a mode is proportional to Δ' .

Most proposed and operational stabilization schemes involve limiting the growth rate and island width of the $m = 2/n = 1$ mode by applying an external helical field. This field will alter the flux function in such a way that Δ'_{mn} is reduced or even made to be ≤ 0 , the condition for a stable, fluctuation-free 2/1 mode. There is a range of values for $\Delta' > 0$ which do not result in disruption, but do enhance the level of 2/1 fluctuations. Experimentally this technique has been proven to both reduce the fluctuation level and reduce the frequency of disruptions.

Another method of stabilization involves altering the current profile near the $q = 2$ surface. The MHD equations show that the gradient in the flux function is roughly proportional to the gradient in the equilibrium current density, j . Then controlling the current profile (and therefore the q profile since $q \propto 1/B_p$ and $B_p \propto I/r$) is clearly just another way of making $\Delta' \leq 0$. Selectively heating the electrons outside of the $q = 2$ surface will result in a local enhancement of the conductivity, therefore a local enhancement in the current density assuming constant loop voltage.

Unfortunately, if for some reason the heating is done just inside of the $q = 2$ surface (instead of outside), then the 2/1 mode is more strongly *de*-stabilized. Results on the JIPP T-II experiment illustrate the use of this technique. (2.20)

2.2. Tokamak Experiments

2.2.1. Overview

The occurrence of disruptions in experimental devices has been commonplace as long as tokamaks have been in operation. Experiments are often by their very nature designed to push the limits of their operating regime to obtain maximum ohmic heating input and low q . Consequently, the boundaries of stable operation have been determined for many machines with a moderate degree of accuracy. In the course of operation, both intentional and inadvertent disruptions have been documented, giving a large base of data on which to draw. Unfortunately, as previously mentioned, the effects of disruptions are far less studied than the physics of disruptions.

With the occurrence of disruptions so common, the question arises: why are disruptions such a problem? But the tolerability of disruptions in experiments should not be taken as an indication of the safety of reactor-size plasmas. The energy content of a power producing reactor is orders of magnitude higher than present-day experiments - hundreds of megajoules compared with a couple of megajoules. In fact, even in small experimental devices physical damage has been done by disruptions - particularly by corroding, melting, bending, or breaking the limiter.

An extensive literature search was performed to identify the major experimental efforts in the world to examine plasma disruptions, including ALCATOR, PLT, TFR, TOSCA, PULSATOR, and LT-3. The types of measurements are described together with a brief discussion of their results.

2.2.2. Diagnostics Used

The principal source of data for studying disruptions comes from measurements of MHD magnetic activity, which is a fairly commonplace procedure for Tokamak experiments. Magnetic field measurements can help determine the current density, transform profile, and detailed structure and growth rate of the various magnetic perturbations. In addition to MHD activity, observations of other plasma characteristics also help elucidate the process of disruption. These related phenomena include in particular the large negative voltage spike associated with a disruption, plasma shifts, X-ray and H_{α} emission, temperature profiles, and impurity behavior.

The two most widely used diagnostics for studying disruptions are Mirnov coils (magnetic pickup loops) and X-ray detectors. Mirnov coils operate by intercepting a small amount of flux outside the plasma. Using Faraday's law, the magnetic field strength can be obtained by integrating the induced voltage across the loop. Characteristics of the current and magnetic field structures within the plasma can then be inferred from the external fields produced. In rare instances where the plasma is quite cold (such as LT-3), coils can be placed directly inside the plasma, allowing for a much simpler and more accurate measurement of the poloidal field, current density, and q-profile.

X-ray detectors are usually mounted in arrays which image a cross section of the plasma. By observing the emissivity of the plasma to X-rays, temperature and impurity fluctuations can be studied and correlated to the MHD results.

2.2.3. Some Results

Experimental evidence clearly shows that MHD activity rises before and during disruptions. In particular, strong $m = 3/n = 2$ and $m = 2/n = 1$ modes are observed in agreement with the resistive MHD theory.

In addition to simple observations, TOSCA and PULSATOR have stabilized and induced disruptions with external helical field coils.^(2.21—2.23) Low levels are seen to lower the critical current at which disruptions are observed, presumably due to altered q profiles and the hindrance of mode rotation. At some field level, the perturbation becomes great enough to destabilize the plasma and *cause* a disruption.

In PLT and LT-3, impurities are observed to build up prior to the disruption.^(2.24—2.28) This leads to radiation from the center and lowered temperature. Since resistivity is a strong function of temperature, the current profile is deformed. The effects of impurities on the power balance and on the q profile are probably significant factors in the discharge termination.

2.3. Engineering Analysis

The majority of work on the effects of disruptions has been associated with reactor design studies. In some cases there is a significant amount of analysis which accompanies the design decisions, but more often the designs reflect current opinions and limited investigations. This seems natural since the design of a reactor involves many interrelated concerns, few of which can be carried out in full detail.

One of the first attempts to estimate the consequences of disruptions was performed for the TNS design.^(2.29—2.30) The calculations were largely zero or 1-D methods and concentrated almost exclusively on thermal effects. Force calculations were mentioned, but almost none were attempted. Estimates of eddy current heating suggested that this energy source is much lower than direct deposition of plasma energy and can often be ignored.

Probably the most detailed description of disruption design considerations was done for the FED/INTOR design.^(2.31—2.35) This includes thermal calculations, vaporization and erosion rates, electromagnetic loads, gap voltages and arcing.

Calculations show that a melt layer may form due to the dump of plasma energy onto the first wall. The time constant for the plasma thermal quench is generally believed to be quicker than the current transient. Thus, at the time when melting occurs there is likely to be substantial forces on the melt zone due to induced currents. Abdou has investigated the stability of this melt zone, the erosion rates of the first wall, and lifetime estimates.^(2.31)

Thome, Pillsbury, and Mann have investigated the forces and torques on sectors of FED/INTOR with special emphasis on the effects of segmentation.^(2.32) In addition, gap voltages are computed and the problem of arcing across sectors is examined.

The INTOR Phase I workshop^(2.33) and Critical Issues report^(2.34) document detailed calculations of thermal behavior of the first wall. The energy equation is solved numerically

to produce temperature rise and thermal stress estimates. Variations are made to materials and disruption characteristics and differences in effects contrasted. Electromagnetic forces are also studied in detail. Forces and torques are computed on the first wall, first wall tiles, coolant tubes, and the limiter. The effects of varying L/R time constant, material properties, and segmentation are studied.

Finally, in the 1983 FED Baseline Study, ^(2.35) the effect of a conducting EM shield is examined. The shield is found to have many beneficial effects, including

1. lengthening of the current decay time
2. protecting the other structures by absorbing the induced currents
3. lowering the thermal load on the first wall by keeping the plasma from resistively dissipating the magnetic energy
4. preventing arcing.

One of the distinguishing features of the original FED design was the presence of a large number of graphite armor tiles for protection against the thermal consequences of disruptions. These tiles present many problems for breeding, thermal stress, heat transfer, etc. It is speculated that with the help of an EM shield and less severe assumptions about the disruption characteristics, the graphite tiles can be eliminated in future designs.

Forces are calculated for STARFIRE first wall and limiter ^(2.36). The plasma current is assumed to be toroidal, as is the custom, and spatial distribution about the wall is ignored. Off normal effects in general are not considered as thoroughly as other sources.

The DEMO design ^(2.37) has considerably more discussion of disruptions, but little was done to add to the INTOR results. The thermal calculations, melt layer stability and electromagnetic loads are all treated similarly to INTOR.

References:

- 2.1 B. Carreras et al., "Nonlinear Coupling of Tearing Modes with Self-Consistent Resistivity Evolution in Tokamaks," ORNL/TM-7161, 1980.
- 2.2 H. Hicks, B. Carreras, et al. "Interaction of Tearing Modes of Different Pitch in Cylindrical Geometry," ORNL/TM-6096.
- 2.3 B. Carreras, B. Waddell, "Analytic Model for the Non-Linear Interaction of Tearing Modes of Different Pitch in Cylindrical Geometry," ORNL/TM-6175, 1978.
- 2.4 B. V. Waddell, B. Carreras, et al., "Mechanism for Major Disruption in Tokamaks," Phys. Rev. Lett., vol.42, no.20, pp.1386-1389 or ORNL/TM-6213, 1978.
- 2.5 Holmes, B. Carreras, et al., "Stabilization of Tearing Modes to Suppress Major Disruptions in Tokamaks," ORNL/TM-6707, 1979. (also in Nuclear Fusion, Vol. 19, No. 10, p. 1333-1389, October 1979.)
- 2.6 R. B. White, D. A. Monticello, and M. N. Rosenbluth, "Simulation of Large Magnetic Islands: A Possible Mechanism for a Major Tokamak Disruption," Phys. Rev. Lett., vol.39, no.25, pp.1618-1621, 1977.
- 2.7 R. B. White, D. A. Monticello, and M. N. Rosenbluth, "Simulation of a Major Tokamak Disruption," PPPL-1364, 1977.
- 2.8 H. R. Strauss, "Nonlinear, Three-Dimensional Magnetohydrodynamics of Noncircular Tokamaks," Phys. Fluids, vol.19, 1976.
- 2.9 V. V. Arsenin, "Perturbation Growth Rates Associated With Current Disruption in a Tokamak," Sov. J. Plasma Phys., vol.3, pp.524-525, 1977.
- 2.10 N. Ohyaabu, "Suppression of Plasma Disruptions in Tokamaks," GA-A-15006, 1978.
- 2.11 T. H. Stix, "Current Penetration and Plasma Disruption," Phys. Rev. Lett., vol.36, no.10, pp.521-524, 1976.
- 2.12 A. Rogister and G. Hasselberg, "Interpretation of Precursors of Internal Disruptions," Phys. Rev. Lett., vol.37, no.14, pp.906-909, 1976.
- 2.13 G. Lisitano, "Feedback Mechanism for the Precursors of Major Disruptions," IPP-III/44, 1978.
- 2.14 I. Itoh, S. Indue, and S. Yoshikawa, "Nonlinear Magnetohydrodynamic Instability and Disruptive Instability," J. Phys. Soc. JPN., vol.40, no.6, pp.1757-1761, 1976.
- 2.15 A. B. Rechester and T. H. Stix, "Magnetic Braiding Due to Weak Asymmetry," Phys. Rev. Lett., vol.36, no.11, pp.587-591, 1976.

- 2.16 J. M. Finn, "The Destruction of Magnetic Surfaces in Tokamaks by Current Perturbations," Nuclear Fusion, vol.15, pp.845-854, 1975.
- 2.17 A. Sykes and J. A. Wesson, "Major Disruptions in Tokamaks," Phys. Rev. Lett., vol.44, no.18, pp.1215-1218, 1980.
- 2.18 G. Bateman, MHD Instabilities, The MIT Press, Cambridge Massachusetts, 1978.
- 2.19 H. P. Furth, Propagation and Instabilities in Plasmas, ed. by W. I. Fetterman, Stanford University Press, Stanford California, p.87, 1973.
- 2.20 K. Toi, S. Itoh, K. Kadota, K. Kawahata, and N. Noda, "Suppression of Disruptive Instabilities by Skin Heating in the JIPP T-II Tokamak," IPPJ-Nagoya Research Report, 1978.
- 2.21 K. McGuire and D. C. Robinson, "Major Disruptions in the TOSCA Tokamak," Phys. Rev. Lett., vol.44, no.25, pp.1666-1669, 1980.
- 2.22 D. C. Robinson and K. McGuire, "Magnetic Islands and Disruptions in the TOSCA Tokamak," Nuclear Fusion, vol.19, no. 1, 1979.
- 2.23 F. Karger et al., "Influence of Resonant Helical Fields on Tokamak Discharges," IAEA-CN-33/PD-2, 5th International Conference on Plasma Physics and Controlled Nuclear Fusion Research, Tokyo, 1974.
- 2.24 N. R. Sauthoff, S. von Goeler, and W. Stodiek, "A Study of Disruptive Instabilities in the PLT Tokamak Using X-Ray Techniques," Nuclear Fusion, vol.18, no.10, pp.1445-1458, 1978.
- 2.25 I. H. Hutchinson, "Magnetic Probe Investigation of the Disruptive Instability in Tokamak LT-3," Phys. Rev. Lett., vol.37, no.6, pp.338-341, 1976.
- 2.26 A. H. Morton, "Disruptive Instability Mode Structure in the LT-3 Tokamak," Nuclear Fusion, vol.17, no.4, pp.863-869, 1977.
- 2.27 D. B. Albert and A. H. Morton, "Fast Growing Helical MHD Modes During the Disruptive Instability in LT-3 Tokamak," Nuclear Fusion, vol.17, no.6, 1977.
- 2.28 A. H. Morton and K. G. Srinivasacharya, "Spectroscopic Observation of LT-3 Tokamak Plasma at Disruptive Instability," Nuclear Fusion, vol.18, no.10, pp.1417-1423, 1978. (also PGPP-77-2, October 1977)
- 2.29 R. J. Onega, W. R. Becraft, and E. S. Bettis, "Major Plasma Disruptions in TNS," ORNL/TM-6616, 1979.
- 2.30 R. J. Onega, W. R. Becraft, C. A. Kukielka, "The Thermal Consequences to the First Wall of a Deuterium-Tritium-Fueled Tokamak Due to a Major Plasma Disruption," Nuclear Science and Engineering, vol. 75, pp. 243-257 (1980).

- 2.31 M. A. Abdou, "INTOR Impurity Control System," ANL/FPP/TM-173, April 1983.
- 2.32 R. J. Thome et al, "Sector Gap Voltages and Induced Loads Following Plasma Disruption In FED/INTOR," DOE/ET-51013-64 (also FED-INTOR/MAG/82-2)
- 2.33 W. M. Stacey, Jr. et al, "The U.S. Contribution to the International Tokamak Reactor Phase-1 Workshop," INTOR/81-1, Vol. I, pp 189-219, June 1981.
- 2.34 U.S. FED-INTOR Critical Issues Vol. 1, USA FED-INTOR/82-1, pp 149-196.
- 2.35 P. H. Sager et al, "FED Baseline Engineering Studies Report," ORNL/FEDC-82/2, chaps. 4 and 6, April 1983.
- 2.36 "STARFIRE, A Commercial Tokamak Fusion Power Plant Study," ANL/FPP-80-1, Sept. 1980.
- 2.37 "A Demonstration Tokamak Power Plant Study (DEMO)," ANL/FPP-82-1, pp 5-87 to 5-103, sept. 1982.

Mechanical Strain Test

3.1. Purposes

One of the fundamental constraints on the strain experiments performed for this work is the limitation on the level of sinusoidal current which can be produced using available power supplies and amplifier circuitry. The maximum expected strain level is derived and plotted in section 4.2. Roughly, the strain scales as

$$\epsilon \sim \frac{I^2}{h} \quad (3.1)$$

where h is the structure thickness and I is the induced current level. Operation of the experiment at the level of kiloamps, rather than megamps to tens of megamps as in a full-size tokamak, will result in forces 10^6 to 10^8 times smaller. The fact that reactor structures are larger than the 0.4 mm shell used in the Electromagnetic Strain Test (EST) is a mediating effect. The net result is that reactor strains of 1 to 10% scale down to less than 10^{-6} in the simulation experiments. From this general scaling it is clear that the strain levels will be low with respect to generally accepted standards, where 10^{-6} is considered low and 10^{-7} is very low.

It is critical to know just how small a strain can be measured in order to design large enough power supplies such that a measurable strain is obtained. Therefore, before designing a current-driven strain test it was decided to operate a preliminary test which would guide the design and selection of appropriate goals for the main experiment. This preliminary experiment is called the Mechanical Strain Test, or MST.

The semiconductor strain gauge was chosen as the preferred detection device due to its sensitivity, simplicity, and cost. This choice also defines the nature of the whole detection system. A gauge circuit is used with the gauges acting as variable resistors. The extremely low signal levels lead to the need for sophisticated electronic signal handling; for these experiments, sinusoidal loading was applied so that synchronous detection could be used. The most important piece of equipment for synchronous detection is the lock-in amplifier described later in this chapter.

Table 3.1 summarizes the purposes of the Mechanical Strain Test. It was performed in order to mechanically produce small, well characterized strains so that the strain gauge characteristics could be explored and limits could be placed on the minimum detectable strain levels. Experience was gained in the use of both gauges and signal processing techniques which were also used in the principal experiment discussed in Chapter 4 – the Electromagnetic Strain Test.

3.2. Strain Gauge Theory and Circuit Theory

3.2.1. Semiconductor Strain Gauges

Semiconductor strain gauges consist of small, ultra-thin rectangular cross-section filaments of a single crystal of silicon. The piezoresistive properties of silicon make it much more sensitive to strain than conventional metal foils or wires. To demonstrate this, consider the equation for gauge sensitivity:^(3.1)

$$\tilde{S}_a = 1 + 2\nu + \frac{d\rho/\rho}{\epsilon} \quad (3.2)$$

where ν is Poisson's ratio, ρ is the gauge resistivity, and ϵ is the strain along the gauge axis. In common gauge alloys, the term $\frac{d\rho/\rho}{\epsilon}$ ranges from 0.4 to 2.0. For semiconductors $\frac{d\rho/\rho}{\epsilon}$ can be varied between -125 and 175 depending upon the type of impurity doping. Another advantage of semiconductors is their high resistivity; for silicon $\rho = 500\mu\Omega\text{-m}$ (ohm-meters⁻⁶). This allows the use of higher voltages, therefore higher circuit sensitivities, without resorting to the use of long, thin grids.

3.2.2. Gauge Circuits

There are several ways in which a variable resistance can be used in a circuit to display strains. The two most popular are the potentiometer circuit and the Wheatstone bridge circuit. These are sketched in Figures 3.1 and 3.2. V_s is the supply voltage and V_o is the output voltage. The potentiometer circuit is seldom used in static strain measurements due to the large DC offset of the output voltage. In dynamic measurements this DC can be low pass filtered to some extent.

For the Electromagnetic Strain Test, or EST, the bridge voltage must be modulated as part of the detection technique. This reduces the advantage of low pass filtering in a potentiometer circuit because the bridge frequency and the detected strain frequency are less easily separated. Due to the extreme sensitivity of the detection instruments used and the low signal to noise ratio, filtering was considered impractical and a Wheatstone bridge circuit was chosen. Even though the Mechanical Strain Test uses a DC source voltage, the more complicated bridge circuit was also used so that the characteristics of a bridge circuit would be understood for the EST.

Table 3.1 Purposes of the Mechanical Strain Test

1. calibrate and test linearity of gauges
2. determine the minimum detectable strain and the accuracy of measurements
3. explore noise sources and their elimination
4. gain experience with gauges and the use of noise rejection techniques

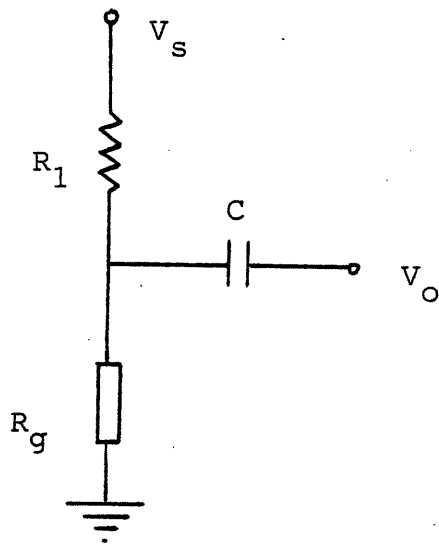


Fig. 3.1 Potentiometer Circuit

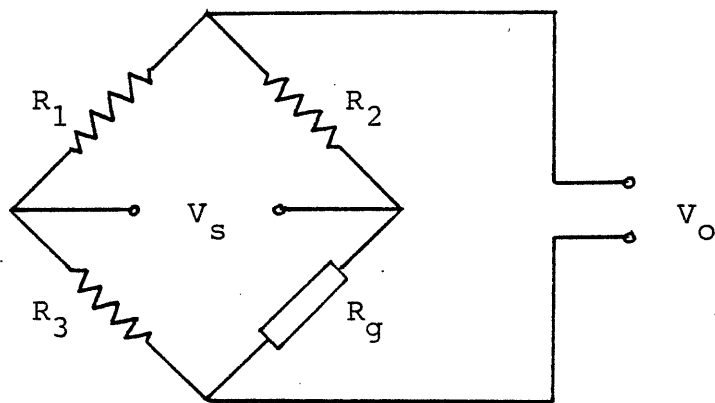


Fig. 3.2 Wheatstone Bridge Circuit

The Wheatstone bridge is operated near its balance point, therefore there is little DC offset of the output signal. Slow fluctuations — primarily in temperature — cause a small DC level to develop. But since all of the measurements are AC, this level is filtered out in the detection electronics. In the Electromagnetic Strain Test, with an AC bridge voltage, an offset results in large noise passage and is therefore more critical. In Chapter 4, the design of a self-balancing bridge circuit is described.

The output of the Wheatstone bridge is given by the expression:

$$V_o = V_s \frac{r}{(1+r)^2} \left(\frac{\Delta R_1}{R_1} - \frac{\Delta R_2}{R_2} - \frac{\Delta R_3}{R_3} + \frac{\Delta R_g}{R_g} \right) \quad (3.3)$$

where $r \equiv R_2/R_1$. Using a circuit sensitivity $S_c = V_o/\epsilon$ and only one variable leg in the bridge, it can be shown that

$$S_c = \frac{r}{1+r} S_g \sqrt{P_g R_g} \quad (3.4)$$

where P_g is the gauge power and R_g is the gauge resistance. Examination of this expression reveals that it is desirable to operate at the maximum power to the gauge. This is generally limited to ≤ 250 mW with a good heat sink. It is also desirable to balance the bridge with large resistors such that r is large. There is a tradeoff here, since the applied voltages can become fairly high with little gain in circuit sensitivity after a point. The value $r = 9$ is often chosen as a good compromise, leading to voltages of less than 100 v.

3.2.3. Performance of Gauges and Circuits

A key feature of these experiments is the treatment of noise, including thermal, electrical, and vibrational. The choice to use synchronous detection offers the possibility of eliminating many of the problems which are normally encountered in strain measurement. Most notably, there is no compelling reason to use temperature compensating circuit elements or self-compensating gauges. Changes in temperature can cause enormous changes in circuit output compared to the strains being measured (the temperature coefficient of gauges is typically $\approx 2.5 \mu\epsilon/^\circ F$). However these changes occur on a time scale hundreds or thousands of times slower than the true signal. Therefore, temperature variations are automatically compensated in the detection electronics.

Electrical and vibrational noise are classic problems for which the application of synchronous detection is only a partial solution. Good vibration isolation and electrostatic shielding are necessary to keep wideband noise from interfering near the detection frequency band and/or saturating the input channel of the amplifiers. Even though the lock-in amplifier is designed to narrow the detection bandwidth, in practice there is a limit to its effectiveness. More discussion on this topic appears in chapter 4.

Often linearity is a problem in strain measurement. The gauges themselves react nonlinearly to strain; the gauge sensitivity is not truly a constant. In addition, the circuit equations derived earlier do not include a nonlinear factor which is important for strains $\geq 5\%$. In the regime of 10^{-7} to 10^{-9} , all of these nonlinear factors should be negligibly small. In future analysis, the gauge circuit signal will be assumed linear with strain.

3.2.4. Rosette Calculations

For rosette calculations, the following formulas are used to obtain the principal stresses from the gauge strains:^(3.2) (refer to figure 3.3 for definition of strains)

Maximum Normal Stress (σ_{max}):

$$\frac{E}{2} \left\{ \frac{\epsilon_1 + \epsilon_3}{1 - \nu} + \frac{1}{1 + \nu} \sqrt{[(\epsilon_1 - \epsilon_3)^2 + (2\epsilon_2 - \epsilon_1 - \epsilon_3)^2]} \right\} \quad (3.5)$$

Minimum Normal Stress (σ_{min}):

$$\frac{E}{2} \left\{ \frac{\epsilon_1 + \epsilon_3}{1 - \nu} - \frac{1}{1 + \nu} \sqrt{[(\epsilon_1 - \epsilon_3)^2 + (2\epsilon_2 - \epsilon_1 - \epsilon_3)^2]} \right\} \quad (3.6)$$

Maximum Shear Stress (τ_{max}):

$$\frac{E}{2(1 + \nu)} \sqrt{[(\epsilon_1 - \epsilon_3)^2 + (2\epsilon_2 - \epsilon_1 - \epsilon_3)^2]} \quad (3.7)$$

Angle from Gauge 1 Axis to Maximum Normal Strain Axis (ϕ):

$$\frac{1}{2} \tan^{-1} \left[\frac{2\epsilon_2 - \epsilon_1 - \epsilon_3}{\epsilon_1 - \epsilon_3} \right] \quad (3.8)$$

Stress at an Arbitrary Angle from Maximum Stress Axis (σ'):

$$\sigma_{max} \cos^2 \phi + \sigma_{min} \sin^2 \phi \quad (3.9)$$

3.3. Lock-in Amplifier Theory and Technique

Since the use of synchronous detection so strongly affects many aspects of these experiments, it is worthwhile to consider the basic operation of a lock-in amplifier. The fundamental components of a lock-in amplifier are a 2-signal mixer and a variable time constant low pass filter. As shown in Figs. 3.4 and Fig. 3.8, the input signal to be measured is sent into a gate which is chopped by a square wave formed from the reference signal. The reference signal must be of precisely the same frequency as the detected signal and is usually derived from the input signal source — in our case

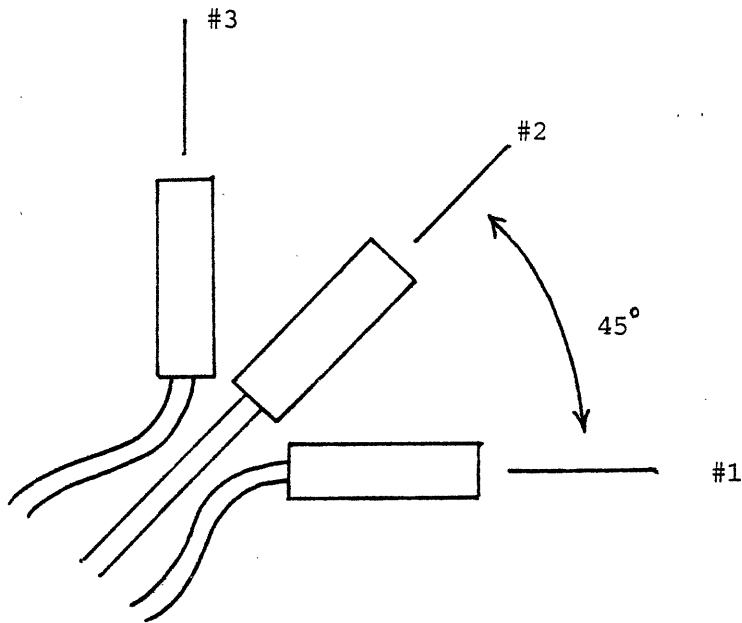


Figure 3.3 45° Rosette Pattern

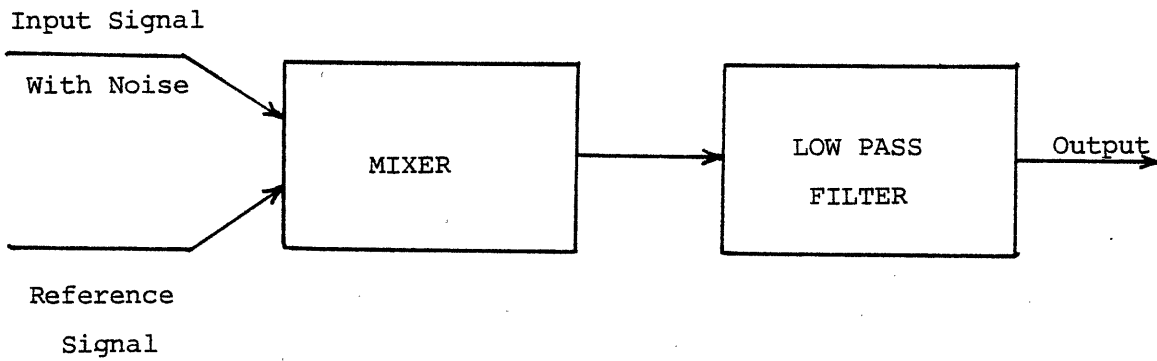


Figure 3.4 Lock-in Amplifier Block Diagram

the currents applied to the electromagnet. A phase angle adjustment on the reference signal allows for exact alignment of the two signals.

Each fourier component of the input signal produces sum and difference frequencies when they are mixed with the reference signal, as in

$$\cos(\omega_1 t) \cos(\omega_2 t + \phi) = \cos[(\omega_1 + \omega_2)t + \phi] + \cos[(\omega_1 - \omega_2)t - \phi] \quad (3.10)$$

(Note: care must be taken due to the fact that the reference signal is converted to a square wave in the lock-in amplifier. This means that additional higher harmonics of the input signal will be detected if they are at a harmonic of the reference signal.) The existence of a signal at zero frequency can be caused only by the one component equal in frequency to the reference (or its harmonics). Therefore, the signal level at zero frequency is proportional to the desired input signal strength. To obtain the DC level, the mixer output is filtered. By increasing the time constant of the filter, the lock-in integrates over more cycles and therefore decreases its effective bandwidth, increasing the sensitivity of the measurement.

3.4. Other Techniques in Small Strain Measurement

The greatest problem encountered in these experiments was detection of small signals in noise. Much thought was given to alternate concepts in ultra-small strain measurement techniques — particularly optical techniques. Future efforts in this area may find it advantageous to switch to one of these alternates. Table 3.2 is presented to summarize the various methods considered. They all fall into two categories: optical techniques and electrical techniques. Electrical devices suffer from the generic problem of electrical noise susceptibility, but are much cheaper and easier to use than optical devices. The choice of semiconductor strain gauges somewhat alleviated the problems with noise due to their excellent sensitivity.

3.5. Experiments and Results

3.5.1. Description of Experiments

Table 3.3 summarizes the measurements which have been performed and their purposes. In brief, the Mechanical Strain Test checks the linearity and calibration of the gauges as compared to a Fabry-Perot interferometer. In addition, the limitations of semiconductor strain gauges at very low signal levels have been explored with and without the technique of synchronous detection. The principal limitation to how small a strain one can detect is due to background noise — both electrical and mechanical/vibrational.

Table 3.2 Techniques in Small Strain Measurement

A. Electrical Techniques

- semiconductor strain gauges
- metal foil strain gauges

B. Optical Techniques

- holographic interferometry (with heterodyning)
- speckle pattern interferometry
- fiber optic sensors
- Fabry-Perot interferometry

Table 3.3 Summary of Measurements Taken for the MST

A. Compare strain gauge circuit output with Fabry-Perot interferometer output

- determine linearity of gauge
- measure circuit sensitivity and compare to calculated sensitivity

B. Calibrate strain gauge circuit output with electromagnet voltage

- determine characteristics of magnet for small strain tests

C. Small strain tests

- determine minimum strain measurable without synchronous detection
- determine minimum strain measurable with lock-in amplifier

The test stand used in these experiments is sketched in Figs. 3.5-3.6. The test piece is a brass cylinder which consists of thick end support sections tapering to the central test section where the strains occur. The central section measures 130 mm long, 16.1 mm in radius, and .127 mm thick. It is supported on top by a heavy Invar frame and from below by a cylindrical electromagnet attached to the frame. The electromagnet is responsible for producing the 1-D strains.

A single semiconductor strain gauge is mounted with epoxy on the active tube section. The axis of the gauge is parallel to the cylinder axis. In addition to the gauge, two 90% reflective mirrors are mounted at the ends of the test section to form the optical cavity for the Fabry-Perot interferometer.

Circuit diagrams are given in Figs. 3.7-3.8 for the Fabry-Perot and the low signal experiments. Component values for the strain gauge bridge circuit are given in Fig. 3.9.

3.5.2. Fabry-Perot Experiment

The Fabry-Perot test measures strain with the gauge and with a Fabry-Perot optical cavity and compares the two. This comparison was used to validate the gauge response in a high strain range.

A Fabry-Perot interferometer works by sending coherent light into an optical cavity formed by two parallel, partly transparent mirrors. When the light reflects off of the mirrors, it interferes with itself. Depending on the exact spacing of the mirrors, the interference can be either constructive or destructive. Due to the fact that the light reflects many times, on the average the waves cancel one another except when the spacing of the mirrors is very close to a half-integral number of wavelengths. In this case, a strong light signal can be detected emanating from the ends of the cavity.

The response of a Fabry-Perot interferometer versus mirror separation is characterized by a mathematical function called the "Airy function". This function is composed of narrow peaks at each $1/2$ wavelength of the laser light. Since the form of the Airy function is well known, it is possible to adjust the mirrors so that their separation places the optical response directly on the side of one of the peaks. Then very small movements of the order of $1/100$ th of the laser wavelength can be discerned. This sort of measurement requires very sensitive measuring and alignment equipment and therefore was not performed. Rather, for this experiment the peaks are counted as the mirror separation is increased. This implies that only fairly large strains can be studied. Smaller strain measurements are made without cross checking with the interferometer.

The test cylinder is typically placed in tension before running any test. This is accomplished by mechanically tightening the flanges at the ends and then applying a DC voltage to the electromagnet coil of 4-8 volts. (The coil was designed to produce ~ 1 lb/volt.) After an operating point is

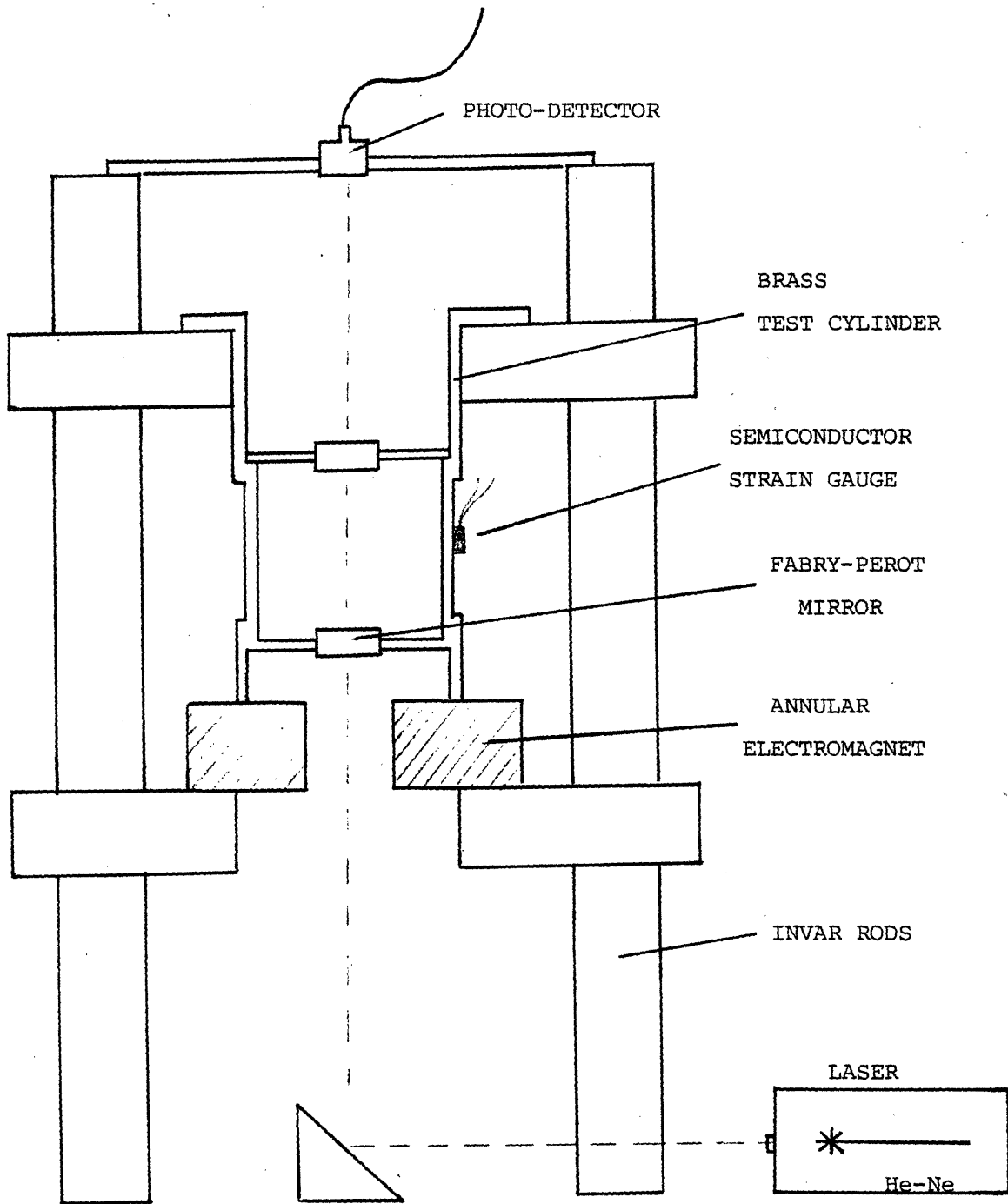
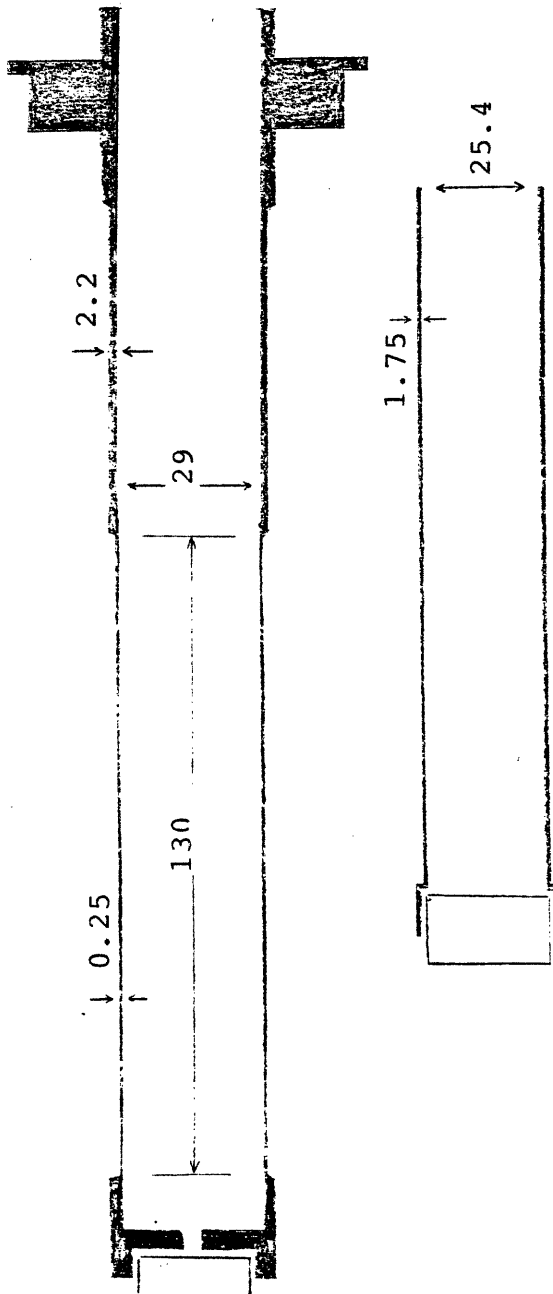


Figure 3.5 Strain Gauge Test Stand



(lengths in mm.)

Figure 3.6 Scale Drawing of Test Cylinder

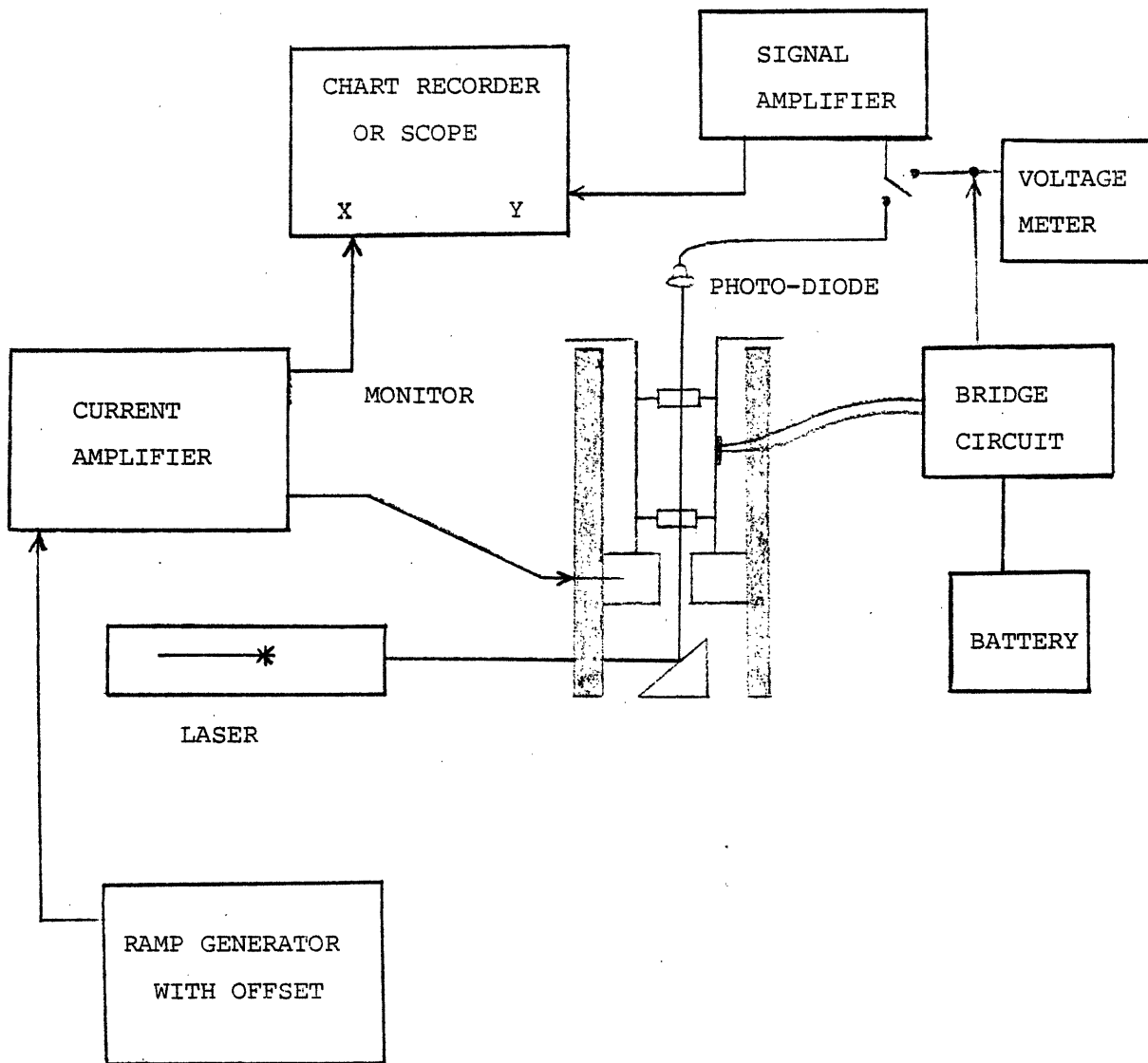


Figure 3.7 Fabry-Perot Experiment Block Diagram

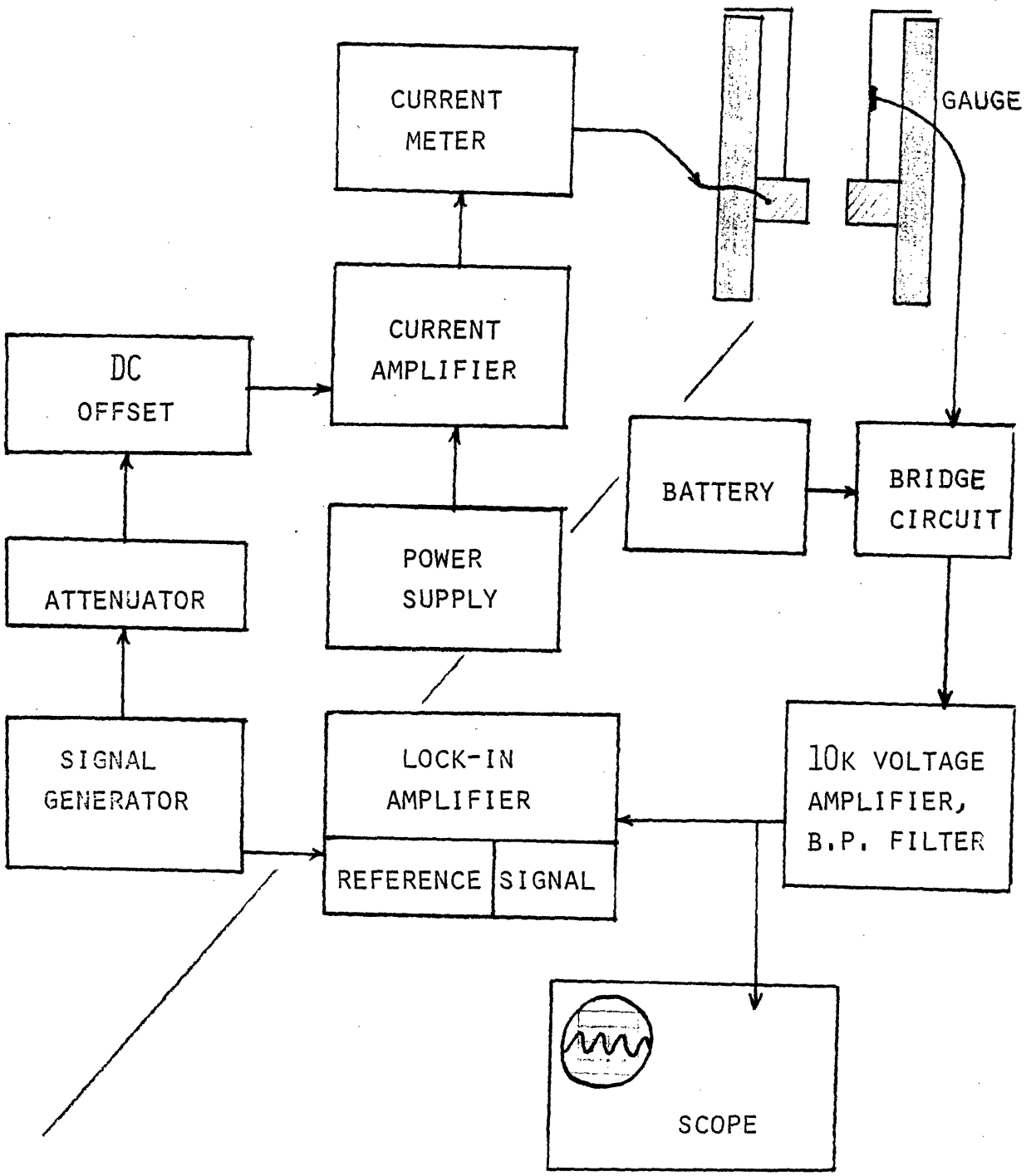


Figure 3.8 Low Signal Experiment Block Diagram

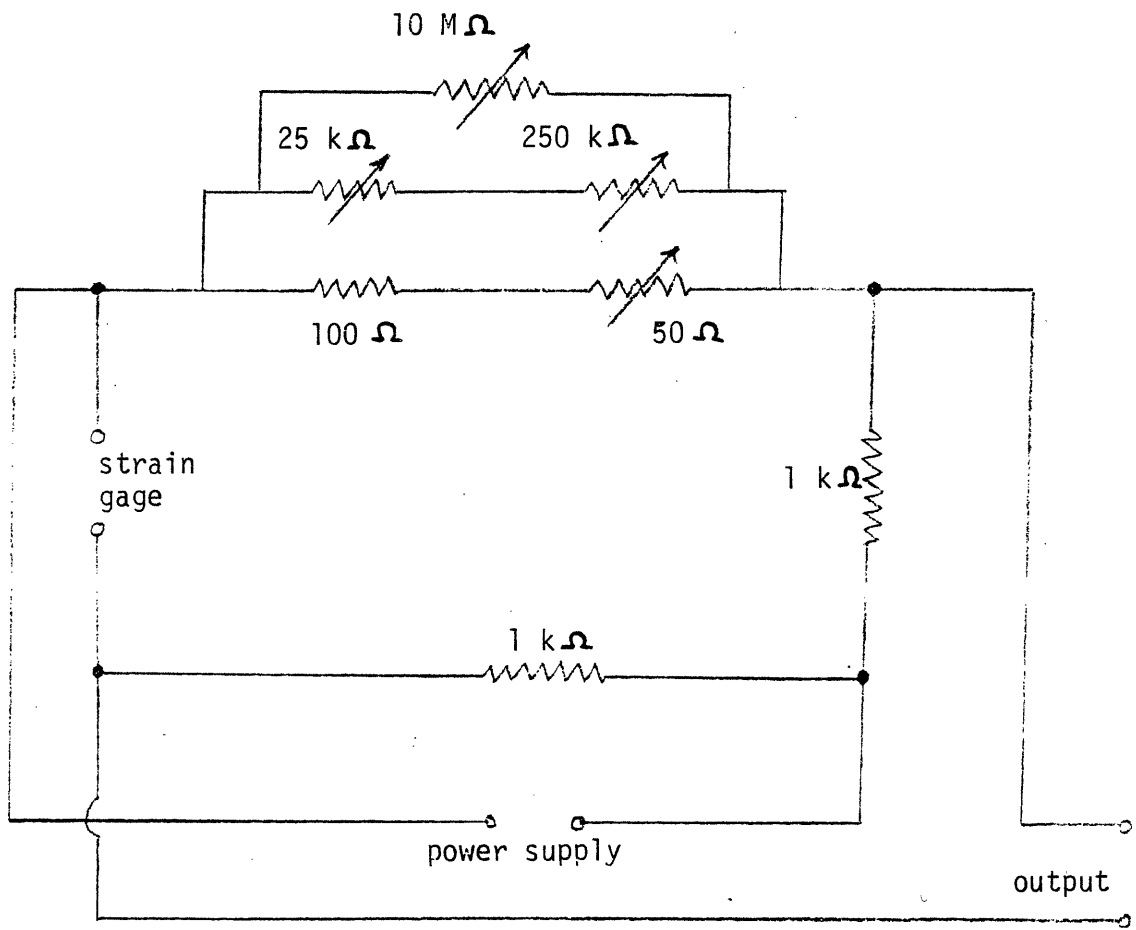


Figure 3.9 Bridge Circuit Schematic

established, small changes are made to the coil voltage. Simultaneous measurements are taken of the optical cavity response as it passes through its interference peaks and the strain gauge circuit response. Figure 3.10 is a comparison of these. It shows good linearity of the strain gauge at these levels of strain. Much of the uncertainty in the DC calibration results is due to poor thermal stability in the laser and in the bridge circuit. Slow drifts require that readings be taken rather quickly. For the data of figure 3.10, an x-y chart recorder was used which swept out the traces in ~ 15 seconds.

Fabry-Perot resonances normally occur every half wavelength of separation between the mirrors, or 3164 Å for the He-Ne laser. However, more than one wavelength exists in the cavity of the laser employed. This is a result of the fact that the laser cavity will resonate whenever an integral number of wavelengths fits inside the cavity, subject to the restriction that the wavelength is within a narrow envelope centered at 6328 Å. It has been demonstrated by close observation of the peaks that there are actually two wavelengths radiating from the laser. Therefore, there are two peaks for every 3164 Å of mirror separation.

Given the test piece length of 13 cm., the expected strain per peak should be

$$\frac{3164 \times 10^{-8}}{2(13)} = 1.217 \mu\epsilon/\text{peak}.$$

Using Fig. 3.10 and the gauge circuit sensitivity given by equation 3.4 of $23.6 \mu v / \mu\epsilon$, we calculate a strain per peak from the gauge of $1.17 \mu\epsilon$ per peak. This is a 4% error compared to the Fabry-Perot results, well within the error of the measurements.

3.5.3. Electromagnet Calibration

For the low-strain experiments, the Fabry-Perot interferometer was not used. Peak counting is not possible at small strains, and the hardware available was not capable of calibrating with a single peak. Therefore, it was necessary to calibrate the strain signal detected versus electromagnet current, where the electromagnet current is related to the force imposed. The calibration is done at large strains and extrapolated assuming local linearity of force versus electromagnet current. The data for the calibration is contained in figure 3.11. The derivative of figure 3.11, smoothed by cubic splines, indicates that the optimum operating point is at a DC current of 1.0 amps. At that point, the value of the derivative is $\sim 300 \mu v$ of gauge circuit output per amp on the magnet, or $\sim 10 \mu\epsilon/\text{amp}$.

In addition to the DC calibration, a more accurate AC calibration was performed at 29 hz. and an operating point of 1 amp. The test was performed at rather large strains of $0.1 \times 10^{-6} \leq \epsilon \leq 4.2 \times 10^{-6}$. The output signal is filtered, amplified, and sent directly to an oscilloscope. The measurement is then taken visually off of the scope, with errors resulting primarily from the

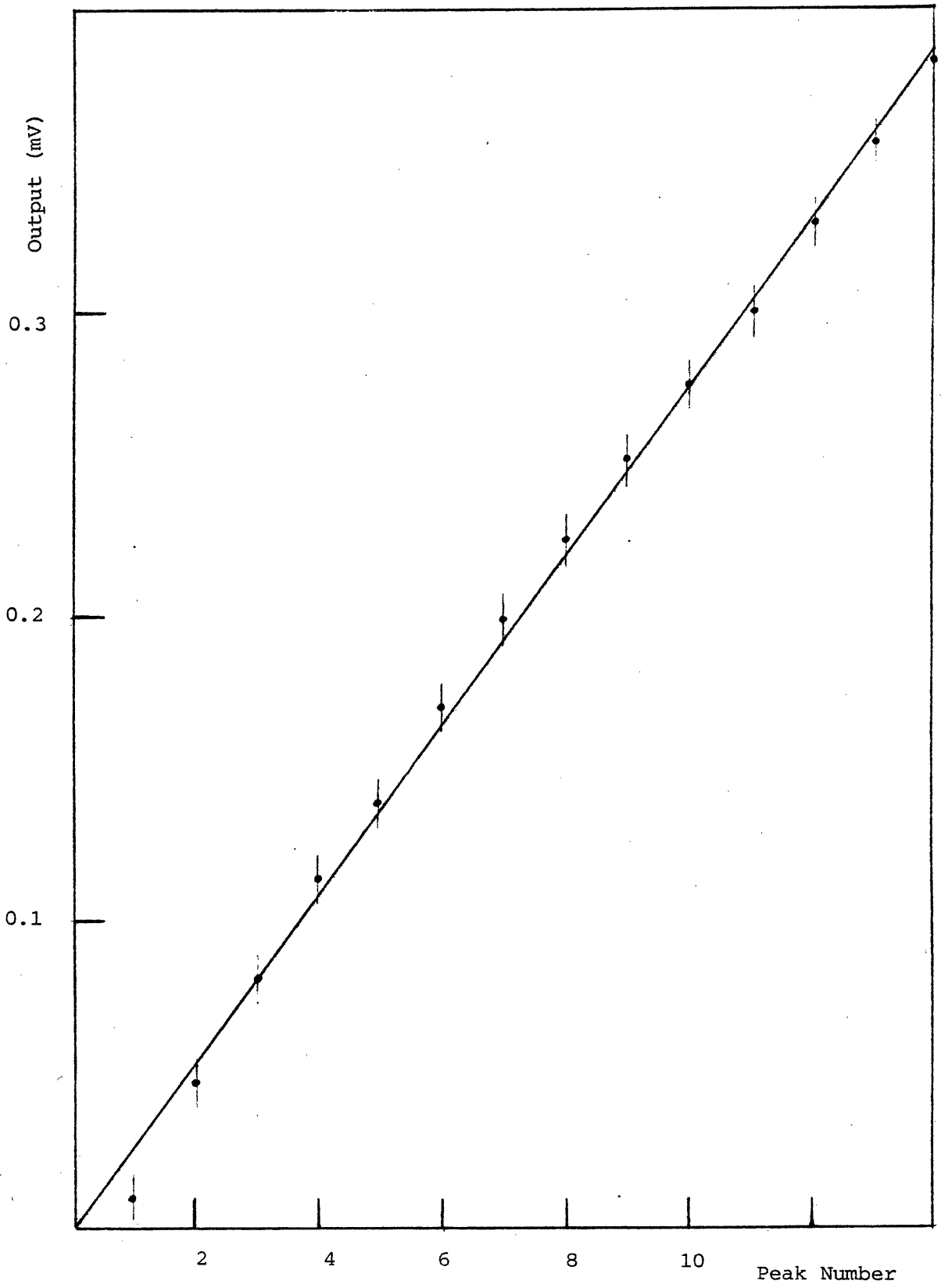


Figure 3.10 Gauge Output vs. Fabry-Perot Peak Number

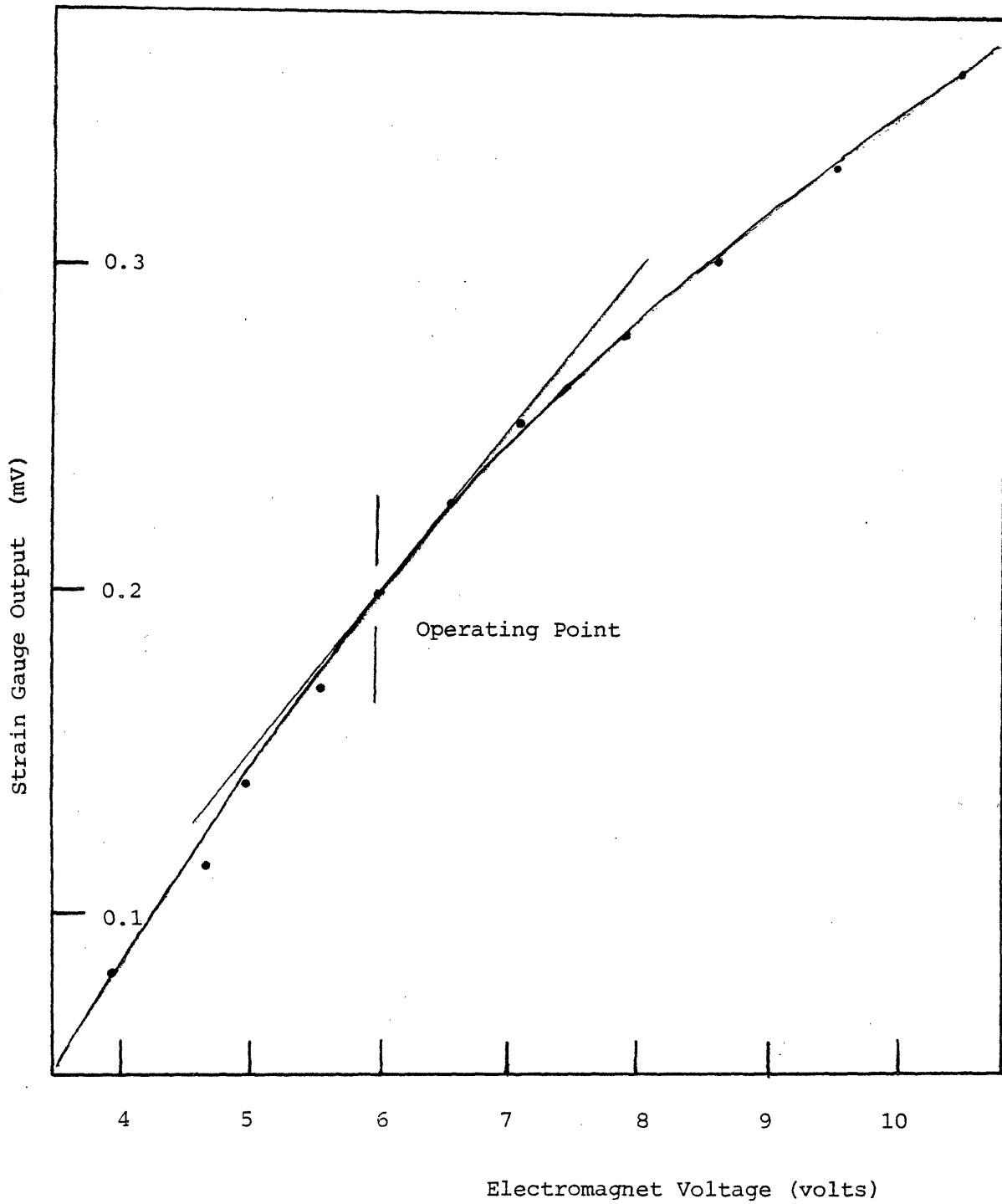


Figure 3.11 D.C. Electromagnet Calibration

inability to read the signal strength over the ambient noise level of ~ 1 microvolt. The results show that at the level of noise present, strains below 3×10^{-7} are not easily measured directly. The calibration gives $2.7 \mu\epsilon$ /amp at strains below 10^{-6} (see figure 3.12).

3.5.4. Small Strain Tests

The small-strain tests were executed by applying a small, sinusoidally varying signal to the electromagnet and observing the gauge circuit response. They were operated at strains of $10^{-9} \leq \epsilon \leq 400 \times 10^{-9}$ and frequencies of 29 hz. and 21 hz. Again, the strain is computed from the output voltages using the AC calibration of section 3.5.3. However, for these tests, the signal is sent to a lock-in amplifier which generates a DC level proportional to the RMS input signal strength. The lock-in reference frequency is obtained from a synchronous pulse produced by the signal generator. For these data, integration time constants varied between 3 and 100 seconds, depending on the strain range. Generally speaking, for strains $\geq 10^{-7}$, 3 seconds was sufficient. For $\epsilon \geq 10^{-8}$, 10 seconds was sufficient. And for $\epsilon \leq 10^{-8}$, a 30 second time constant was necessary. The low-pass/high-pass pre-filter was set at 3 db frequencies of (30 hz low, 30 hz high) for the 29 hz experiment, and (10 hz low, 30 hz high) for the 21 hz experiment.

Data of lock-in signal versus calibrated strain appear as figures 3.13-14. The calibrated strain is computed from the magnet current, using figure 3.12. The lock-in signal is converted to strain using $29.3 \mu v / \mu\epsilon$ for the circuit sensitivity. The difference in circuit sensitivity as compared to the Fabry-Perot experiment is explained by a change in bridge voltage. The data show that down to about 3×10^{-9} the amplifier can lock in and follow these small strains. The absence of frequency dependence in the results indicated that induced voltage pickup from the magnet and reduced magnet response are not being observed. Induced voltages were additionally tested for by unscrewing the test cylinder and repeating the measurement with the gauge close to its normal position. No signal was observed under these conditions.

3.5.5. Conclusions

Using standard off-the-shelf strain gauges and no particularly sophisticated means for noise removal other than filtering, semiconductor strain gauges were operated and calibrated down to $\sim 10^{-9}$ m/m. For $\epsilon \geq 10^{-7}$, strains can be picked out of the noise by eye. For $5 \times 10^{-9} \leq \epsilon \leq 10^{-7}$ the lock-in amplifier can easily track the signal in the noise. For $\epsilon \leq 5 \times 10^{-9}$ the lock-in accuracy begins to deteriorate ($\sim 10\%$), and at $\epsilon \leq 2 \times 10^{-9}$ it is difficult to lock in to the signal at all.

The primary sources of noise were studied to determine simple ways to improve the sensitivity of measurement. Noise sources must be minimized because the limitations on detectability and accuracy are determined by the noise levels and the noise-to-signal ratios obtainable in the detection

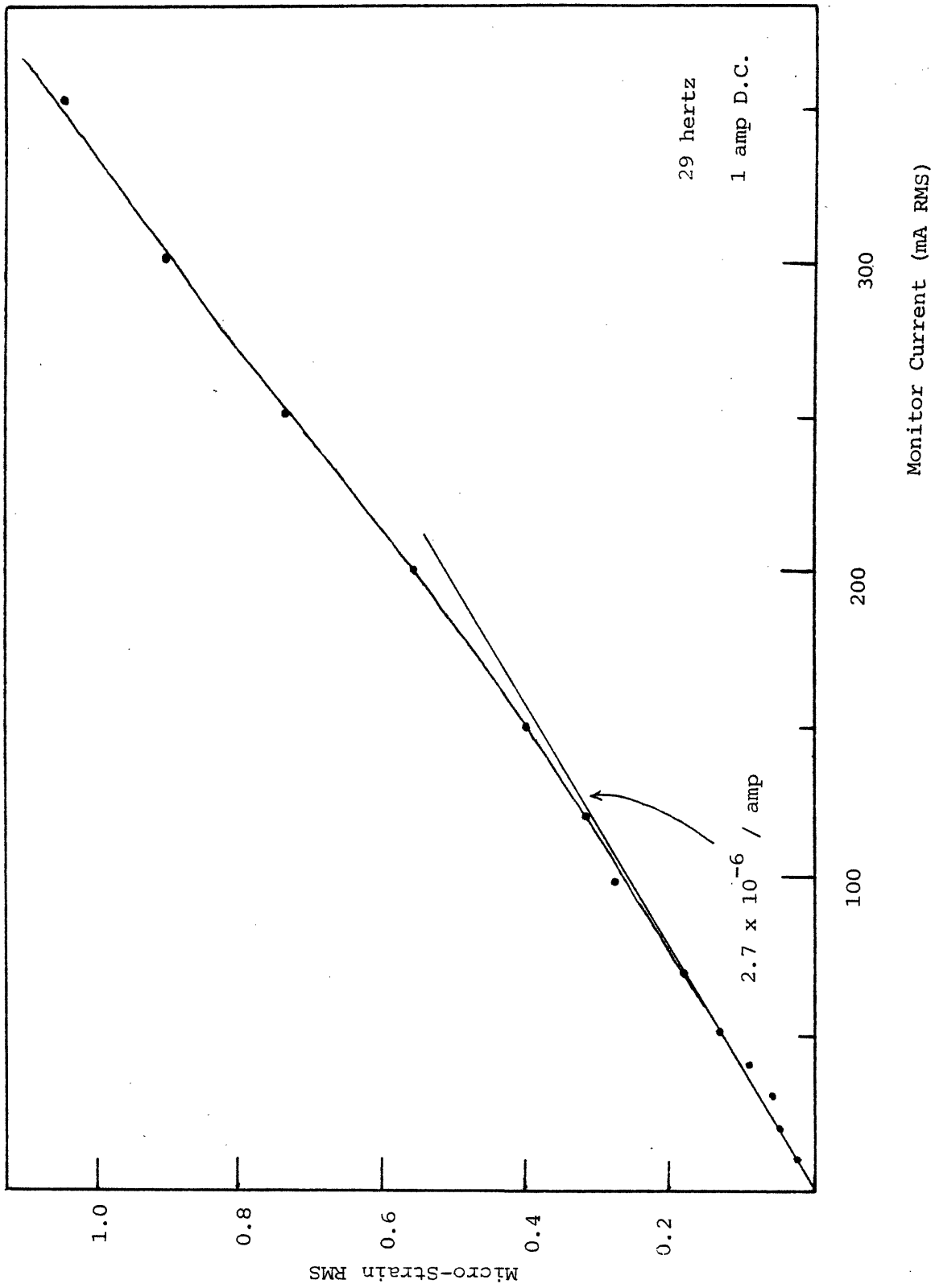


Figure 3.12 A.C. Electromagnet Calibration

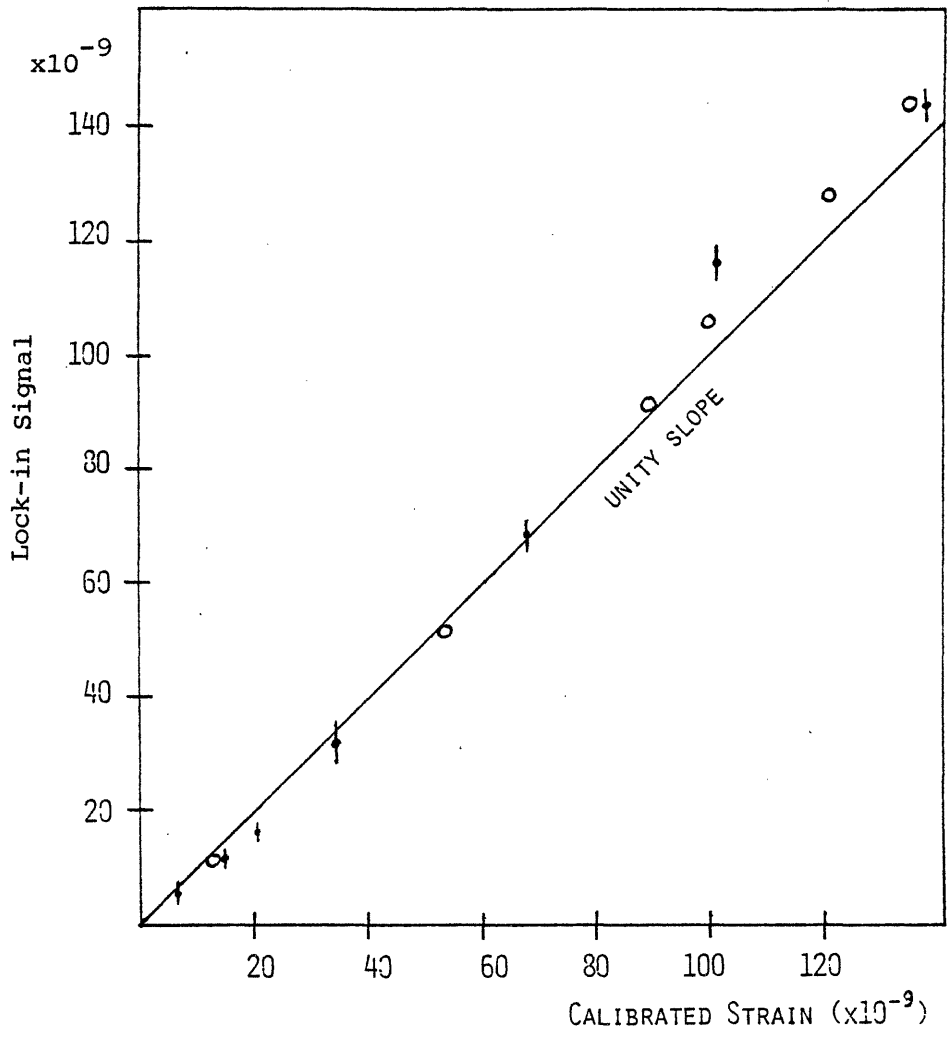


Figure 3.13 Lock-in Response at 29 Hz,
High Strain Range

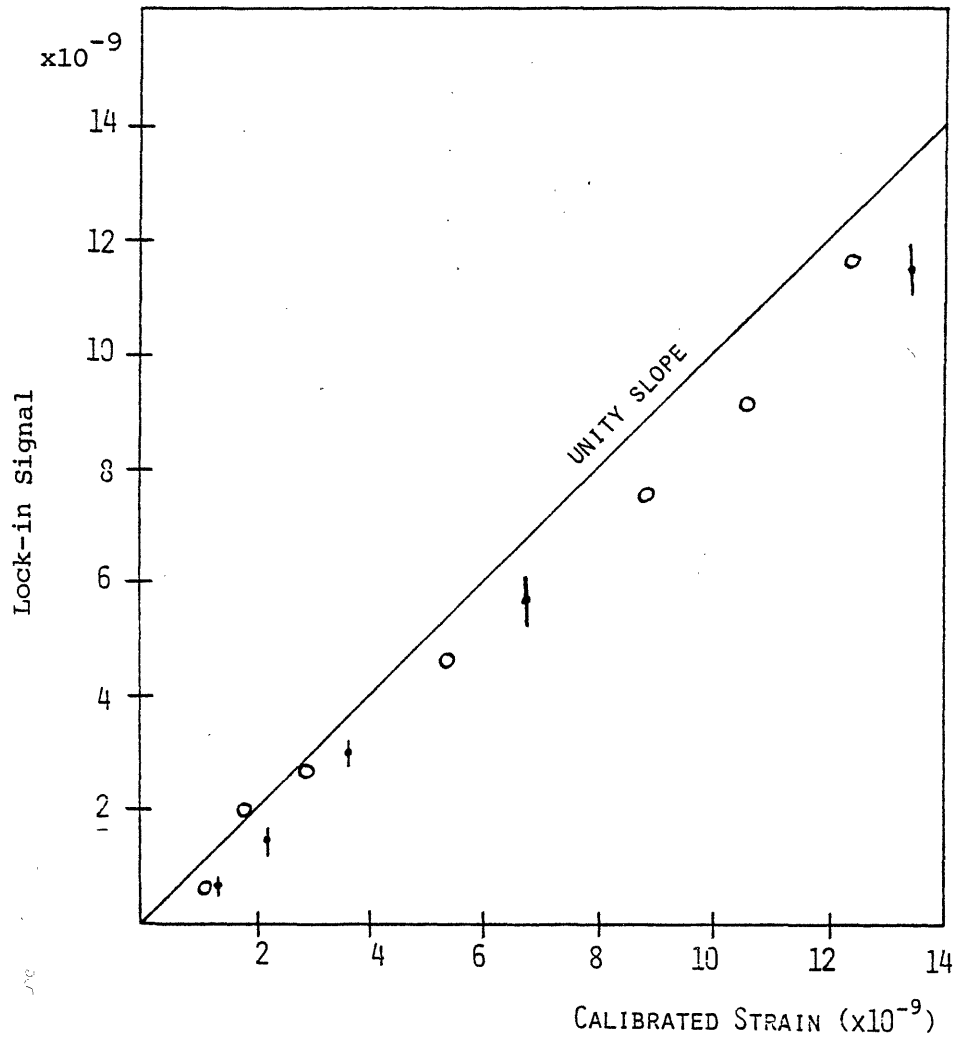


Figure 3.14 Lock-in Response at 29 Hz,
Low Strain Range

electronics. Proper application of gauges and gauge lead wires as well as careful attention to noise reduction techniques in the wiring of instruments can be major factors in determining the quality of data obtained.

Active bandpass filtering was attempted, but the 60 hz coming through from the filter power supply overshadowed the usefulness of this technique. Even though the signal to be recorded is not near 60 hz, a sufficiently strong noise signal will saturate the pre-amplifier and make detection impossible. This problem accentuates the fact that batteries should be used whenever possible. A battery powered filter was not attempted on this experiment.

Another technique for noise reduction which was tested is electrostatic shielding of the test apparatus. This was relatively ineffective because the majority of the noise is being picked up in the shielded cables and electronic instruments. Multiple shielding of the cables is desirable in future experiments.

Tests were performed on the effect of varying the bridge circuit sensitivity. The results show ambient electrostatic noise can become much smaller relative to the signal by increasing the bridge voltage. However, the level of vibrational noise also increases in proportion to this voltage. The net result is that detection is no easier. This points to the need for effective vibration isolation for future experiments. Improvements in this area alone could improve the detection sensitivity by an order of magnitude.

Table 3.4 summarizes some of the problems and sources of noise which limited the range and accuracy of the measurements. There is good reason to believe that further measures in noise reduction such as shielding of cables and vibration isolation will allow operation in the range $10^{-10} \leq \epsilon \leq 10^{-9}$. This is desirable in order to detect the details of the current distributions in the future experiments.

The success of this first experiment in no way guarantees the ability to detect these same strains in the simulation experiment. Strains in the simulation experiment are induced by electric currents flowing within the structure itself. If these currents are oscillating at a frequency ω_0 , then forces are expected at 0 , ω_0 , and $2\omega_0$. The absence of electric currents in the strained structures of the Mechanical Strain Test made it easy to lock in to the real signal, since there was essentially no synchronous noise. Therefore, the critical test lies ahead in the Electromagnetic Strain Test.

References:

- 3.1 J. W. Dally and W. F. Riley, Experimental Stress Analysis, McGraw Hill, 1978.
- 3.2 BLH Electronics, SR-4 Strain Gauge Handbook, Waltham Massachusetts, 1980.

Table 3.4 Major Problems Encountered with the MST

A. Fabry-Perot Experiment

1. multiple Fabry-Perot peaks
2. poor thermal stability of laser
3. poor thermal stability of Wheatstone Bridge

B. Low-strain experiment

1. strong 60 hz from instruments
2. low frequency noise at $f < 30\text{hz}$
(primarily vibrations)
3. mechanical resonances at $f > 400\text{hz}$
4. poor response of electromagnet at $f > 30\text{hz}$
5. large inductive effects at $f > 400\text{hz}$
in both magnet and coupling to cables

Electromagnetic Strain Test Design

4.1. Overview

In the Electromagnetic Strain Test, strains are produced by mechanisms similar to those in a tokamak during disruption. Current-carrying "source" filaments simulate plasma currents, passing through the center of a cylindrical copper shell. The ends of the shell are connected with a low resistance return current path to allow the flow of axial current which is the principal component induced. The time-varying filament currents induce shell currents in the cylinder which then undergo $J \times B$ forces with their own self field as well as with the filament fields. In addition, an external magnetic field coil is included to simulate interactions of the shell currents with the main toroidal magnetic field in a tokamak. The decision to use cylindrical geometry was made due to the overwhelming difficulty of building a toroidal structure as compared to a cylinder.

Two different test geometries were examined. In the first test the structure was a continuous cylinder and the source currents were given spatial variation. (The principal case studied was a 2/1 helical pitch with $(1 + \cos(2\theta))$ variation in magnitude.) For the second test a circular hole was machined into the cylinder. The hole was then instrumented with gauges and the source current was changed to a uniform, axially-directed current at the center of the cylinder.

There are three principal purposes of the Electromagnetic Strain Test. These are summarized in Table 4.1. First, the tests establish the capability and techniques of measuring small electromagnetically produced strains. These techniques can then be extended and/or modified to be used in other experiments — in particular ones with real plasmas. Second, the experiment generates data for computer code verification in the simplified cylindrical geometry. The calculational part of this thesis is tested against these measurements. Third, the data can be analyzed together with scaling arguments to determine directly the expected levels of strain in a larger machine.

For the purposes of discussion, the EST apparatus can be considered to consist of four functional parts. As shown in Fig. 4.1, these are:

Table 4.1 Purposes of the EST

- verify the measureability of electromagnetically produced strains
- study techniques for improving the measurements
- generate data for computer code verification
- provide data for direct scaling to reactors

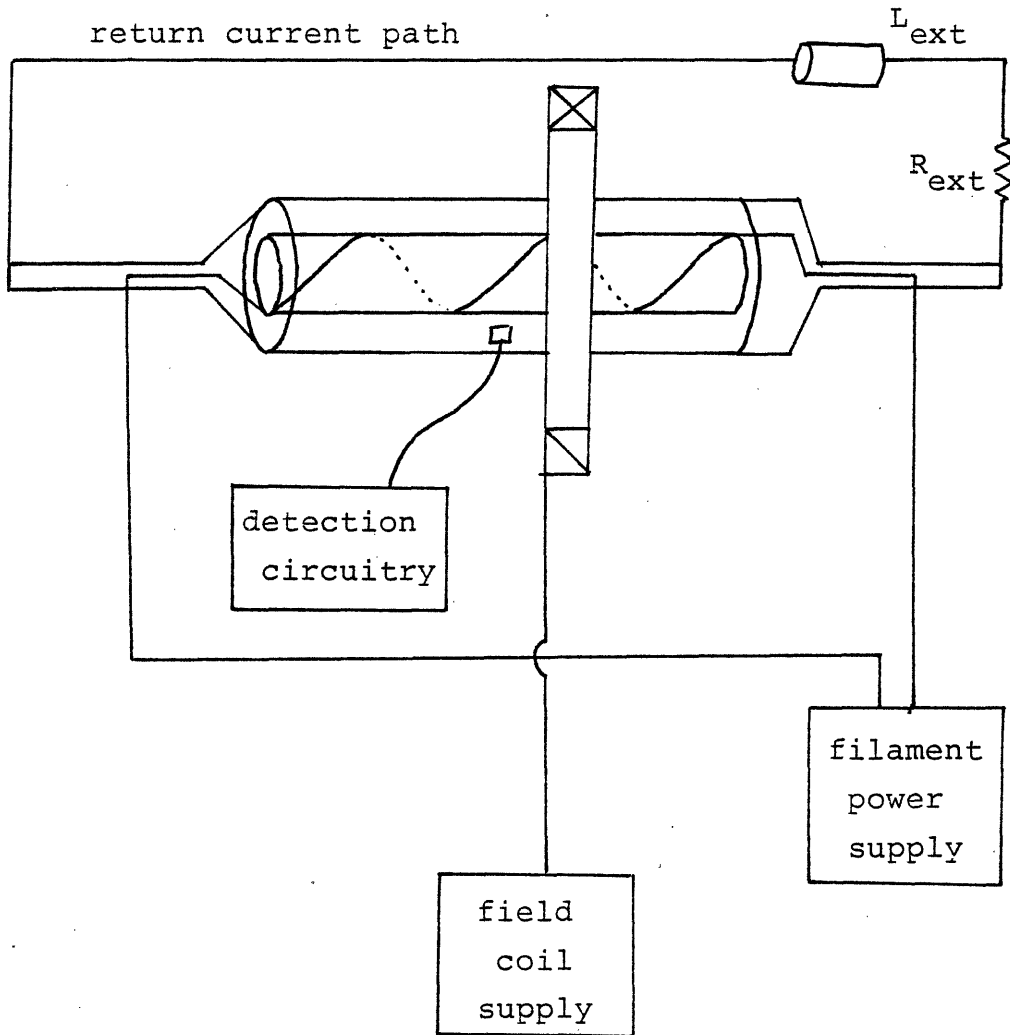


Figure 4.1 Electromagnetic Strain Test
Functional Block Diagram

- test piece and return current path
- filaments and filament power supply
- magnet and magnet power supply
- detection circuitry.

The apparatus is constructed in a cylindrical shape for ease of construction and to improve access. Although all toroidal effects are ignored, both spatially nonuniform source currents and a spatially nonuniform structure are treated. The question naturally arises as to what important effects are being omitted. One way to address this objection is to point out the types of problems which the cylinder *can* model. For the eddy current problem, the differences seem small.

The main difficulty with using existing eddy current codes has been their inability to treat multiply-connected structures. Since the cylinder test includes connectedness, it is a valid test of the code's capabilities in this area. Another possible objection to using a cylinder is the extra degree of symmetry it possesses. An example problem where this shows up is the torus with a poloidal cut as compared to a cylinder with an axial cut. In the case of the torus, large currents will still flow when an axial current transient is imposed, whereas for the cylinder there will be no currents induced. However, the inclusion of asymmetric source currents and asymmetric structural discontinuities in these tests makes this a lesser concern.

For the structural calculation it is less clear that the cylinder is a good approximation of a torus. As discovered in the experiments, the structural response tends to depend strongly on boundary conditions and constraints which are quite different for the two cases. In this case, since well tested finite element codes are used, it is assumed that if good results are obtained in cylindrical geometry, then there is no reason to suspect that toroidal geometry would be problematic.

The current level passing through the shell is approximately 1 kAmp RMS sinusoidal steady state. The reason for sinusoidal currents was discussed in the previous chapter where synchronous detection was treated. Since any time dependence can be treated as a sum of Fourier components, no significant loss of information is inherent in this method. In practice, the limitations of the filament power supply restrict the frequency range to a fairly narrow band between 100-1000 Hz. In order to obtain the relatively high level of current, a transistor amplifier power supply was constructed using common bipolar power transistors. The output of this amplifier is passed through an iron core transformer which was wound especially for this application. The amplifier and the filaments are both water-cooled, dissipating on the order of 2-3 kW each.

The external magnetic field coil also has water cooling and is capable of supplying 0.1 Tesla on axis, with a 250 mm diameter bore. Like the transistor amplifier, the DC power supply used for driving the current is a modified Airco "Bumblebee" type arc welder.

The detection circuitry consists of rosettes of semiconductor strain gauges which are used as elements in a self-balancing AC Wheatstone bridge circuit. The output of the bridge circuit is passed through amplifiers and filters, and finally sent to a Keithley lock-in amplifier for processing. The reference channel of the lock-in is driven by electronic circuitry which picks out only the frequency at which the strains are expected to occur. For self-interactions and interactions of shell current with filament fields, the proper frequency is the sum of twice the filament current frequency plus the Wheatstone bridge frequency. For interactions with the external field, the correct frequency is the simple sum of the filament current frequency and the bridge frequency, since the external field is DC

4.2. Test Piece and Return Current Path

The strain gauges are mounted on a copper cylinder which is situated just outside the three sets of filaments. (see Figs. 4.2-4.3) The total shell length is 305 mm, with approximately 25 mm extra on each end after the filament pitch is discontinued. The thickness is 0.38 mm, with a fairly large tolerance of $\pm 20-30\%$. It was machined as thin as possible without risking breakage in order to maximize the strains observed. The cylinder is mounted with its axis vertical and securely fastened (*encastré*) at the lower plane. The upper edge is allowed to move freely in the axial direction in response to the stresses induced. A small flange at the top rim was necessary to maintain the circular cross section. In the design, this rigidity was not expected to influence the important strain patterns away from the top. On the other hand, with a substantial mass at the top, low frequency structural vibrations are expected. These limit the usable frequency range for the source currents in the filaments.

It is desirable to analyze the strains induced in the test piece with a static strain calculation even though it is being driven with a sine wave, $I = I_0 \sin(\omega t)$. In order that this analysis be correct, two factors must be taken into account. First, phase angle relationships between the source current and the induced currents will occur due to the inductive and resistive impedances involved. Second, we must ensure that the frequency at which the strains are being driven is well below the natural vibration frequencies of the structure. The satisfaction of this latter criterion makes the problem "quasi-static".

In order to find the appropriate frequency range for operation, three of the lowest frequency structural modes associated with the top flange were examined: the pure longitudinal mode, the pure torsional mode, and the cantilever mode. In all cases, the following data are used to evaluate the expressions: (see nomenclature for definitions)

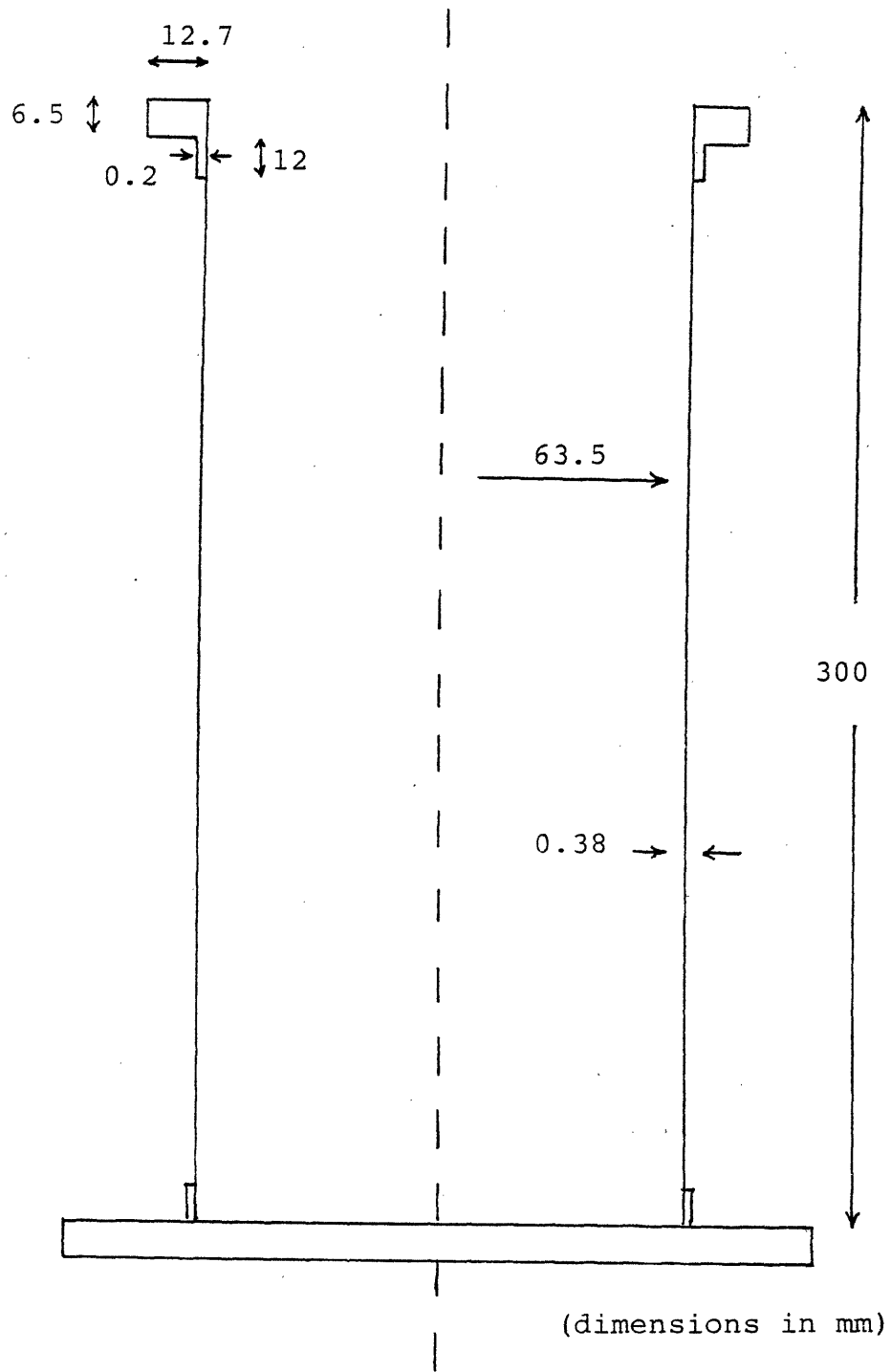


Figure 4.2 Diagram of Test Section

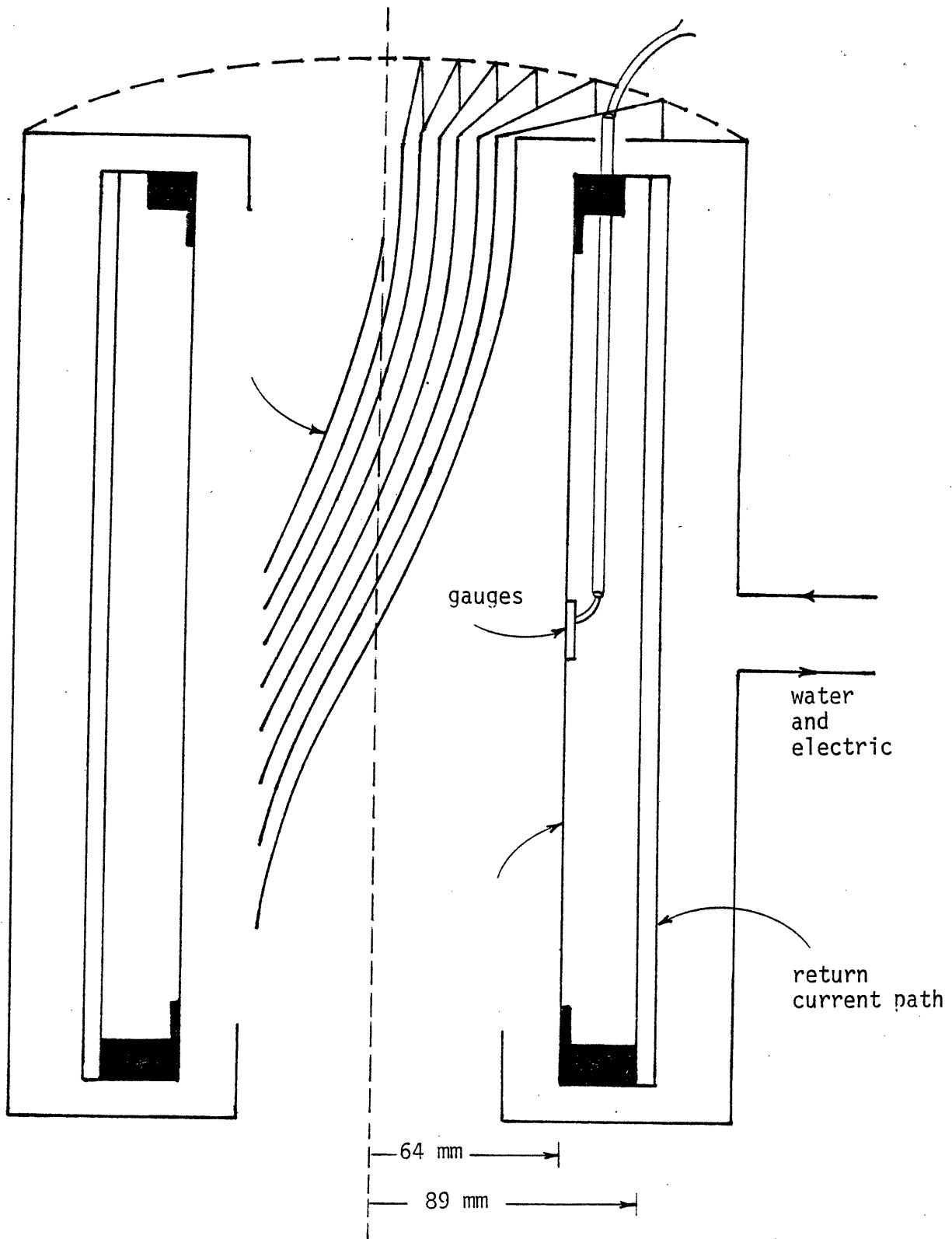


Figure 4.3: Cross Section of Filaments and Shell

$$E = 11.7 \times 10^{10} N/m^2$$

$$r = .0635m$$

$$L = .254m$$

$$I = \pi r^3 t = 3.065 \times 10^{-7} m^4$$

$$G = 4.4 \times 10^{10} N/m^2$$

$$t = 3.8 \times 10^{-4} m$$

$$A = \pi r^2 = .0127 m^2$$

$$f = \omega/2\pi$$

In addition, for all cases we assume that the entire test piece mass is concentrated at the top flange. This is a fairly good approximation which greatly simplifies the calculation and is conservative since lower frequencies result. The simple spring equation is applied for each case:

$$m \frac{d^2 x}{dt^2} + kx = 0 \quad (4.1)$$

where x is an arbitrary 1-D displacement. The solution is a sine wave with frequency

$$\omega = \sqrt{\frac{k}{m}} \quad (4.2)$$

where k is the spring constant, force per unit displacement. The method used to find the lowest resonant frequency is to apply a unit force, compute the expected displacement, and divide by the mass as in eqn. 4.2.

1) Longitudinal Mode

For the longitudinal mode, the movement is axial. If x is the vertical displacement of the flange away from the equilibrium position, then

$$\epsilon = \frac{x}{L} \quad (4.3)$$

The axial stress is easily obtained as

$$\sigma = \frac{F}{2\pi r t} \quad (4.4)$$

combining with the definition of E , we get

$$E = \frac{\sigma}{\epsilon} \quad (4.5)$$

$$k = \frac{F}{x} = \frac{2\pi r t E}{L} = 6.98 \times 10^7 N/m \quad (4.6)$$

$$f = \frac{1330}{\sqrt{m}} \text{ Hz} \quad (4.7)$$

2) Torsional Mode

For thin-walled cylinders, the flange can twist through an angle θ , thus producing a shear strain given by

$$\gamma = r \frac{d\theta}{dL} \quad (4.8)$$

The shear stress is proportional to the torque, T,

$$\tau = \frac{T}{2\pi r^2 t} \quad (4.9)$$

$$F = \frac{T}{r} = \frac{2\pi r^2 t \tau}{r} \quad (4.10)$$

$$x = r\theta = \gamma L \quad (4.11)$$

Using the definition of the shear modulus $G = \tau/\gamma$, we get

$$k = \frac{F}{x} = \frac{2\pi r^2 t G}{rL} = 2.63 \times 10^7 \quad (4.12)$$

$$f = \frac{817}{\sqrt{m}} \text{ Hz} \quad (4.13)$$

3) Cantilever mode

The governing element of the flexibility matrix is: ^(4.1)

$$k = \left[\frac{L}{GA} + \frac{L^3}{3EI} \right]^{-1} = 6.54 \times 10^6 \quad (4.14)$$

therefore

$$f = 407/\sqrt{m} \text{ Hz} \quad (4.15)$$

With a total flange mass of .322 kg, the lowest resonant frequency is the cantilever mode at 717 Hz.

After preliminary data had been taken, it became clear that other resonances existed in addition to the top flange modes. These are the class of vibrations termed "modal resonances" in which the boundaries remain fixed but the structure deforms radially according to

$$w = w_o \cos\left(\frac{2\pi m x}{L}\right) \cos(n\theta) \quad (4.16)$$

As it turned out, these were the more significant resonances; much more detailed discussion on them appears later in this chapter.

The current path for the test piece must be closed in order to allow circulating currents. This is done by soldering copper conductor at the top and bottom flanges of the test section. For the

initial data runs, braided ground wire was used in order to avoid extra structural constraints being added at the top flange. However, trouble with the coupling between the filaments and the shell circuit led to its replacement with solid copper bars 25 mm wide by 300 mm long by 1.6 mm thick. The approximate radius for the return current path is 90 mm — just inside the filament return current paths.

The return current path was designed in such a way as to direct the return currents along the axial direction. In this way the interaction of the fields from the return currents should be minimized, since in the ideal case of an infinitely long cylinder carrying axial current there is no internal magnetic field generated. Deviations from this approximation occur mainly near the cylinder edges where the current flow is radial. The gauges were always placed as far from the edges as possible in order to minimize this effect. The same strategy was also used for the filaments where inside the shell they are helical, but outside they flare out radially and return along the axial direction. By spacing the return filaments as close together as possible and keeping their currents equal, a cylinder is approximated with only axial currents.

4.3. Filament and Power Supply Design

In order to insure a measurable level of strain consistent with the experimental goals, the simple case of forces generated by a single straight central filament was analyzed. Pressure is given by

$$p = K \times B = \frac{\mu_o I^2}{4\pi^2 a^2} \quad (4.17)$$

where K is the axial surface current density and B is the poloidal magnetic field. The stress and strain are obtained using

$$\sigma = \frac{pa}{t} \quad (4.18)$$

$$\epsilon = \frac{\sigma}{E} = \frac{\mu_o I^2}{4\pi^2 atE} \quad (4.19)$$

Using values relevant to the experiment, we obtain $\epsilon = 1.2 \times 10^{-14} I^2$. Fig. 4.4 is a plot of this equation, from which we see that currents of 1000 amps or greater will give us strains of $\geq 10^{-8}$. This is a reasonable strain level with synchronous detection. In order to insure detectability of the smaller longitudinal strains, an approximate goal of 3 kAmps was set. This is accomplished using ~ 15 passes of the filaments at 200 amps/turn.

4.3.1. Filament Geometry

The filaments were chosen to be 4.75 mm OD hollow copper refrigerator tubing to allow for easy removal of the 2 kW of heat being dissipated during operation. They run through the center of the test piece with pitch angles defined by the strongest tearing modes expected during a plasma

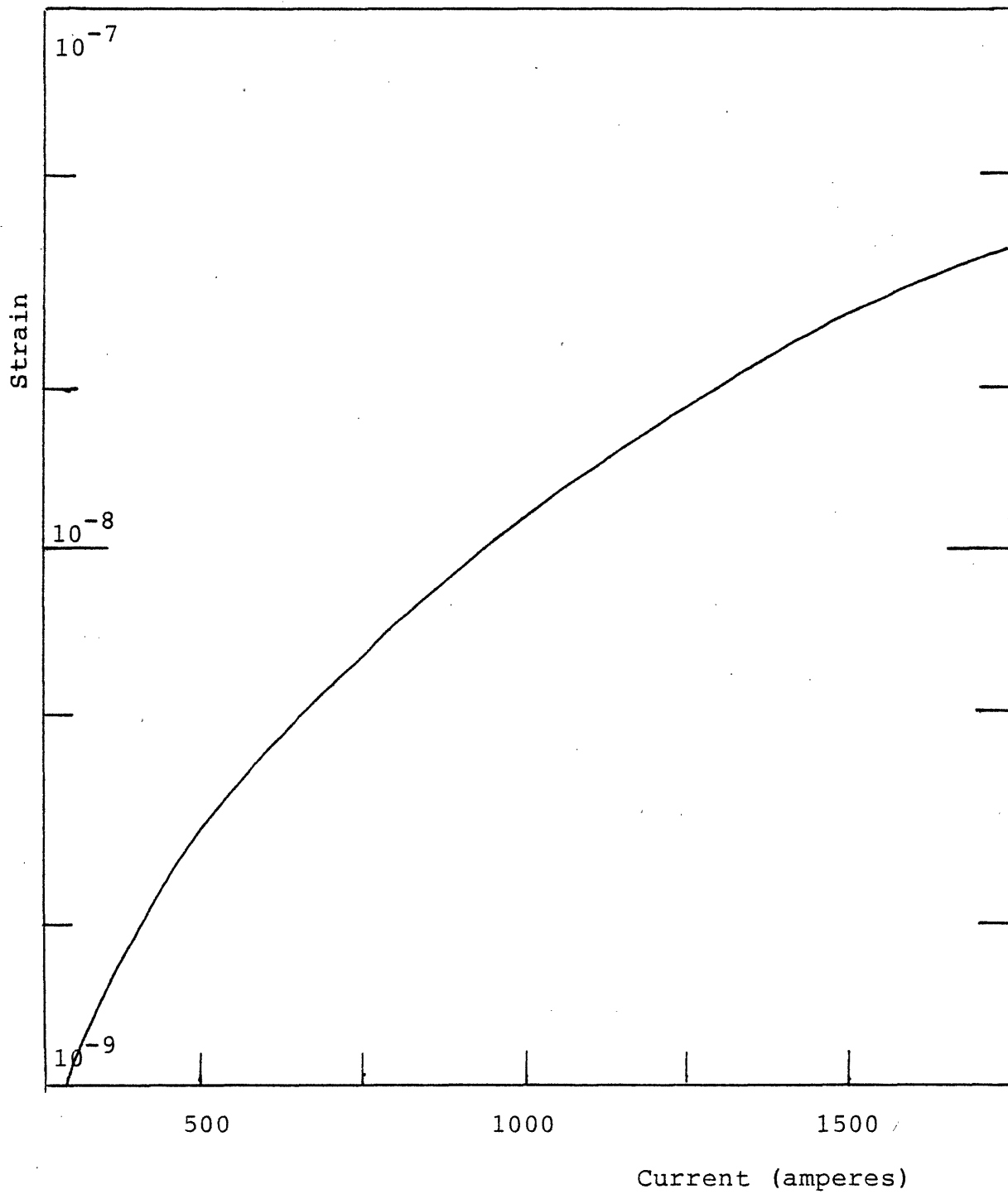


Figure 4.4 Strains for a Symmetric Axial Current

disruption. One filament set runs along the axis to simulate the main toroidal plasma current (see Fig. 4.5). The need to include helicity is subject to debate since the amount of helicity is small and the main effects of disruptions are expected to be a result of the main toroidal current. However, it was decided early on in this investigation that interactions of the poloidal currents should not be discarded. The $J \times B$ interaction of poloidal currents with the main toroidal field is expected to have the same order of magnitude as toroidal currents with poloidal fields. In addition, smaller effects due to the poloidal currents may still be important when the effects of the main toroidal current are mitigated.

Each filament runs through the test piece and connects on top to 6.35 mm tubing which bends around to the 12.7 mm tubing outer return current path. Larger cross section filaments are desirable to increase cooling capacity and to decrease the electrical resistance. Decreasing resistance means less heat to remove and also less power to be supplied by the power amplifier.

4.3.2. Amplifier Design

The goal of supplying 2 kW at 3 kamps can be met by a variety of amplifier types. The first constraint is that it must be "home-made", since the cost of a commercially available a.c. power supply would be prohibitive. There were two main concepts studied: a parallel resonant circuit and a transistor amplifier.

The idea of a resonant circuit is attractive due to its simplicity. A large capacitor and inductor are placed in parallel and connected to a high voltage supply. The equivalent impedance of this circuit is very high at the resonant frequency, drawing little current from the power supply. Within the legs of the resonant circuit, however, large currents flow. The filaments would be located in one of these legs.

The problem with this idea is that very large nonpolar capacitors are needed — much larger than were available. So the idea of a high current power amplifier was chosen. The final design was a push-pull configuration with all npn transistors and an output coupling transformer (see Fig. 4.6). The main source of power is a 200 ampere Airco DC arc welder. A push-pull amplifier was chosen for its high efficiency (ideally as high as $\pi/4$) and more importantly due to its absence of net DC current through the output coupling transformer. This is important since even a small imbalance of 10-20 amps will saturate the core, degrading the transformer's ability to pass power without distortion. Distortion is one of the major problems experienced with the amplifier.

The transistors used were Motorola MJ15022's. These are low cost, 16 ampere, 200 volt silicon transistors capable of dissipating 250 watts each at room temperature. Each side of the push-pull consists of 8 transistors in parallel driven by a Darlington transistor for beta enhancement. The transistors are mounted on a 5.5 mm copper plate which has copper tubing soldered on for cooling.

Table 4.2 – Summary of Filament Design Parameters

Filament Geometry	
maximum filament current	~ 200 amps
filament length	406 mm
outer diameter	4.8 mm
inner diameter	3.2 mm
# turns, 3/2 mode	5 × 3
# turns, 2/1 mode	8 × 2
# turns, 1/1 mode	16 × 1
resistance of 1 filament set	.017Ω

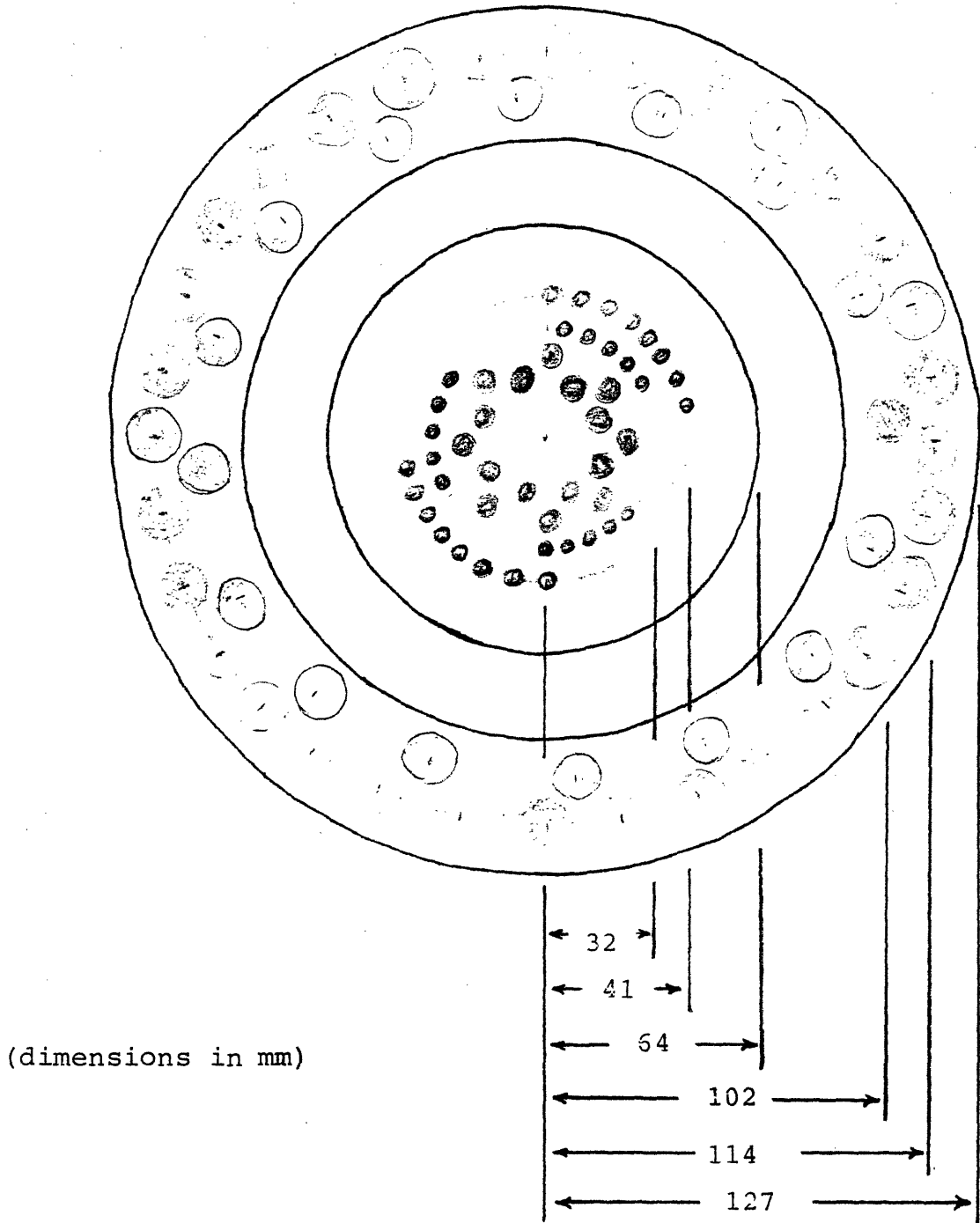


Figure 4.5 Filament Configuration

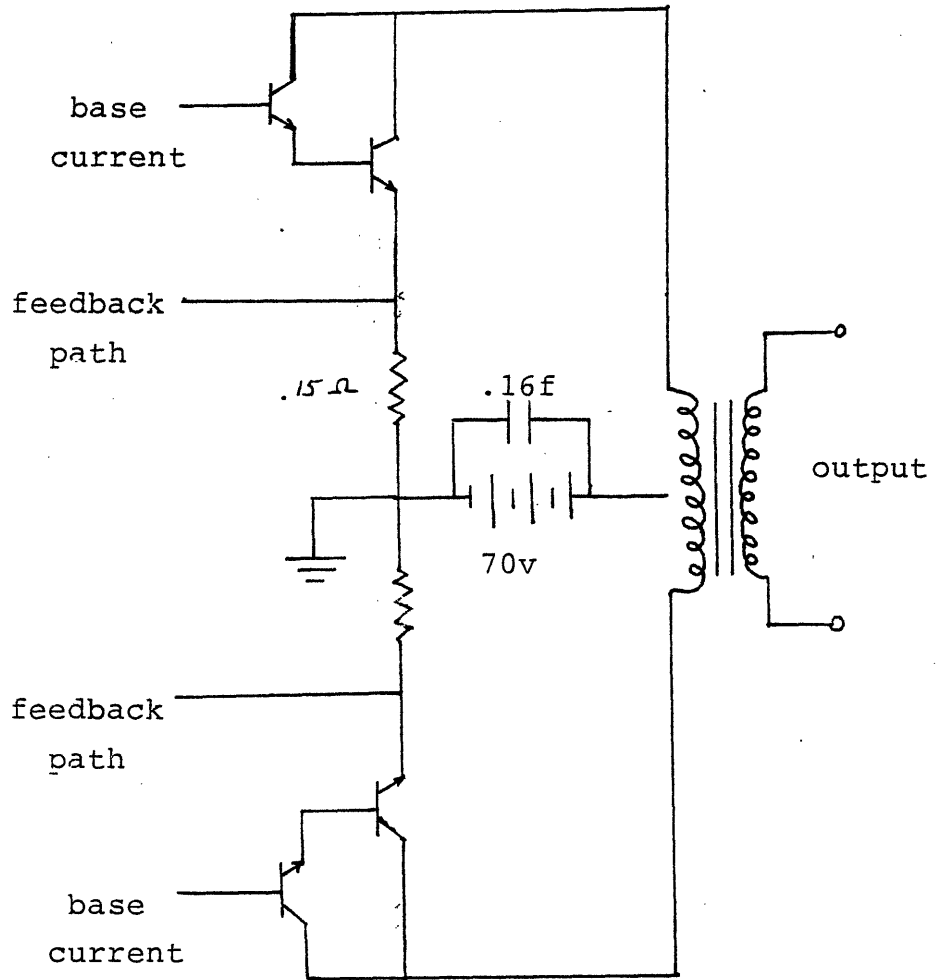


Figure 4.6 Push-Pull Power Amplifier Schematic

All of the bases are in parallel and the emitters are connected through individual 0.15Ω current sharing resistors to ground. The bases are driven by a separate current source circuit.

Design of the base drive circuitry was complicated by problems inherent with high power signal processing. Owing in part to the poor characteristics of the transistors, the power amplifier delivers an output signal with large amounts of harmonic distortion. The strong dependence of β , the current gain, on temperature and current level results in output which is far from purely sinusoidal. It is also characteristic of push-pull amplifiers to exhibit cross-over distortion; that is, sharp voltage spikes which occur when the current is transferred from one side of the amplifier to the other. Voltage feedback to the bases is particularly enhanced by these high frequency noise components.

The level of distortion (i.e. signal at other than the fundamental harmonic) at full power without treating the problem approaches 10–20% at the transformer primary. This is intolerable for two reasons. Since the signal must pass through the power transformer and then through the filament-to-shell path which is effectively another transformer, the higher frequency components are amplified with respect to the fundamental. The shell currents end up far from sinusoidal. Second, harmonic distortion results in inaccurate strain readings. Harmonics of current and field will mix and be detected by the lock-in amplifier in ways which can not be properly accounted for. The end result of these effects is that a simple voltage drive to the bases is not possible. A rather complicated base drive circuit was designed to improve the signal to the filaments.

The final circuit which was used consists of two nearly identical channels with several stages (Fig. 4.7). The first stage is an "ideal" diode with zero forward voltage drop which cuts off one side of the voltage input sine wave for each channel. This signal is buffered and on one channel inverted so that only positive currents are provided for the npn power transistors. The third stage lifts the voltage slightly above zero so that the power transistors never turn off completely. It is at this point that the voltage feedback is also applied from the push-pull emitters to keep the final waveforms sinusoidal. The last stage is a voltage-to-current convertor to supply the power transistor bases with a signal relatively insensitive to voltage fluctuations. The only point where parasitic feedback oscillations are possible now is at the feedback points, where care can be taken to minimize the problem.

4.3.3. Transformer Design

The collector current of the push-pull amplifier is coupled to the load through a large iron core transformer. The transformer acts to increase the current available from the power supplies and also to isolate the load from the transistor amplifier. This implies less power dissipation and greater efficiency, since the load dissipates no DC power at the operating point. The filament design dictates the design goals for the transformer: 1) With all filaments connected, we want 200

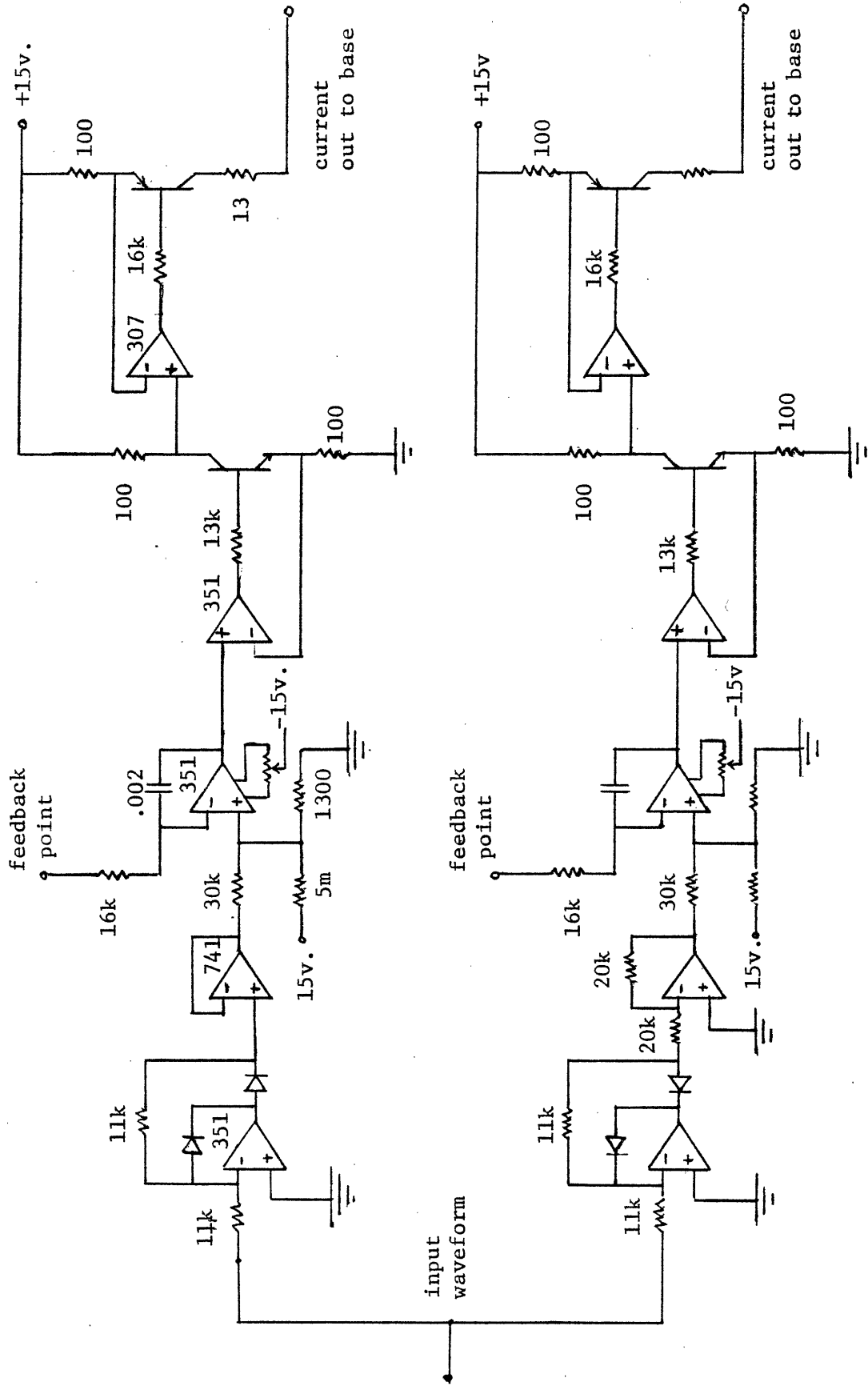


Figure 4.7 Base Drive Circuit Diagram

amps rms through 50 m Ω . This implies that the core must be able to pass 2 kW. 2) In order to be able to operate with either one, two, or all three sets of filaments and still deliver 2 kW there must be taps on the secondary allowing for 2.8:1, 3.4:1, and 4.9:1. 3) The primary side characteristics are 200 amps peak-to-peak maximum and 100 volts peak-to-peak maximum. This assumes that the load is entirely resistive. As was discovered after construction, this is not the case. 4) The load resistances are approximately 17, 34, and 51 m Ω .

The core chosen is a standard "H" core with a 75 x 105 mm cross sectional area (Fig. 4.8). The core is rated for 9 kW operation at 60 Hz. Choice of the core was made primarily because of its availability. The wire size used to wrap the core was selected to operate at steady state without overheating.

Due to the small load resistance, leakage inductance can easily cause most of the voltage on the transformer to be dropped across the leakage reactance. When the reactive impedance becomes larger than the load resistance the phase angle between the primary voltage and current increase, thus degrading the power transfer capability of the core.

Several techniques were used to minimize the leakage reactance:

- small winding radius (tight winding)
- small winding thickness (one layer)
- large winding length (use the whole core)
- small number of turns (gain by N-squared)
- low frequency

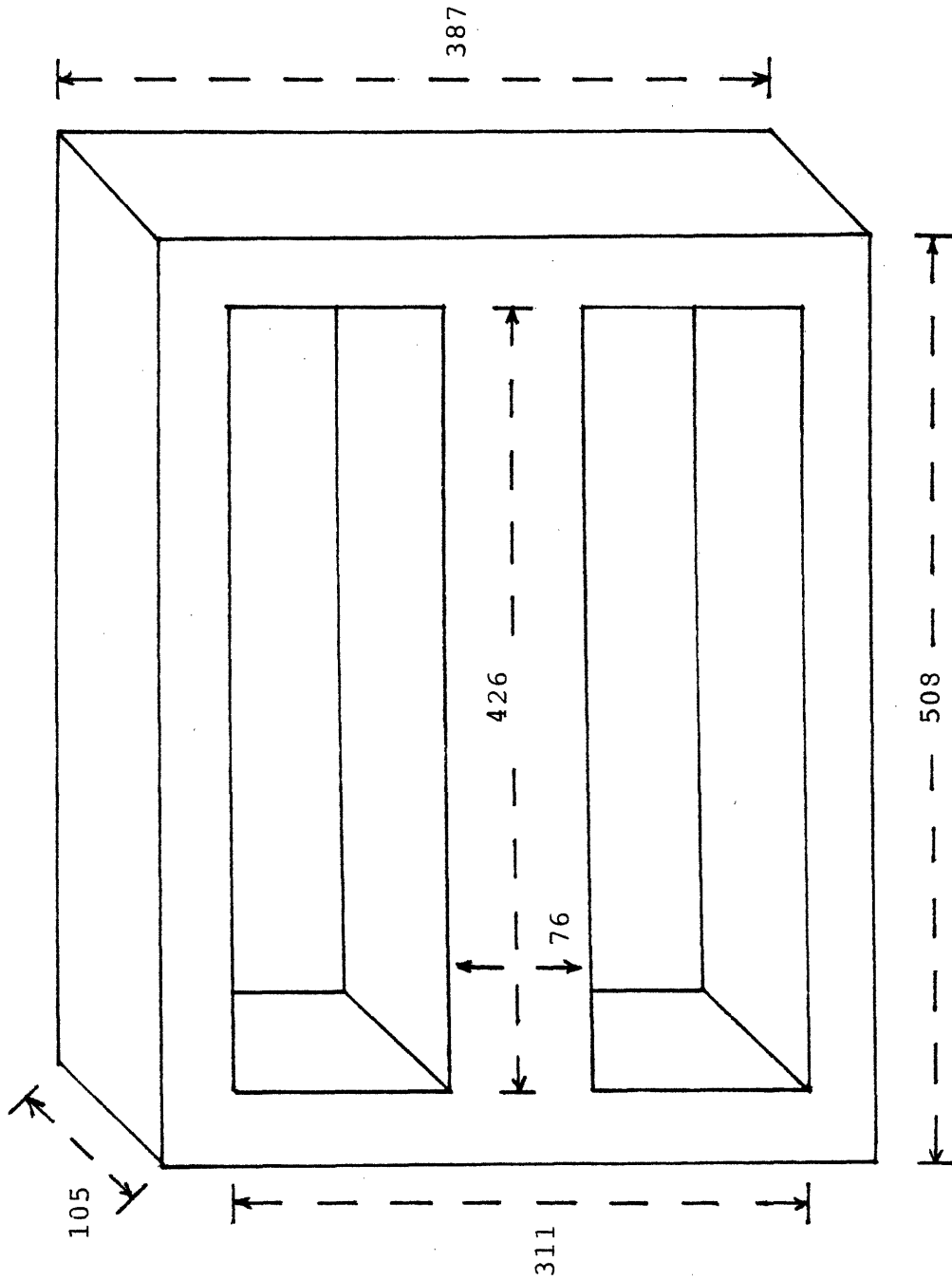
The most important of these is the absolute number of turns, since the inductance scales as N-squared. There are of course limitations to how far the number of turns can be decreased. The final design uses 23 turns on the primary and taps for 4, 6, and 7 turns on the secondary. These turns ratios are very close to the optimum coupling ratios given above.

4.4. Magnet and Magnet Power Supply

The single magnetic field coil is composed of 3 pancakes of wound copper ribbon with copper tubing placed between the segments for cooling. It has an inner radius of 127 mm, an outer radius of 254 mm, and an axial thickness of 102 mm. The coil has a resistance of 4.58 Ω and the field on axis is 43 Gauss/ampere. Operation at 0.1 T therefore requires 23.25 amps at 106.5 volts. A modified DC arc welder power supply is used to drive the magnet.

4.5: Detection Circuitry

When detecting strains produced by electric currents, there are two distinctly different types of noise to be treated. These are termed synchronous and asynchronous. The asynchronous noise is



(dimensions in mm)

Figure 4.8 Iron Core Transformer Dimensions

precisely the type dealt with in the Mechanical Strain Test. It is primarily due to the natural noise environment, especially 60 hertz and its harmonics. The level is somewhere in the neighborhood of 1 μ volt and can be controlled to a large extent by proper shielding and grounding of all components and cables. In addition, there are Johnson noise, shot noise, and thermal-induced fluctuations. The Mechanical Strain Test showed that strains of 10^{-9} or less could be adequately detected in noise fields of this type. The corresponding currents which produce $\epsilon = 10^{-9}$ in our experimental apparatus are ~ 300 amps.

If this were the only type of noise present, then it would be fairly easy to detect the strains in the Electromagnetic Strain Test. Synchronous noise unfortunately exists when strains are driven electromagnetically, and this noise cannot be treated with the same techniques as asynchronous noise. The synchronous noise exists because the electric currents in the strained structure produce magnetic fields proportional to the current. The magnetic fields thus produced link any strain gauge element or wires near the structure and induce voltages which can be much larger than the signal voltage to the gauge circuit.

To illustrate this, consider the field near a current sheet,

$$B = \frac{\mu_o K}{2} \quad (4.20)$$

If we take $I = 5$ kamp, $f = 200$ Hz, and a conservative perpendicular gauge area estimate of 1 mm² exposed to the field, then the resulting voltage induced is $5\mu V$. Compare this with the Wheatstone bridge response to a rather large strain of 10^{-7} . If the circuit sensitivity is $25\mu V/\mu\epsilon$, we calculate $2.5\mu V$. Since the strain and the induced voltage are both excited by the same frequency source current, it is difficult to know what part of the signal is due to a real strain. Techniques of frequency separation appear useless.

There is one important complication of this problem which must be addressed: the strains due to currents at the source current frequency ω_1 do not all occur at the same frequency ω_1 . Only the interaction of the currents with the d.c. external field are at ω_1 . The interaction of the currents with their own magnetic fields occurs at $2\omega_1$ and at zero. This is due to the fact that strains are caused by $J \times B$, and both J and B are varying as $\cos \omega t$. One might conclude from this that the self-force can be synchronously detected at $2\omega_1$ without the noise at ω_1 being a problem. However, the problem still exists since the strains are at *exactly* $2\omega_1$. The normal operation of the lock-in amplifier will result in a reading at $2\omega_1$ due to the strong 2nd harmonic of the synchronous noise at ω_1 . A better solution in both of these cases is to detect at a frequency which is totally unrelated to ω_1 .

This is accomplished by adopting a scheme which exploits the gauge circuit output dependence on bridge voltage. Since the strain signal is affected by the bridge voltage but the synchronous

noise signal is not, we can drive the bridge sinusoidally. Strains are then detected at the sum frequency $\omega_1 + \omega_2$, where ω_1 is the source current frequency and ω_2 is the bridge circuit frequency. For self-strains, the desired signal is at $2\omega_1 + \omega_2$.

The components of the detection electronics are discussed individually in the following sections. Fig. 4.9 is a block diagram including the important circuits. Briefly, the lock-in amplifier is the basis for the measurement. One side of the electronics drives the reference channel using the frequencies extracted from the bridge and power amp signal generators. The other side drives the signal channel from the amplified gauge response.

Before going on to discuss the techniques of bridge modulation and synchronous detection, it is a good idea to reflect on other possible options. In the calculation of voltages done above, a circuit sensitivity of only $25\mu V/\mu\epsilon$ was assumed. If this could be increased by 1-2 orders of magnitude, then perhaps synchronous noise would not dominate the output. This is an important point because the strain signal scales more favorably with current than with noise in a reactor size device. It is possible that the complicated techniques used for this experiment could be avoided. Another way to enhance the signal to noise ratio and eliminate synchronous detection is by improving the circuit sensitivity. The circuit sensitivity is proportional to both the gauge sensitivity and the bridge voltage. Gauge sensitivities substantially greater than those in use are just not available. Also, the gauge voltages planned are already ~ 30 V peak-to-peak. Substantial improvement in this area would require a high voltage a.c. source. For this small experiment, direct detection does not look promising.

4.5.1. Gauges and Lead Wire Configuration

The gauges are semiconductor strain gauges with gauge factors of ~ 110 . They were purchased from BLH in Waltham, MA. BLH sells many different gauges for special applications; however the standard low cost model SPB3-06-12 was chosen. These are singly packaged, backed gauges with 1.5 mm length and resistance of $\sim 120\Omega$.

The gauges are laid out in 45° rosettes of three gauges at various locations on the shell. For the structurally continuous shell test, the circumferential angle of the gauges is irrelevant since they are rotated through a full 2π radians. The entire shell structure with return current bars and attached gauges and lead wires is free to rotate between the filaments and the filament return current tubes. The rosettes are located at two axial positions: one at the center of the shell (and also the center of the magnet bore), and the second at 76 mm above the first. The rosette angles are approximately 45° , although an error during the epoxying procedure resulted in the central set being off by 10° . (see Fig. 4.10) This has no effect on the results, except that the different angle must be included in the calculation of peak strain and principal axes.

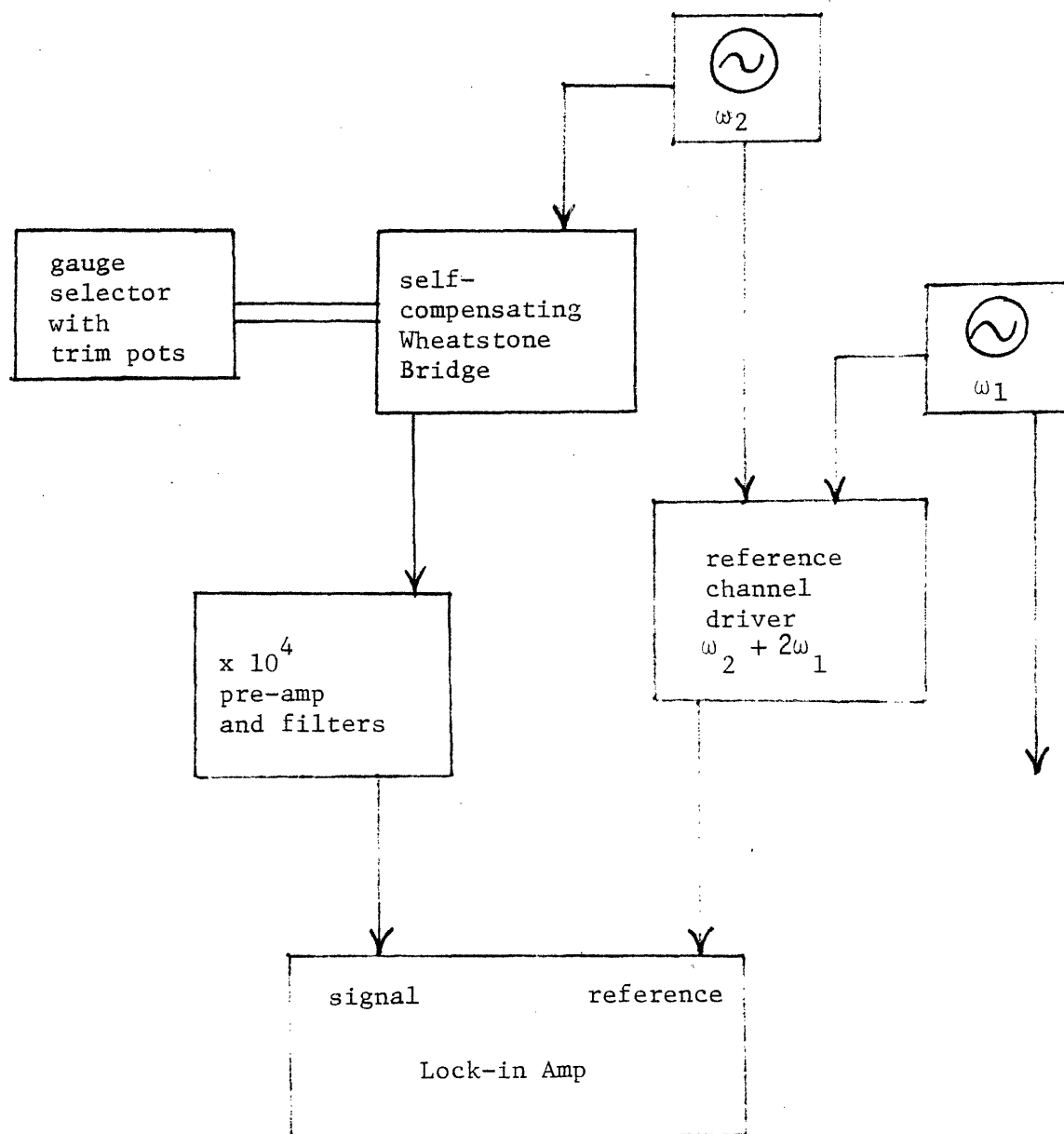


Figure 4.9 EST Detection Electronics
Block Diagram

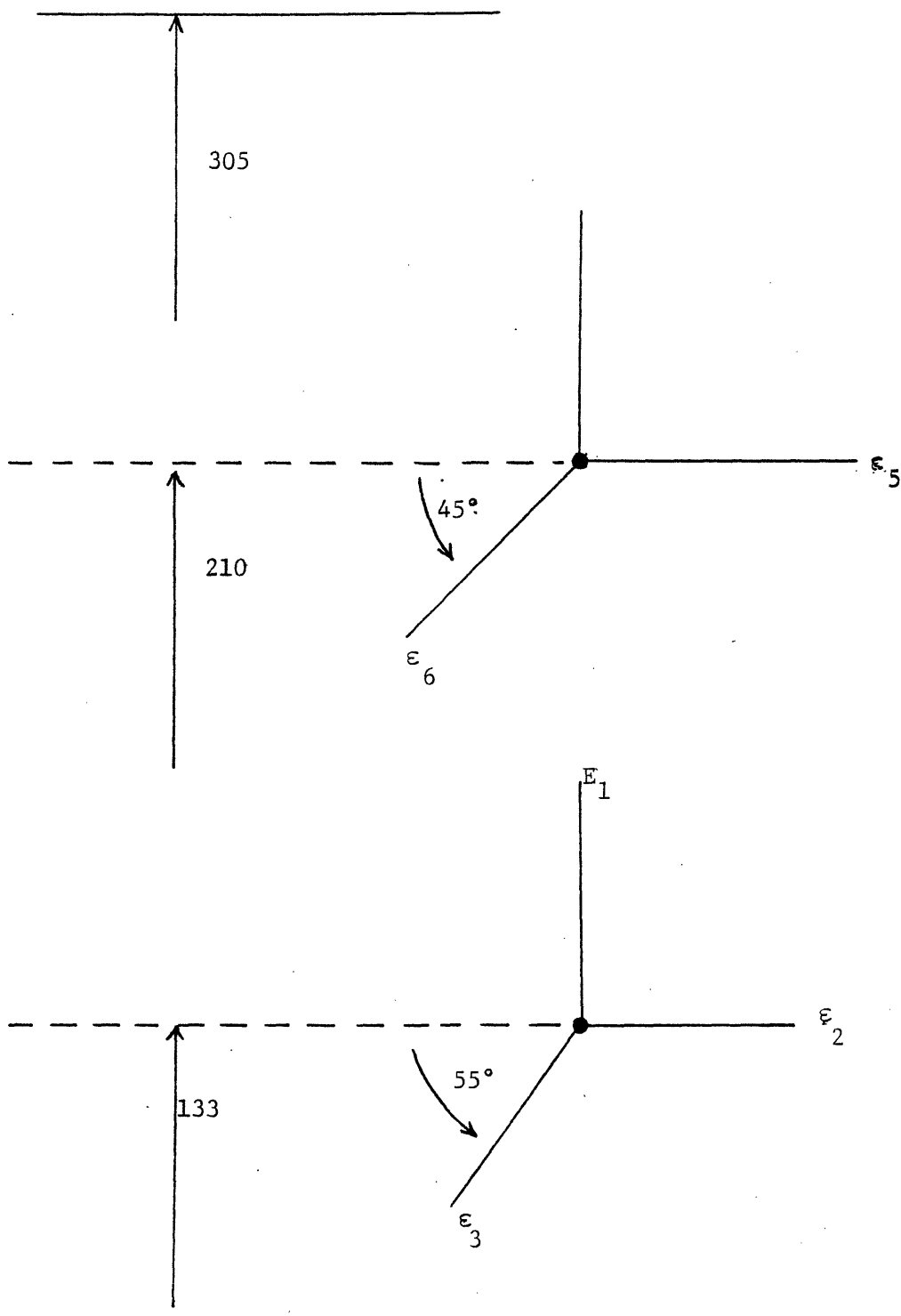


Figure 4.10 Strain Gauge Positions

For the test with the circular hole drilled in the shell, the source current is circumferentially and axially uniform, so the position of the gauges depends only on their distance from the hole in both θ and z . Fig. 4.11 shows that 5 rosettes were used. 3 rosettes cover one quadrant of the hole, a fourth extends away from the hole 2 hole radii from the center of the hole in theta, and the 5th is used to test symmetry. The two rosettes from the previous test are still in place π radians away from the hole. They are used to measure effects "far" from the structural discontinuity.

4.5.2. Self-Compensating Wheatstone Bridge

The Wheatstone bridge was chosen again as the detection circuit. Due to the problems with balancing a bridge, it would generally be better to use a potentiometer circuit where a blocking capacitor allows only the AC signal to pass. However, the need to sinusoidally drive the bridge circuit at a frequency comparable to the strain frequency means that huge noise signals would pass through at approximately 1 volt (the bridge is driven at ~ 10 volts). This problem can be eliminated to some extent with a balanced bridge since in the balanced state no output appears regardless of the input.

Unfortunately, the degree to which the bridge must be balanced is quite high. If the imbalance is one part in 10^6 , then the leakage of the bridge applied voltage will be comparable to the strain signal. Actually, a leakage of 10 times the strain signal would not be a big problem with the use of the lock-in amplifier. Still, small thermal drifts quickly upset the bridge balance and make a measurement impossible. For this reason a DC self-balancing Wheatstone bridge circuit was developed (see Fig. 4.12).

The basis of the self-balancing bridge is a low resistance power JFET (junction field effect transistor). FET's are to a good approximation linear resistors when operated in the saturation state. The condition of saturation is met for most FET's when $V_{gs} \leq 0.2$. This imposes the requirement that the resistance is less than 15 ohms, since the bridge resistors on one side sum to about 1000 ohms and the peak voltage is 15 volts. A power FET must be used, since small signal FET's generally have much larger "on" resistances.

The gate of the FET is driven by op-amps which sample and amplify by about 10^6 the DC error signal at the bridge output points which is supplied by a C-type dry cell. By correctly choosing the positive and negative inputs to the op-amps, a negative feedback path is set up. Then if an imbalance appears, the FET adjusts its resistance in such a way as to return to balance. Since the FET requires about 4 volts on its gate, an error signal of $\sim 4 \mu\text{volts}$ can be achieved. This is only true if the op-amp offset voltage is well balanced and no current is drawn through the op-amp inputs. These conditions are met by choosing the LF355/LF356 FET input op-amps with externally adjustable, temperature compensated offset.

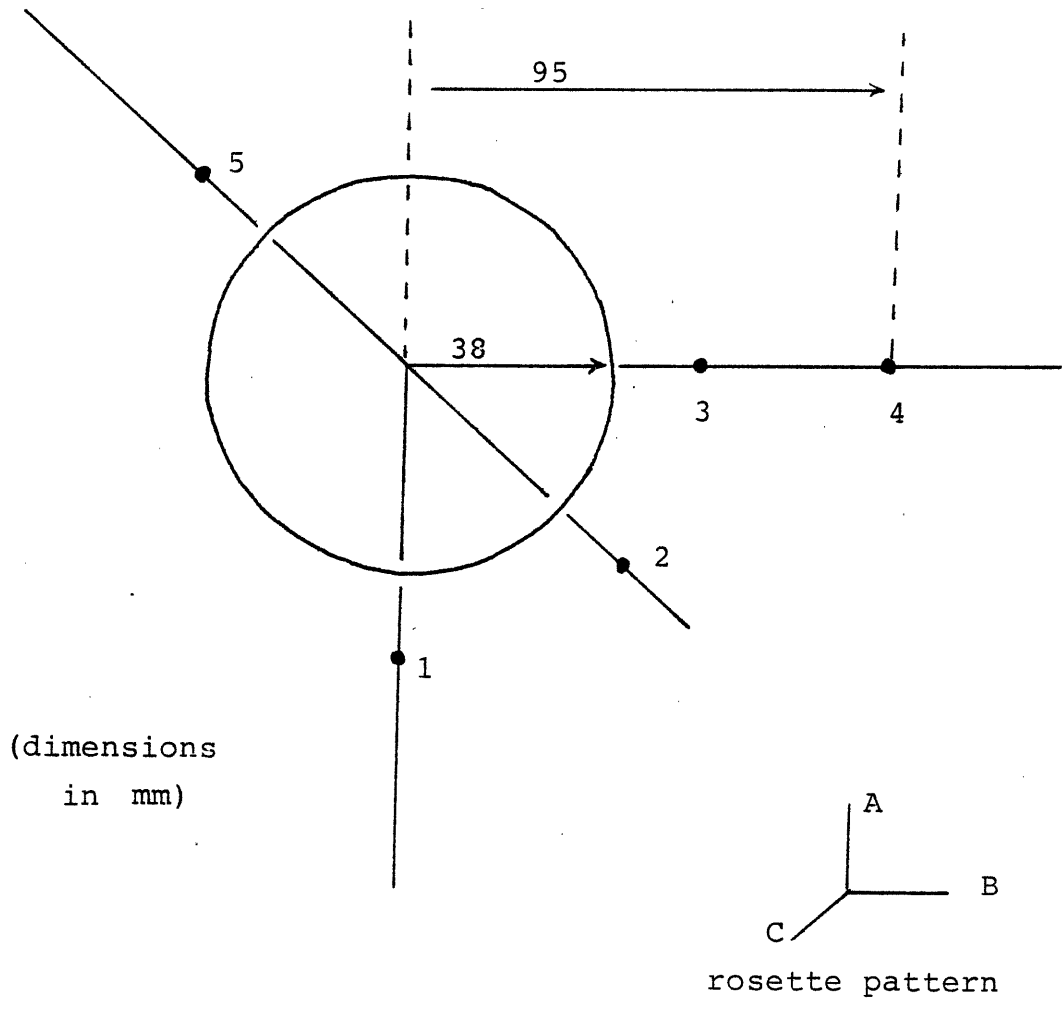


Figure 4.11 Gauge Locations Around the Hole

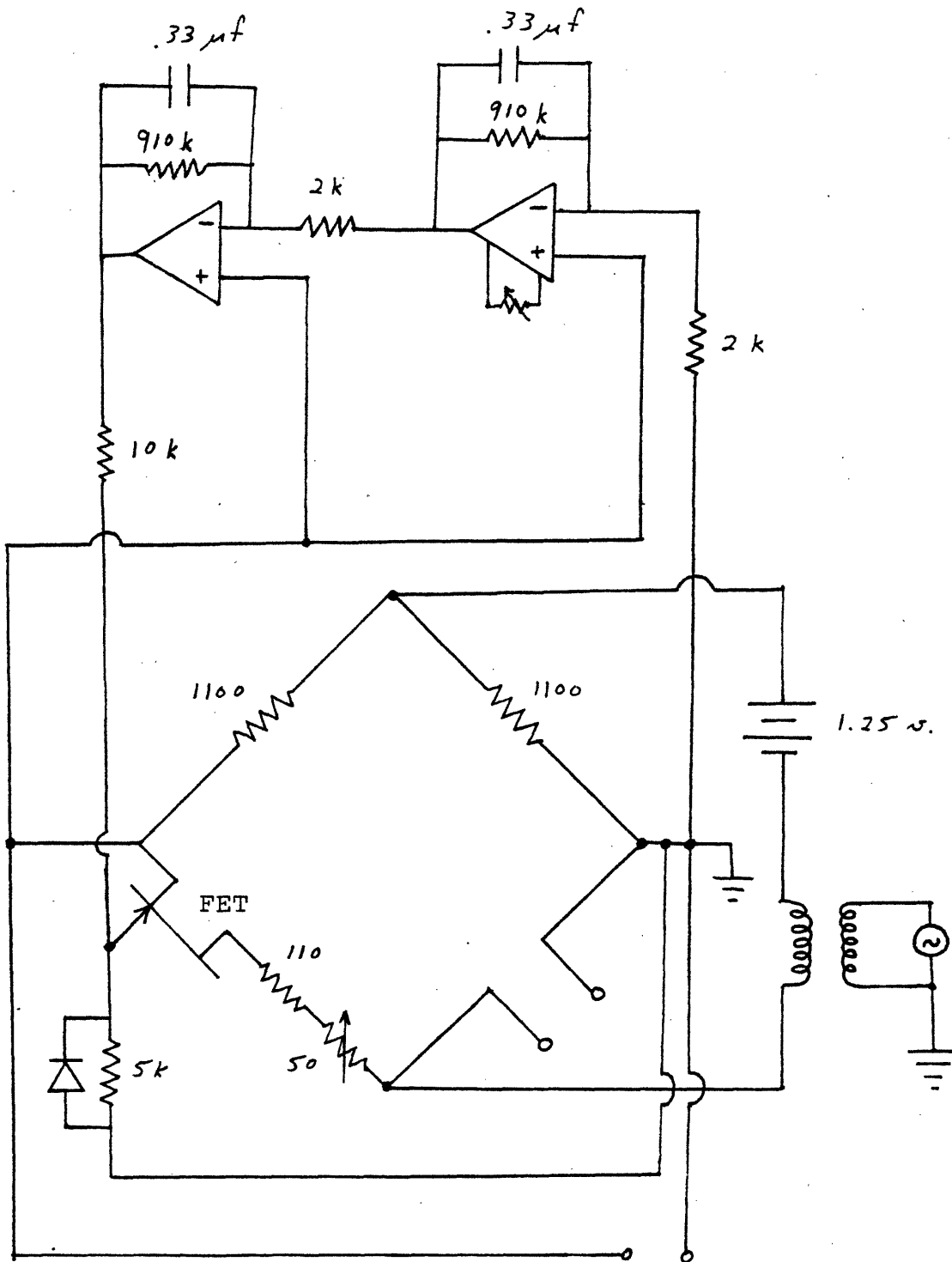


Figure 4.12 Self-Compensating Wheatstone Bridge Circuit

The use of feedback would be pointless if all unbalance signals were corrected, since then no signal would ever appear. The op-amp amplifier stages are therefore made into high gain low-pass filters so that frequencies over 10 hertz are not balanced.

One of the greatest problems with this circuit is the limitation on dynamic range because of the needed sensitivity. Since the FET can change resistance by only one or two ohms, the circuit must be fairly close to balance to begin with. To alleviate this condition, small trim pots for each gauge are included in a gauge switching unit. Periodic adjustments were made to keep the total gauge resistances equal to within 0.1Ω .

4.5.3. Signal Filtering

One of the worst problems encountered in the acquisition of data relates to the large noise-to-signal ratio of the incoming waveform at the lock-in inputs. The majority of the noise is at the Wheatstone bridge frequency $\omega_2 \sim 400$ Hz due to imperfect bridge balance and 2nd harmonic distortion from the FET non-linearity. There is also some noise coming through the gauges at the filament current frequency $\omega_1 \sim 350$ Hz. This noise has a tendency to overload the the input stage of the lock-in amplifier, especially when thermal drifts cause movement in the FET operating point. The lock-in pre-amp has a 3dB/octave filter built in; however this is insufficient since it only attenuates the noise by less than a factor of 2 at best. (Note: the signal of interest is at $\omega_1 + \omega_2$ or $2\omega_1 + \omega_2$. The separation between signal and noise is approximately one octave.)

An active filter was constructed to operate at the pre-amp output with the sole purpose of avoiding lock-in overloads. The design is a 0.5 dB pass-band ripple, 6th order Chebyshev high pass filter with the 3 dB point at approximately 600 Hz. Measurements show a factor of approximately 50 attenuation between the signal and noise frequencies. Gain at $\omega \rightarrow \infty$ is unity.

Each of the three second order stages has a transfer function given by

$$H(s) = \frac{s^2}{s^2 + (B\omega_c/C)s + \omega_c^2/C} \quad (4.21)$$

where $s=i\omega$. The constants B and C are called the normalized filter coefficients and the quality factor, Q, is defined by

$$Q = \sqrt{C}/B \quad (4.22)$$

The magnitude of H(s) is given by

$$|H(s)| = \frac{\omega^2}{\sqrt{[(\omega^2 - \omega_c^2/C)^2 + (B\omega_c\omega/C)^2]}} \quad (4.23)$$

Each stage was constructed in the VCVS (voltage-controlled voltage source) circuit configuration shown in Figure 4.13 with $f_c = 600$ Hz and $C_1 = .01\mu f$. Filter data appears in Table 4.3. (4.2)

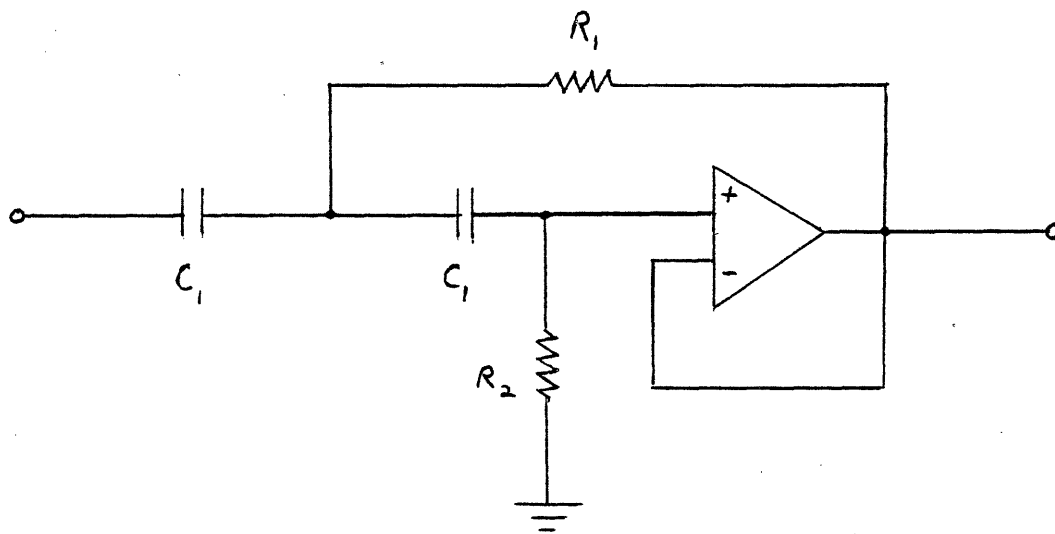


Figure 4.13 VCVS Active Filter Schematic
(single stage)

Table 4.3 Filter Parameters

stage	B	C	R_1	R_2
1	.1553	1.023	2062 Ω	349k Ω
2	.4243	0.590	5625 Ω	73.8k Ω
3	.5796	0.157	7687 Ω	14.4k Ω

The filter was very successful in eliminating the problem with input channel filtering as well as giving a larger temperature range of operation of the Wheatstone bridge. With less noise getting through to the input channel, the exact balance of the bridge becomes less critical and all facets of the measurement are made easier. A plot of the analytically expected filter characteristic is included as well as a photo of the measured response (Fig. 4.14-4.15).

4.5.4. Reference Channel Driver Circuit

In order to detect signals at the desired frequency, it is necessary to supply the reference channel of the lock-in amplifier with precisely that frequency. This must be derived from the same signal generators which drive the currents and the Wheatstone bridge. Otherwise, the signal-to-noise ratio is limited and frequency drifts are not automatically compensated. A circuit was designed and built to supply the sum frequencies $\omega_1 + \omega_2$ and $2\omega_1 + \omega_2$ to the lock-in. Fig. 4.16 is a schematic of the circuit.

There are three main sections of the reference channel driver: the frequency doubler, mixer, and band-pass filter. Frequency doubling is achieved with a phase-locked loop by locking together the input frequency ω_1 with the VCO (voltage controlled oscillator) output sent through a divide-by-two counter. The phase-locked loop forces the VCO output to be $2\omega_1$ such that the counter output exactly matches the input frequency.

Mixing is accomplished by gating a unity gain amplifier between its inverting and non-inverting output states. The control pulses for the gate are extracted either from the frequency doubler or directly from the input signal. The effect of the mixer is to multiply the bridge-derived signal $\sin(\omega_2 t)$ by a square wave. The fundamental of the square wave yields the product

$$\sin(\omega_2 t) \sin(\omega_1 t + \phi) \quad (4.24)$$

which is reduced using trigonometric relations to

$$\cos[(\omega_1 - \omega_2)t + \phi] - \cos[(\omega_1 + \omega_2)t + \phi]. \quad (4.25)$$

The band-pass filter passes the sum frequency, while attenuating the difference frequency and the higher harmonics due to the Fourier decomposition of the square wave. Leakage of the difference frequency through the band-pass filter tends to cause jitter in the output signal by modulating it. This effect can be minimized by proper selection of frequencies.

References:

- 4.1 J. J. Connor. Analysis of Structural Member Systems, New York: Ronald Press Co., 1976.

MST 20:37:52 Tuesday, 15th June, 1982

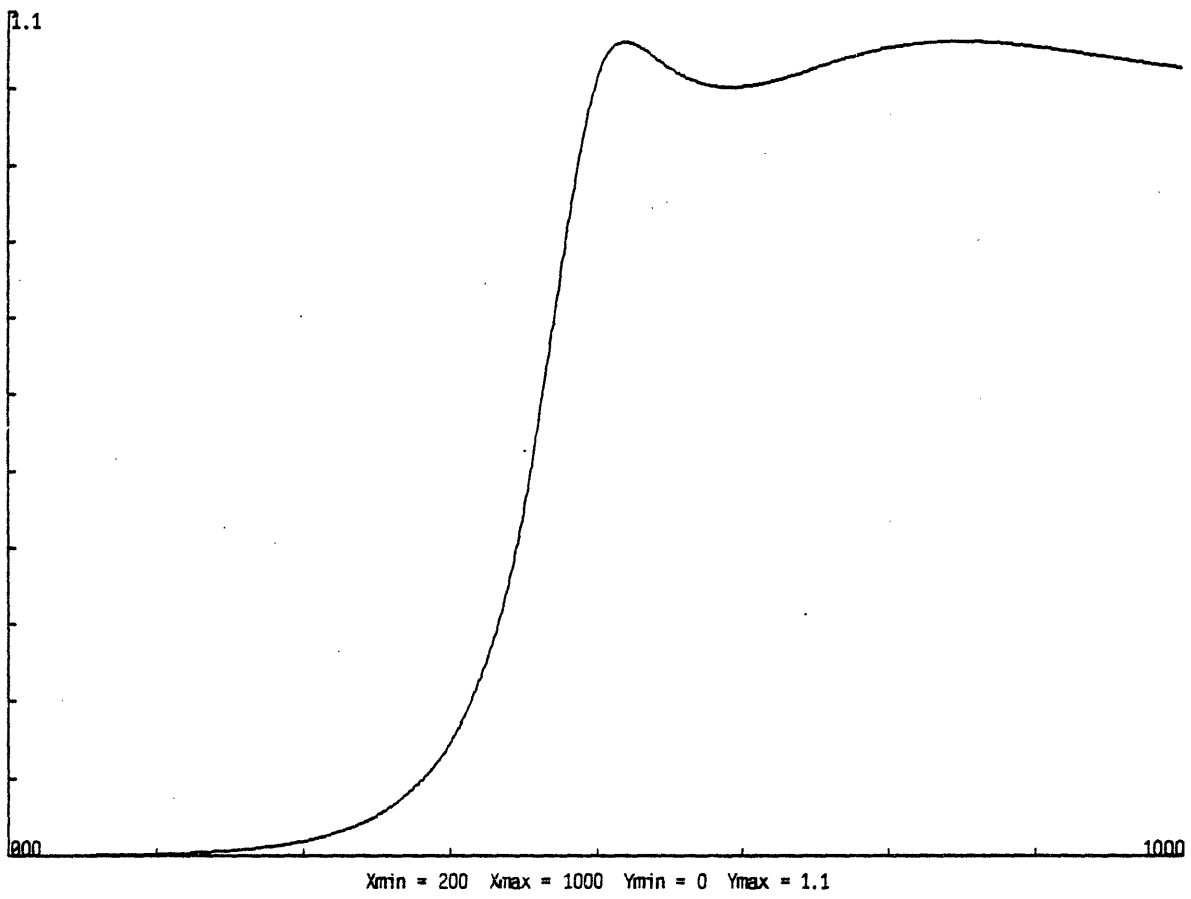


Figure 4.14 6th Order Band Pass Filter
Analytic Response

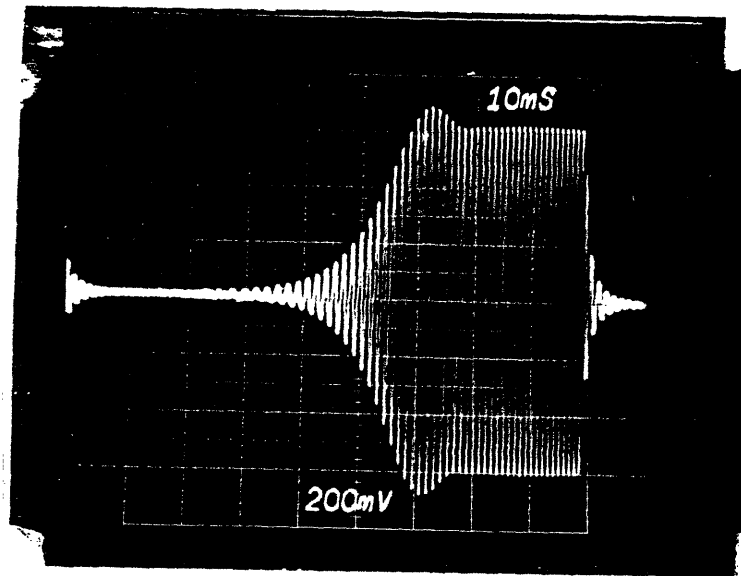
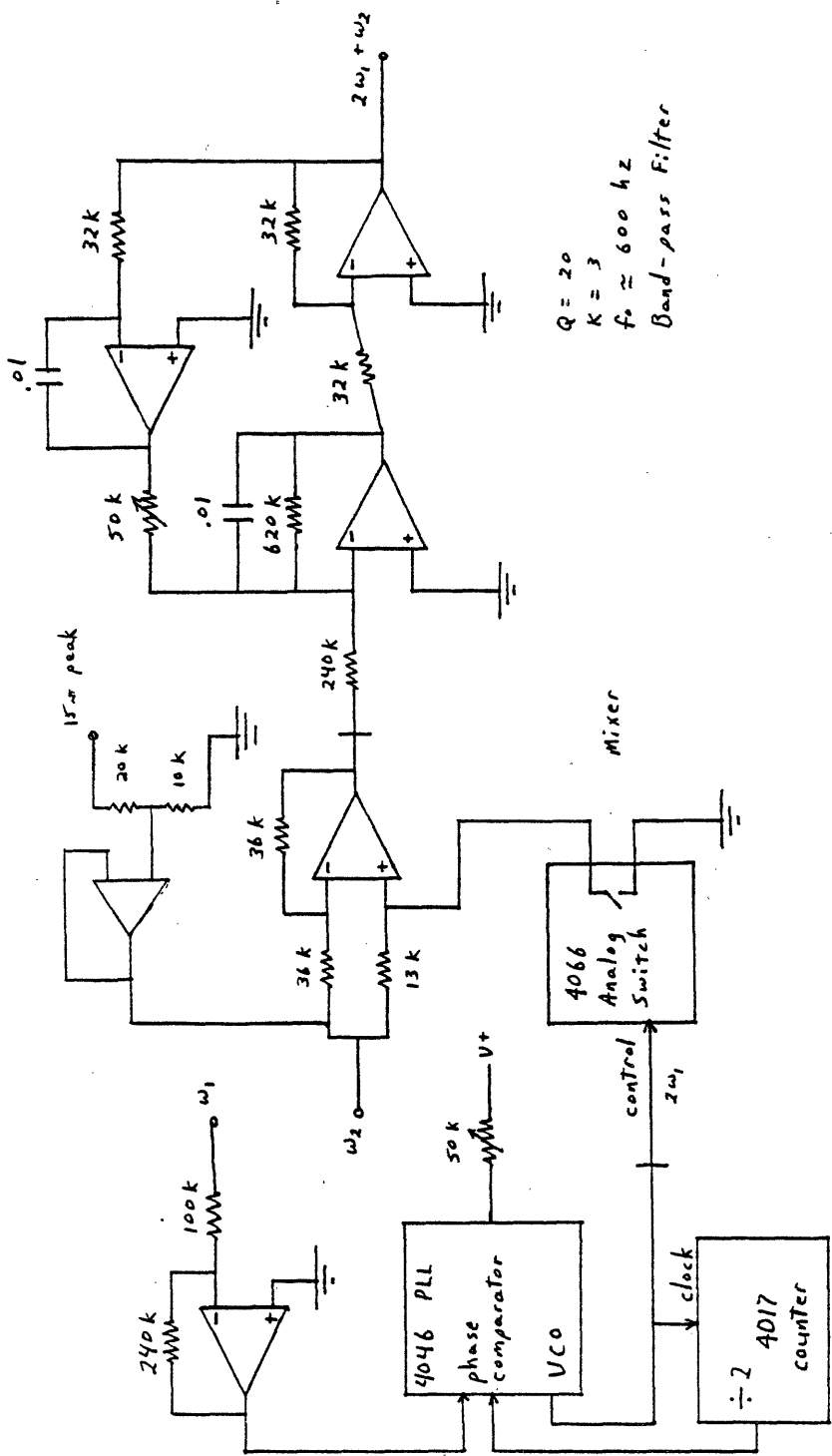


Figure 4.15 6th Order Band Pass Filter
Measured Response



$Q = 20$
 $K = 3$
 $f_0 \approx 600 \text{ Hz}$
 Band-pass Filter

Figure 4.16 Lock-in Reference Channel Driver

Electromagnetic Strain Test Results

5.1. Operation of the Experiment

In all of the tests, the principal source of data was the gauge response as measured by the lock-in amplifier at the selected frequencies — $(\omega_1 + \omega_2)$ for the external field interaction and $2\omega_1 + \omega_2$ for the self-interactions and filament-shell interactions. The shell was instrumented with a small number of gauges which are organized into 45° rosette sets. For the continuous shell experiments (with helical source currents), the shell is rotated with respect to the filaments in order to simulate the existence of many gauges located around the circumference.

The strain is a secondary quantity in the sense that it results from the induced currents and fields which are the primary consequence of the source current transient. This fact makes sources of error difficult to trace, since there is no directly measured indication of the details of the induced currents in the experiment. A direct measurement of the full induced current pattern would be useful, but very difficult.

The only knowledge of currents in the shell comes from a single measurement of total axial current using a pair of Rogowski coils. Beyond that, other available techniques have been considered but not implemented. One such technique is infrared temperature measurement of the structure. This provides a low resolution indication of the magnitude of the currents which result in ηI^2 eddy current heating. Another method of measuring the full current distribution passively (i.e. without interfering with the currents themselves) is to cover the shell with magnetic field pick-up loops or hall probes. These probes measure either static or time varying magnetic fields near the structure. The currents are inferred from the fields they produce. These techniques were considered too involved for the scope of these experiments.

5.1.1. Sources of Error

To understand the results it is important to appreciate the accuracy of the data and sources of error. The general philosophy of the EST experiment was to accept sources of error when

they could be reduced to 10-20%. The effort to substantially improve on this was considered unwarranted; in some cases this effort would significantly increase the cost and complexity of the experiment. In many ways these experiments push the limits of the apparatus, including the currents available from the power supply, the sensitivity of the detection electronics, and the noise levels present. With the available equipment, it was sometimes difficult to detect any signal at all; a net accuracy of 40-50% was accepted and efforts were made to try to understand how these sources of error affect the results.

The errors are categorized as machining and spatial measurements, power supply characteristics, and detection electronics. In the first category, one of the sources of error is the finite size of the gauges. The maximum resolution of a measurement is ~ 1.5 mm along the gauge axis due to the active length of the crystal, and a similar distance perpendicular to the gauge resulting from the alignment and epoxying technique used. In order to minimize these numbers, part of the backing was trimmed off of the gauges.

In addition to gauge positioning on the shell, there is an uncertainty of several degrees in the poloidal position measurement and errors due to machining imprecision. Perhaps the largest contribution of all is from the variation in shell thickness which was measured to be 20-30%. Since the gauges are permanently attached to one shell location, this error does not affect the spatial variation, but only the absolute magnitude of the measurements.

The second category includes measurement of currents and waveform shape. The filament current is fairly well characterized. A current shunt measures the current into the filaments directly. With the shell current, it is impossible to direct the current through a shunt, so Rogowski coils were used. Due to the geometry, a loop around the shell also must include current through the filaments (see Fig. 4.5), so a second coil around only the filaments is used to subtract off that portion of the signal. The Rogowski coil circuits have a frequency dependence which is not always precisely cancelled in the measurements. In addition, readings are taken directly off of the oscilloscope which is not a very accurate technique. The net result is at least a 10% uncertainty in the current which, since strain varies as current squared, results in $\sim 20\%$ error.

The waveform through the series of transformers is far from purely sinusoidal. Significant effort went into designing feedback into the base drive circuitry and most measurements were made at below full power in order to alleviate this problem. Cross-over distortion was fairly well eliminated, however a 5-10% component of distortion remained primarily due to the current-dependent voltage of the transistor amplifier. Since higher harmonic waveform distortion is at multiples of the base frequency, this "noise" tends to pass through to the detection electronics for one reason or another. One way is for frequency mixing of currents and fields in the shell. Another possibility is for the higher frequency components to pass all the way to the lock-in amplifier where

they can pass due to the nature of the synchronous detection procedure. (The mixer signal is a square wave. See Chapter 3.)

The final category of error sources includes all of the signal paths from the gauges to the lock-in amplifier. The gauges all have slightly different gauge factors and resistances. The gauge factors are all between 114 and 124. This error of less than 10% was not corrected. The problem of different resistances had to be treated because of the sensitivity of the self-balancing bridge circuit. If the resistors are not equal to within 1%, then each measurement requires rebalancing of all of the adjustments in the bridge circuit. The gauges were balanced by including trimming resistors in the gauge selector box. These resistors have the undesirable effect of altering the gauge effective sensitivity, since now not all of the resistance in the active leg of the bridge is responding to the strains. The variation in resistances of the gauges is dependent on temperature and bonding. The factory specs give a range of backed resistances between 115 and 120 Ω . This 5% error is particularly difficult to compensate since it is a time-dependent property.

After the gauge selection box, the signals pass into the Wheatstone bridge circuit which, as discussed earlier, has a simple high pass filter so that DC variations are compensated. The unwanted filtering of part of the real strain signal results in a frequency dependent error. Using the transfer function for a high pass filter

$$H = \frac{1}{[1 + (f_o/f)^2]^{1/2}} \quad (5.1)$$

with $f_o = 10$ Hz, we can calculate an attenuation at 500 Hz of 2%. Similar errors are introduced by high and low pass pre-filters after the bridge but before the lock-in amplifier.

The final source of error to be considered here is the lock-in amplifier reading. The output signal from the Keithley model 840 lock-in amplifier is taken directly from a needle gauge on the front panel. This itself introduces at least a 5-10% error simply because of the coarseness of the scale. For many of the measurements there was a substantial error signal with no current flowing in the shell. This was assumed to be a result of wideband noise emanating from the bridge circuit and associated electronics. This error signal was subtracted off, but still affects the accuracy of the measurements.

5.1.2. Selection of Operating Frequencies

Another quantity important to the understanding of the data is the operating frequency of the source currents and the Wheatstone bridge. There are various hardware limitations on the achievable frequencies.

1. The power supply performance degrades outside a fairly narrow range of frequencies. At less than 200 Hz, the amount of current transferred to the shell becomes lowered due to the

lowered inductive reactance. The mutual coupling between the filaments and shell improves with increasing frequency. Above 400 Hz, the transformer losses become large and the waveform begins to degrade.

2. The reference channel driver has a limitation on the frequency range to which its phase locked loop can follow. Because of the need to operate in the two modes $\omega_1 + \omega_2$ and $2\omega_1 + \omega_2$, the range of useable source current frequencies is further limited.
3. The rapid roll-off high pass filter has a cutoff frequency near 650 Hz. Since the optimum Wheatstone bridge frequency tends to be about 300-400 Hz, this limits filament frequencies to $> 250\text{Hz}$ for external field interactions.
4. The Wheatstone bridge frequency should be as high as possible but not close to an integral multiple of the filament frequency. Unfortunately, frequencies much above 300 Hz result in an increasing amount of second harmonic leakage of the bridge voltage through the filters. The final selection of frequencies which gives good results for both self and external field interactions is limited to approximately 250 Hz for the filaments and approximately 300 Hz for the bridge.

In addition to hardware limits, the presence of resonant behavior throughout the allowable range of frequencies adds a further limitation. The largest structural resonances are easy to locate, as they tend to be more distinct. It is very important for reproducibility of the data that an operating point is not chosen on the side of a large resonance. In this case, small variations in the signal generator or the structural response can cause large changes in output. Significant changes in the resonant frequency can come about due to temperature changes or small changes in the structural supports.

5.1.3. Circuit Sensitivity and Data Conversion

For all of the measurements described in this chapter, the Wheatstone bridge voltage was kept constant. This, together with the fact that the gauge factors were all approximately equal, implies that the circuit sensitivity for all measurements was constant.

The circuit sensitivity is obtained from

$$S_c = \frac{r}{1+r} S_g \sqrt{P_g R_g} \quad (5.2)$$

This equation must be altered to take into account the time dependence of the voltages and strains. Using the values in Table 5.1, we have

$$S_c = 43.5 \cos \omega_2 t \quad (5.3)$$

Table 5.1 Bridge Circuit Sensitivity Data

gauge resistance	110 Ω
gauge factor	118
<i>r</i>	10
bridge voltage	3.15 v. RMS

Now note that the strains are related to the output voltage by the relation

$$V_o = S_c \epsilon \quad (5.4)$$

With all of the correct time dependences included (the measured strains are at the frequency $(2\omega_1 + \omega_2)$),

$$V_o \cos(2\omega_1 + \omega_2)t = (43.5 \cos \omega_2 t)(\epsilon \cos 2\omega_1 t) \quad (5.5)$$

Remembering that

$$\cos x \cos y = \frac{1}{2}(\cos(x + y) + (\cos x - y)) \quad (5.6)$$

the result at the frequency $2\omega_1 + \omega_2$ is $V_o = 21.75\epsilon$. Since the voltages measured are RMS voltages and the desired strains are the peak values, the conversion from RMS voltage to peak strains (hereafter called the circuit sensitivity) is $S_c = V_o/\epsilon = 15.38\mu v/\mu\epsilon$.

5.1.4. Resonant Behavior

After observing a level of irreproducible in the data which far exceeded the measurement accuracy, attempts were made to discover any unexpected dependencies of the strain signal. One of the measurements made was a scan of source current frequencies for the shell current. The range of frequencies was limited on the low end by the supply voltage. The power amplifier saturates at a lower voltage when the coupling between the filaments and the shell is reduced at low frequency. On the high frequency end, a point is reached where the phase locked loop circuitry in the reference channel driver can't lock in. In addition, above a strain frequency of 600 Hz, the structure begins to respond so slowly due to finite inertia effects that nonresonant strains become small.

A plot of strain over the power supply frequency range $280 \leq f \leq 650$ Hz was obtained by electromagnetic loading, subject to these limitations. Both self interactions and external field interactions were measured at gauge #2, position 8. This gauge and position were chosen because of the high quality of the data obtained in previous measurements. The results show several resonances of amplitude about ten times the background level – much larger than the measurement error. The strain frequencies of the two most pronounced peaks were measured from the self interactions data at 660 Hz and 840 Hz (330 and 420 Hz for the currents). In addition, other small bumps were detected at 360 and 550 Hz from the external field interaction data. Figs. 5.1 and 5.2 show the data, with the two independent measurements corroborating the fact that these are indeed structural resonances.

After selecting an operating point near 240 Hz, careful measurements were made by scanning frequencies in 1 Hz steps about a desirable operating point. This was done by using the VCO (voltage controlled oscillator) feature of the Wavetek signal generator (model 144). An example

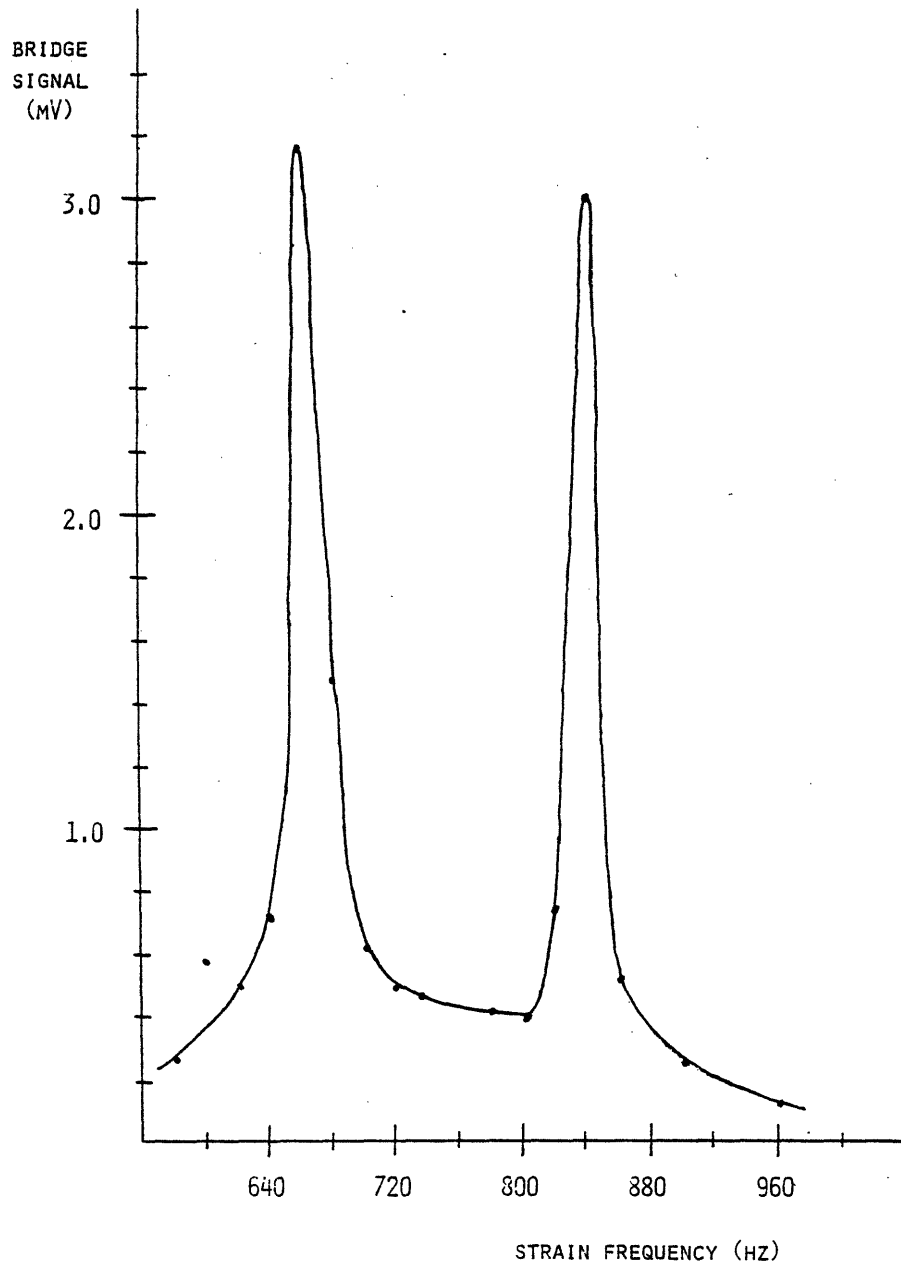


Figure 5.1 Strain Resonances from Self-Interactions

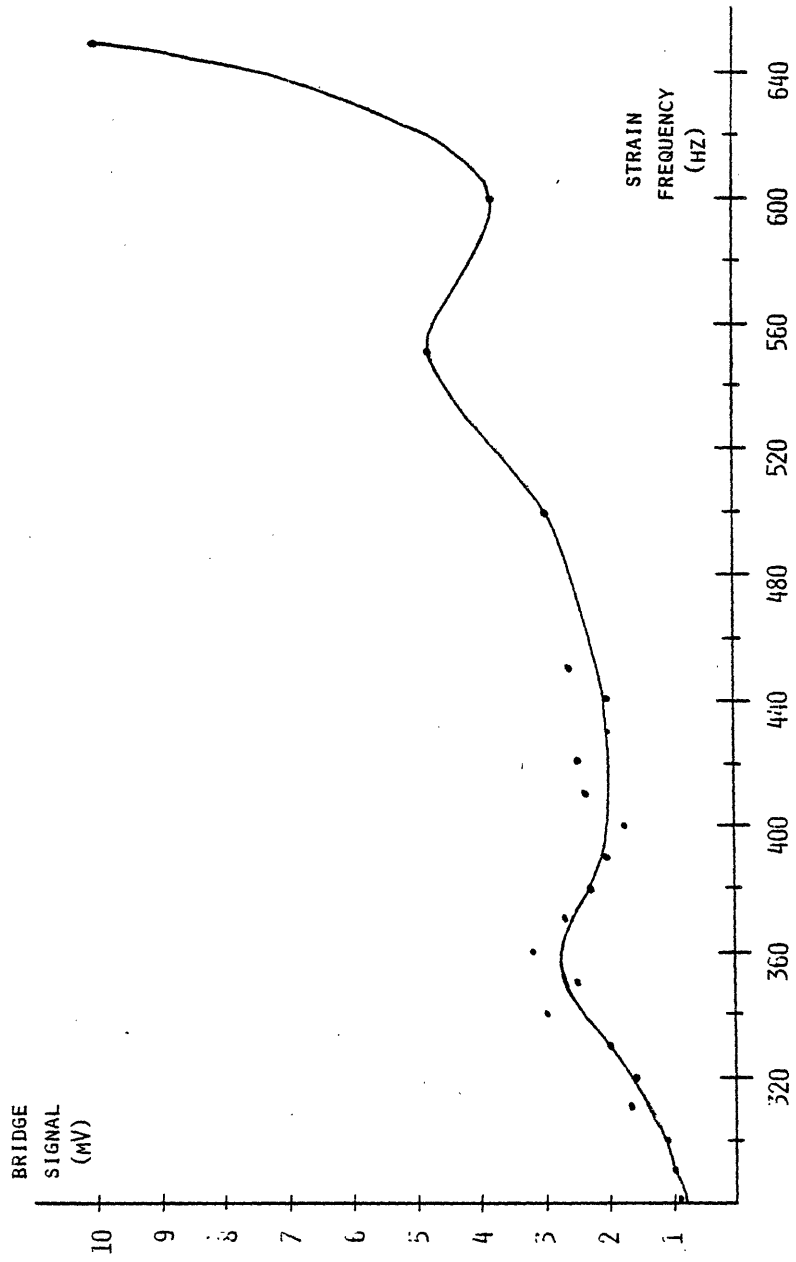


Figure 5.2 Strain Resonances from External Field Interactions

plot of the frequency scan is shown in Fig. 5.3. One notable observation is that there appears to be no single frequency which is completely free of resonant behavior. This will be an important point when the data is analyzed.

After identifying these structural resonances with electromagnetic loading, a more controlled analysis was attempted to chart out these and other resonances. A Tektronix 1L5 audio spectrum analyzer was connected to the amplified output of the Wheatstone bridge. The frequency range 0–2 kHz was scanned and 15 resonances charted.

In order to improve the resolution of the peaks and also to extend the frequency range, the cylinder was driven mechanically. A motor driven device was constructed to tap the cylinder at rates between 5–25 Hz. This results in loading which is nearly a series of delta functions in time. This should excite all frequencies, since an ideal delta function contains all fourier components in equal proportions. The rapid tapping results in some frequencies being more strongly excited, however the purpose of this measurement is only to identify the location of the resonances and not their strength.

The results are tabulated in Table 5.2 and a plot of the data appears as Fig. 5.4. The low frequency photo clearly shows 0 Hz, 60 Hz and the multiples 180 and 300 Hz. There are three real peaks in the frequency range of the experimental data, 200–1000 Hz. These correspond to the resonances previously measured at 550, 660, and 840 Hz. Finite element analysis predicts resonances near these values due to the modes $m/n = 1/2, 1/3,$ and $1/4$ as well as several higher n numbers for $m = 1$ and 2 . The most pronounced peaks for the electromagnetically loaded case are expected to be the $1/2$ and $1/4$ modes due to the fact that the loading is principally $\sin 2\theta$.

Further experimentation was done to try to verify exactly which modes were being driven. The cylinder was fastened to a rotary table. As the table was rotated, the loading was moved with respect to the gauge positions, thereby causing the vibrational nodes to move through the gauges. These could be easily detected as peaks and valleys in the output. Each frequency could be examined independently by tuning the spectrum analyzer to a specific frequency of interest.

The results were surprising. The 815 Hz peak clearly exhibited a circumferential mode number $n=5$, and the 630 Hz resonance showed $n=6$. It is suspected that these high mode numbers resulted from the narrow spatial shape of the driving function. As seen in Fig. 5.5, for axial mode numbers $m=1$ and 2 , there are different circumferential modes at very nearly the same frequency. The evidence is still compelling that during distributed electromagnetic loading it is the $n=2$ and 4 modes which appeared.

The basic conclusion of all of the experimental, analytic, and computational work done on resonant behavior is that there are many overlapping resonances even with the idealizations of a uniform cylinder removed. The overlapping of this multitude of resonances over most of

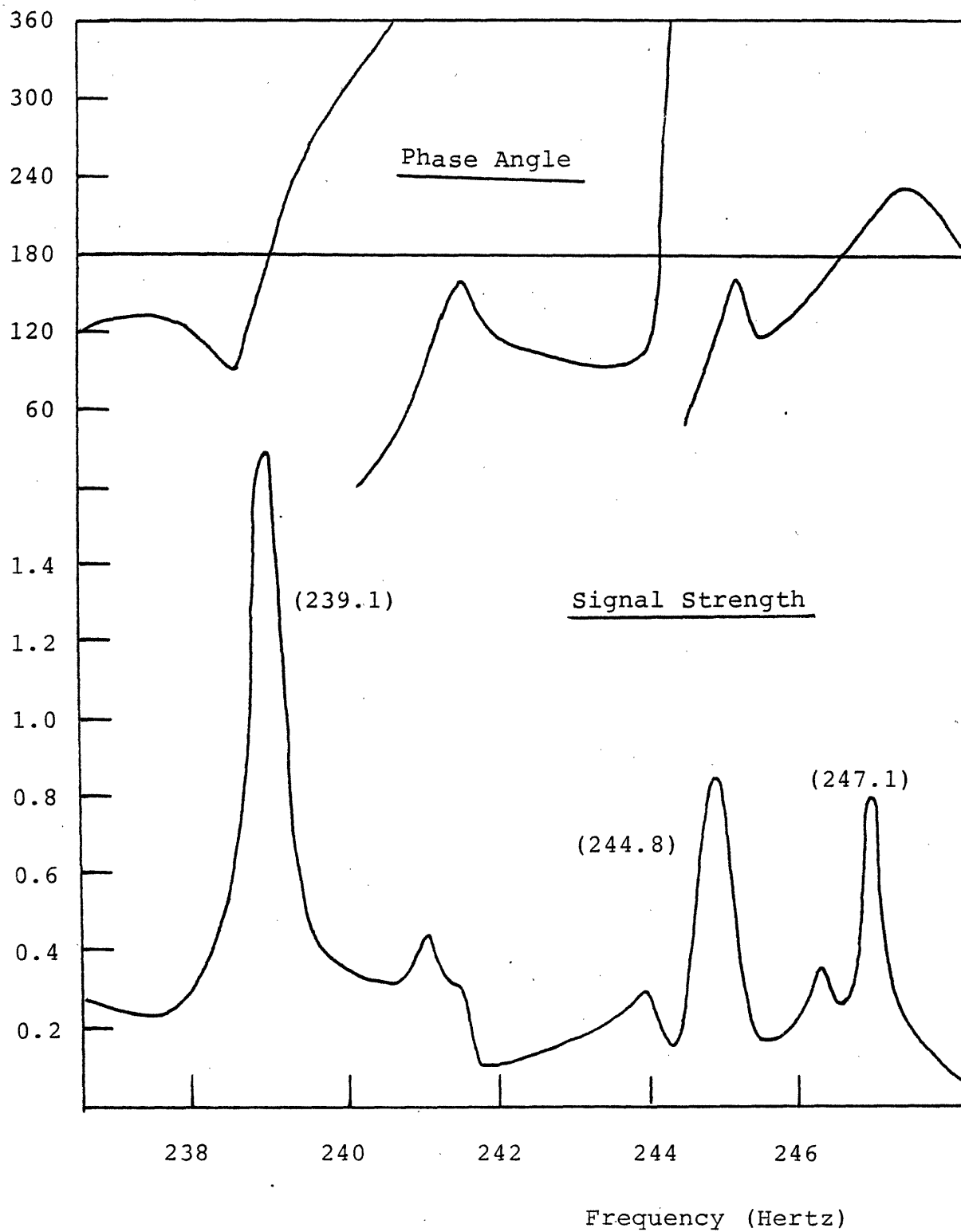
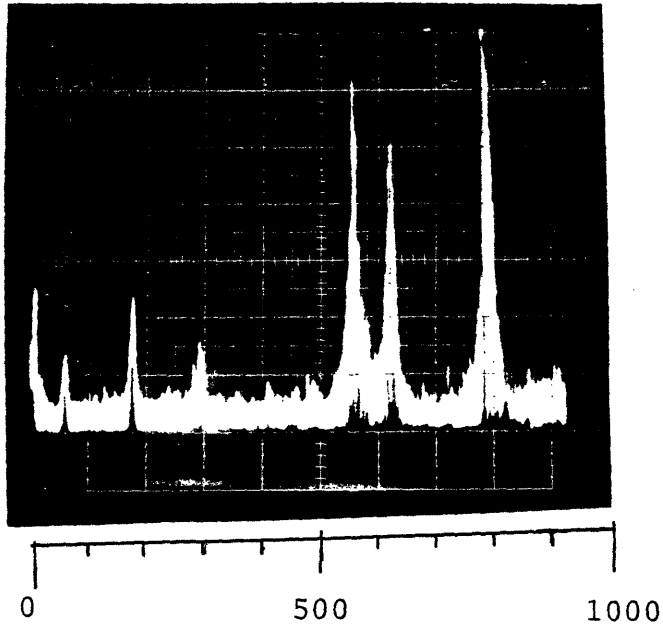


Figure 5.3. Filament Frequency Scan Near 240 Hz



frequency (Hz) →

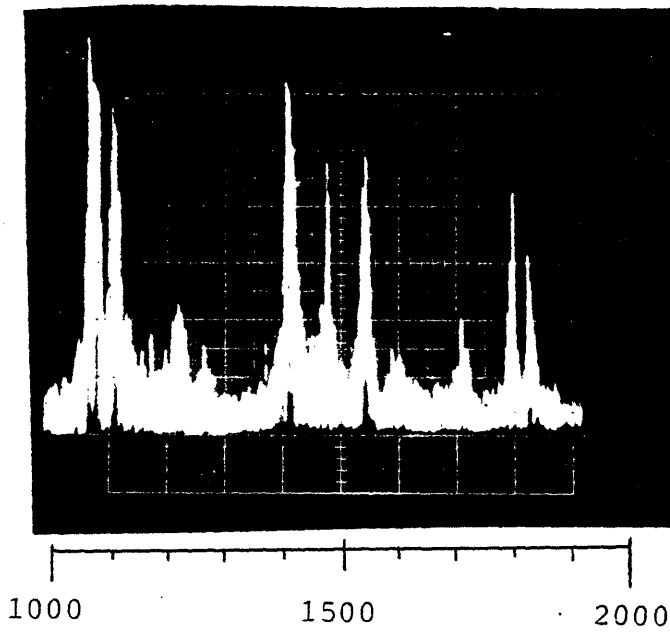


Figure 5.4 Mechanical Strain Resonance Data

Table 5.2 Measured Mechanical Resonances

575	1405
605	1475
630	1540
815	1595
1065	1710
1100	1800
1220	1825
1260	1960

the available frequency range was a constant problem with the measurements and also with the interpretation of the numerical results. Since the resonant behavior is so sensitive to structural properties, it is not possible to exactly predict the structural response at any given frequency.

Unfortunately, the initial set of data for the experiment was taken at 340 Hz which translates to a 680 Hz strain frequency for the self interactions. This could very well explain some of the difficulty in reproducing the data, since it is on a very steep slope section of the resonance at 660 Hz. Small variations in either the operating point or the structural properties (e.g. boundary conditions) could result in large changes in strain signal. On the other hand, operation at this resonance has shown that modal resonances exist and that it is difficult to find an operating point far enough away from them such that resonance behavior could be ignored in the analysis. In a reactor situation it is to be expected that the same trouble will occur, since tori are also subject to modal resonances.

Analysis of the Resonances

The problem of computing resonant frequencies is fundamentally very different from that of computing the response of a structure to a particular loading. Resonant behavior depends only upon the geometry of the structure. No indication of the magnitude of the response for any given loading can be given. It is not a time dependent problem as is sinusoidal loading at a particular frequency.

An analysis of the modal vibrations of a cylinder was attempted after the discovery of large resonances in the experimental data. Much work in this area has been done early in the century. The pioneering work was done by Lord Rayleigh who published the book "The Theory of Sound" in 1877.^(5.1) In it he derived the formula for $m=0$ vibrations (where "m" is the axial mode number and "n" is the circumferential mode number) with free end boundary conditions:

$$f = \frac{1}{2\pi} \sqrt{\left(\frac{Eh^2}{12\rho a^4(1-\nu^2)}\right) \left(\frac{n^2(n^2-1)^2}{n^2+1}\right)} \quad (5.7)$$

This he did by equating the kinetic energy at the mean position to the strain energy at the maximum displacement.

In the 1930's and 40's, studies were continued and in 1948 Arnold and Warburton published a work which analytically specified the resonant frequencies for the full spectrum of m and n numbers for the boundary conditions called "freely supported ends".^(5.2) Freely supported ends are allowed to move freely in the axial direction, but the end shape is constrained to remain circular. This is actually quite similar to the conditions of the Electromagnetic Strain Test where one end is clamped and the other is free to move, except for the existence of the flange which enforces circularity at the top. In the paper by Arnold and Warburton, the strain energy is expressed in

terms of sinusoidal displacements and the Lagrange equation is applied. A cubic equation results, the roots of which give three frequencies for each combination of m and n . Two of the three frequencies tend to be very high (inaudible).

The results of Fig. 5.5 for a connected structure are qualitatively much different compared to a simple plate type body. There is a characteristic dip in the resonant frequency as the circumferential mode number is increased. A minimum occurs at 4 or 5 for the $m = 0$ set of resonances, and at higher n numbers as m is increased. This type of behaviour is not present in simply connected structures where frequency monotonically increases with both mode numbers. The explanation is as follows:

There are two contributions to the total strain energy. One of these is called stretching energy, i.e. due only to extension of the middle surface of the deformed body. The other is bending energy — due to perpendicular movement of the shell with no extension of the middle surface. Stretching tends to entail higher energy for a given displacement. This can be seen by comparison of the bending rigidity

$$K = \frac{Et^3}{12(1 - \nu^2)} \quad (5.8)$$

versus the extensional rigidity

$$D = \frac{Et}{1 - \nu^2} \quad (5.9)$$

Since t is a small parameter in the thin shell approximation, Bending rigidity is much smaller than extensional rigidity. When a structure is reconnected, certain mode shapes require that both stretching and bending take place simultaneously. The very lowest m and n numbers require a great deal of stretching in order to accommodate that particular mode shape. Higher mode numbers require mostly only bending. At very high mode numbers, the effect of normal mode number scaling overtakes this decrease in stretching energy contribution.

In addition to the analytic comparison, modes and frequencies were analyzed using the structural analysis code PAFEC. PAFEC is described in Chapter 7. It is not necessary to fully understand the code for this calculation. The experimental apparatus was modelled using axisymmetric elements. For each poloidal mode number, the code finds eigenvalues of the stiffness matrix which results in the resonant frequencies for that mode. These results are also presented in Fig. 5.5. They show excellent agreement with the results using the theory of Arnold and Warburton. This is an indication that the freely supported end condition truly applies. The figure also includes the location of three of the experimentally observed resonances with electromagnetic loading. It is very plausible that the observed resonances are 2/1, 4/1, and 6/1. It is also possible that an $m = 2$ resonance exists, since three of these overlap with the frequencies observed.

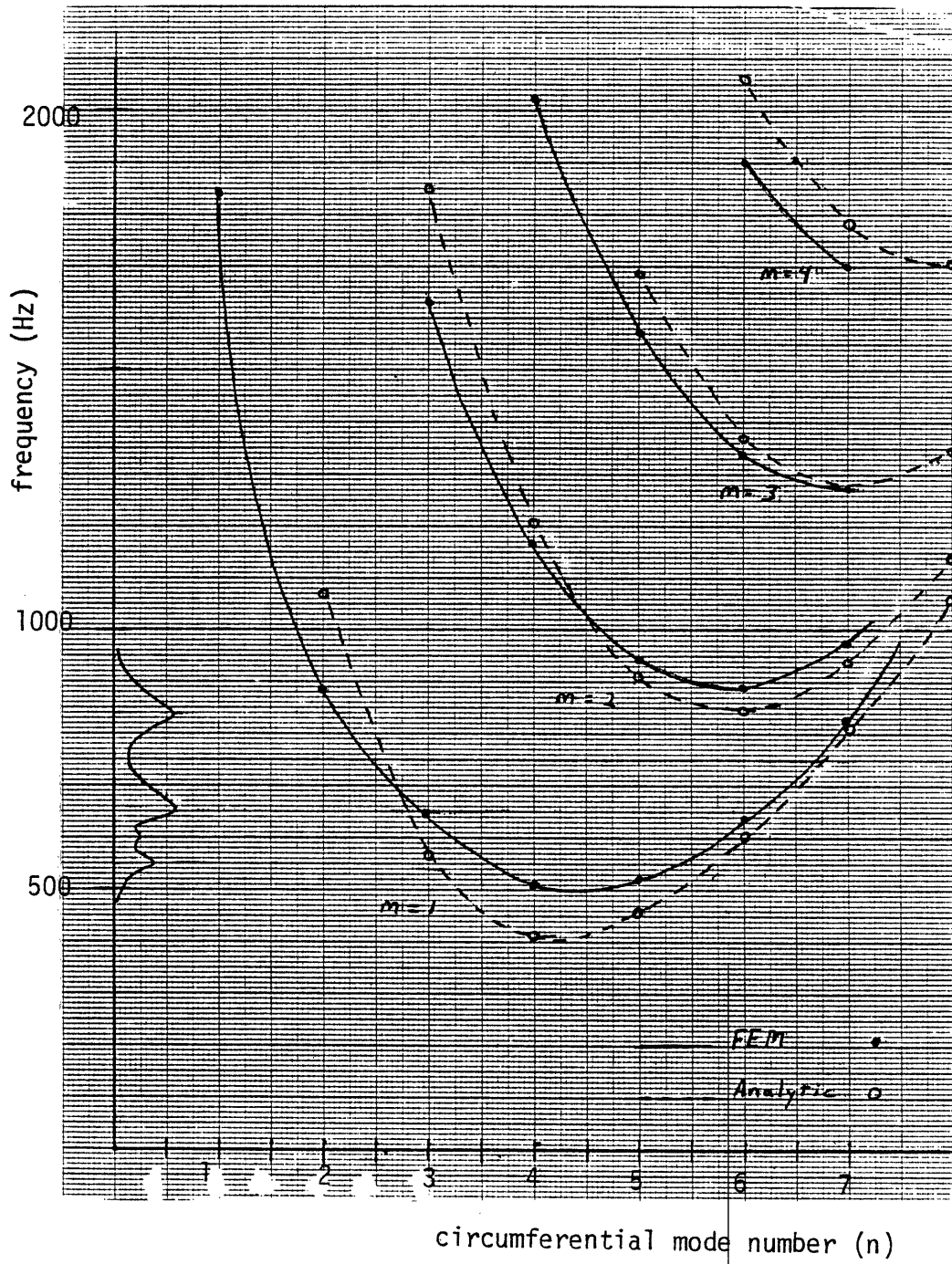


Figure 5.5 Modal Resonances of the Cylinder

5.1.5. Data Taking Procedure

For the experiment with a helical source current, there is a spatial dependence of currents, fields, and strains on the poloidal angle. The 2/1 filament set is composed of two groups of filaments each of which covers 90° of the circumference. In order to acquire the spatial behavior of the strains, the shell was rotated with respect to the filaments, covering a full period of the source current. Twenty equal spacings were used circumferentially, giving one reading per centimeter along the shell. Most of the spatial detail of the strain pattern is preserved with this number of readings; measurements using fewer positions tended to look random due to the fine structure of the strains.

At each shell position a reading was taken for each of the 6 gauges. The reading is accomplished by adjusting the lock-in phase angle and noting both the phase and the RMS value of the signal. Checks were made often for reproduceability and to check the I^2 dependence of strain vs. current (cf for external field interactions strain is proportional to current). These tests helped to determine the amount of interference from noise. Another test sometimes used was to vary the bridge voltage and note whether or not the signal strength was proportional to the bridge voltage. In some cases, especially at extremely low signal levels, the tests failed and data was discarded. By making small changes to the bridge frequency and/or filament frequency, resonant electrical and structural behavior was avoided.

5.2. Results for the Continuous Cylinder

The results of the Electromagnetic Strain Test are presented in the following two sections with interpretation of the general strain behavior. It is possible to present the magnitudes and general spatial behavior without numerical analysis. The raw data is presented here with scaling of the magnitudes and a Fourier decomposition of the spatial dependence. Analysis is postponed until after a discussion of the analytic and computational work.

5.2.1. Self-Interactions

There were two complete sets of measurements which were taken on the EST. The first set is not presented here. It was useful in pointing out deficiencies which were corrected with upgrades in several areas. First, the angle of rotation of the shell with respect to the filaments was increased to a full 360°. This was necessary due to the unexpected level of detail found in the strain response. The ability to rotate through a larger angle gives a better appreciation of the overall strain pattern. In addition, the levels of strain observed before the rebuild were close to unmeasurable. It was essential to increase the current transferred to the shell. This was accomplished by reworking the return current path, moving it out from the shell to increase the mutual coupling.

Another benefit of the first set of readings was the identification of structural resonances. In the second data set, more attention was given to the precise location of the measurements in frequency. The number of positions where data was taken were increased fourfold to accurately map the rapidly varying component of strain. In general, the preliminary data was very unpredictable, presumably because of the presence of resonant and fine scale behaviors.

The second set of data showed much improvement. The test conditions are given in Table 5.3 and the data for the continuous shell are given in Figs. 5.6-5.7 and Figs. 5.10-5.11. Each gauge is scanned through 20 positions which cover 180° of the shell poloidal angle. The phase angles of the gauge signals were used to determine when the signal passed through zero. At that time, the structure goes from tension into compression or vice versa. This is accompanied by a 180° phase shift of the observed signal. These phase angles are only relative, since the absolute value depends upon the exact tuning of the reference channel circuitry, frequency, phase-locked loop settings, etc.

The form of the data strongly suggests that the strains are composed of a series of fourier components. A nonlinear least squares fitting of the data was performed using a constant term and 4 cosines with the phases of the cosines also free parameters. The fits are plotted with the data in Figs. 5.6-5.7. The results of the fitting are tabulated in Table 5.4.

Using equations 3.5-3.8, the full plane stress state can be obtained for these tests. The results appear as Figs. 5.8-5.9.

There is a simple way to understand why the various harmonics exist by considering the imposed current loading. The source current is given by

$$I = I_o(1/2 + 2/\pi(\cos 2\theta) - 2/3\pi(\cos 6\theta) + \dots + 2/k\pi(-1)^{(k-1)/2} \cos 2k\theta) \quad (5.10)$$

for k odd. The response current (shell current) will contain the same harmonics, except that the coefficients of the terms will be different. As a gross generalization, the terms fall off as 1/n. The field at the shell has components due to the filament current as well as the shell current. Again, each harmonic is represented. The net loading is derived from a cross product of current and field,

$$\underline{P} = \underline{K} \times \underline{B} \quad (5.11)$$

Therefore, mixing will generate the even harmonics in the loading. Table 5.5 demonstrates this mixing process with a list of the field and current harmonics which generate the various strain harmonics. It suggests that the 1 and 3 harmonics in the strains are large due to the contribution of the 0 harmonic fields and currents. (The 0 harmonic is a constant.)

Several observations can be made concerning the fourier decomposition of the data.

1. The strain is dominated by the first two terms: a constant and a $\cos 2\pi x/L$. Gauge #1 is an exception.

Table 5.3 Test Conditions for the Continuous Shell Tests

Filament Current	1086 amps RMS
Shell Current	740 amps RMS
Phase Angle	36°
External Field	540 Gauss
Bridge voltage	$0.9 + 4.7\cos(\omega_2 t)$
Bridge frequency with B*	450 Hz
Bridge frequency w/o B	360 Hz
Filament frequency with B	320 Hz
Filament frequency w/o B	217 Hz

* (tests with and without external field
had different frequencies)

Table 5.4 Fourier Decomposition of the Data

Magnitudes					
Harmonic Number					
gauge #	0	1	2	3	4
1	-.017	.219	.056	.063	.386
2	.143	.239	.073	.039	.048
3	.121	.352	.063	.012	.072
4	.138	.181	.026	.003	.041
5	.069	.120	.069	.034	.025
6	.020	.213	.021	.015	.061

Phases (frac. of 2π)				
Harmonic Number				
gauge #	1	2	3	4
1	.224	.217	.233	.131
2	.385	.268	.278	.244
3	.331	.150	.167	.172
4	.648	.120	.303	.121
5	.355	.205	.293	.081
6	.641	.052	.302	.154

Table 5.5 Harmonic Loading of the Shell

loading harmonic	source current	source field
0	0	0
1	0	1
1	1	0
2	1	1
3	0	3
3	3	0
4	1	3
4	3	1

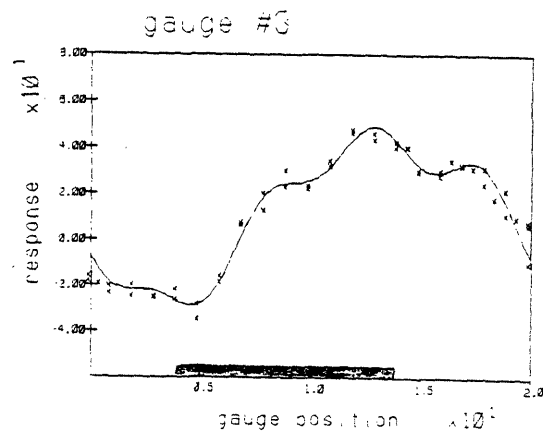
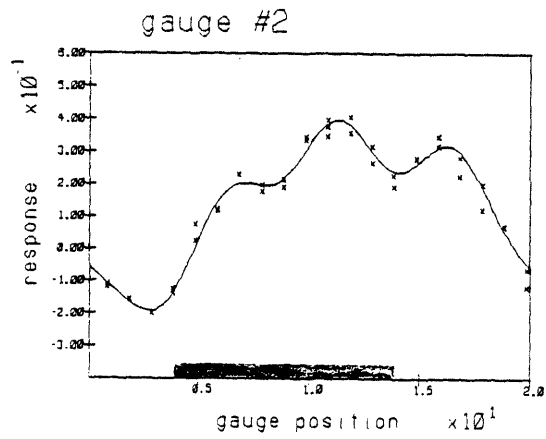
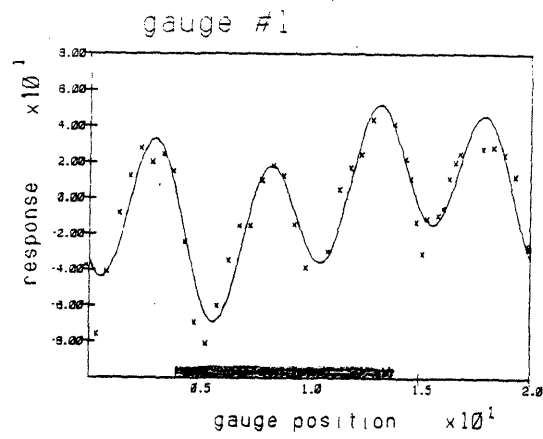


Figure 5.6 Fitted Data for Center Gauge, Self Interactions

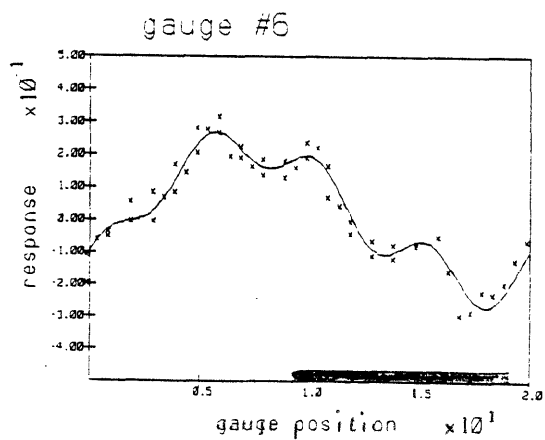
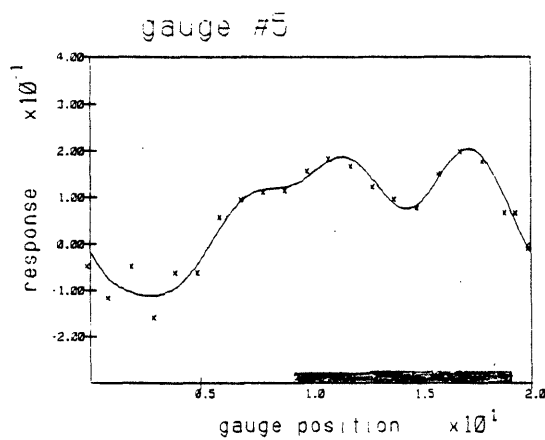
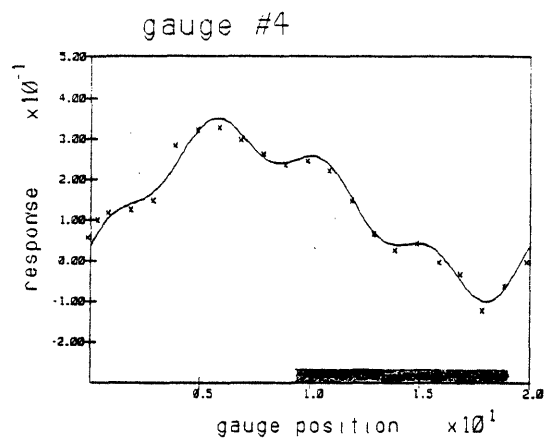


Figure 5.7 Fitted Data for Upper Gauge, Self Interactions

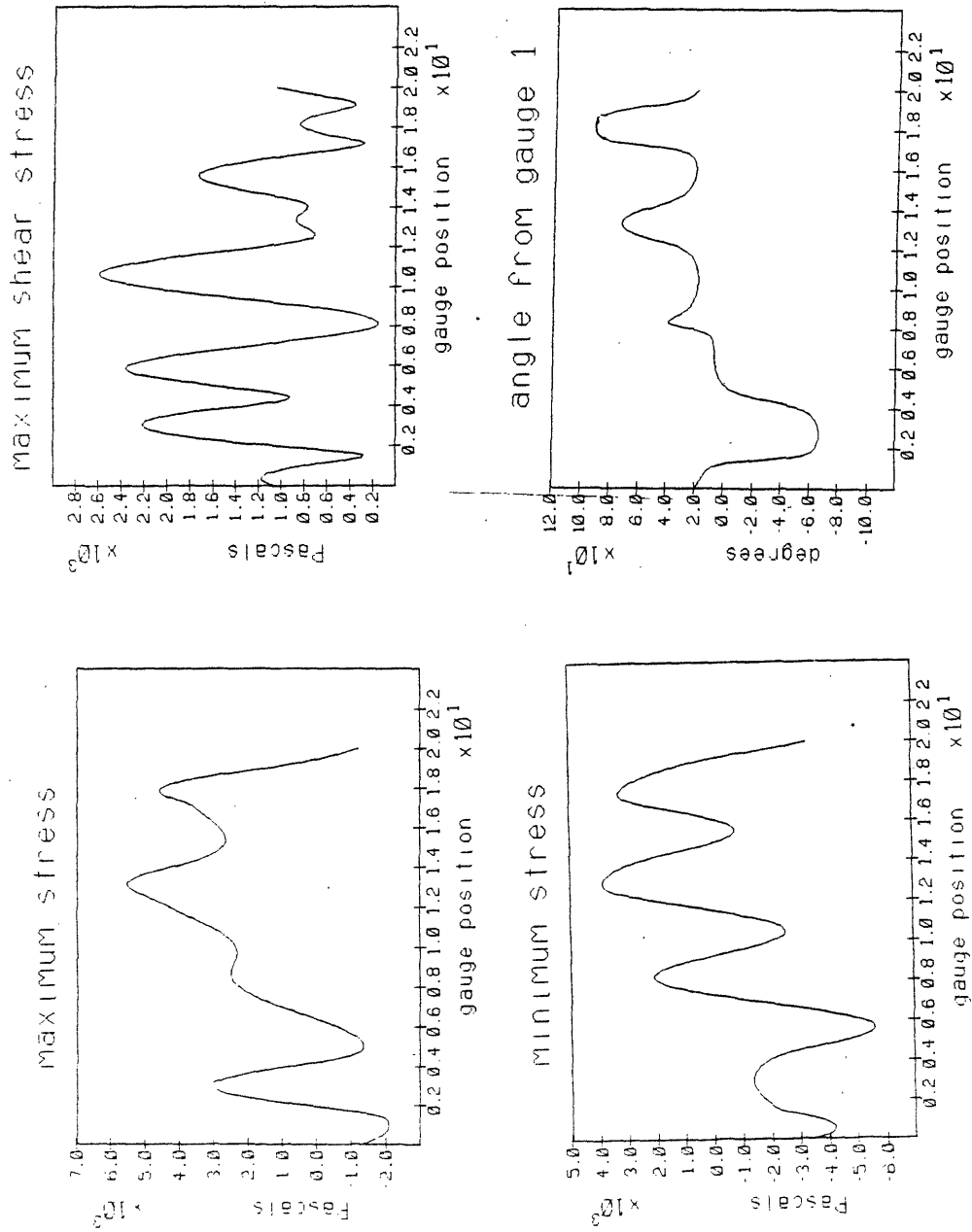


Figure 5.8 State of Stress for Center Gauge, Self Interactions

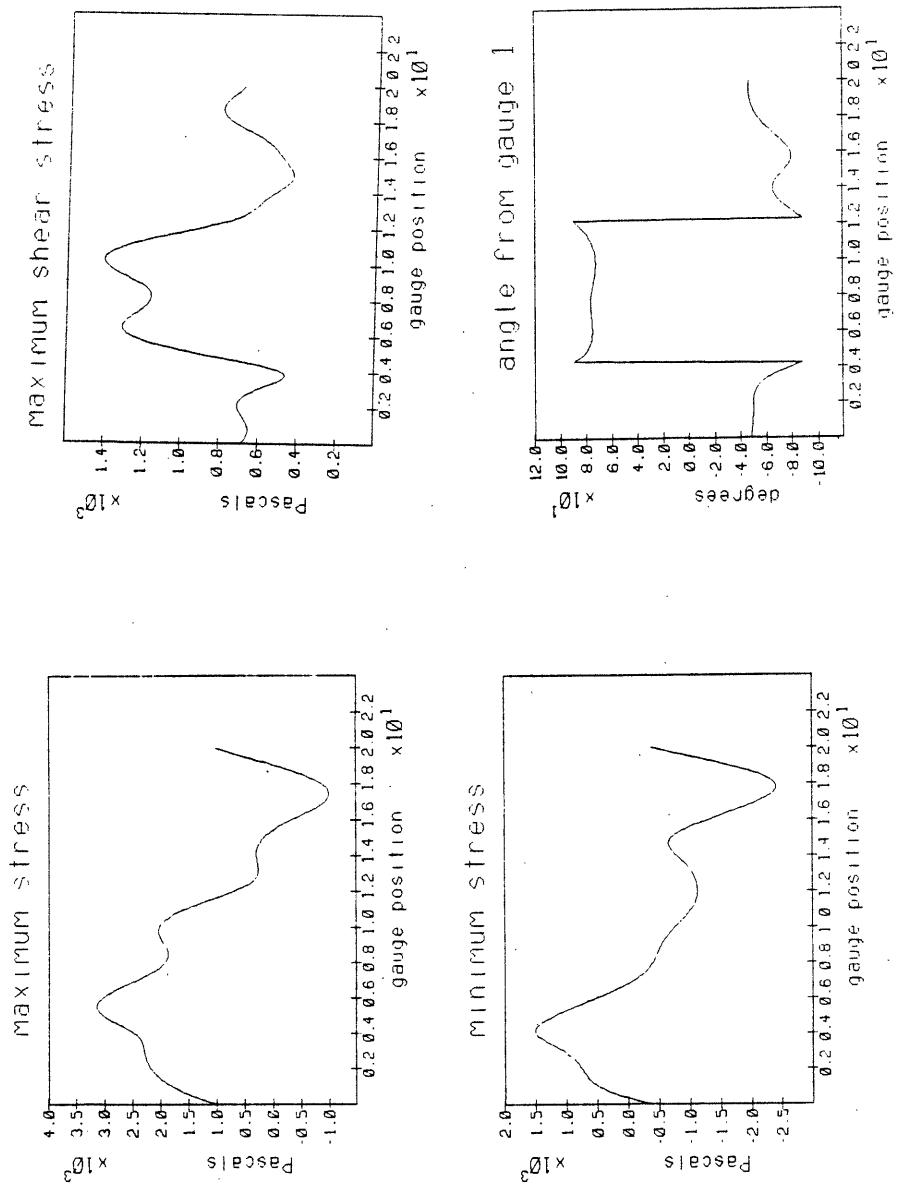


Figure 5.9 State of Stress for Upper Gauge, Self Interactions

2. The top and center rosettes *do not* behave identically. The central set has a magnitude approximately twice the upper set and the behavior of the angle to the principal axis appears to have changed.
3. The higher mode number phases are expressed mod($1/m$). If a phase is greater than $(1/2m)$, it indicates that a negative sign should appear on the magnitude.

In order to scale these observed results, we can estimate the strains expected from a uniform radial pressure given by the axial currents. The peak stresses observed are 6000 Pa RMS and the average values are between 1000-2000 Pa. For a shell current of 1050 amps, the expected stress for the axisymmetric problem is predicted to be 2300 Pa RMS. (The equations used for this calculation are found in Chapter 7.)

5.2.2. External Field Interaction

Data for the external field interactions are clearer for two reasons. First, the strain levels are somewhat larger due to the fact the the external field was larger than the induced fields. Second, since there is only one interaction taking place, the force pattern *should* be simpler – only the 0 harmonic of the field is important. The data in Fig. 5.10-5.11 shows that the poloidal dependence is dominated by the first harmonic with almost no higher harmonics evident. In this case, the upper gauge set shows slightly larger strains compared to the central gauge set. This is presumably a result of the fact that a radial field is absent for the central gauge set.

As with self-interactions, the magnitude of these strains can be easily scaled. For an average radial field of 40 Gauss and currents of 550 amps, the expected shear stress is 3100 Pa RMS. The stress is obtained for the data and plotted in Fig. 5.12-5.13. The average values are between 4000-8000 Pa RMS. These axisymmetric estimates are not meant to be critically compared. The similarity in their order of magnitude is taken as a sign that the measurements are at least in the range one might expect.

5.3. Results for the Cylinder with a Hole

After all of the data had been accumulated for the continuous shell tests, a $1\frac{1}{2}$ inch hole was drilled into the center of the shell with a hole saw. The helical filaments were disconnected and replaced with uniform axial filaments at the center of the shell. As shown in Fig. 4.11, five rosettes were fastened around the hole in addition to the original two rosettes which were left in place 180° away from the hole circumferentially. This set of experiments tests the effects of simple source currents on discontinuous structures. The structural discontinuity not only affects the induced currents and loading, but more importantly it results in large stress concentrations near the hole.

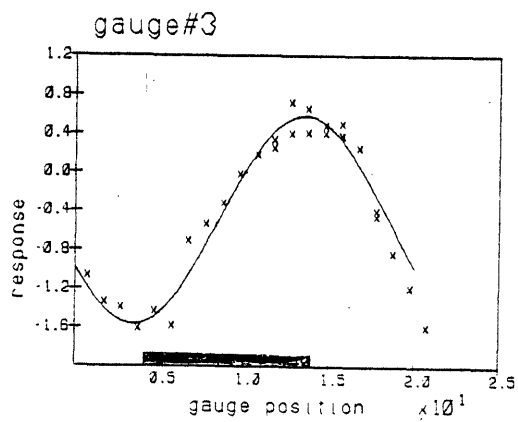
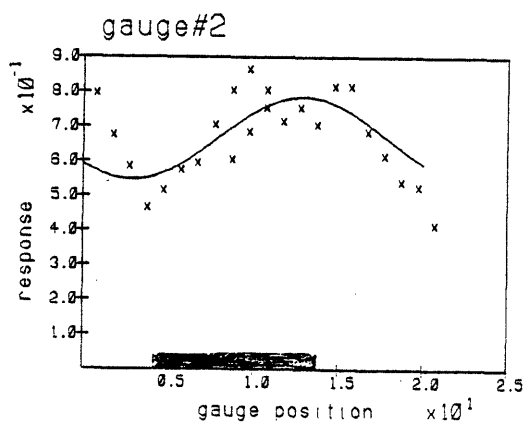
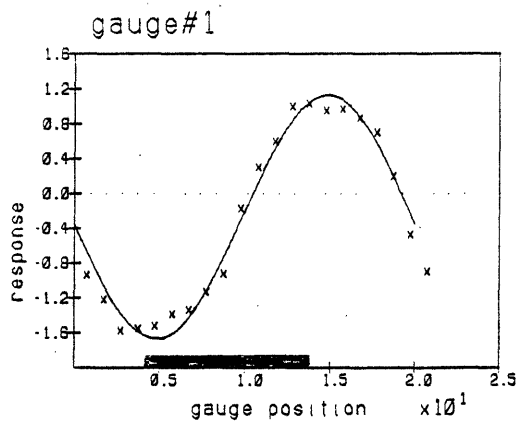


Figure 5.10 Fitted Data for Center Gauge, External
Field Interactions

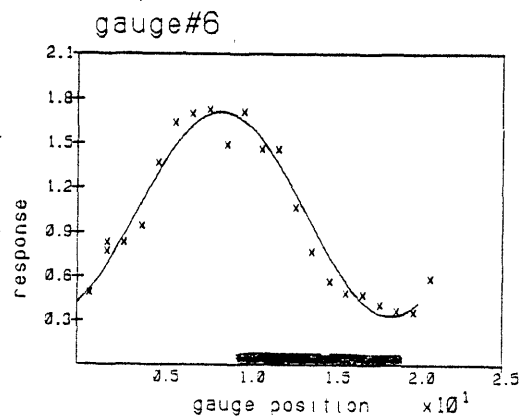
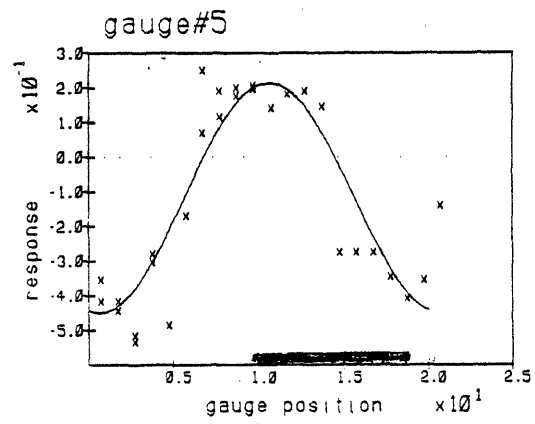
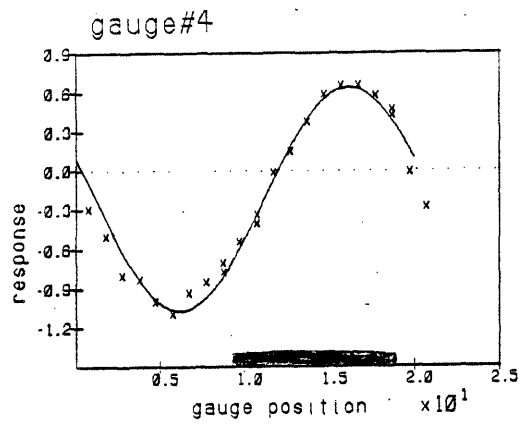


Figure 5.11 Fitted Data for Upper Gauge, External
Field Interactions

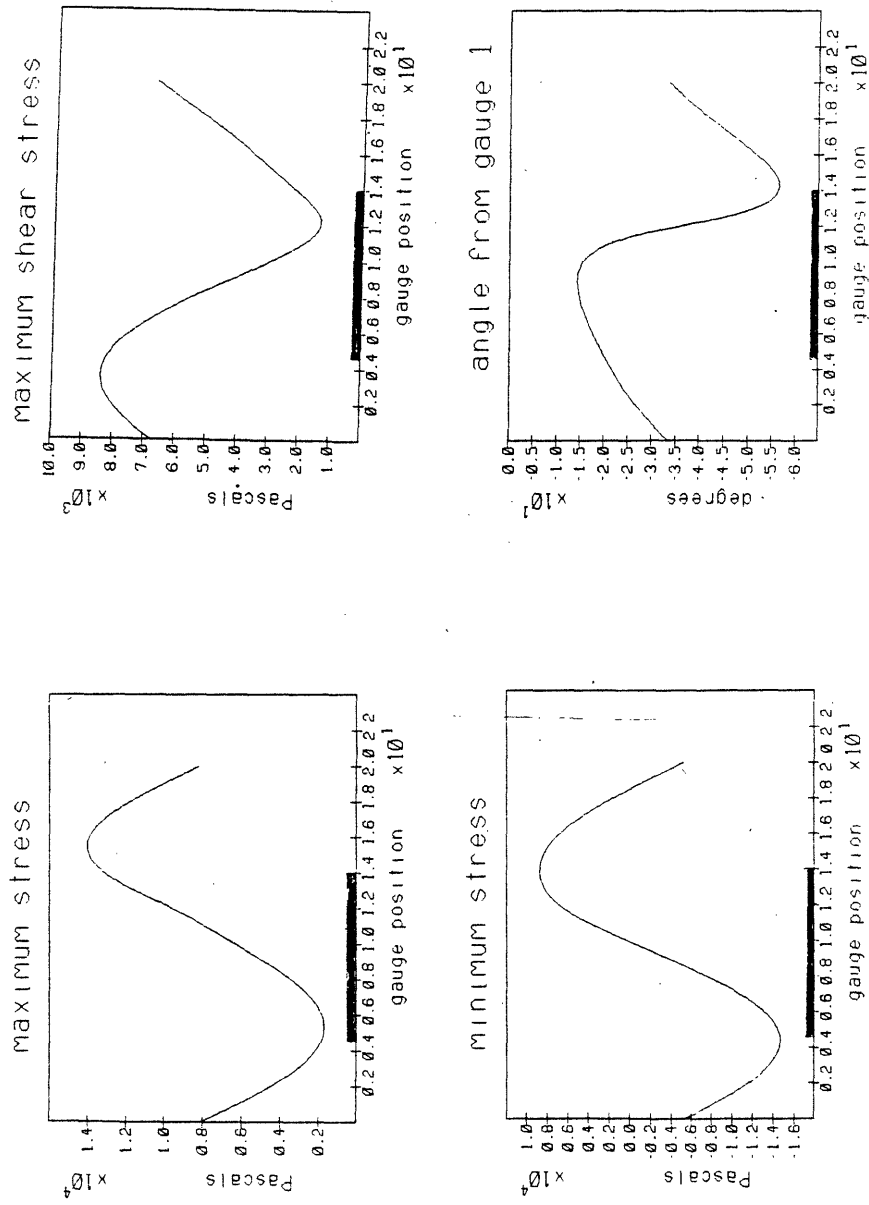


Figure 5.12 State of Stress for Center Gauge, External Field Interactions

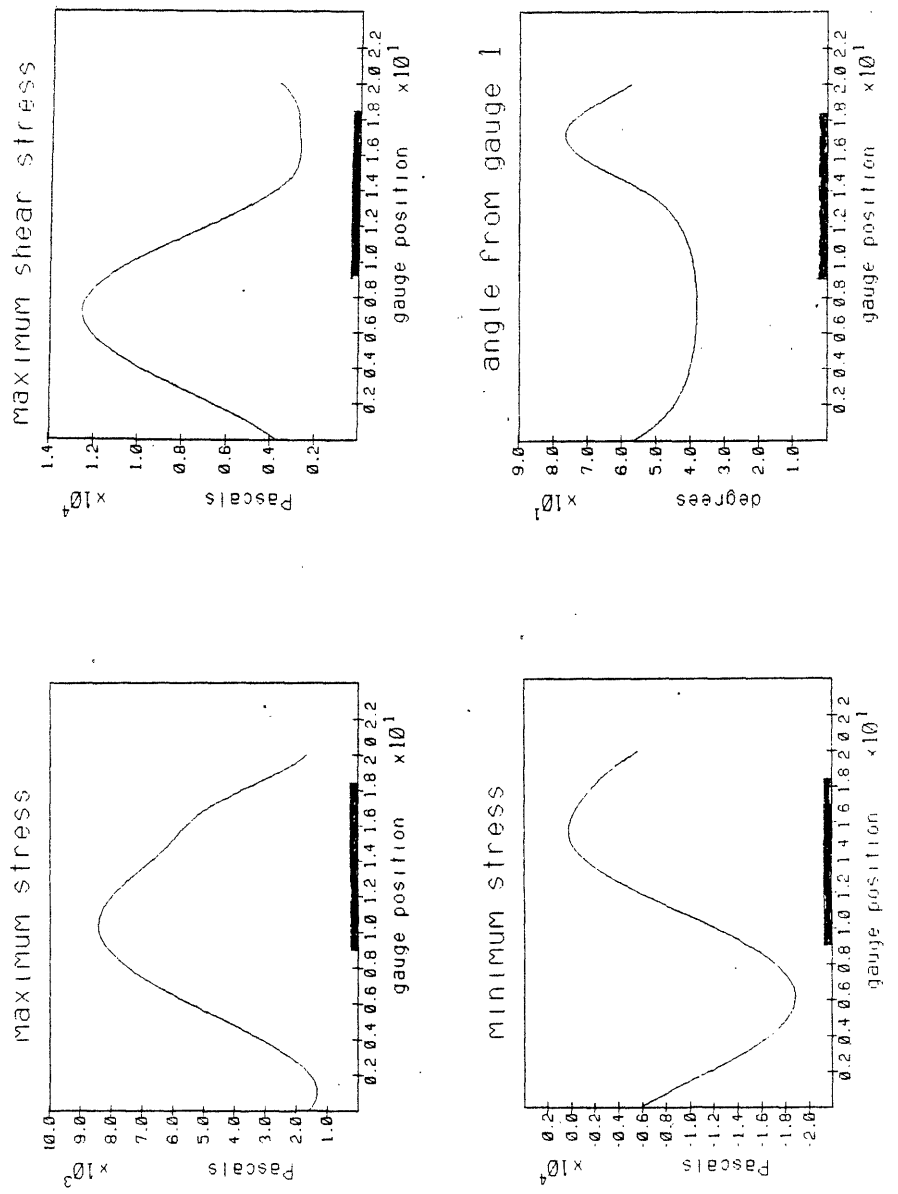


Figure 5.13 State of Stress for Upper Gauge, External Field Interactions

For these tests, the data is considerably easier to accumulate. With no angular dependence of the driving function, only one shell position is required. Therefore, the data appears in tables rather than graphs. Other than this, the data taking procedure is similar to the continuous shell tests. The test conditions are listed in Table 5.6.

Only the processed stresses are presented for the tests with the hole. These appear in Table 5.7. The stresses are presented as principal stresses with the angle measured from the horizontal to the maximum stress axis. This data can then be easily transformed to stresses at any other angle.

Due to the small amount of data required, the tests were repeated. All of the data which was taken is included in the table. The main points drawn from a quick look at the data are:

1. The stress concentration factor around the hole is approximately a factor of 10.
2. The symmetry gauges (2 and 5) differ substantially from one another.

References:

- 5.1 J. W. S. Rayleigh. The Theory of Sound, Vol. 1, Dover Publications, New York, 1945.
- 5.2 R. N. Arnold and G. B. Warburton, "*Flexural Vibrations of the Walls of Thin Cylindrical Shells Having Freely Supported Ends*," Proc. Roy. Soc. London, 197, pp238-256 (1949).

Table 5.6 Test Conditions with the Hole Present

Filament Current	1700 amps p-p
Shell Current	1116 amps p-p
Phase Angle	36°
External Field	540 Gauss

(for measurements of gauges 6 and 7
the currents are doubled)

Table 5.7 Data for the Cylinder with a Hole

test1 gauge data, self-interactions				
gauge no.	max. stress	min. stress	shear stress	angle
1	0.138E+05	0.484E+03	0.666E+04	-10.68
2	0.321E+04	-0.672E+04	0.497E+04	-13.86
3	0.120E+05	0.135E+04	0.532E+04	40.12
4	0.617E+04	0.359E+04	0.129E+04	10.64
5	0.378E+03	-0.383E+04	0.210E+04	2.11
6	0.494E+03	-0.120E+04	0.845E+03	18.43
7	0.122E+04	0.884E+03	0.169E+03	-45.00

test2 gauge data, self-interactions				
gauge no.	max. stress	min. stress	shear stress	angle
1	0.124E+05	0.261E+03	0.606E+04	-9.22
2	0.270E+04	-0.621E+04	0.445E+04	-9.22
3	0.107E+05	0.268E+04	0.399E+04	38.47
4	0.639E+04	0.414E+04	0.112E+04	8.76
5	0.202E+04	-0.331E+04	0.266E+04	9.89
6	-0.948E+03	-0.140E+04	0.228E+03	1.06
7	0.134E+04	0.104E+04	0.151E+03	13.28

test3 gauge data, self-interactions				
gauge no.	max. stress	min. stress	shear stress	angle
1	0.977E+04	-0.288E+03	0.503E+04	8.30
2	0.585E+04	-0.269E+04	0.427E+04	2.27
3	0.733E+04	0.472E+04	0.131E+04	-6.87
4	0.567E+04	0.358E+04	0.105E+04	-2.32
5	0.631E+04	-0.104E+04	0.367E+04	8.24

test1f gauge data, external field interactions				
gauge no.	max. stress	min. stress	shear stress	angle
1	0.213E+05	0.106E+05	0.533E+04	0.45
2	-0.632E+03	-0.229E+05	0.111E+05	-34.54
3	0.132E+05	-0.235E+05	0.184E+05	-43.60
4	-0.188E+04	-0.690E+04	0.251E+04	-22.50
5	0.271E+05	0.147E+05	0.617E+04	6.73
6	0.720E+04	0.240E+04	0.240E+04	33.22
7	0.382E+04	0.197E+04	0.928E+03	29.97

test2f gauge data, external field interactions				
gauge no.	max. stress	min. stress	shear stress	angle
1	0.124E+05	0.102E+04	0.571E+04	13.98
2	0.522E+04	-0.156E+05	0.104E+05	-33.97
3	0.117E+05	-0.203E+05	0.160E+05	-43.94
4	0.199E+04	-0.854E+04	0.527E+04	-31.31
5	0.171E+05	0.141E+05	0.148E+04	29.52
6	0.658E+04	-0.353E+04	0.505E+04	29.57
7	0.331E+04	-0.155E+04	0.243E+04	22.50

Axisymmetric Calculation of Currents and Strains

6.1. Introduction

In order to estimate the order of magnitude of the stresses and strains in reactors it is natural first to try an axisymmetric calculation. This type of analysis is quite limited in that most problems of real interest are not axisymmetric. It is anticipated that the peak effects will take place at structural nonuniformities. Nevertheless, because of its inherent simplicity it is much easier to use the results of such a calculation to establish an intuitive understanding of the nature of the forces at work. In this chapter, this framework of understanding is developed. Then in the following chapter a full 3-D analysis is undertaken. Because the experimental apparatus used for comparison was a cylinder, the 3-D analysis is all done in cylindrical geometry. For that work the emphasis is on the aspects of nonuniformity rather than the toroidicity of the problem.

For the axisymmetric analysis, an efficient set of $1\frac{1}{2}$ -D computer routines was developed to compute the induced currents, pressure loading, and structural response in thin toroidal shells. The method is described here and example results are presented for designs which include higher field strengths, a shifted plasma, and an electromagnetic shield. A more detailed comparison of reactor types has been published elsewhere ^(6.1) using the same method.

The analysis is called $1\frac{1}{2}$ -D because the currents are represented as 1-D, toroidally directed and axisymmetric, whereas the resulting fields are 2-D in the r - z plane. The 2-D pressures resulting from the eddy current solution are used in the analysis of the structural response, including displacements, moments, shears, and strains. This part of the problem can be reduced to 1-D with toroidal axisymmetry and the poloidal angle being the independent variable.

6.1.1. Overview of Pressures

The first step in the analysis is the determination of induced currents and pressures arising from $J \times B$ forces. The eddy current problem has 1-D currents directed along θ and 2-D magnetic

fields which contain both r- and z-components (see Fig. 6.1). The structure includes a conducting toroidal shell whose inner volume contains current-carrying plasma. This current is called the source current. When the plasma currents experience a transient, there are currents induced in the shell which attempt to maintain the field pattern unchanged. These currents are called the induced currents. If the magnetic diffusion time of the torus is long compared to the transient time constant, then the structural currents are large and shield the region outside the torus from the transient. In this case the structural currents die away slowly due to the resistance of the structure. This is the case for the examples studied in this thesis.

For a source current at the center of the torus, the induced currents are peaked toward the major axis. The main reason for this is the lower resistance of the inner edge due to a shorter path length around the torus. In addition, the field due to a current loop is larger inside the loop, therefore the linked fluxes are larger on the inside of the shell (see Figs. 6.2 and 6.3). The result is larger induced currents. Of course, if the current is shifted outward with respect to the shell axis, then this would not necessarily hold true. Even disregarding this nonuniform field effect, at early times in the transient the inner edge of the torus shields the outboard side from the flux swing through the central hole. This also results in the existence of peaked currents.

The forces generated by a disruption can be analyzed in three main components:

(i) Minor Radius Compression

The induced currents always flow in the same direction as the source current. This results in a minor radius compressive force due to both shell current interaction with the shell current field (called "self interactions") and shell current interaction with the source current field (called "source interactions").

(ii) Hoop Force Expansion

The hoop force attempts to expand the shell towards a larger major radius. On the inboard side it is aligned with the major radius component of the compressive force. On the outboard side the two forces tend to cancel. This is a principal source of the poloidal asymmetry observed. The source field also has a hoop force effect on the shell current. Early in the disruption when the currents are peaked on the inside, the source current draws the shell outward (and the source current is itself drawn inward).

(iii) Vertical Field Interaction

The vertical field interaction with the shell current yields a force directed towards the major axis, opposite to the hoop force. Depending on the geometry, field strength, and time during the transient, the three forces become more or less influential with respect to one another. The result is that in some cases there is substantial poloidal variation of the forces but in other cases there is little variation. The magnitude of the vertical field is the primary cause

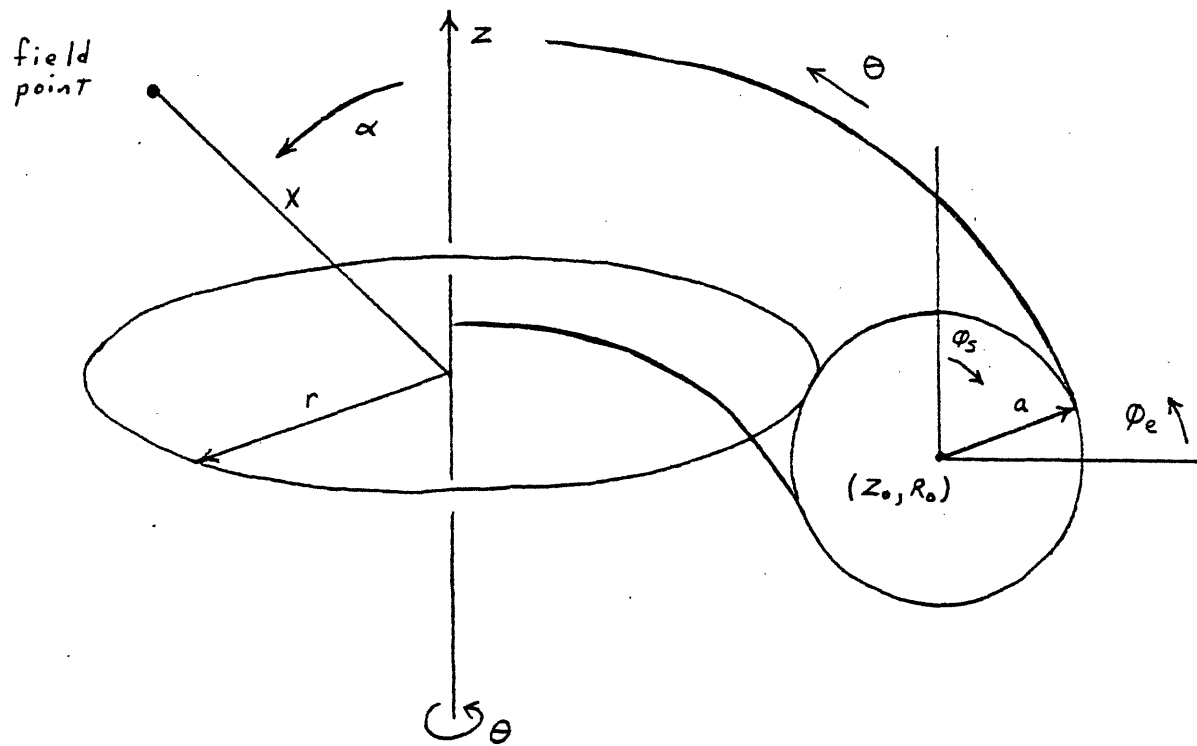


Figure 6.1 Definition of Coordinates

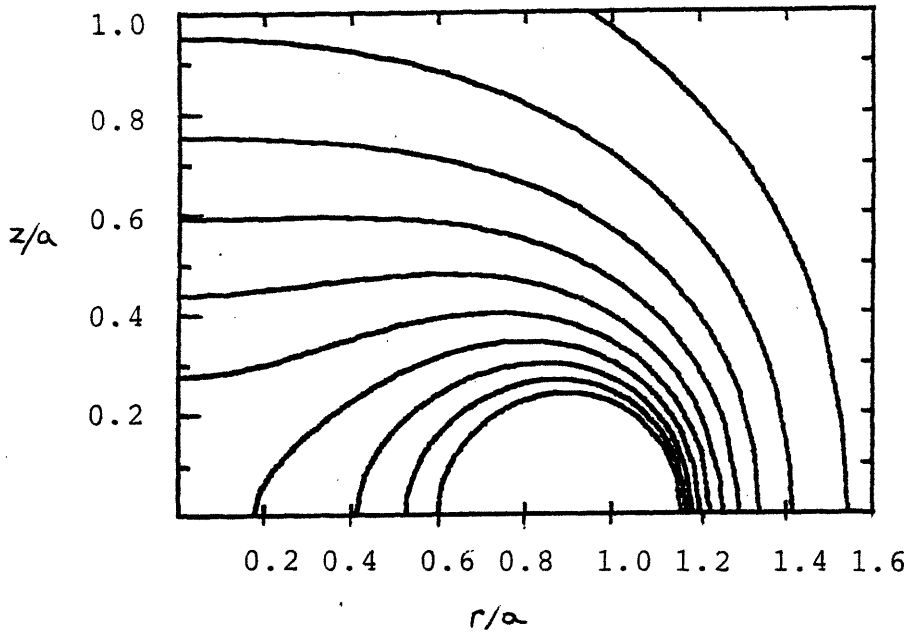


Figure 6.2 Contours of Constant B from a Current Loop

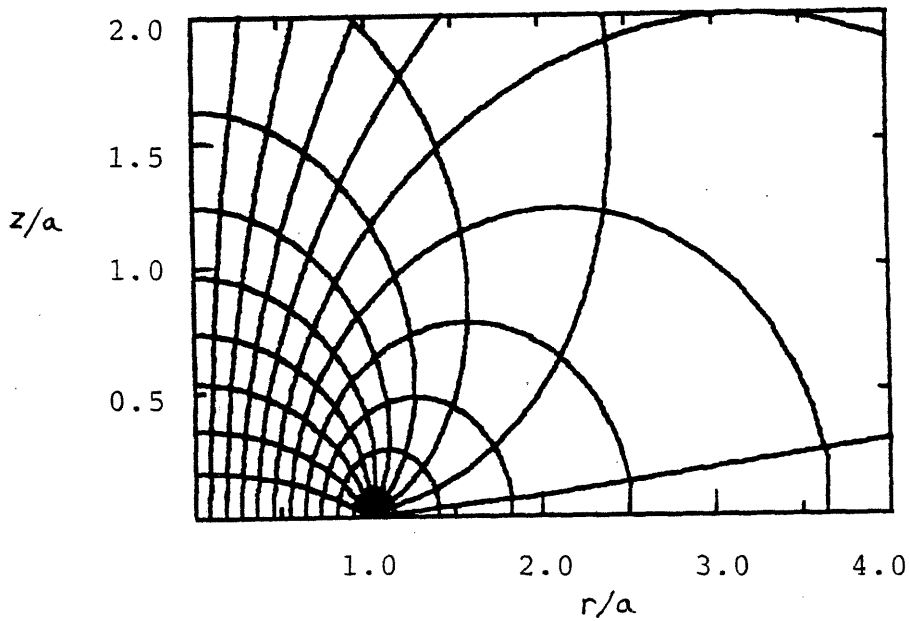


Figure 6.3 B-Lines and Equipotentials from a Current Loop

for differences in the time evolution of the loading for different geometries. In some cases the forces are radially inward throughout most of the disruption time and in other cases the inboard side forces are radially outward.

Since the vertical field interaction scales as I and the other two forces as I^2 , it is always true in problems with long structural time constants that near the end of the current transient the forces tend to be directed toward the major axis.

6.1.2. Overview of Stresses

If the pressure loading is known, the response of the shell can be obtained. Although it is substantially more complicated than the eddy current problem, the general behavior of the first wall structural response can be summarized qualitatively.

One of the most interesting aspects of the stress problem in toroidal shells is the existence of "singular points" at $\phi_s = 0$ and $\phi_s = \pi$. An incompatibility arises due to the imbalance of the net forces on the inboard and outboard sides of the torus. This occurs even for the case of a uniform pressure loading. These points are really singular only when linear membrane theory is used. There are two possible methods to eliminate this problem. One of these is to allow for a nonlinear response, i.e. solve the equations at the deformed points rather than the undeformed points as in a linear treatment. The other technique - the one adopted here - is to relax the assumptions of membrane theory and allow bending moments and shears.

Another feature of the structural problem results from the competition between major and minor radii forces. With uniform pressure loading, the inboard side tends to displace less since the two forces balance, whereas on the outboard side they tend to add. Strains are moderated there somewhat due to the $1/r$ major radius dependence

$$r\epsilon_\theta = v \cos \phi_s + w \sin \phi_s \quad (6.1)$$

where v and w are the circumferential and radial displacements respectively. With eddy current loading, the pressures are inward toward the minor axis and displacements are greater on the inboard side.

The pressurized torus example was used to verify the structural part of the calculation. The commercial Finite Element code PAFEC was used with 3-noded axisymmetric thin shell elements.^(6.2) The results are not presented here, but in general the agreement was within ~5-10%. In all likelihood, the PAFEC calculation was less accurate since fewer elements were used. Figs. 6.4-6.5 display the deformed shell and its moments resulting from uniform pressure loading of arbitrary magnitude. High moments correspond to areas of high curvature in the displacements.

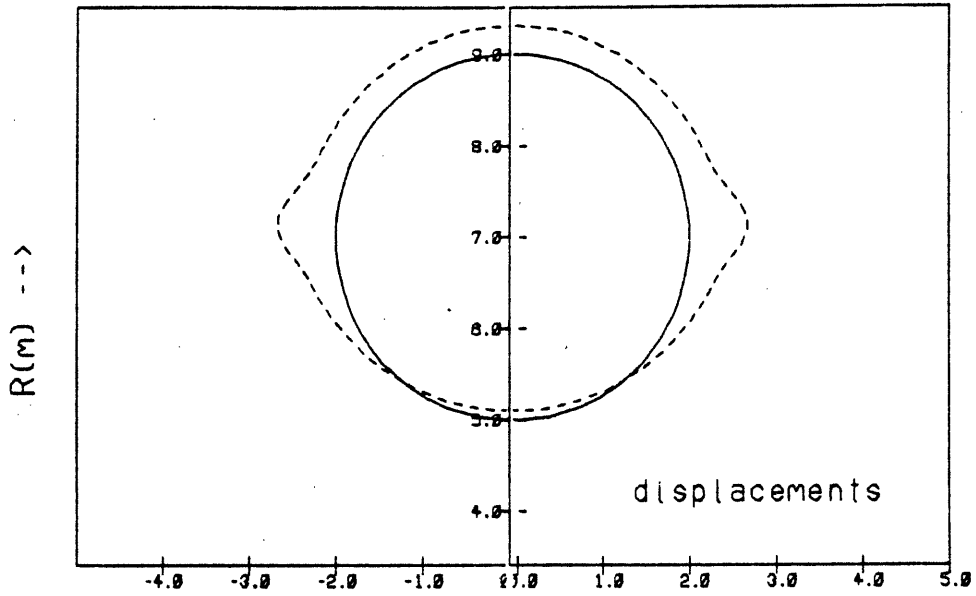


FIGURE 6.4 Pressurized Torus Displacements.

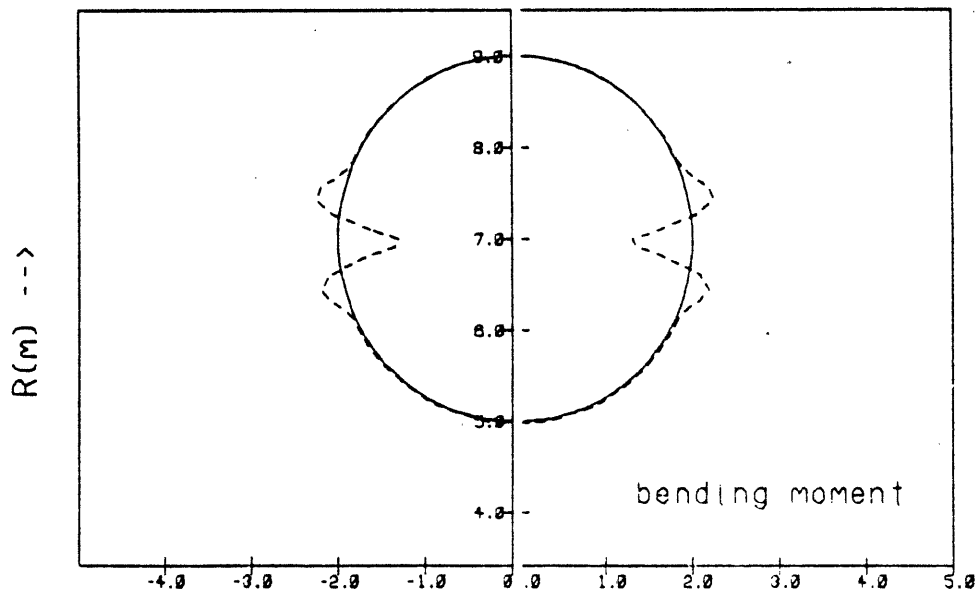


FIGURE 6.5 Pressurized Torus Moments

6.2. Description of Computational Method

There are several steps for computing currents, pressures, and finally strains. Broadly, they can be grouped into two problems: the eddy current problem (including calculation of $\mathbf{J} \times \mathbf{B}$ forces) and the structural problem.

6.2.1. The Eddy Current Problem

The eddy current problem is solved using an electric circuit analog. The structure is broken into a large (typically ~ 100) number of filamentary loops concentric with the source current. Each loop has a resistance, R , and self-inductance, L , associated with it.

$$R = \frac{\eta 2\pi r}{ha\Delta\phi} \quad (6.2)$$

$$L = \frac{\mu_o}{2\pi} \left(\ln \frac{8r}{b} - 1.75 \right) \quad (6.3)$$

$$b = \sqrt{ha\Delta\phi/\pi} \quad (6.4)$$

$\Delta\phi$ is the poloidal angle subtended by each loop, r is the major radius, h is the shell thickness, and a is the minor radius.

In addition, each loop couples with the source current and each of the other loops through a mutual inductance. This mutual inductance is computed using the vector potential A_ϕ . The vector potential and the fields, B_r and B_z , used to compute forces are given analytically in terms of the complete elliptic integrals of the first and second kind $E(k)$ and $K(k)$ ^(6.3).

$$A_\phi = \frac{\mu_o r}{\pi} \frac{(2 - k^2)K(k) - 2E(k)}{k^2 \sqrt{r^2 + X^2 + 2rX \sin \alpha}} \quad (6.5)$$

$$B_r = \frac{-\mu_o}{4\pi} \frac{2K(k) - E(k) \left(\frac{2 - k^2}{1 - k^2} \right)}{\tan \alpha \sqrt{r^2 + X^2 + 2rX \sin \alpha}} \quad (6.6)$$

and

$$B_z = \frac{\mu_o}{4\pi} \frac{2K(k) - \left(2 - k^2 \left(\frac{r + X \sin \alpha}{X \sin \alpha} \right) \right) E(k) / (1 - k^2)}{\sqrt{r^2 + X^2 + 2rX \sin \alpha}} \quad (6.7)$$

where

$$k^2 = \frac{4rX \sin \alpha}{r^2 + X^2 + 2rX \sin \alpha} \quad (6.8)$$

α is the angle measured from the vertical, and X is the distance from the center of the loop to the field point.

The relationship between the distributed quantity Λ_ϕ and the discrete mutual inductance is derived from

$$V = \int \mathbf{E} \cdot d\mathbf{l} \quad (6.9)$$

Substituting the expressions

$$V = M \frac{dI}{dt} \quad (6.10)$$

$$\text{and} \quad \int \mathbf{E} \cdot d\mathbf{l} = 2\pi r \frac{dA_\phi}{dt} \quad (6.11)$$

we arrive at

$$M = 2\pi r \bar{A}_\phi \quad (6.12)$$

where \bar{A}_ϕ is the vector potential per unit source current.

One of the great simplifications involved in this 1-D model is the absence of "mutual resistances". In a 2-D model where currents are broken into a mesh of loops, bordering loops must share line elements. This feature is absent in the 1-D analysis where each loop has a resistive voltage drop independent of its neighbors.

The solution of the equations as a function of time is accomplished with a simple explicit differencing scheme where the circuit equation

$$\underline{\underline{M}} \cdot \frac{d\mathbf{I}}{dt} + R\mathbf{I} + M_o \frac{dI_o}{dt} = 0 \quad (6.13)$$

is rewritten in two parts using the definitions of R and b :

$$\mathbf{A} = \underline{\underline{M}} \cdot \mathbf{I} + M_o I_o \quad (6.14)$$

$$\frac{\eta}{\pi b^2} \mathbf{I} = -\frac{d\mathbf{A}}{dt} \quad (6.15)$$

The diagonal of $\underline{\underline{M}}$ now contains the self-inductances, and the factor $2\pi r$ has been absorbed into $\underline{\underline{M}}$. The vector notation (underlining in this case) represents the column of values where each loop contributes one element in the vector.

The difference equations are:

$$\frac{dA_i}{dt} = \frac{A_{i+1} - A_i}{\Delta t} \quad (6.16)$$

$$A_{i+1} = A_i - \Delta t \frac{\eta}{\pi b^2} I_i \quad (6.17)$$

$$I_{i+1} = \underline{\underline{M}}^{-1} \cdot (A_{i+1} - I_o(t)M_o) \quad (6.18)$$

where the subscript i is a time step identifier. After the currents are known at each time step, the fields due to these currents are computed using the elliptic integral representations. The pressure loading is a simple cross product of the induced current and the magnetic field:

$$p = K \times B \quad (6.19)$$

where

$$K = hJ = (I/a\Delta\phi)\hat{\phi} \quad (6.20)$$

Verification of the eddy current part of the computations was performed using the general purpose electric circuit analysis program SPICE. The resistances and inductances were entered into SPICE and an exponential source voltage was applied. Agreement with SPICE was excellent. This agreement only verifies the numerical methods used. It does not verify the assumptions made to break the structure into loops, since the same assumptions went into the SPICE runs.

6.2.2. The Structural Problem

The structural part of the problem takes the pressures as input and then, at any given time step, computes the quasi-static structural response in terms of the displacements, strains, shears, moments, etc. The elimination of the inertial terms in the equilibrium equations is not strictly valid. A dimensionless frequency parameter, Ω , is defined by

$$\Omega = \frac{2\pi f r}{c} \quad (6.21)$$

where c, the speed of sound in the material, is given by

$$c = \sqrt{E/\rho} \quad (6.22)$$

E is the modulus of elasticity and ρ is the material density. In steel, c is ~ 5 km/s. Hence, for scale lengths on the order of 5 m (and accounting for the factor 2π), the transition to a

time-dependent problem should take place at characteristic times ($1/f$) of ~ 10 msec. This is very close to the 25 msec used in the following analysis. A full time-dependent problem would be easy to implement, but would require orders of magnitude more computer time. The quasi-static assumption is probably conservative, since at early times when the forces and time derivatives are largest, the inertia tends to decrease the displacements. The derivation of the static equations follows closely the work of Flugge ^(6.4) and Timoshenko. ^(6.5)

In these equations, we use the abbreviations for the bending rigidity and flexural rigidity

$$K = \frac{Eh^3}{12(1-\nu^2)} \quad (6.23)$$

$$D = \frac{Eh}{1-\nu^2} \quad (6.24)$$

In addition, by virtue of the somewhat untraditional coordinate system, the radial distance from the axis of symmetry is given by

$$r = r_o + a \sin \phi \quad (6.25)$$

Equilibrium Equations

A force balance on the shell element is performed in the ϕ - and r -directions, and a moment balance perpendicular to r and ϕ , yielding

$$(rN_\phi)' - aN_\theta \cos \phi - rQ_\phi = -arp_\phi \quad (6.26)$$

$$(rQ_\phi)' + aN_\theta \sin \phi + rN_\phi = arp_r \quad (6.27)$$

$$(rM_\phi)' - aM_\theta \cos \phi - arQ_\phi = 0 \quad (6.28)$$

Deformation Relations

Then, using the strain-displacement relations:

$$a\epsilon_\phi = \frac{dv}{d\phi} + w \quad (6.29)$$

$$r\epsilon_\theta = v \cos \phi + w \sin \phi \quad (6.30)$$

$$a^2\chi_\phi = \frac{d}{d\phi} \left(v - \frac{dw}{d\phi} \right) \quad (6.31)$$

$$ar\chi_\theta = \cos \phi \left(v - \frac{dw}{d\phi} \right) \quad (6.32)$$

and Hooke's law:

$$N_\phi = D(\epsilon_\phi + \nu\epsilon_\theta) \quad (6.33)$$

$$N_\theta = D(\epsilon_\theta + \nu\epsilon_\phi) \quad (6.34)$$

$$M_\phi = -K(\chi_\phi + \nu\chi_\theta) \quad (6.35)$$

$$M_\theta = -K(\chi_\theta + \nu\chi_\phi) \quad (6.36)$$

we derive the deformation relations:

$$N_\phi = D \left[\frac{1}{a} \left(\frac{dv}{d\phi} + w \right) + \frac{\nu}{r} (v \cos \phi + w \sin \phi) \right] \quad (6.37)$$

$$N_\theta = D \left[\frac{1}{r} (v \cos \phi + w \sin \phi) + \frac{\nu}{a} \left(\frac{dv}{d\phi} + w \right) \right] \quad (6.38)$$

$$M_\phi = \frac{K}{a} \left[\frac{d}{d\phi} \left(\frac{1}{a} \frac{dw}{d\phi} - \frac{v}{a} \right) + \frac{\nu \cos \phi}{r} \left(\frac{dw}{d\phi} - v \right) \right] \quad (6.39)$$

$$M_\theta = \frac{K}{a} \left[\frac{\cos \phi}{r} \left(\frac{dw}{d\phi} - v \right) + \nu \frac{d}{d\phi} \left(\frac{1}{a} \frac{dw}{d\phi} - \frac{v}{a} \right) \right] \quad (6.40)$$

These are then solved together with the 3 equilibrium equations, making 7 equations and 7 unknowns. Due to the form of the deformation relations, it is easy to eliminate equations if desired. In the analysis described in this report, M_θ , N_θ , and N_ϕ were eliminated leaving four equations in w , v , Q_ϕ , and M_ϕ . The moment results are expressed in terms of the bending stress which is related through the relation:

$$\sigma_b = \frac{6M_\phi}{h^2} \quad (6.41)$$

Before continuing on to describe the method of solution for the structural equations, it should be noted that the limitation on the pressure data due to the N^2 nature of the eddy current problem is no longer a factor since the structural problem has storage and execution scaling as N (where N is the number of elements). The pressure data is therefore interpolated using cubic B-spline interpolating functions. As many as 1000 points are typically used in the structural problem.

Finite Element Method

A finite element method (FEM) is employed in order to convert the set of coupled partial differential equations into a matrix of algebraic equations which requires only one large matrix inversion for their solution. For a one-dimensional problem broken into N elements with M unknowns to be solved at each point, the matrix is $N \times N \times M \times M$. With pentic spline basis functions, each equation involves only five points, therefore the matrix rows contain only 5 blocks each

with full MxM blocks. Most of the matrix is filled with zeros. By using a special purpose block penta-diagonal banded matrix system solver, a tremendous savings is made. Whereas the execution time of a full matrix inverter scales as N^2 , the penta-diagonal system scales as N .

The B-spline basis functions $B_i(\phi)$ used in the FEM analysis are plotted in Fig. 6.6 and described in more detail in Ref. 6.1. As far as the equations are concerned, B-splines are simply 5th order polynomials. Mathematically, they must result in the same solution as any 5th order polynomial. The primary reason for using them is their simplicity and ease of application, resulting mainly from the absence of matching conditions at the element boundaries. The four unknown quantities are approximated in terms of the basis functions (using matrix notation) as follows:

$$w(\phi) = \sum_i \alpha_i B_i(\phi) = \alpha_i B_i(\phi) \quad (6.42)$$

$$v(\phi) = \beta_i B_i(\phi) \quad (6.43)$$

$$Q_\phi(\phi) = \gamma_i B_i(\phi) \quad (6.44)$$

$$M_\phi(\phi) = \delta_i B_i(\phi) \quad (6.45)$$

The sums contain only five terms since B_i is zero except for

$$(\phi_i - 3\Delta\phi) < \phi < (\phi_i + 3\Delta\phi) \quad (6.46)$$

At each point for each of the unknowns the splines B_i are evaluated and the contributions of the neighbors are added in

$$u(\phi_i) = u_i = \alpha_{i+2} + 26\alpha_{i+1} + 66\alpha_i + 26\alpha_{i-1} + \alpha_{i-2} \quad (6.47)$$

Similarly for the derivatives,

$$u'(\phi_i) = u'_i = 5\alpha_{i+2} + 50\alpha_{i+1} - 50\alpha_{i-1} - 5\alpha_{i-2} \quad (6.48)$$

$$u''(\phi_i) = u''_i = 20\alpha_{i-2} + 40\alpha_{i-1} - 120\alpha_i + 40\alpha_{i+1} + 20\alpha_{i+2} \quad (6.49)$$

These forms are substituted into the reduced set of structural equations, which results in four equations (one for each j) at each point x_k

$$A_{ij}(x_k)\alpha_i + B_{ij}(x_k)\beta_i + C_{ij}(x_k)\gamma_i + D_{ij}(x_k)\delta_i = p_j \quad (6.50)$$

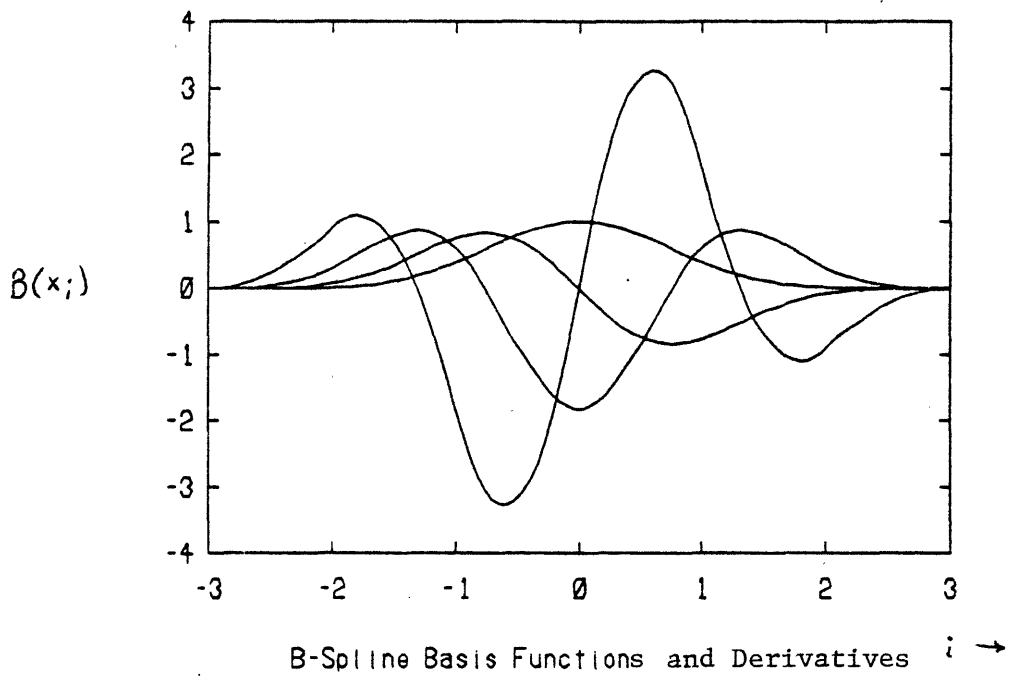


FIGURE 6.6

where p_j contains the terms with the externally applied pressure and the i sums range only from $k - 2 < i < k + 2$ since the splines are zero elsewhere. A, B, C, and D contain all of the information from evaluating the coefficients of the structural equations at each point. We can also write a more general form, redefining A and replacing the four equations with

$$A_{ijl}\alpha_{il} = p_j \quad (6.51)$$

The l index ranges through the 4 coefficients of the 4 unknowns. The entire system of equations can now be expressed as one matrix equation

$$A_{ijkl}\alpha_{il} = p_{jk} \quad (6.52)$$

where α_{il} is the generalized N by 4 spline coefficient matrix and, to reiterate, i and k are point indices, j is an equation index, and l is a variable index (one for each variable). A_{ijkl} is a block penta-diagonal matrix since it has 4x4 blocks full with the equation information only at a given point and its four nearest neighbors.

5th order B-splines were not the original choice of basis functions. Cubic B-splines were attempted, but the discontinuity in their third derivative resulted in the solution being dependent on the number of nodes, particularly for the moments which enter the equations as the highest derivative of the displacements. By approximating the third derivative as the average value at the discontinuity, accurate displacements were obtained, but moments and shears were not consistent. Inspection of the structural equations reveals that even the 4th derivative enters into the moment equations.

6.3. Results

In order to demonstrate typical results from the axisymmetric analysis, the STARFIRE reactor designed was modeled with a circular cross section, constant thickness, constant resistivity shell. The reactor parameters appear in Table 6.1. The current transient was modeled with a 25 msec exponential decay. The results are presented in Figs. 6.7-6.13.

From the time histories Fig. 6.7-6.8 it can be seen that the structure L/R time is approximately 100 msec. The total current transferred is 6.25 MA, or 62.5% of the driving current. The peak pressures are obtained before the peak induced current due to the interaction of the shell and driving currents.

Figs. 6.9-6.11 show the spatial profiles at different times in the disruption. The poloidal asymmetry is somewhat larger for the pressures than for the currents, primarily due to the I^2 dependence of pressure. The circumferential pressures are about an order of magnitude smaller than the radial pressures.

Table 6.1 Reactor Data for STARFIRE Analysis

Property	Base Case	High Field Case
resistivity η	5.54 $\mu\Omega$ -cm	
thickness h	1.5 mm	
modulus E	190 GPa	
Poisson's ratio ν	0.3	
minor radius a	2.0 m	1.24
major radius R	7.0 m	4.35
toroidal current I	10.1 MA	8.96
toroidal field B_t	7.0 T	10.0
poloidal field B_p	0.35 T	0.5
vertical field B_v	.067 T	.067

(fields measured on axis)

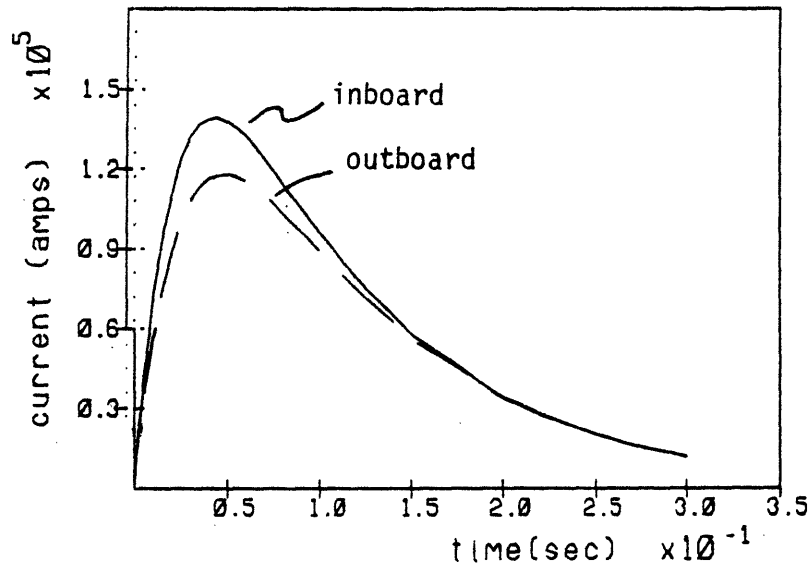


Figure 6.7 Base Case Current Histories

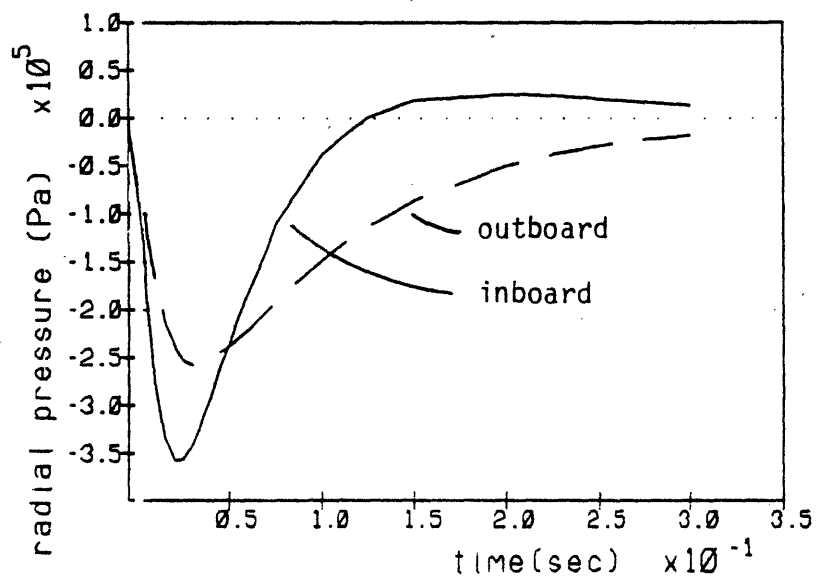


Figure 6.8 Base Case Pressure Histories

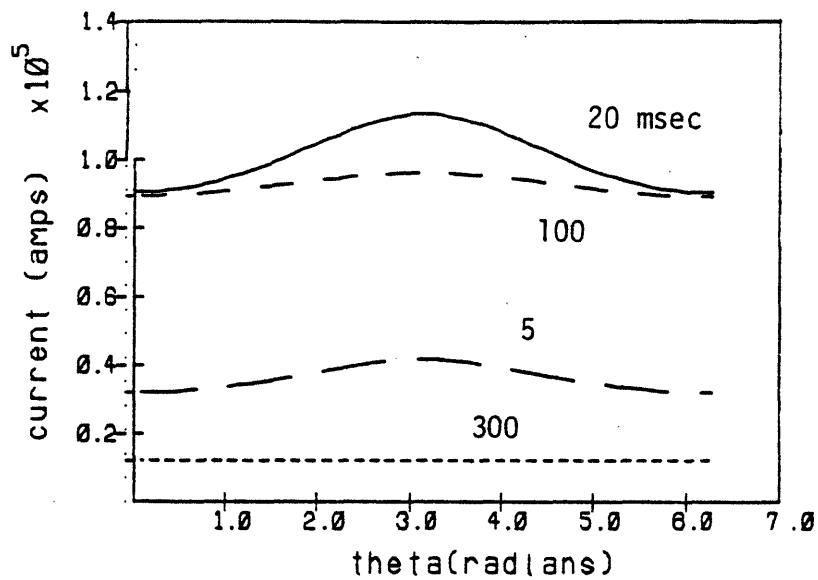


Figure 6.9 Current Profiles

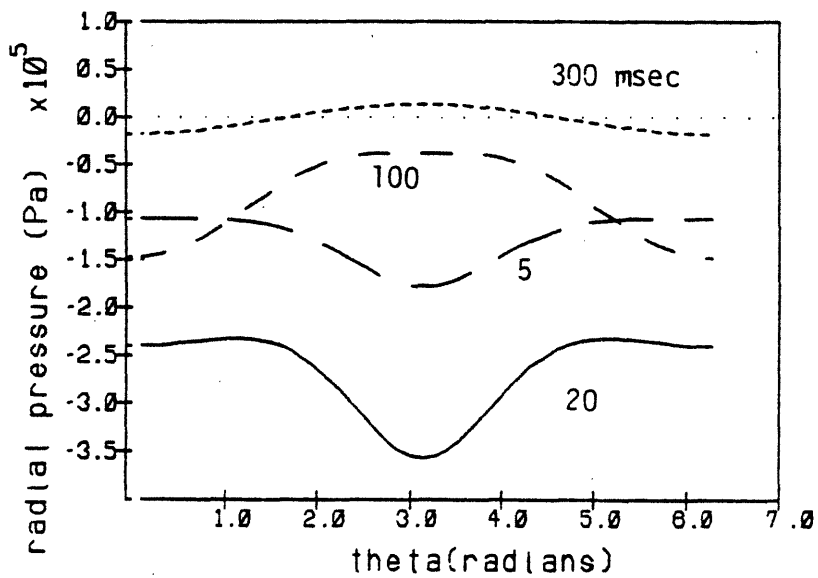


Figure 6.10 Radial Pressure Profiles

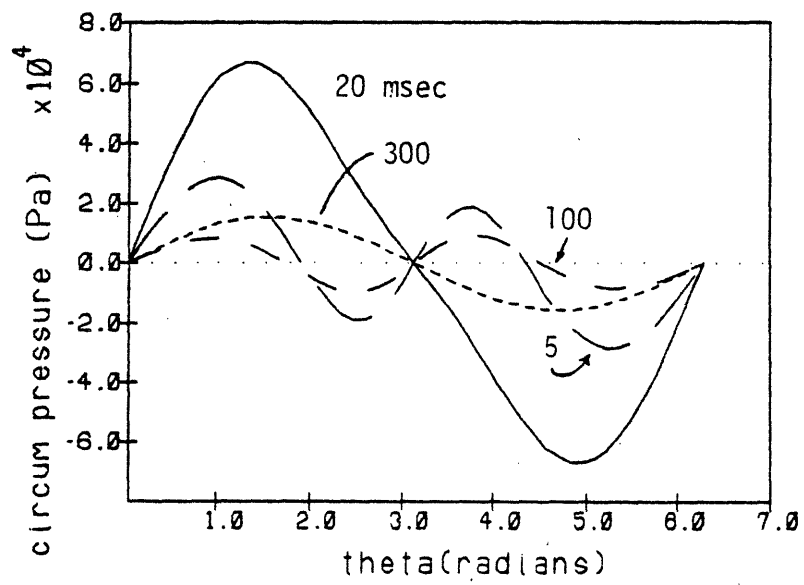


Figure 6.11 Circumferential Pressure Profiles

The displacement plots, Figs. 6.12-6.13, show that at early times the hoop force dominates and the structure is pushed outward. Later on, as the currents die away, the vertical field interaction becomes dominant and the torus is pushed inward toward the major axis. The peak displacements of 2-5 mm are deceiving, since this amount of motion would likely be constrained in a reactor design. The method of constraint is important, since significant stress concentrations are capable of exceeding the strength of the materials.

The peak strain of 5×10^{-4} and peak bending stress of 1 MPa are not particularly dangerous from the standpoint of structural failure. For most materials the yield point is between 20-200 MPa, or strains between 5-10%. The only way problems would occur with this magnitude of loading is in the event of stress concentrations. These occur at places in the structure where discontinuities exist or at support points where forces from a large section of the wall are supported by reaction forces. This kind of effect is very dependent on design and therefore cannot be briefly discussed.

In some ways, the base case example does not indicate worst case effects. Different reactor types – such as higher β , higher field, or lower aspect ratio – may be expected to show significantly higher strains. These cases are all examined in more detail in Ref. 6.1. There are three examples examined here which give an idea of how the strains can be expected to vary. The first example has a plasma shifted out 25%. The second case shows the mediating effect of a conducting “electromagnetic shield.” The third case is a compact, high field design which represents the worst case studied in Ref. 6.1.

The example with a plasma shift had the same characteristics as the base case except that the driving current loop was placed at a 25% larger radius. The same 25 msec time constant was used for the source current decay. The results are more easily understood by referring to Fig. 6.2-6.3. By displacing the current relative to the shell, the equipotentials more closely follow the contour of the shell. The field lines are very close to being perpendicular to the shell. In this case, 25% was enough to actually pass this point. The result is that the inboard radial pressure is always more positive than the outboard pressure (Fig. 6.14). The peak pressures are larger because the driving current is closer to the shell. This increases the mutual inductance as well as the fields. Fig. 6.16 shows the altered structural response.

The next test case is similar to the base case in all respects except that a second shell concentric to the first was added at a radius 10 cm larger. 2 cm of stainless steel was used, as this has been quoted in the STARFIRE design to be a desirable amount for plasma stability. The resulting shape of the pressure profiles is relatively unchanged. The magnitude is decreased by about a factor of two; at 20 msec the peak value is .35 MPa compared to .17 MPa for the base case (Fig. 6.15). The effective structural time constant is increased by the presence of the shield. In this example the conductance of the wall and the shield are approximately equal. It is probably safe to assume that a higher conductivity shell would have an even greater moderating effect. The

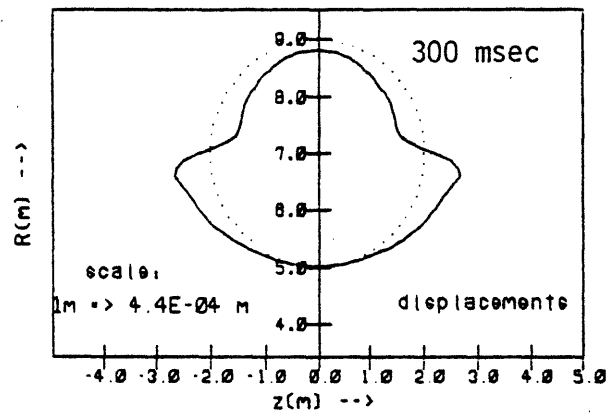
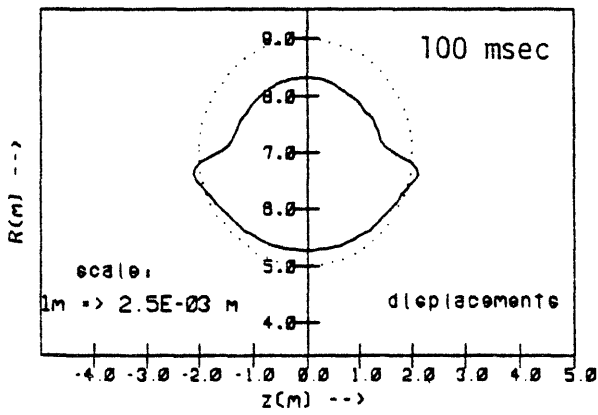
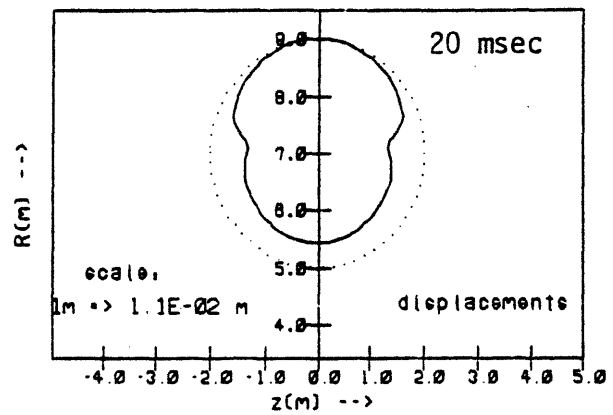
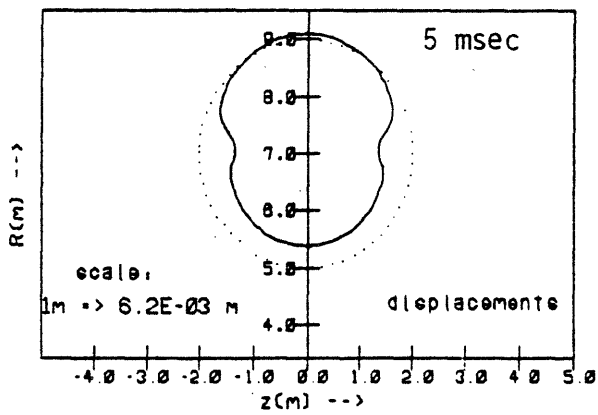


Figure 6.12 Base Case Displacements

(note: plots have different scales)

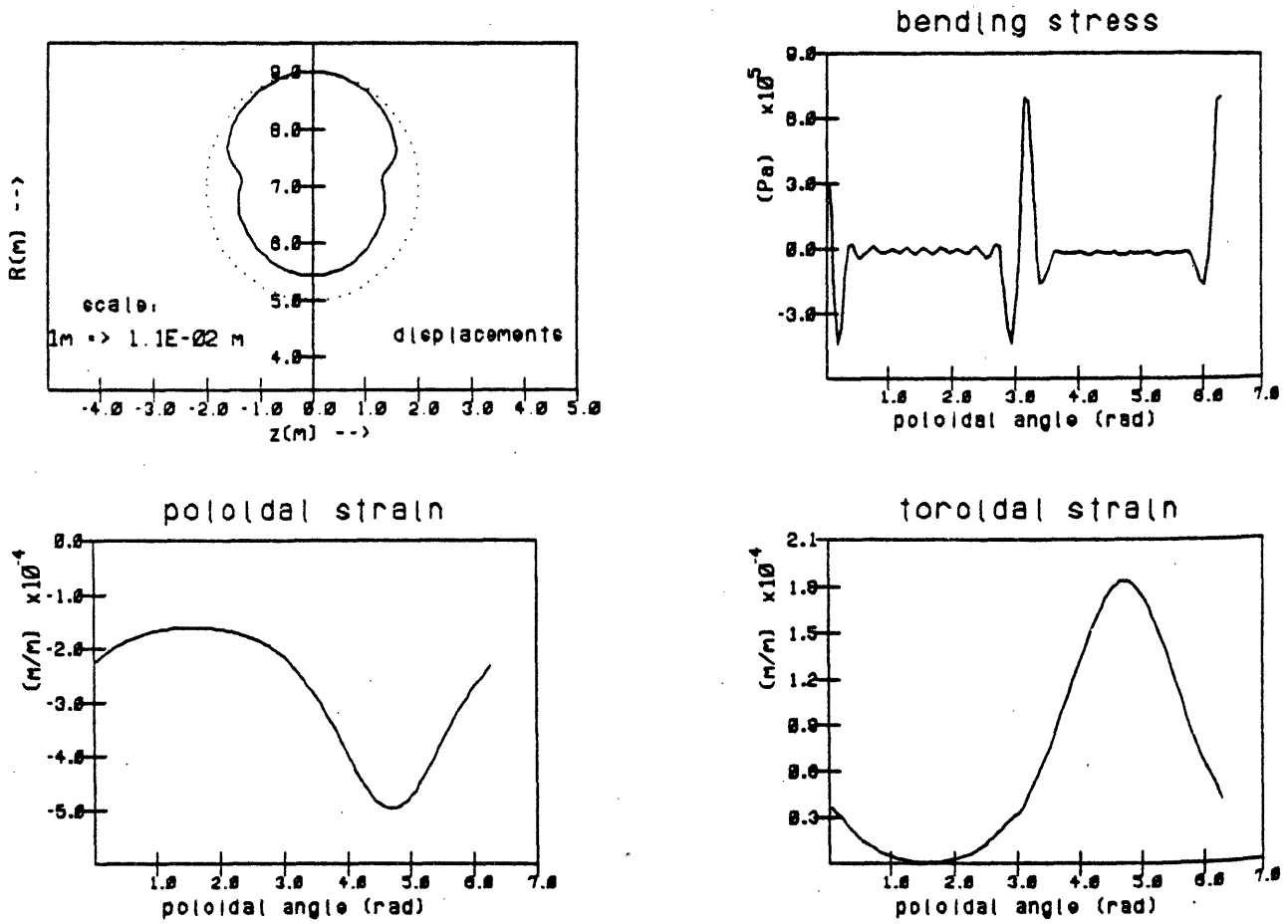


Figure 6.13 Base Case Structural Response at 20 msec

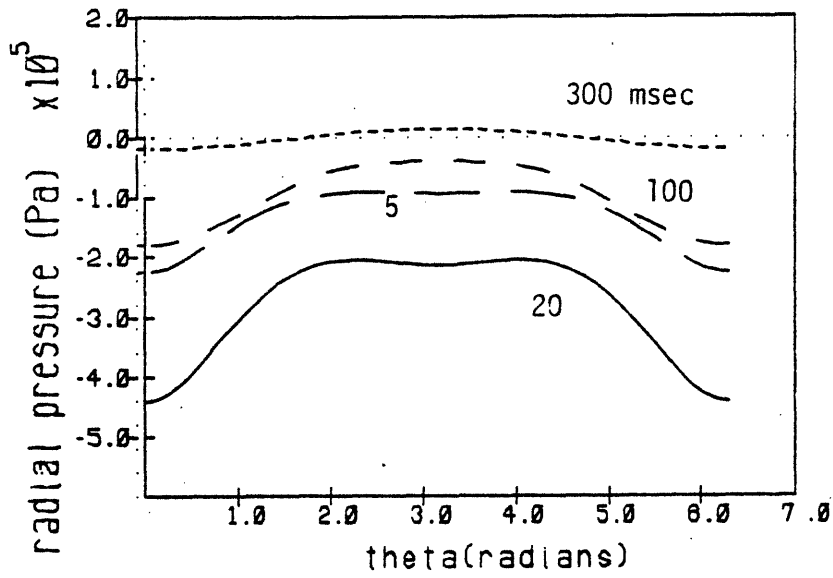


Figure 6.14 Radial Pressure with Plasma Shift

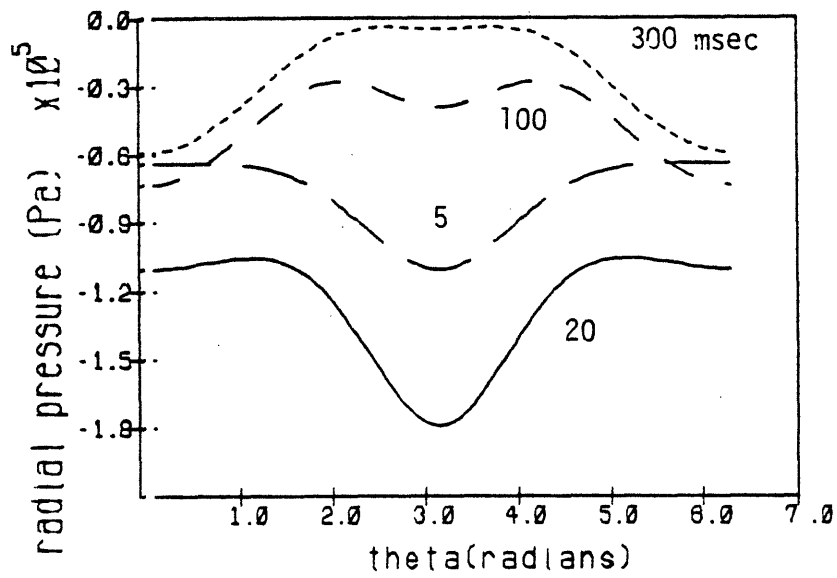


Figure 6.15 Radial Pressure with EM Shield

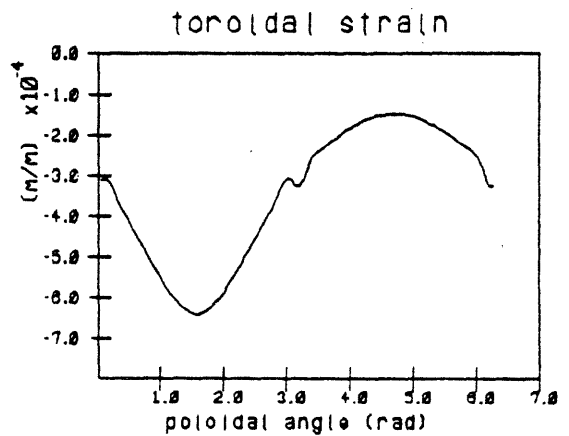
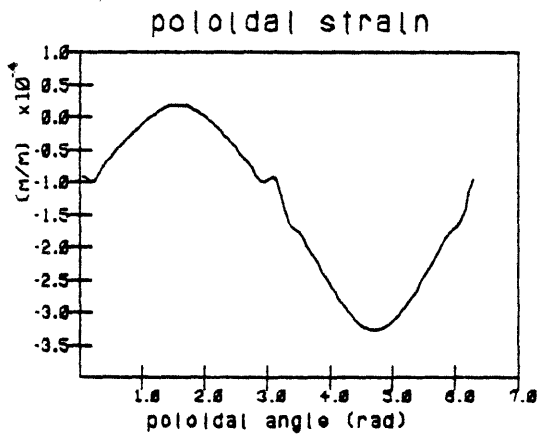
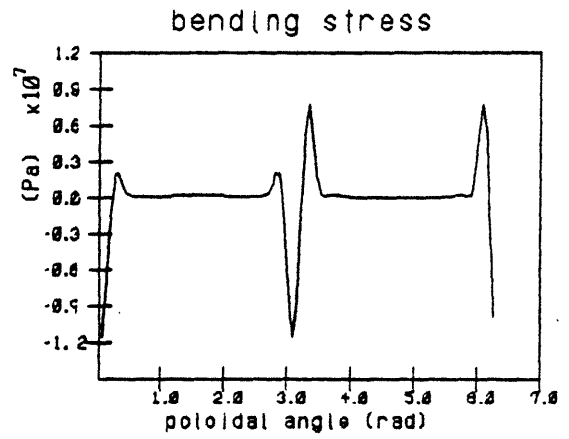
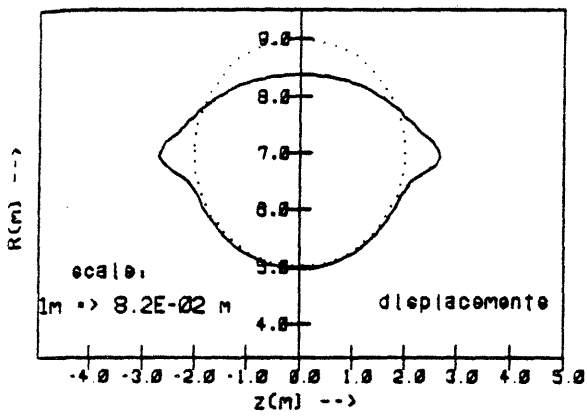


FIGURE 6.16 Structural Response at 20 msec for Plasma Shift.

structural response is qualitatively the same as for the base case except that all of the effects are reduced by about a factor of two. The stresses and strains are presented in Fig. 6.17 .

The last case to be analyzed was a high field compact design. Rather than simply increase the fields, an attempt was made to keep the design self consistent. This was accomplished by fixing the reactor power, plasma rotational transform, and maintaining the vertical field equilibrium. The resulting design parameters are included in Table 6.1.

The results are presented in Figs. 6.18-6.19. Qualitatively there is little difference. The main effect is a factor of two increase in pressures, stresses, and strains. The conclusions about structural failure remain essentially intact.

References:

- 6.1 M. S. Tillack, "A Study of Structural Responses to Plasma Disruptions in Toroidal Shells," PFC/RR-83-16, June 1983.
- 6.2 PAFEC 75 Theory Manual, PAFEC Ltd., Nottingham England, 1976.
- 6.3 J. D. Jackson. Classical Electrodynamics, John Wiley and Sons, New York, 1975.
- 6.4 W. Flugge. Stresses in Shells, Springer-Verlag, New York, 1966.
- 6.5 S. Timoshenko and S. Woinowsky-Krieger. Theory of Plates and Shells, Mc-Graw-Hill, New York, 1959.

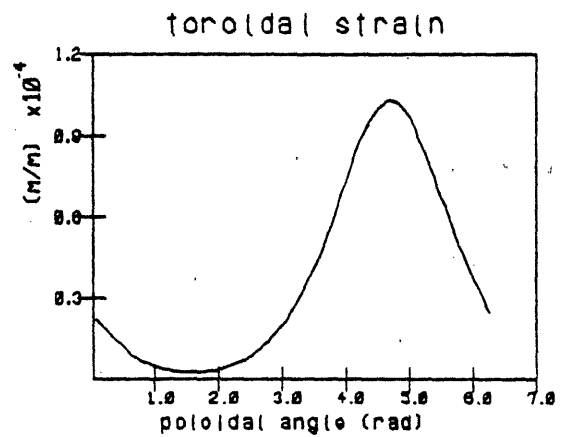
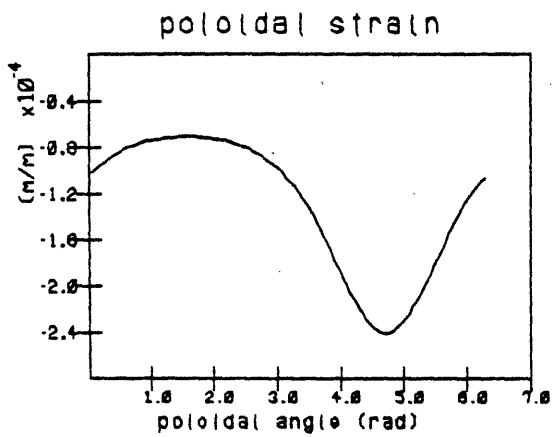
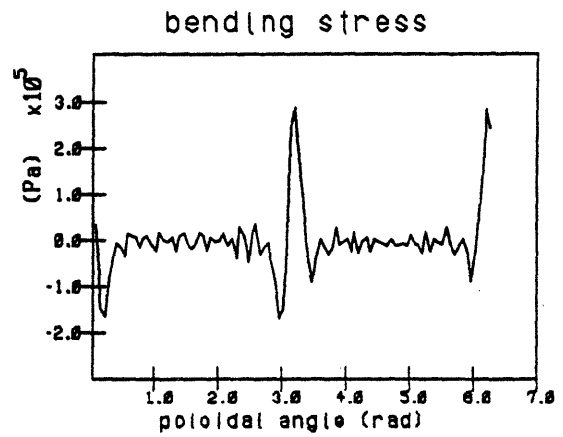
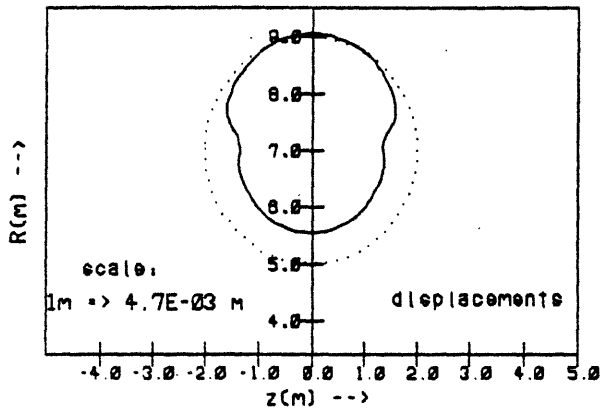


Figure 6.17 Structural Response at 20 msec for EM Shield.

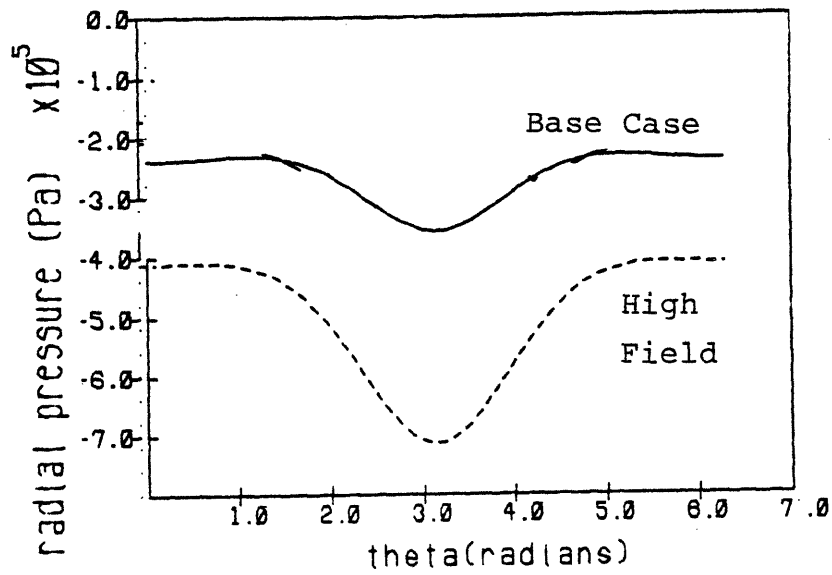


Figure 6.18 Radial Pressure for High Field Example

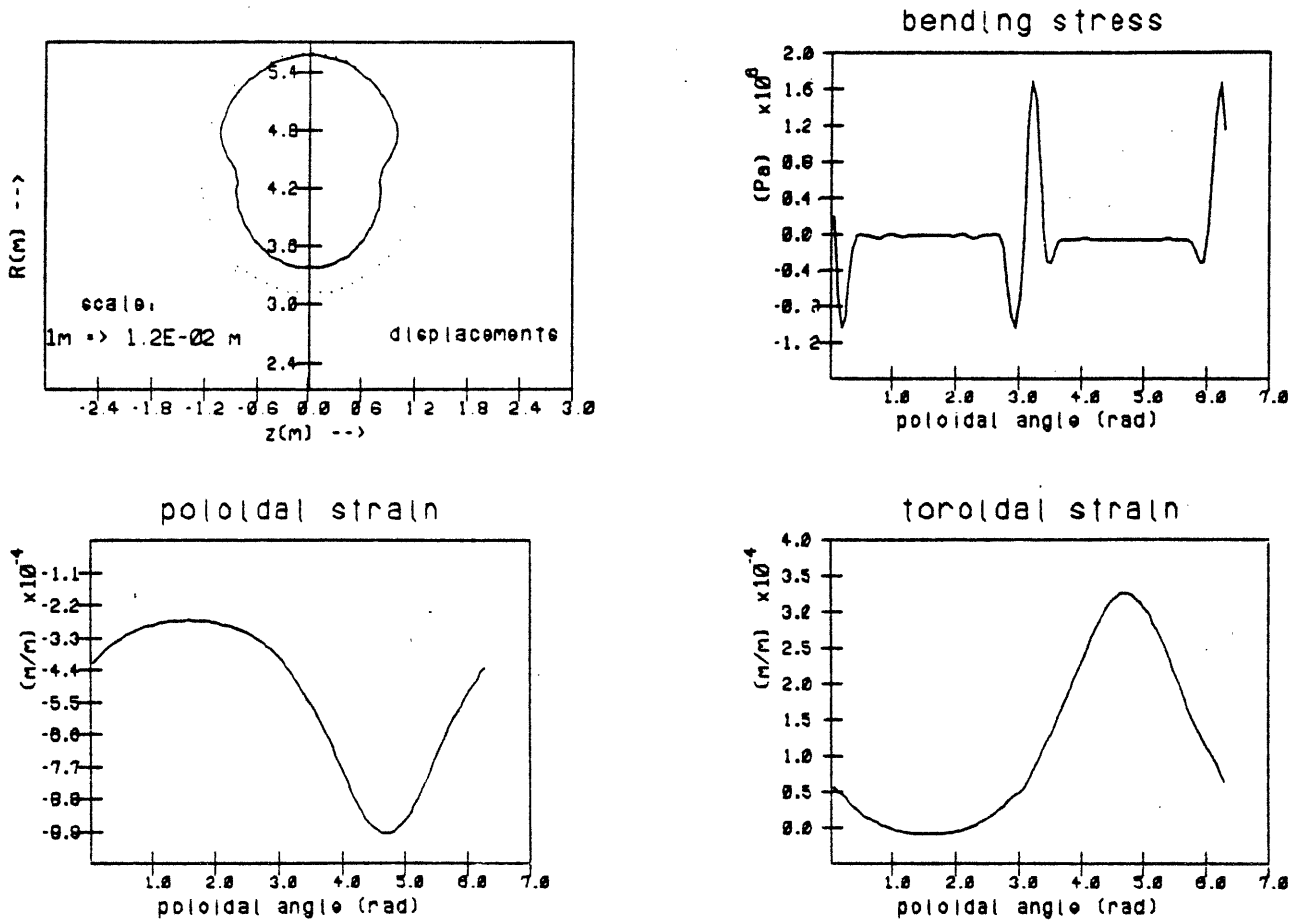


Figure 6.19 Structural Response at 20 ms
for High Field Example

3-D Calculation of Currents and Strains

7.1. Introduction

A truly complete solution of the problem of induced currents and strains would incorporate the coupling of the plasma behavior, the induced currents, and the structural response, including the nonlinear feedback processes which exist. For simplicity, in this work the plasma current is assumed to be a known input and the solution is obtained in two separate steps — a time dependent eddy current solution and a static structural analysis.

Even in this simplified form, an analytic solution of induced currents is possible to solve exactly in only a few special geometries. In a uniform cylinder for example, it is shown in Appendix A that a solution exists for a helically symmetric driving function which can be expressed as a Fourier expansion series. The problem of a uniform toroidal shell may be solved in a similar manner, although the peculiarities of toroidal coordinates makes the solution more cumbersome. In general, the slightest deviation from symmetry, such as a hole or break, makes an analytic solution intractable. Similarly, if the problem is not strictly symmetric, then the structural analysis which follows the calculation of induced currents and fields is one level deeper in complexity. In general, the most practical method of solution is a numerical one.

For this thesis, a suitable existing eddy current code could not be found, so one was written. The development and application of this code are discussed in this chapter. For the solution of the structural part of the problem both analytic and numerical analyses are done. Several finite element structural codes exist and it was possible to use one of these without modification.

7.2. Eddy Current Codes and FASTEDDY

7.2.1. Methods for Eddy Current Problems

The problem of finding induced eddy currents in structures precedes research in fusion. Much of the previous work was inspired by the need to understand more fully the operation of electrical

machines, such as motors and transformers. Usually AC steady state was assumed. Magnetic materials were usually emphasized and force calculations rarely done. Recently, fusion researchers have also become interested in the problem and papers have been published at a more rapid rate. Fusion applications are significantly different than problems with electrical machines. Fusion designers are principally interested in the time dependent forces on Tokamak vacuum vessels, field coils, and limiters in addition to the problem of finding field perturbations and electric fields.

As a result of this surge in interest, today there are numerous programs which use different approaches for the solution. Yet there is an apparent paradox here, since it was necessary to develop still another code for this thesis. There are a couple of reasons for this. First, most of the new codes are still under development, which makes them generally unavailable. There are as yet no accepted standard codes. Secondly, the problem of induced eddy currents is unlike other standard problems in numerical analysis. The inherent non-localization of the E&M problem leads both differential and integral formulations of the problem to become extremely large in size when any geometric complexity is desired. Thus, extreme efforts to reduce the size of the problem are usually made and the end result is many special purpose codes designed to work in restricted geometries or exploiting various symmetries.

There are currently good survey articles available for the induced current problem. C.J. Carpenter ^(7.1) surveys the theory of various methods which are available. R.J. Lari ^(7.2) lists the programs reported at the March 1982 IEEE COMPUMAG Conference, representing a good sample of the state of the art in eddy current codes. Following is a brief summary of the methods and their advantages and disadvantages.

The two major classifications of eddy current codes are differential and integral. Differential formulations attempt to solve Maxwell's equations using the finite element formulation for the fields. Usually a set of basis functions are defined to model the fields in terms of a small number of parameters and the differential equations are reduced to a set of algebraic equations for the unknown parameters. This method tends to be more cumbersome if the problem is small. Since the fields are the unknown quantities, the solution requires modeling the space outside the structure of interest.

The integral formulation only requires the current carrying elements to be modeled, since the unknown to be solved for is the current, or some related quantity such as the current stream function. If the problem is small, then this can be a definite advantage. The integral nature of the problem, if properly exploited, can result in an improvement in accuracy with respect to the differential formulation. This can reduce the required number of elements for a given accuracy. As the size of the problem increases, the integral formulation begins to require larger amounts of execution time to form the inductance matrices, scaling as n^2 . For very large problems, it is usually desirable to use a differential formulation.

Given the restrictions on time and manpower, it was not practical to produce a general purpose computer model. Instead, the specific problem of doubly connected shells was attempted which treats all of the cases of interest here. The natural choice for a problem of limited size, scope, and accuracy was to select an integral method. The code which was developed, FASTEDDY, uses a circuit network analog formulation. It is related to finite element formulations of the integral method if the basis functions are assumed constant over the elements.

In FASTEDDY, the continuous structure is broken into a number of loops which are assigned averaged properties, including resistance, self inductance and mutual inductance. The edges of the loops are "sticks" which carry the currents. A matrix circuit equation is thus formed and solved as an initial value problem. Appendix B contains a user's guide and a more complete description of the operation of FASTEDDY. Following is a brief description of its special features.

7.2.2. Special Features of FASTEDDY

FASTEDDY has several features which distinguish it from other integral codes. One of the most important features is the coordinate systems in which it operates. The mesh is composed of quadrilaterals and is rectangular in logical coordinates, where "logical coordinates" define the sequential numbering scheme of the nodes. This rectangular logical mesh is relaxed by fixing certain points, for example points around a hole, and then allowing the other points in the mesh to move in such a way that the total length of all the lines between nodes is minimized. The relaxed mesh is then fitted onto various types of 3-D surfaces. Either non-connecting surfaces or doubly-connecting surfaces, which are topological tori, can be described.

The application to connected structures requires care in three areas. First, the loops into which the structure is divided should reconnect at the boundaries. This is explicitly taken into account. Secondly, since the structure forms a closed surface, one of the loops must be eliminated from the equations to avoid overdetermining the system. In other words, any one equation can be formed by properly adding together the remaining equations. Another way of explaining this is that Gauss' Law applies to any closed structure, adding an additional equation implicitly into the matrix. Thirdly, two extra circulating loops must be added to link the fluxes through the torus "holes" - this flux would otherwise not be sensed by any loops. These two special loops cover the hole outside the torus volume at $\theta = \pi$ and the hole inside the torus volume at $\phi = 0$ (see Fig. 7.1).

The circulating loops are treated somewhat differently than the normal quadrilaterals since they are composed of an arbitrary number of line segment elements. For this reason the calculation of mutual inductances are done using the definition of enclosed flux,

$$\Phi = \oint \underline{A} \cdot d\underline{l} \quad (7.1)$$

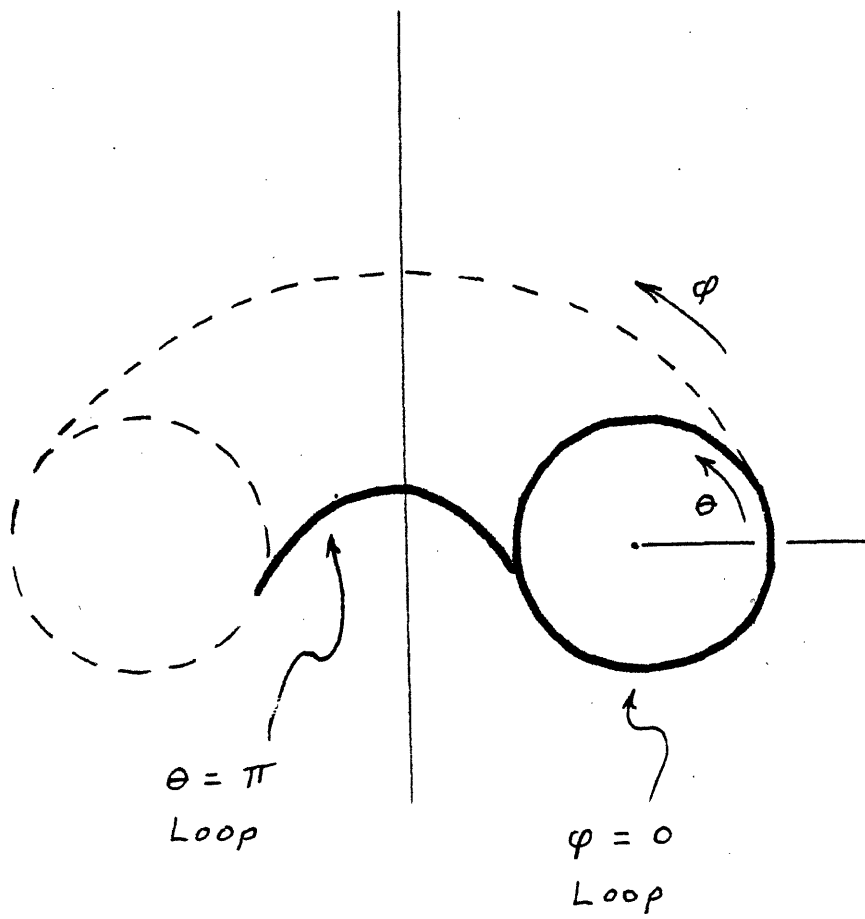


Figure 7.1 Location of Circulating Loops
in FASTEDDY

rather than

$$\Phi = \int \underline{B} \cdot d\underline{a} \quad (7.2)$$

The latter form had originally been used for the quadrilateral loops with \underline{B} estimated at the centroid. However, the vector potential formulation turned out to be so much more accurate that it was adopted for *all* mutual inductance calculations. This also results in a significant increase in computer time to set up the matrices.

By adopting the vector potential formulation, a problem arises because "stick" self inductances must be calculated. In reality, an infinitely thin stick has an infinite self inductance. What is needed is to ascribe a perpendicular dimension to the sticks. One of the parameters which is used to define the modeling of the structure with sticks in FASTEDDY is the geometric mean distance (GMD)^(7.3). This defines the appropriate averaging over the cross section of a continuous conductor which allows the self inductance to be calculated as if the conductor was composed of two filaments separated by a distance which is a fraction of the actual element width. It is possible in some cases to prescribe the exact value of mutual inductance in this way. For example, for a flat rectangular plate with uniform current density, Grover computes a value of GMD equal to $e^{-1.5}$, or 0.223.^(7.3)

Another significant feature of FASTEDDY is its extensive use of spline fitting. After the stick currents are obtained, the current densities are formed and fitted with cubic B-splines. Experience with the integral method has shown that the average results are very accurate even with a coarse mesh. By spline fitting the coarse results with a smooth function, the coarseness of the mesh is somewhat compensated. The fits are also very useful for data presentation and further analysis.

7.2.3. Benchmarking FASTEDDY

7.2.3.1. 2-D Disk Benchmark

Initial benchmarking of FASTEDDY was done with an unconnected mesh for a disk described in Table 7.1. This tests many of the features of the code, but keeps separate all of the problems associated with connected shells. Since connected shells are the strongpoint of FASTEDDY, further benchmarking was done with a connected toroidal shell.

The first benchmark test case was chosen to be a flat, circular disk subjected to a step change in the normal component of the external magnetic field. The field starts out at 1 Tesla and is suddenly dropped to zero. The use of a step function driving term allows the examination of transient behavior of the code, and also makes the distinction between the structure time constant and the transient time constant very apparent. In addition, since the resulting current distribution due to a step change has a large gradient associated with it, important questions about spatial resolution can be answered.

Figs. 7.2 and 7.3 show the meshes used for this test. Fig. 7.2 is a 6x6 mesh and Fig. 7.3 is 12x12. These meshes give the equivalent of 3 and 6 effective circulating paths respectively. Backward differencing was used for this test since the Runge-Kutta method had not yet been incorporated.

The data for comparison was obtained numerically from a routine called DISK, developed especially for this purpose. In DISK, the circular plate is broken into a large set of concentric loops and the mutual inductances are calculated from an exact evaluation of the vector potential due to a circular loop involving complete elliptic integrals. There is no resistive coupling between the loops, since it is essentially a 1-D problem. Therefore, the mutual inductance matrix can be directly inverted and the solution carried out using forward differencing. The differencing scheme follows very closely that of the 1-D toroidal analysis described in Chapter 6.

Due to numerical limitations at the instant when the step change is imposed, the initial current distribution is computed using a separate method. The field, B_j , at point j is given by the expression

$$B_j = F_{ij} I_i \quad (7.3)$$

where F_{ij} describes the mutual coupling between current loop i and point j . The initial current is obtained by setting $B_j = 1$ and inverting F_{ij}

$$I_i = F_{ji}^{-1} B_j \quad (7.4)$$

The initial current density found by DISK is plotted in Fig. 7.4. From this initial condition, the DISK code follows the current distribution in time as it drops to zero.

There are three important questions to be answered in the disk benchmark.

1. Does FASTEDDY match the DISK solution?
2. What dependence on mesh size does the result have?
3. What dependence on time step does the result have?

These are answered by examining Figs. 7.5-7.9. In Figs. 7.5-7.7, the DISK solution is plotted as a solid line and FASTEDDY results appear as individual points. The FASTEDDY data is obtained at loop centroids by averaging the line currents at the four edges of the loop. The line currents are divided by their associated triangular areas and multiplied by the line length to obtain a current density. For the 6x6 mesh there are only 3 effective circular loops and therefore only 2 data points at the centroids. By symmetry the current at the center is necessarily zero. The data points are chosen along a single radius of the disk. From the output it is obvious that symmetry exists. For the 12x12 mesh there are 6 loops and 5 data points.

The figures show very good agreement for both meshes, with the larger mesh slightly better in areas of large gradient. It is somewhat of a surprise that the 6x6 mesh does so well. The DISK

Table 7.1 Disk Benchmark Description

composition	copper ($1.67 \times 10^{-8} \Omega - m$)
thickness	5 mm
radius	30 cm
initial field	1 Tesla
field at $t = 0^+$	0 Tesla

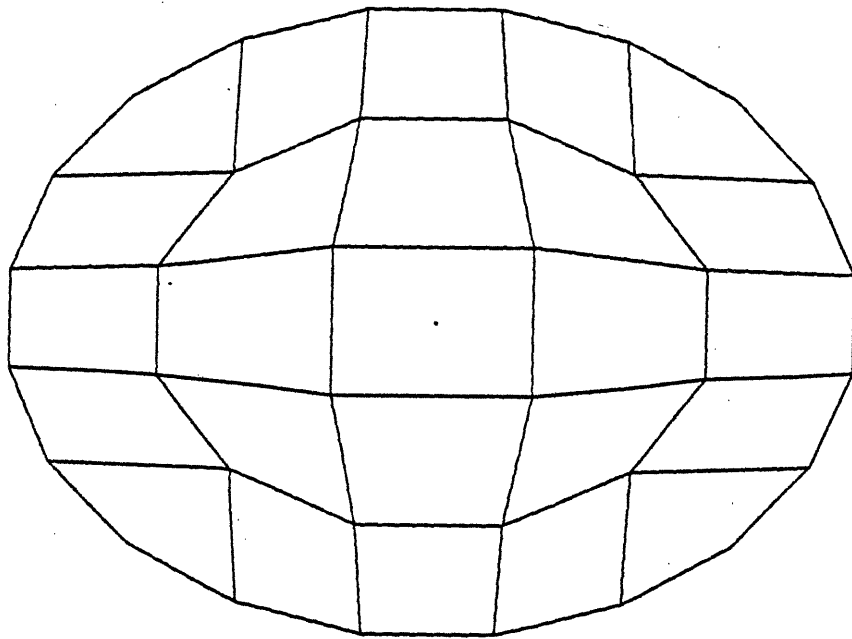


Figure 7.2 6x6 Mesh for the Disk Benchmark

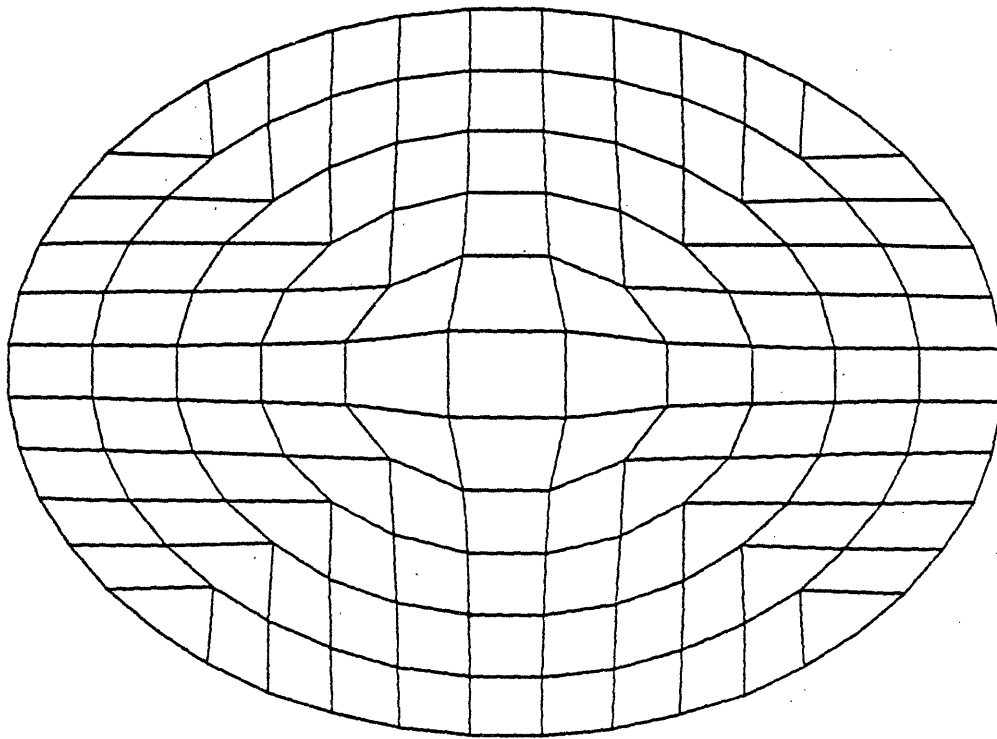


Figure 7.3 12x12 Mesh for the Disk Benchmark

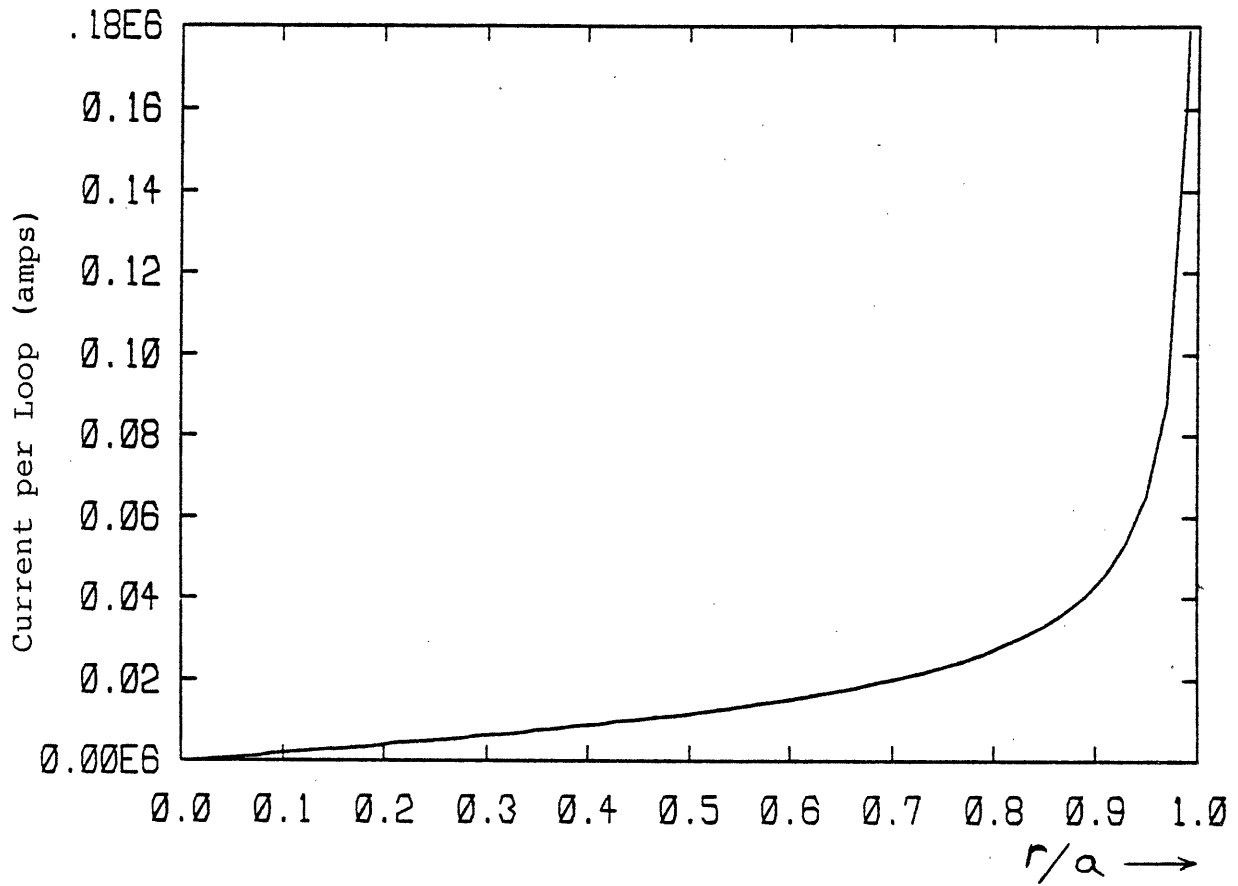
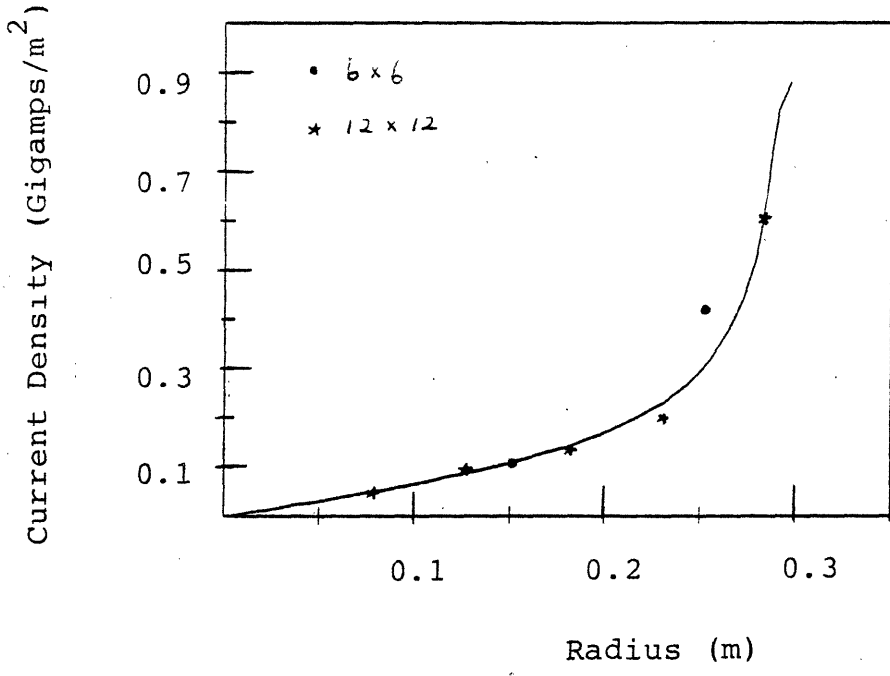


Figure 7.4 initial current density for Disk Benchmark



(solid line is DISK calculation. Points are FASTEDDY)

Figure 7.5 Disk Current Comparison at 1 msec

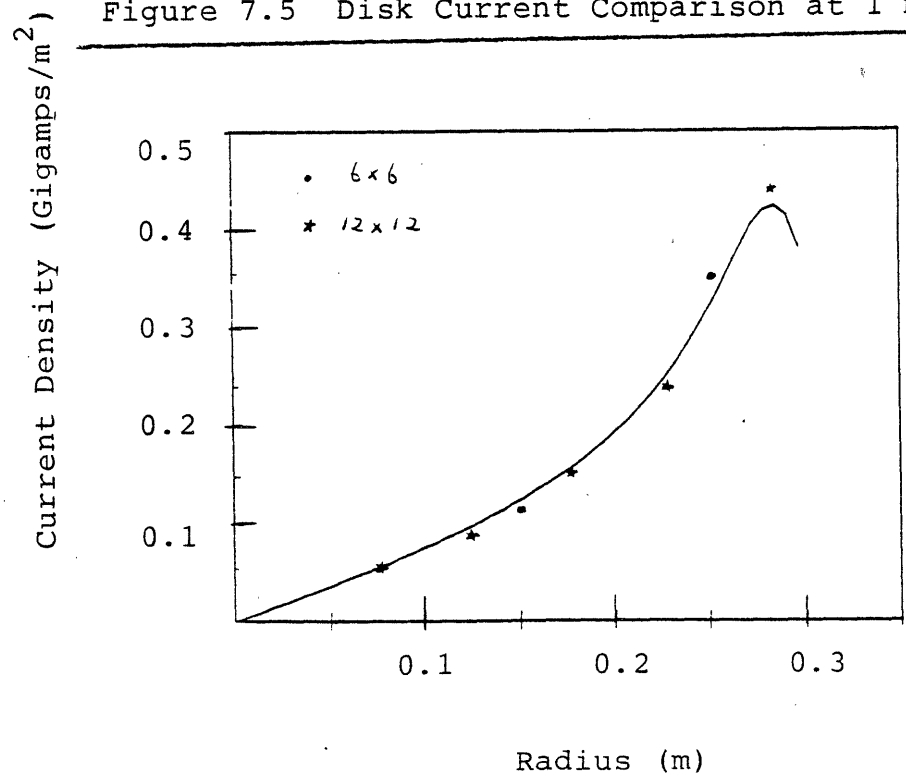
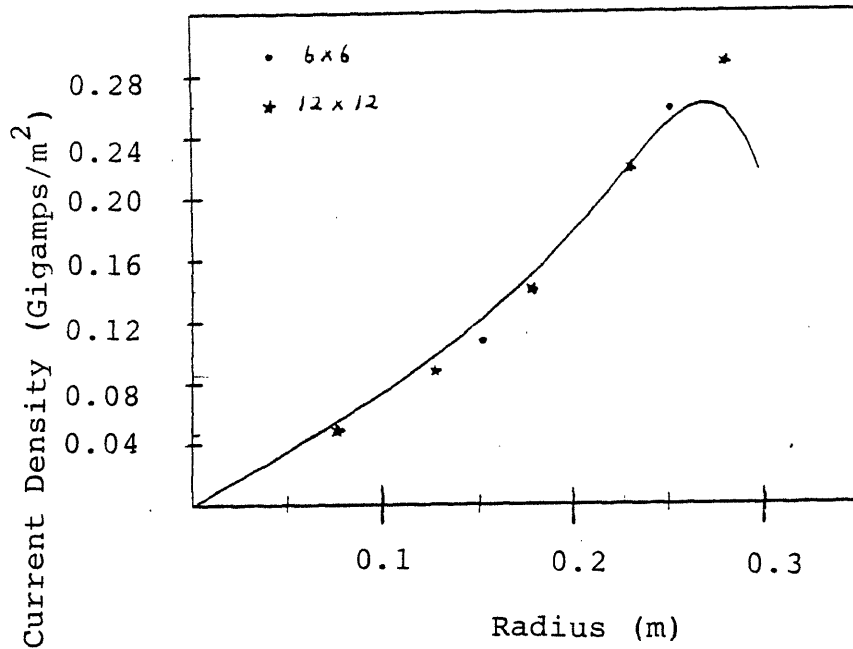


Figure 7.6 Disk Current Comparison at 5 msec



(Solid line is DISK calculation. Points are FASTEDDY)

Figure 7.7 Disk Current Comparison at 10 msec

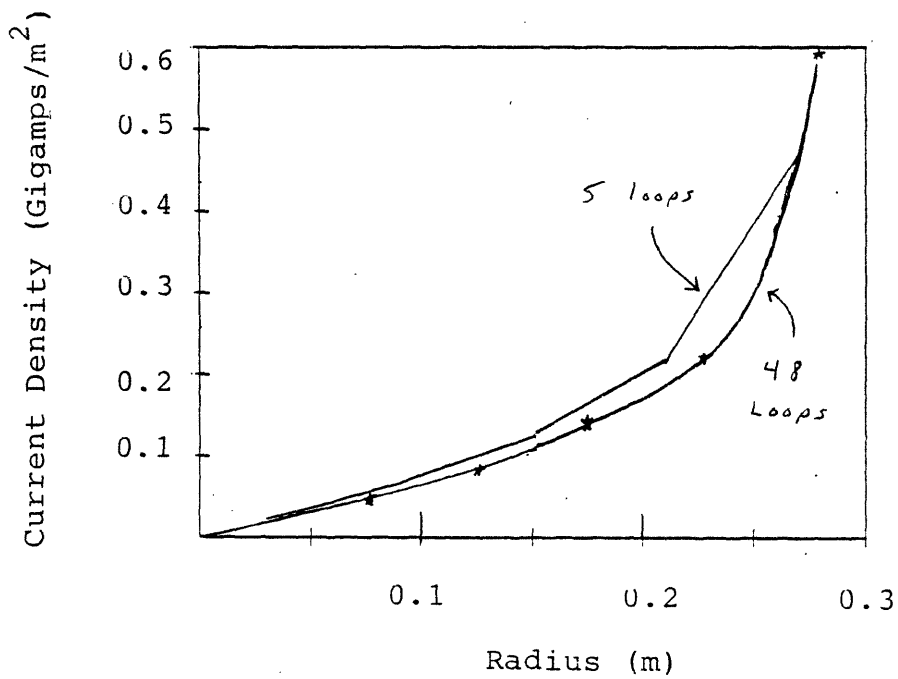


Figure 7.8 5-Loop Disk Comparison at 1 msec

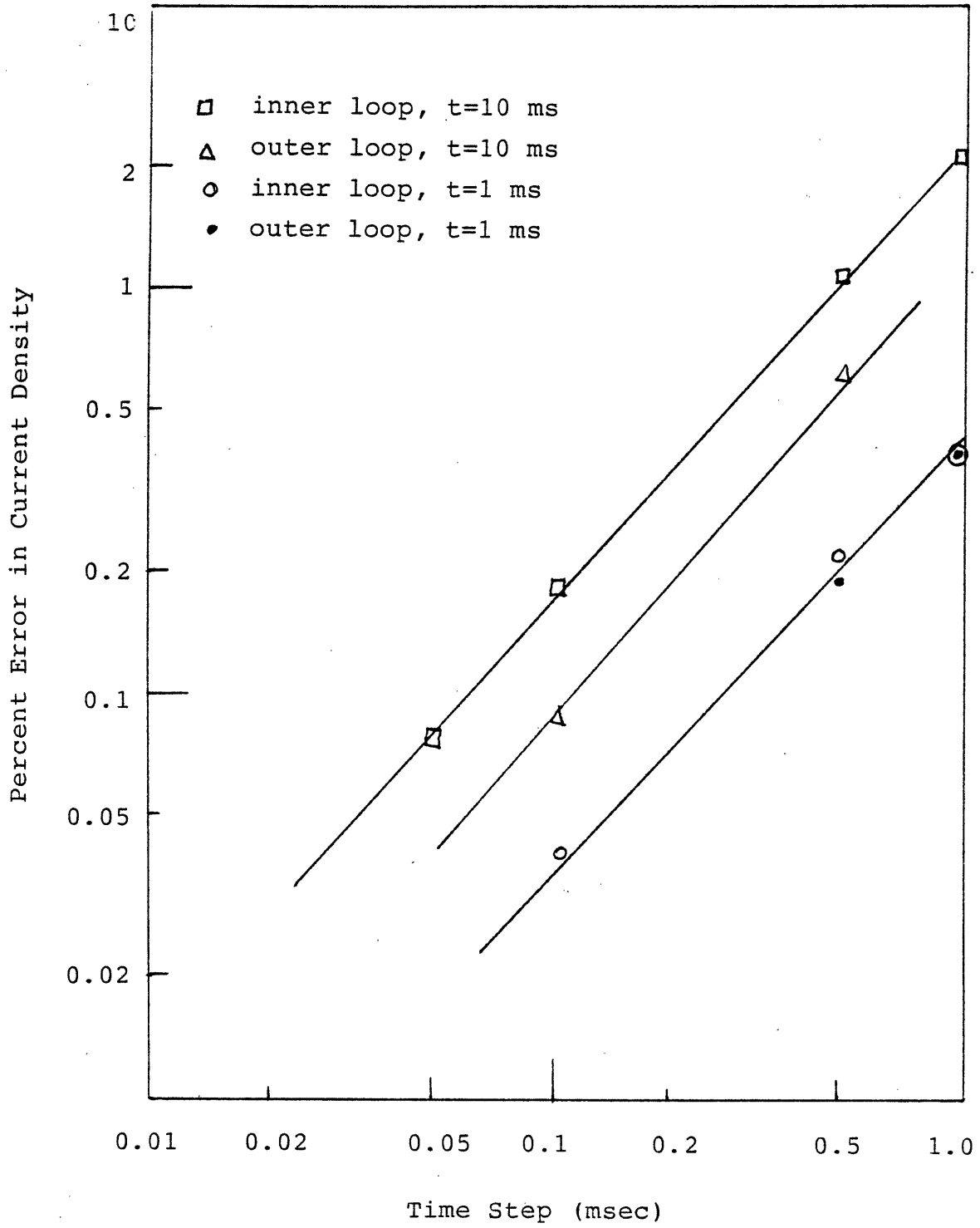


Figure 7.9 Error in the Calculated Current
for the Disk Benchmark

program was executed with 5 loops and results are shown in Fig. 7.8. FASTEDDY seems to do better. It is speculated that this is a result of the different types of coupling used in the two codes. In the DISK code, each loop is contained *within* other loops, making the solution more sensitive to the discretization. FASTEDDY has no loops contained within other loops. Most of the loops are far away from the majority of other loops, making the mutual inductance matrix naturally more diagonally dominant.

An error analysis was performed using the 6x6 mesh and varying the time step over 2 orders of magnitude, from 1 msec to .01 msec. The natural L/R time constant for this problem is on the order of 1-10 msec. No analysis was performed for time steps lower than .01 msec, since accuracies better than this are not needed. Results are plotted in Fig. 7.9 which shows the percentage error with respect to the result at .01 msec. Data are plotted for both of the two loop centroids at 1 msec and 10 msec. Errors of 1% or less are achieved easily for time step < 0.1 msec, i.e., for roughly 1-10% of the global time constant of the problem.

7.2.3.2. 2-D Torus Benchmark

The connected shell benchmark was performed with a continuous toroidal shell and a step change in current at the center of the torus, directed toroidally (along ϕ). This test case was chosen due to the availability of both analytic and numerical data for comparison^(7.4,7.5).

The first part of the benchmark is the instantaneous response at $t = 0^+$. For this test the time step $\Delta t = 0.1$ msec was used with both an 8x4 and a 16x16 mesh. In describing the size of the connected meshes, the first number is the number of loops in the toroidal direction and the second is either poloidal or axial, depending on the coordinate system. Fig. 7.10 is a plot of the 16x16 mesh, and Fig. 7.11 contains the results. The results exhibit accuracy of better than 10%. This is reasonable, since the primary application of the code is a comparison with experimental data which has errors greater than 25%.

A sensitivity test of the geometric mean distance used for stick self-inductance calculations showed that a factor of 2 change resulted in only 5-10% change in current ϕ density. Values of GMD less than 0.2 gradually pull the entire profile down below the correct result.

The second part of the test is the time dependent decay of the induced current. For this comparison, the total resistive power is plotted versus time for FASTEDDY and also using the 1-D program described in Chapter 6. This is plotted in Fig. 7.12 with a 4x8 and an 8x8 mesh. In addition, the spatial profiles are presented at several time steps using $\Delta t = 1.0$ msec in Figs. 7.13-7.15. The initial step response is higher than for the 0.1 msec case and slightly more peaked. This behavior is carried along through most of the early transient, up to ~ 100 msec.

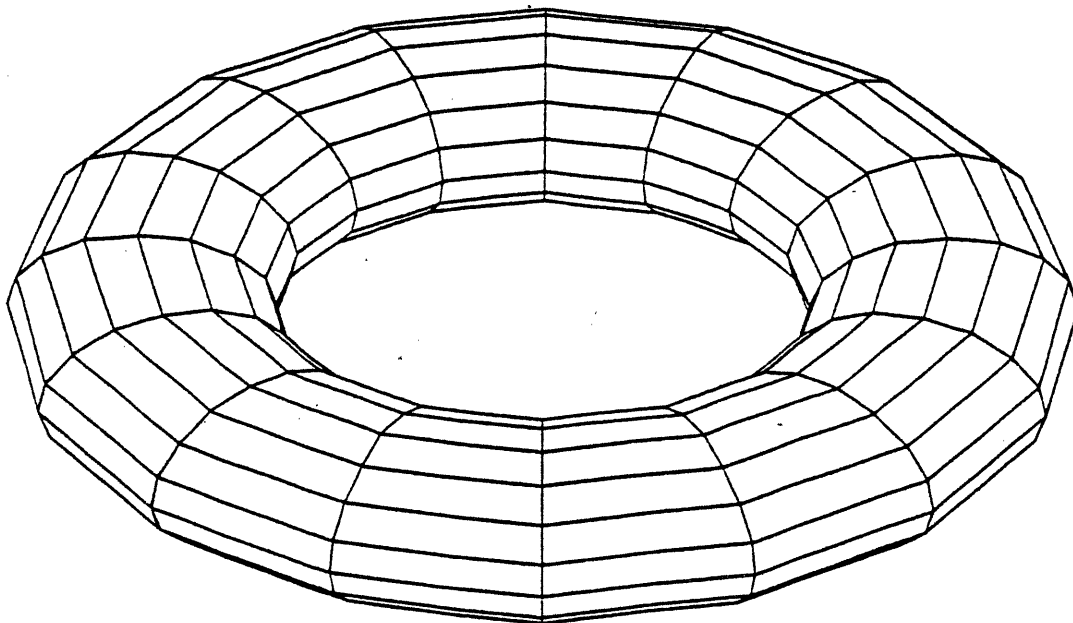


Figure 7.10 16x16 Toroidal Mesh

Generated by FASTEDDY

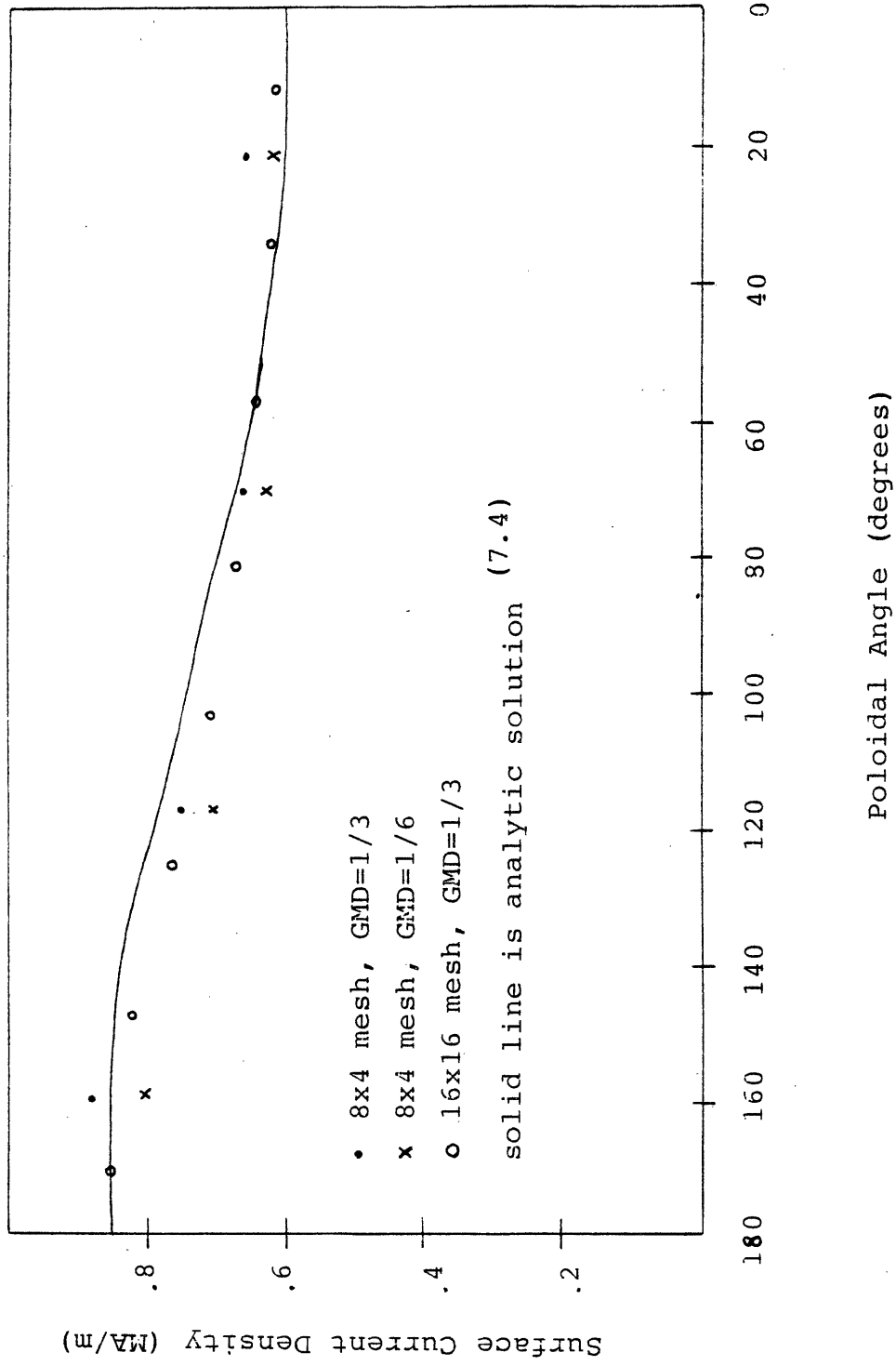


Figure 7.11 Instantaneous Response of the Toroidal Benchmark

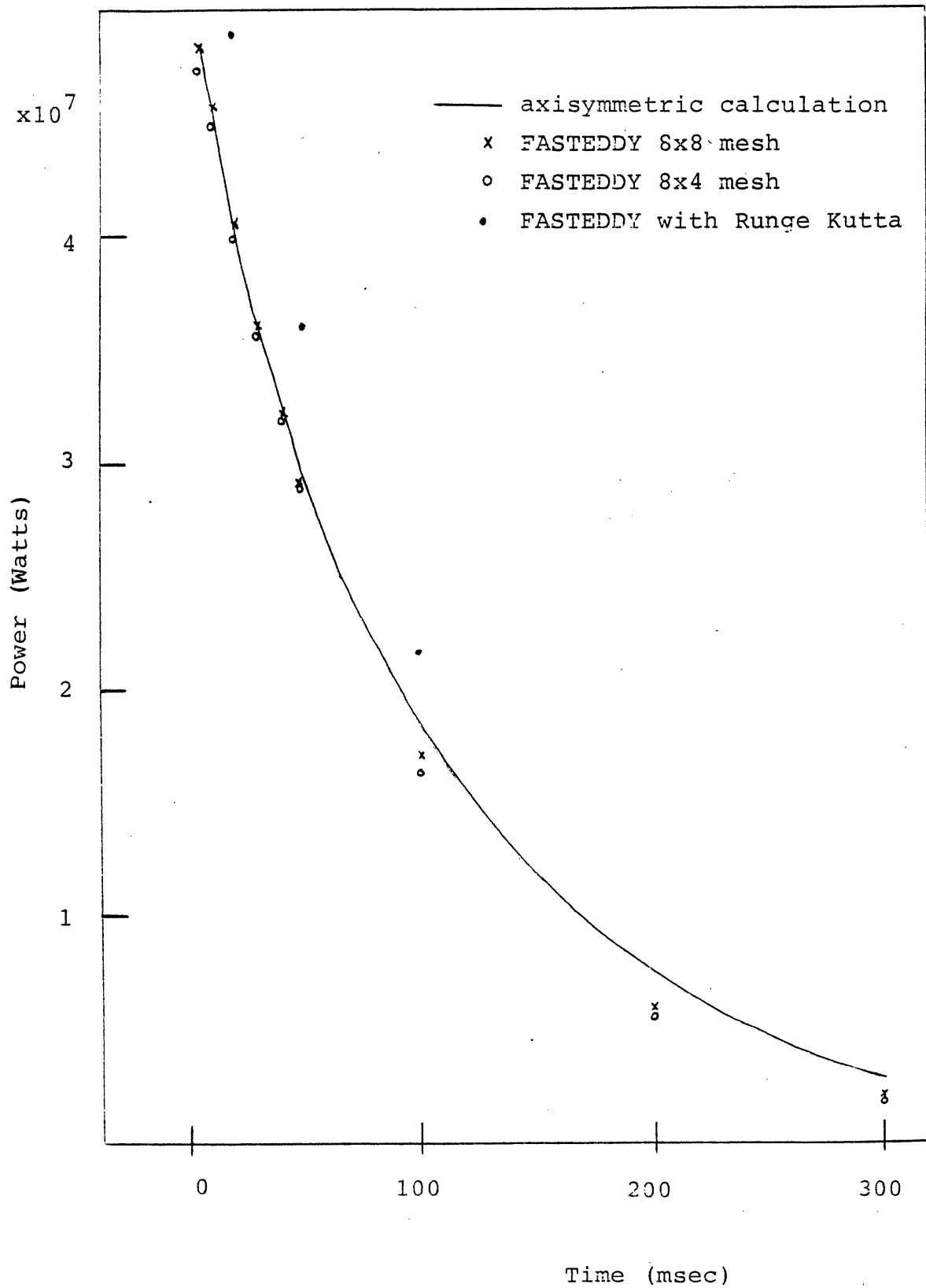


Figure 7.12 Toroidal Benchmark - Power vs Time

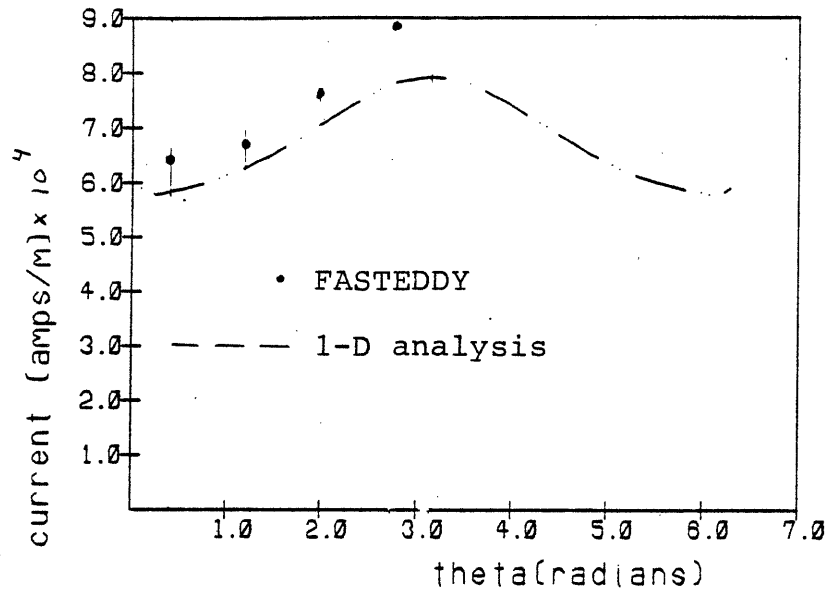


Figure 7.13 Toroidal Benchmark Current Profile at 6 ms

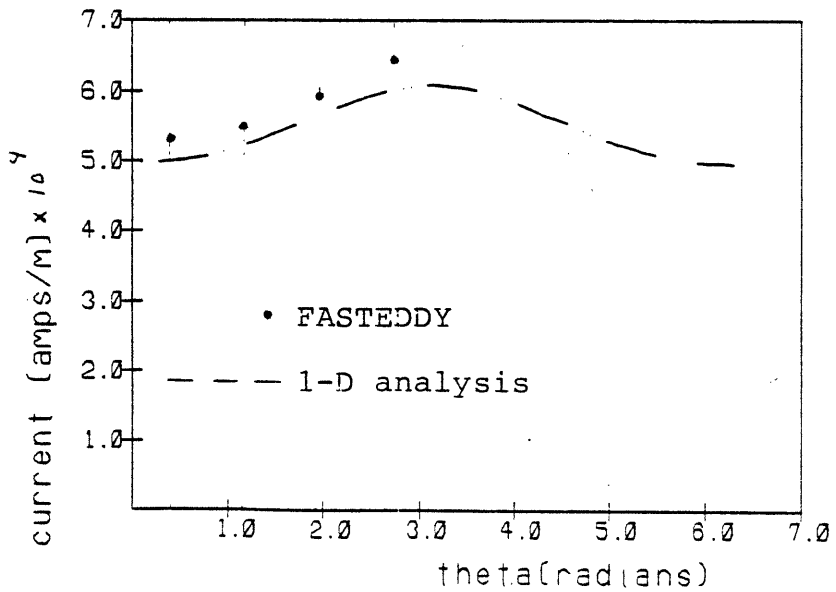


Figure 7.14 Toroidal Benchmark Current Profile at 50 ms

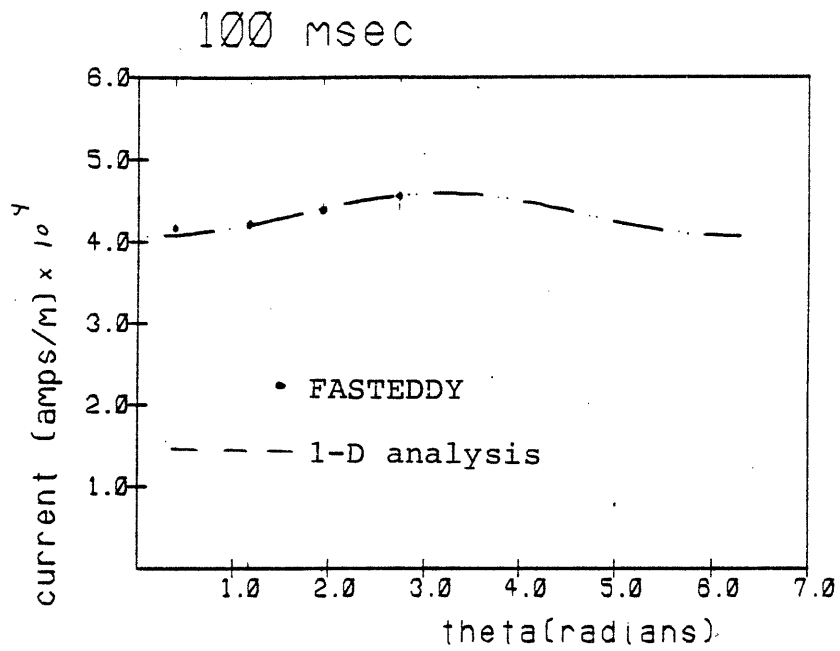


Figure 7.15 Toroidal Benchmark Current Profile at 100 ms

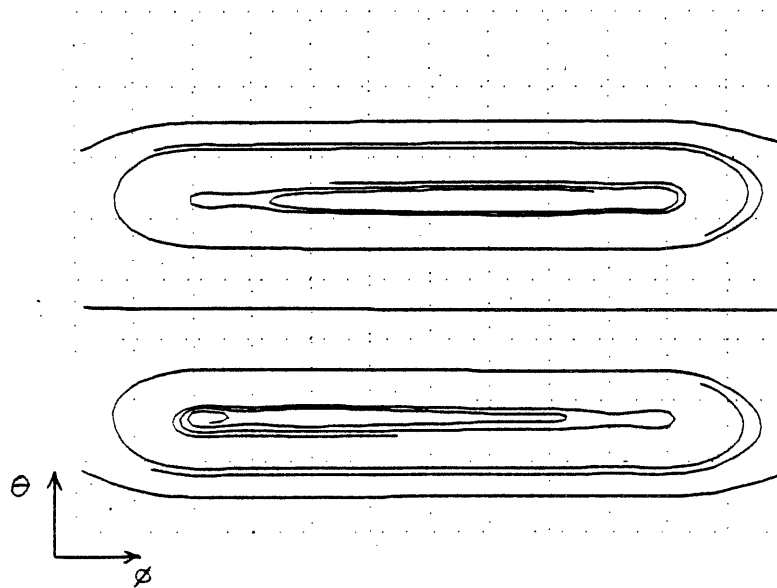


Figure 7.16 Current Streamlines at t=0

for the Torus with a Poloidal Break

One of the lessons learned from this benchmark was the importance of consistent modeling of the source term and the structure. As an example, consider a torus broken into an 8x8 mesh. The network analog of the smooth torus actually consists of straight sticks which meet at an angle. If a central source current is desired, then the driving current should possess 8 straight segments rather than one circular loop. When a circular filament is used, the solution is far less accurate for a small mesh. Since the inductances of the structure were computed using the vector potential, it is more appropriate to also use the vector potential in calculations with the source currents.

7.2.3.3. 3-D Sample Run

The torus benchmark was satisfactory, however it still does not test the full 3-D capabilities of the code. In order to provide an example of a fully 3-dimensional test problem, a torus with a poloidal break was examined using the same driving current as the continuous shell. No benchmark data was available for comparison with this case. The problem is identical to the symmetric torus except for the existence of a large resistivity cut across the poloidal cross section at $\phi = 0$. The driving current is unchanged, but the cut results in a noncirculating induced current distribution. Fig. 7.16 is a plot of the current streamlines at $t = 0$. It demonstrates the tendency of the current to flow on the outboard side in the same direction as the benchmark test, but to return in the opposite direction on the inboard side. This is entirely due to the fact that a current loop induces a larger $\oint \mathbf{A} \cdot d\mathbf{l}$ on the outside of the torus.

The streamlines *should* close on themselves. There are two reasons why they don't. First, the initial value solution uses a finite accuracy Runge-Kutta routine. Decreasing the step size had no noticeable effect, implying that this is not the dominant problem. More importantly, the cubic spline fit is not an accurate representation of the actual divergence-free current distribution. The splines give the problem a fictitious net divergence.

7.3. Structural Codes

Three standard finite element structural analysis codes were examined to determine their suitability for use in analyzing the problem of curved shells with distributed time dependent loading. They are NASTRAN, SAP4, and PAFEC - all available on the MFENET (National Magnetic Fusion Energy Network). The features considered desirable in a code are listed in Table 7.2. Based on these desirable features, PAFEC was selected for use.

PAFEC was used for calculations modes and frequencies and for static loading analyses. For the modal analysis, axisymmetric elements were used. These are efficient elements, thereby allowing a greater accuracy within the fixed limits of computer time and space. For the static loading, the symmetry is absent and the entire shell had to be meshed, resulting in larger elements and less accuracy.

Table 7.2 Features of a Desirable FEM Code

- cost
- ability to solve problem
- availability
- user interface

One of the most important decisions in applying the code is the element type to be used. There is considerable flexibility with shell elements, including flat shell, flat shell with bending, curved shell, and several different possibilities for the number of nodes per element. Generally, for a fixed number of degrees of freedom, it is better to use fewer elements with each element carrying more degrees of freedom.^(7,9) The 8-noded, curved shell "semi-loof" elements were the first choice but were abandoned due to the complexity involved in their useage. 8-noded flat "facet shell" elements were somewhat easier to apply, but still had problems with consistant distributed loading vectors. The final choice was the simpler 4-noded flat elements which are presumeably the least accurate of the three but at the same time provide results which are consistant and can easily be interpreted. Since the results are used primarily to compare with the experimental data, which is expected to have uncertainties greater than 25%, high accuracy of the numerical calculation is judged unnecessary.

7.4. Analysis

The experiments are divided into two categories: nonuniform shell and nonuniform source currents. For the nonuniform shell tests, the source currents were axial and uniform, and the shell had a small hole drilled in it. For the nonuniform source current tests, the shell was continuous but the source current was helically directed in two groups of filaments. Data was taken for both of these tests measuring both self interactions and external field interactions. This generates a 2x2 matrix of tests. For all four tests, the eddy current analysis was performed using FASTEDDY. The structural analysis depended on the eddy current results. For the tests with a hole, the results from FASTEDDY indicated that the variation in pressures might be small enough to treat the structural problem with an analytic solution for uniform loading. For the continuous shell tests the pressure loading was considerably more complex, so much so that the self interactions were not analyzed. The external field interactions were more easily characterized and the structural analysis was performed using PAFEC. Table 7.3 summarizes the test cases which have been studied and the methods used to analyze them.

7.4.1. Estimates for a Uniform Axial Current

In the experiment, nonuniform driving currents and nonuniform structures were studied. In order to interpret those results, they are compared to the simple case of a uniform axial current in a uniform cylindrical shell. Both the case of self interactions and external field interactions are analyzed. For the interaction of the axial currents with their self fields and with the source fields (both of which are called self interactions), the pressures are radially directed. This case is analogous to a pressurized cylinder problem. For the interaction of the axial currents with the

Table 7.3 Summary of Cases Analyzed

1. Data was taken for all cases
2. All cases were analyzed with FASTEDDY
3. The structural analysis was done as follows:

	self field interactions	external field interactions
continuous shell, helical currents	no structural analysis	PAFEC 4-noded elements with bending
shell with hole, axial currents	analytic solution	analytic solution

external field (which is axisymmetric, part radial and part axial), the pressures are circumferentially directed. This case is analogous to a cylinder under torsion.

The only significant complication to the symmetric problem is the sinusoidal nature of the currents. For self interactions the observed strains are at a different frequency and phase than either the driving current or the induced current. In order to include the time dependent behavior, the filament-shell circuit of the experiment is approximated with the simple circuit shown in Fig. 7.17. Of course, in the experiment there is no single inductance or current; all of the quantities vary continuously across the structure. For this simplified problem the governing equation is

$$M \frac{di_f}{dt} + L_s \frac{di_s}{dt} + R_s i_s = 0 \quad (7.5)$$

where the subscript s indicates a shell quantity and f indicates filament. This equation is solved by assuming

$$\begin{aligned} i_f &= I_f \cos \omega t \\ i_s &= I_s \cos(\omega t + \phi) \end{aligned} \quad (7.6)$$

Then (dropping the subscripts),

$$\frac{I_s}{I_f} = \frac{1}{\sqrt{(M/L)^2 + (R/\omega L)^2}} \quad (7.7)$$

$$\tan \phi = R/\omega L \quad (7.8)$$

The geometry of the shell dictates that $L=M$, since all of the flux which is responsible for the shell self inductance (shaded area of Fig. 7.18) also passes through the filament circuit. The values of R and L can be computed from

$$R = \sum \frac{\rho L}{A} \quad (7.9)$$

$$L = \frac{\mu_o l}{2\pi} \ln \frac{r_2}{r_1} \quad (7.10)$$

where r_1 is the inner shell radius and r_2 is the return current shell radius (part of the shell circuit). Using values relevant to the experiment, we compute $R \approx 40\mu\Omega$, $L \approx .02\mu H$, and $R/L \approx 2000$. The experimental value of R/L , obtained by measuring I_s and I_f at various frequencies is ≈ 1500 . The discrepancy may be due to errors in the shell dimensions or physical properties.

In order to estimate the pressure, we use

$$\begin{aligned} B_\phi &= \frac{\mu_o I_f}{2\pi r_1} \\ K &= \frac{I}{2\pi r_1} \end{aligned} \quad (7.11)$$

$$p = K \times B$$

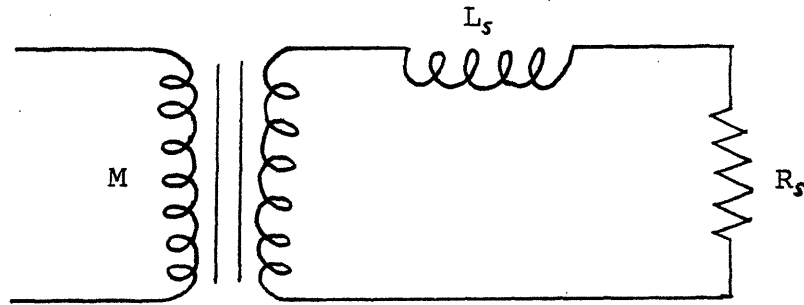


Figure 7.17 Shell-Filament Equivalent Circuit

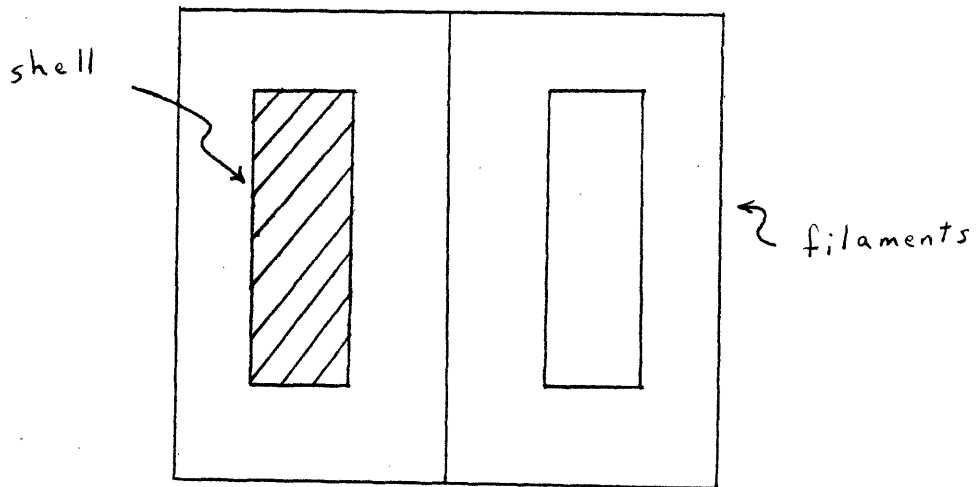


Figure 7.18 Cross Section of Shell-Filament Circuit

The nonzero phase difference between the shell and filament currents results in a slight reduction in pressure which is given by

$$|p_r| = \frac{\mu_o I_s}{(2\pi r_1)^2} \sqrt{I_s^2 + I_f^2 + 2I_s I_f \cos \phi} \quad (7.12)$$

At 250 hz, the computed ratio of currents is $(I_f/I_s) = 0.72$ and $\phi = 36^\circ$. The measured values are 0.66 and 36° .

Using the measured values, we reduce the pressure equation to

$$|p_r| = 2.27 \left[\frac{\mu_o I_s^2}{(2\pi r_1)^2} \right] \quad (7.13)$$

As a numerical example, the measurements with the hole were taken at $I_s \approx 550$ amps peak, which leads to a peak pressure estimate of 5.4 Pa. With $\sigma = (pr_1/t)$, we estimate a circumferential stress of 900 Pa. For measurements with the continuous shell, the current was 1050 amps peak, and the peak pressure and stress are 20 Pa and 3300 Pa respectively.

For the case of a cylinder under torsion, the pressure is simply

$$p_\theta = \frac{I_s B_r}{2\pi r_1} \quad (7.14)$$

The peak radial field in the experiments was ~ 80 Gauss (.008 T). If we assume an average field of 40 Gauss acting over the shell and a peak shell current of 550 amps, then the total torque, T, is .0425 N-m. The shear stress from this torque is

$$\tau = \frac{T}{2\pi r^2 t} = 4400 \text{ Pa} \quad (7.15)$$

7.4.2. Comparison with the Shell with a Hole

The tests with the hole drilled in the cylinder were performed with a uniform axial driving current. The filaments run up the center of the cylinder, fan out radially in equal spacings in theta, pass axially down to the bottom of the cylinder, and then reconnect to the neighboring filament. The restriction on the return current flow path to be purely axial (the outer shell is composed of axial strips) has a pronounced effect, due to the close coupling of the inner and outer shells. The result is that the currents in the inner shell are constrained to be very close to axial. As observed in the FASTEDDY results, the perturbation due to the hole remains localized near the hole. At a distance greater than 1-2 hole radii there is little deviation from the expected pressure distribution of a continuous shell. The existence of a second shell differs from the simplest approximation to a reactor first wall where the wall is assumed to be the dominant conducting structure. However,

these results indicate that conductors near the first wall can be expected to have a significant influence in the direction of the induced currents as well as their magnitudes.

The main effect of the hole is to cause a rise in the axial current near the hole. The majority of the current is still axial, so, in the case of self interactions, the fields are principally circumferential and the pressures are over 90% radial. At the edges of the hole there is a radial field contribution which acts circumferentially to push in on the hole.

7.4.2.1. Description of FASTEDDY Results

The mesh used to compute induced currents is presented in Fig. 7.19. It is 12 loops wide in the circumferential direction and 18 loops total in the axial direction. The hole comprises four meshes which are assigned a large resistivity in the calculations. A first order attempt is made to correctly model the hole by fixing the points in contact with the edge of the hole onto a circle of the correct radius. The rest of the mesh is relaxed around these fixed points. Fig. 7.20 shows the mesh as it appears unwrapped. This unwrapping procedure is important, since all of the data are presented on a flat plane. A cut is made poloidally at $z = 0$ and axially at $\theta = 0$. The double cylinder is then laid out so that running from the bottom to the top of the mesh is equivalent to passing from the bottom of the inner cylinder to the top, then to the top of the outer cylinder and back down to the base.

Figs. 7.21-7.22 show the time histories of the source current and induced power. (The magnitudes do not coincide with the actual magnitudes present in the experiment. The results were appropriately scaled afterwards.) The induced power is an averaged indicator of the level of current in the shell. A phase shift of $\sim 50^\circ$ between the source and induced currents is observed, compared to an experimentally measured phase of 36° . The ratio of induced current to source current predicted by FASTEDDY is 0.47 rather than the experimentally observed value of 0.66. This discrepancy is believed to be due mostly to the method used to model the circulating loops in FASTEDDY. Currently FASTEDDY computes the properties of the circulating loops by adding the properties of the sticks which comprise the circulating loops. A method which incorporates whole body properties rather than local properties would probably prove more suitable.

Figs. 7.23-7.24 show the spatial variation of the induced currents in streamline form and in magnitude. The magnitude appears from two perspectives, with one showing the entire shell circuit including the return current path which has a flat distribution. The plots represent the cylinder slit open and laid out on a plane as discussed above. For the magnitude plot, the displacement of the surface away from the zero plane, drawn with a dashed line, represents the level of the function being plotted. For the streamline plot, streamlines are started off at equal spacings in theta. The space between the streamlines does not necessarily represent the amount of current present.

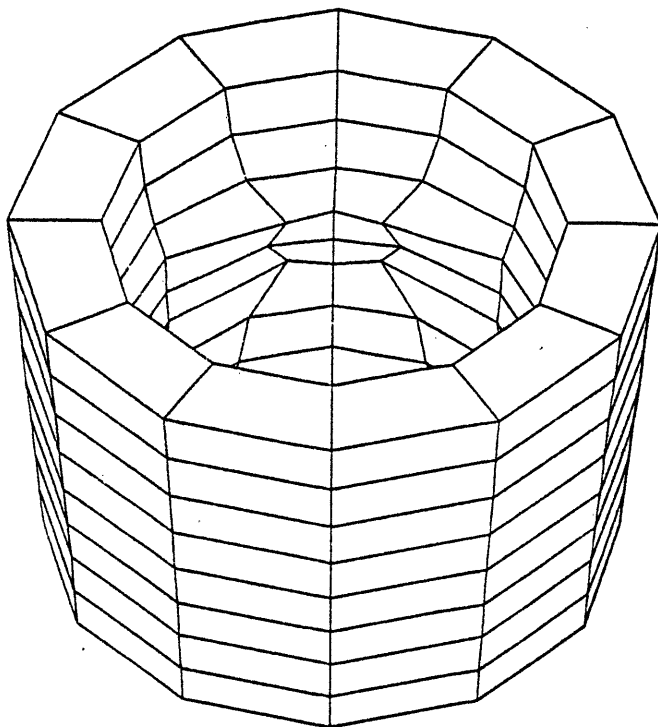


Figure 7.19 FASTEDDY 12x18 Mesh of the Cylinder
with a Hole

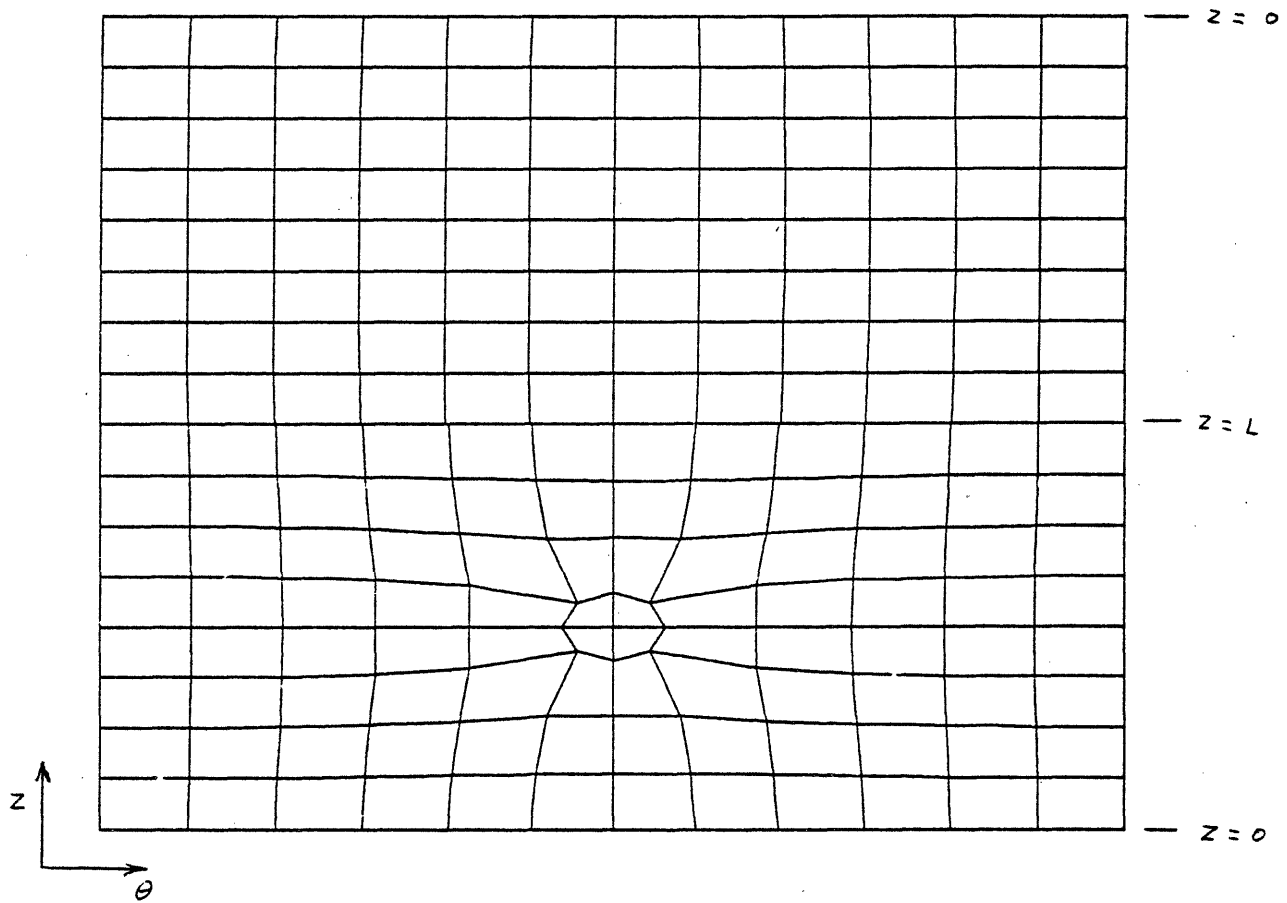


Figure 7.20 FASTEDDY Logical Mesh (Laid Open)

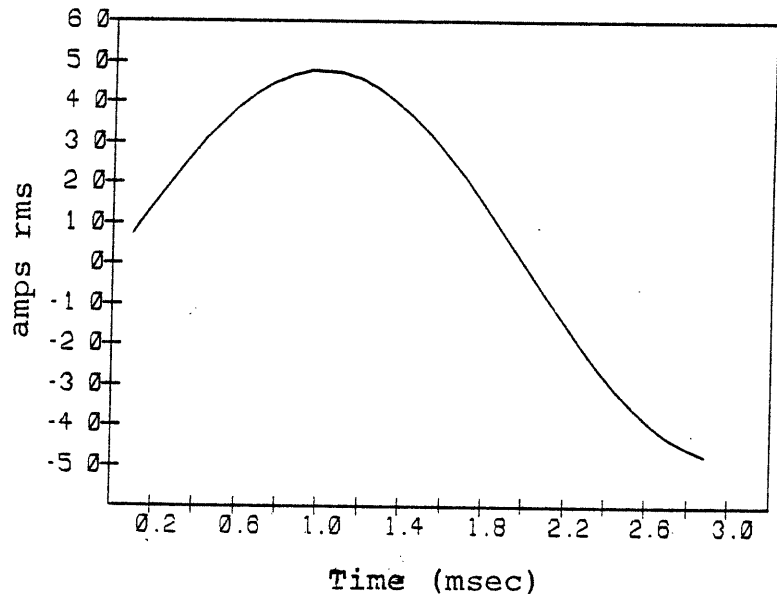


Figure 7.21 Source Current History

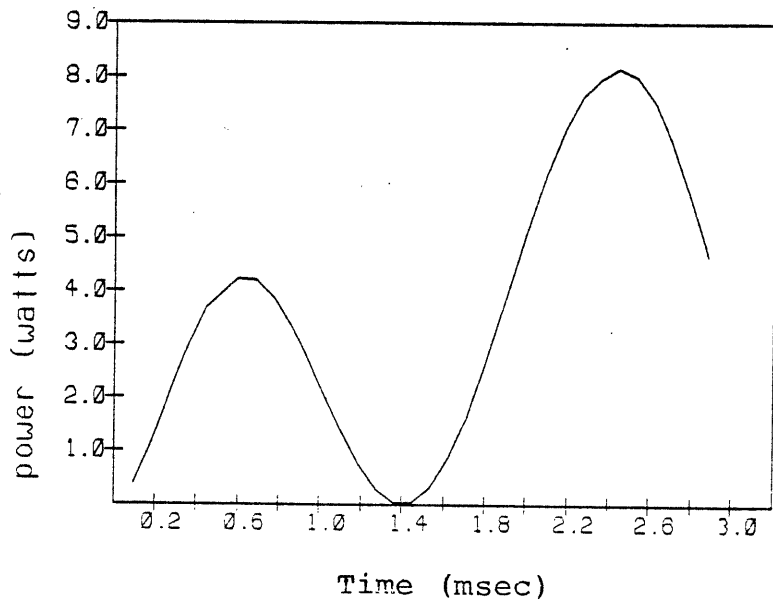


Figure 7.22 Total Resistive Power

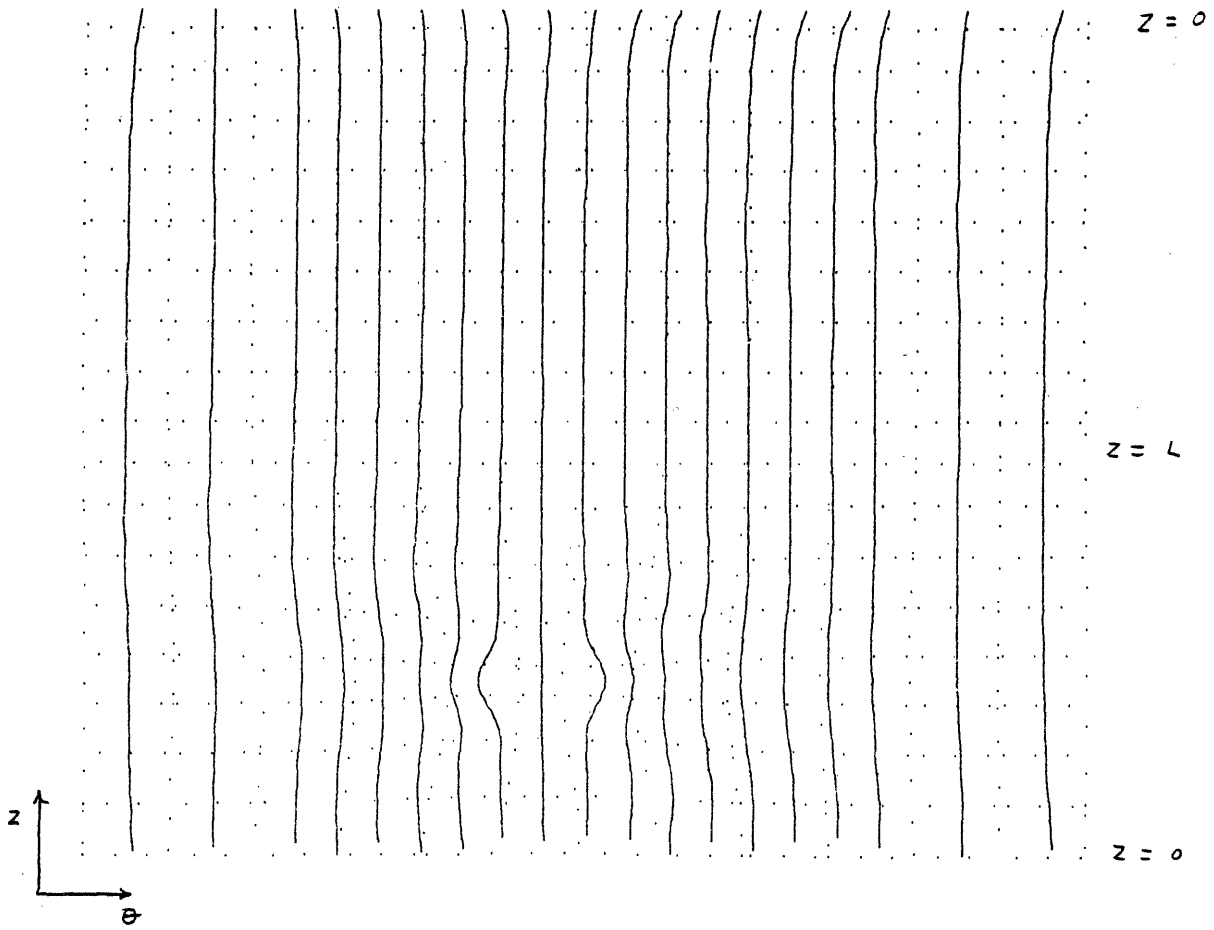


Figure 7.23 Current Streamlines with the Hole Present

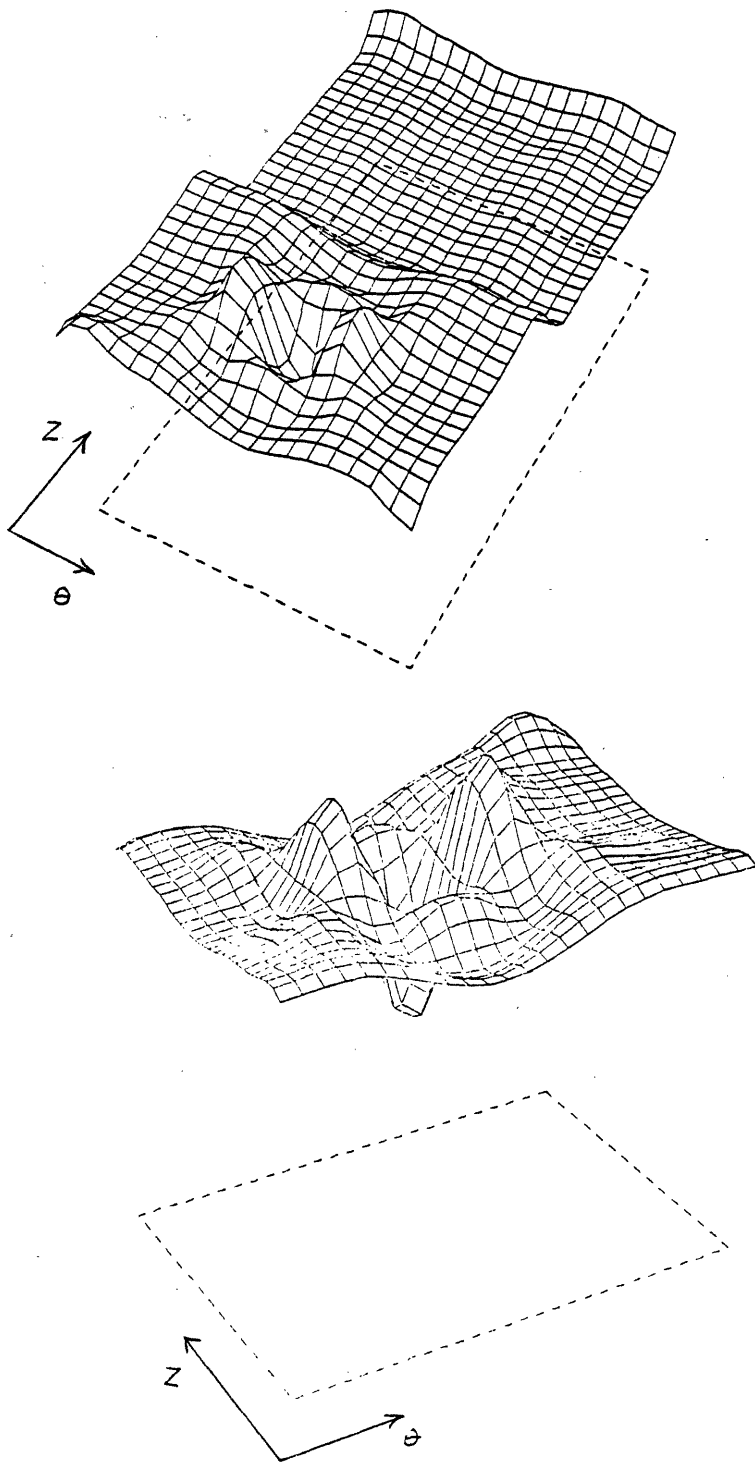


Figure 7.24 Induced Current Magnitude
with the Hole Present

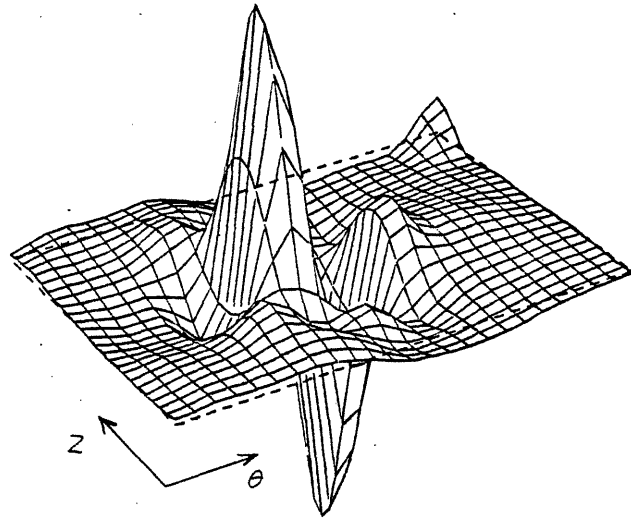


Figure 7.25 Radial Magnetic Field - Self Interactions
with the Hole Present

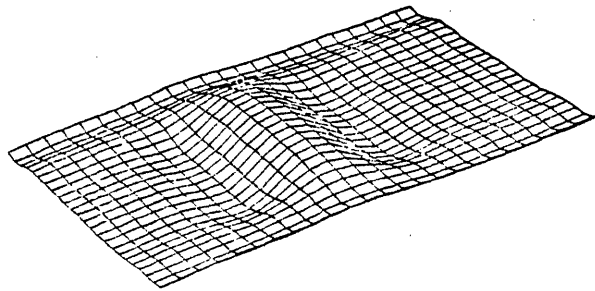
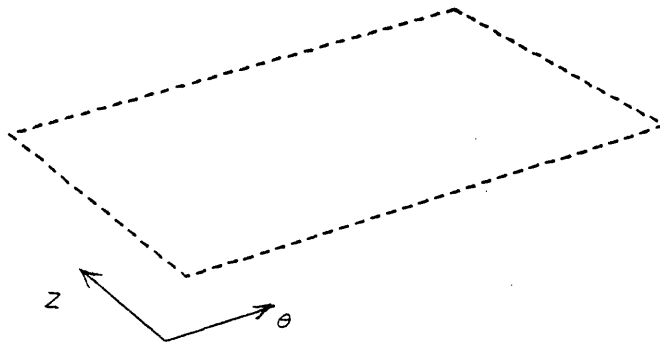


Figure 7.26 Toroidal Magnetic Field - Self Interactions
with the Hole Present

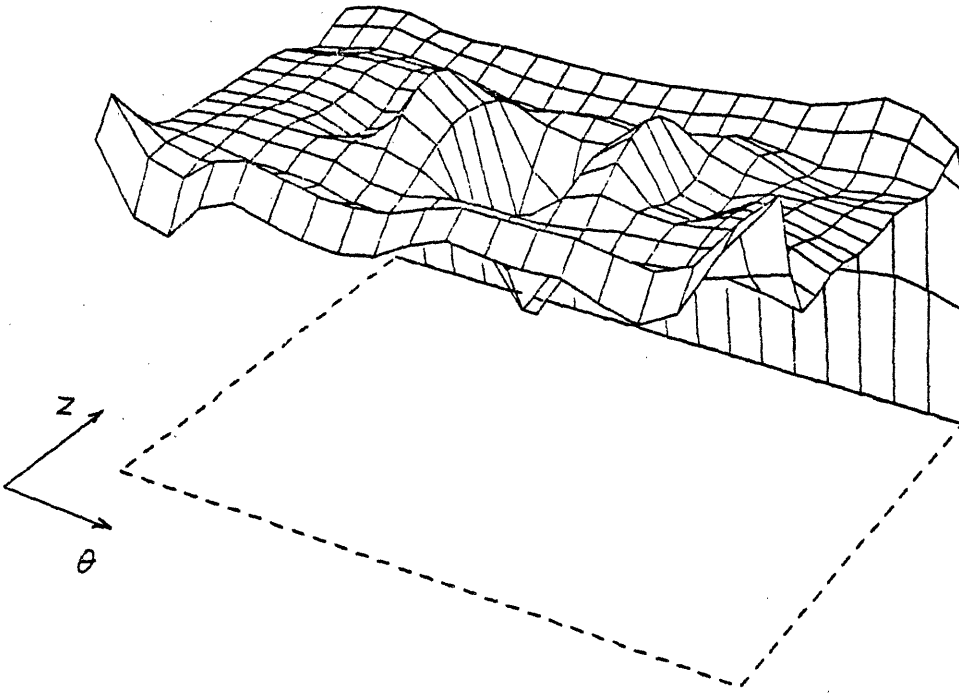


Figure 7.27 Radial Pressure - Self Interactions
with the Hole Present

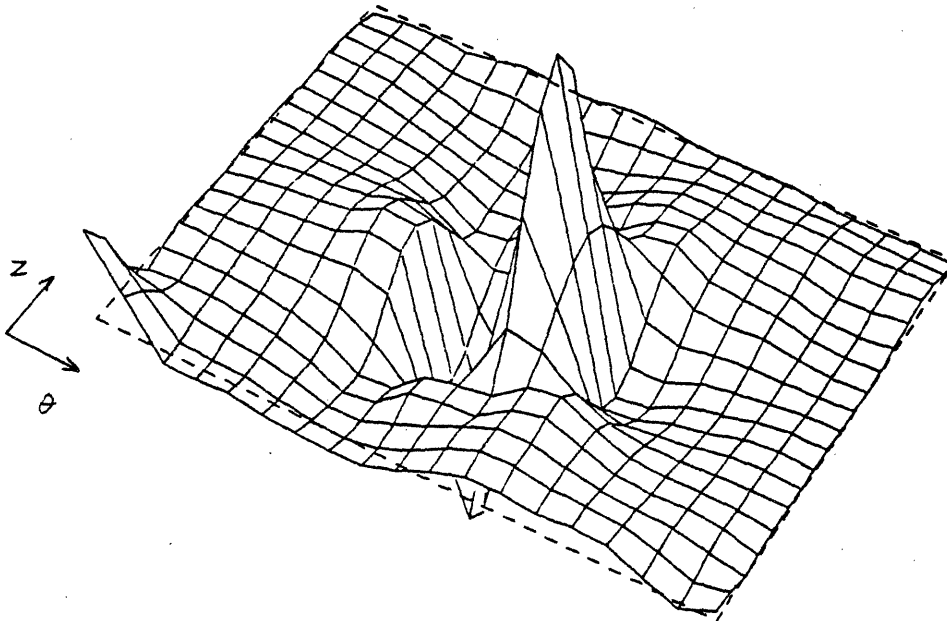


Figure 7.28 Axial Pressure - Self Interactions
with the Hole Present

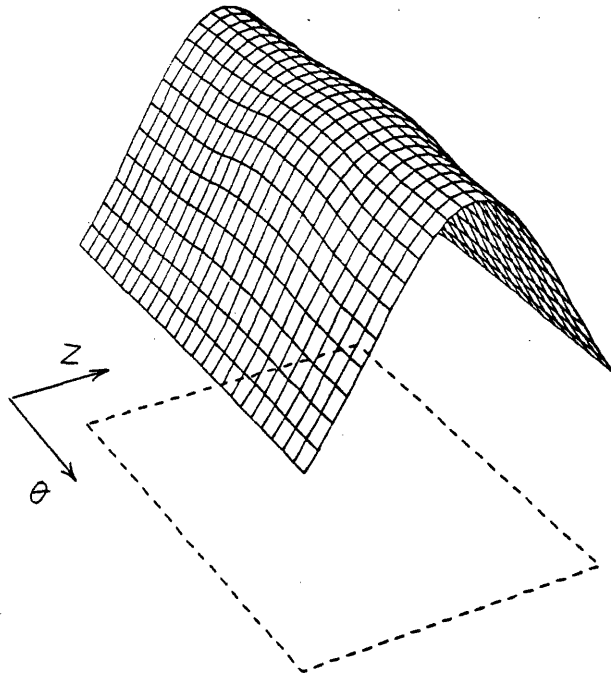


Figure 7.29 Axial Field from the External Field Coil

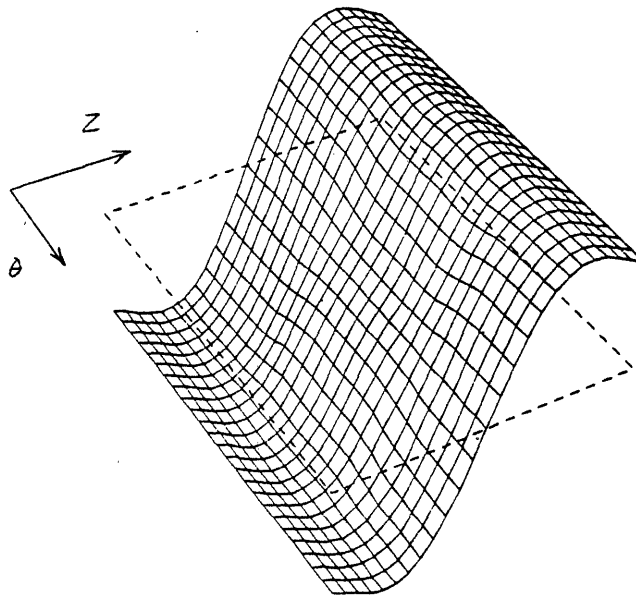


Figure 7.30 Radial Field from the External Field Coil

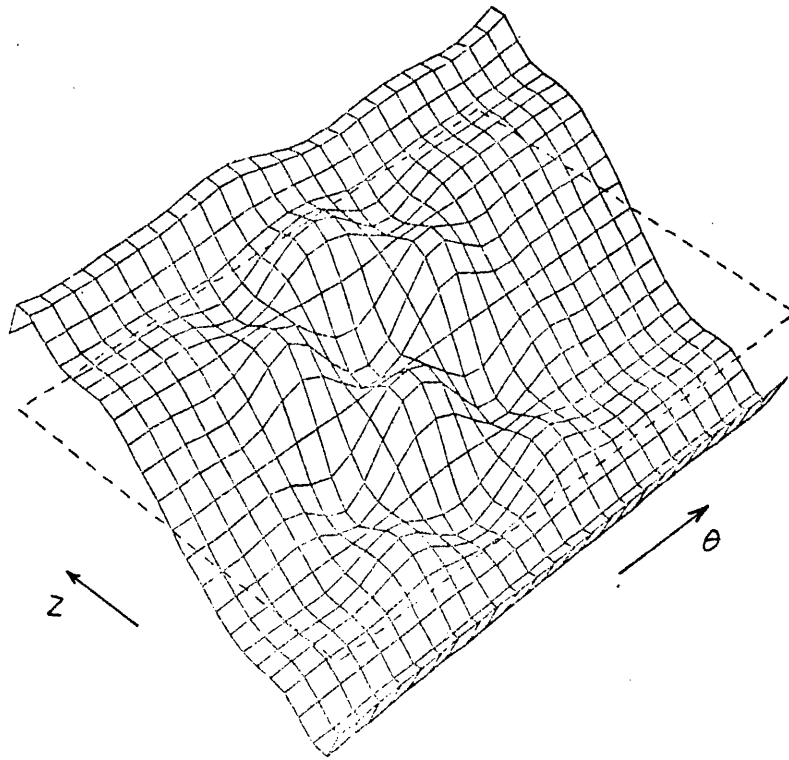
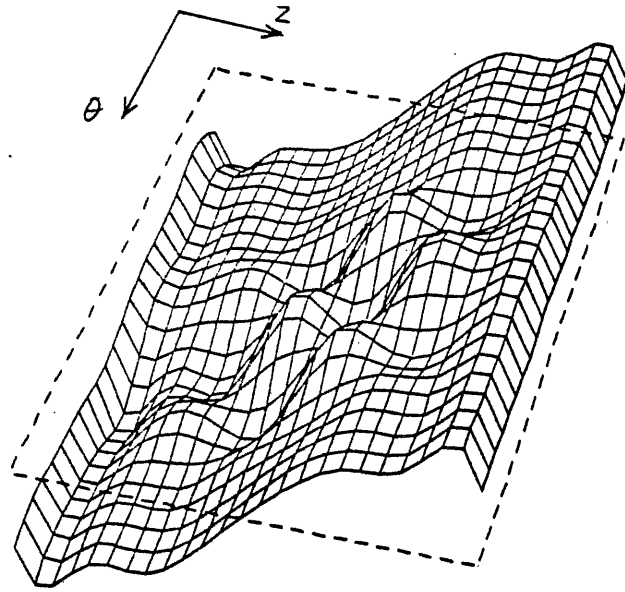


Figure 7.31 Toroidal Pressure - External Field with Hole

Present

The results at different time steps are very similar, with the main difference being in the magnitudes. They show that the current is similar to a uniform shell except very near the hole. The principal effect is an increase in the axial current due to bunching at the sides of the hole. This results in large radial fields generated in and around the hole.

The pressures behave similarly. For the first case analyzed (the self interactions) the largest component is the radial one, with axial and toroidal pressures down by 1-2 orders of magnitude. This is consistent with the fact that the pressures are dominated by the axial current and the circumferential field. Figs. 7.25-7.28 depict the fields and pressures for the case of self interactions with the hole. The toroidal pressure is not presented; it behaves very similarly to the axial pressure except that the peaks are rotated 90° around the hole.

For the external field interactions, the largest component of pressure comes from the interaction of axial currents with the radial field. This is a torsion, or circumferential pressure. Figs. 7.29-7.31 show the fields and pressures for this case.

7.4.2.2. Analytic Theory and Comparison with Data

The observation that the resulting pressures are dominated by either a radial or circumferential component, and are relatively constant over most of the shell suggests that an analytic estimate of stresses can be attempted with some success for this case. The problem of a uniformly loaded cylinder with a hole has been studied before by Peter Van Dyke ^(7,6) and others. Some results are presented in Figs. 7.32-7.34. They show a radial variation of approximately an order of magnitude in the stresses near the hole – much larger than the variation of the electromagnetic pressures. This indicates that the structural effects dominate the problem and the uniform pressure approximation is a good one. The coordinate system used by Van Dyke requires explanation. The radial distance, r , is the distance from the edge of the hole normalized to the hole radius, a . The angle coordinate, θ , measures the position around the hole, starting from the lowest axial position. The stresses are expressed as elements of the stress tensor. For example, $\sigma_{\theta\theta AV}$ is the circumferential stress at the middle surface. The normalization σ_{∞} is the value of axial stress far away from the hole.

The experimental data has been reduced for comparison with the theoretical predictions. Due to the extremely steep gradients near the hole, the data is not expected to be very accurate. The uncertainty in gauge position of 1-2 mm is significant since the slope of the stress function is so steep there. Also, because of the limited amount of data, a complete comparison with the theory is impossible. Instead, the trends are compared and the consistency of data and theory is analyzed.

The curvature parameter for the experiment, β , is defined by Van Dyke as:

$$\beta^2 = \frac{a^2 \sqrt{12(1 - \nu^2)}}{8Rt} \quad (7.16)$$

For our case this results in $\beta = 2.5$, which is close enough to the value of 2.0 in Figs. 7.32-7.33 so that qualitatively they are similar. However, this adds yet another source of error in the comparison.

For comparison with the analytic theory, the experimental stresses in Table 5.7 were converted to components normal and tangential to the hole. The results are presented in Table 7.4. In this table, the normal direction for gauge sets 6 and 7 is defined to be vertical. (Remember that gauge sets 6 and 7 are away from the hole.)

The pressure results of Fig. 7.32 are used to compare with the self interaction data in the table. In the figure, the tangential stress at 90° does not peak as high as at 0° and 45° . Gauge sets 3 and 4 are at 90° . They consistently show slightly larger normal stresses compared to tangential. This is in agreement with the theory when one considers the fact that gauge sets 3 and 4 are at 0.5 and 1.5 hole radii away respectively. At $r/a = 0.5$, the normal stress has already come up from zero and the tangential stress has passed through zero to a positive value approximately equal to the normal stress. In the data, gauge set 4 has a slightly smaller stress than set 3. From the figure it is apparent that the 90° case has approximately level response between 0.5 and 1.5 hole radii.

Gauge set 1 shows the most dramatic stress concentration of between 8 and 12. This is well up the curve for $\sigma_{\theta\theta}$. The normal component is down by over an order of magnitude as expected. Gauge set 2 at 45° agrees with the behavior of gauge set 1 in that the tangential component is much larger than the normal component. The peaking is 2-3 times less – a result which may be explained by the inaccurate placement of the gauges.

One final observation for the pressure data is that the symmetry gauge – gauge set 5 – does not agree very well with gauge set 2 as expected. In addition, the gauge set 5 response is not as repeatable as the other sets. It is suspected that one of the gauges in this set may have been malfunctioning or that some other extraneous factor influenced the response.

The torsion results of Figs. 7.33-34 are used to compare with the external field interaction data in Table 7.4. From Fig. 7.34 it is seen that at *exactly* 0° or 90° , the tangential stress is zero. Also in the figure it is seen that a small deviation away from these precise values results in large variations in stress. Note especially the difference between 80° and 90° . This is an unfortunate state of affairs, since the majority of the gauges in the experiment were placed at 0° and 90° . This fact makes comparisons almost impossible. Not only is there a rapid radial variation near the hole for the case of torsion, but there is an additional strong angular dependence around the hole. This points out once again that the structural response is much more sensitive to structural discontinuities than the eddy current response.

Gauge set 2 is the 45° set which is expected to present the most consistent data. Similar to the pressure results, the stress is primarily tangential and shows a stress concentration of between 6 and 11. It is assumed that the source of the large variation in the predicted stress concentration

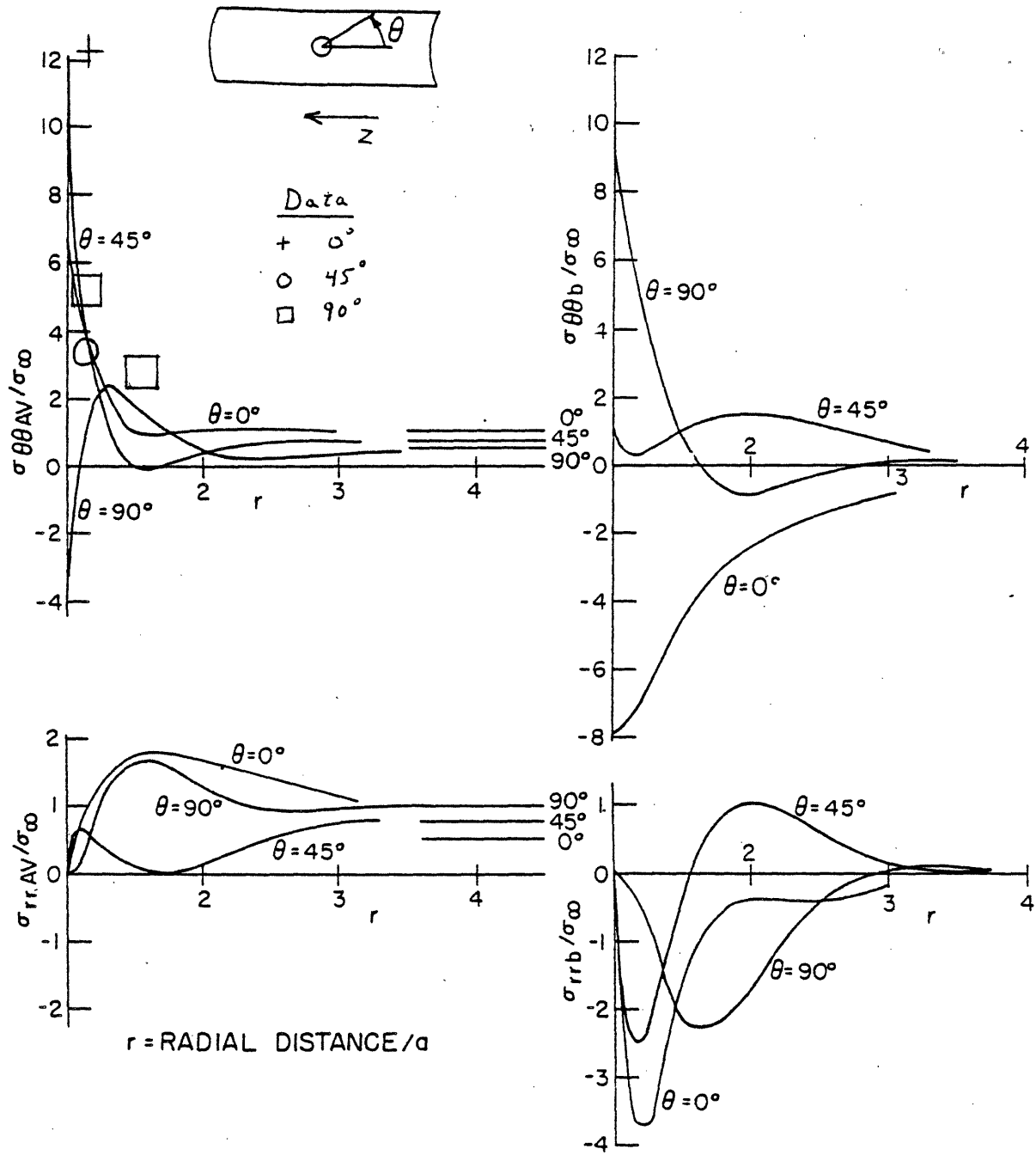


Figure 7.32 STRESSES IN THE SHELL - $\beta = 2.0$ - PRESSURE (Van Dyke)

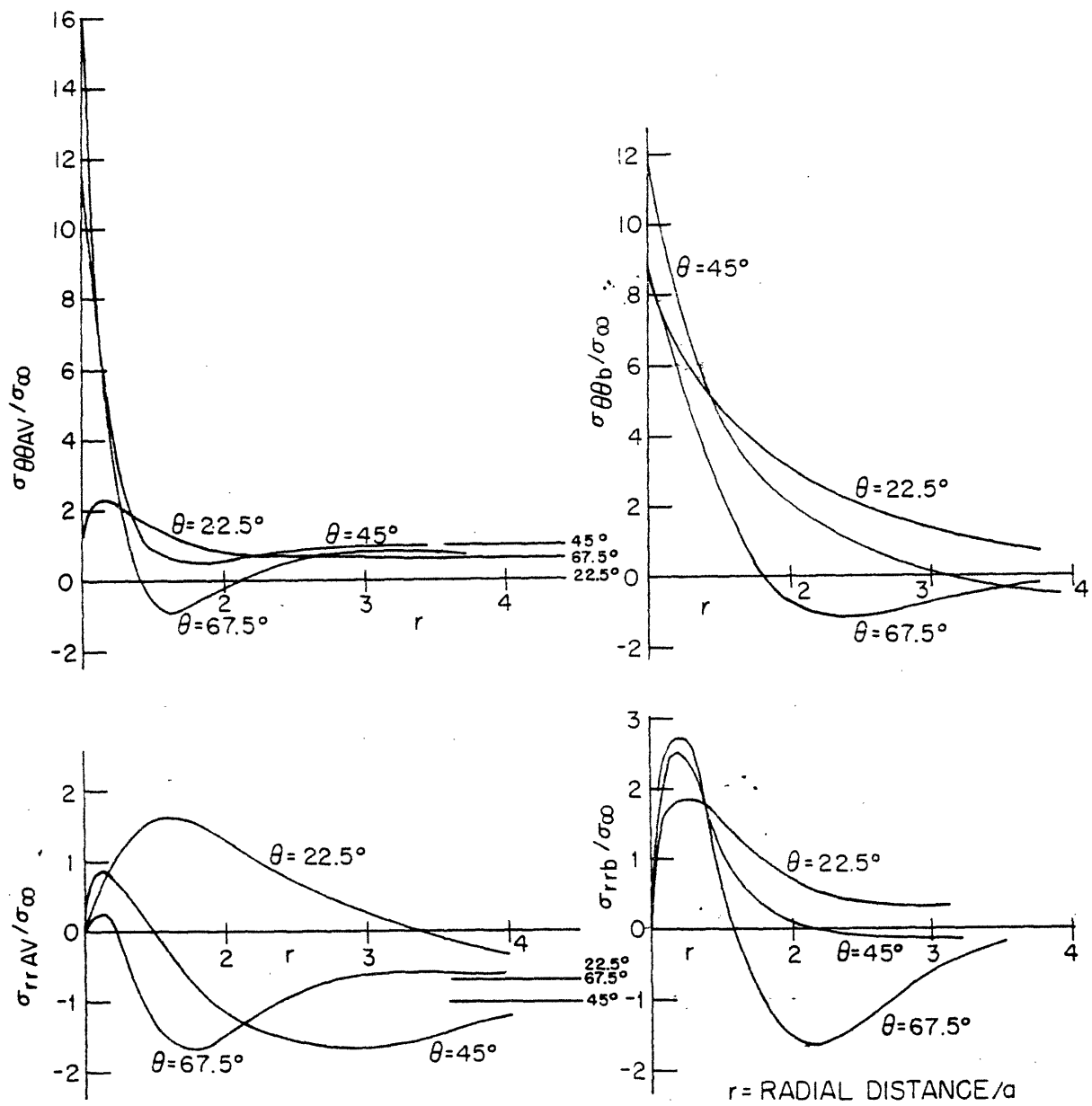


Figure 7.33 STRESSES IN THE SHELL - $\beta = 2.0$ - TORSION (Van Dyke)

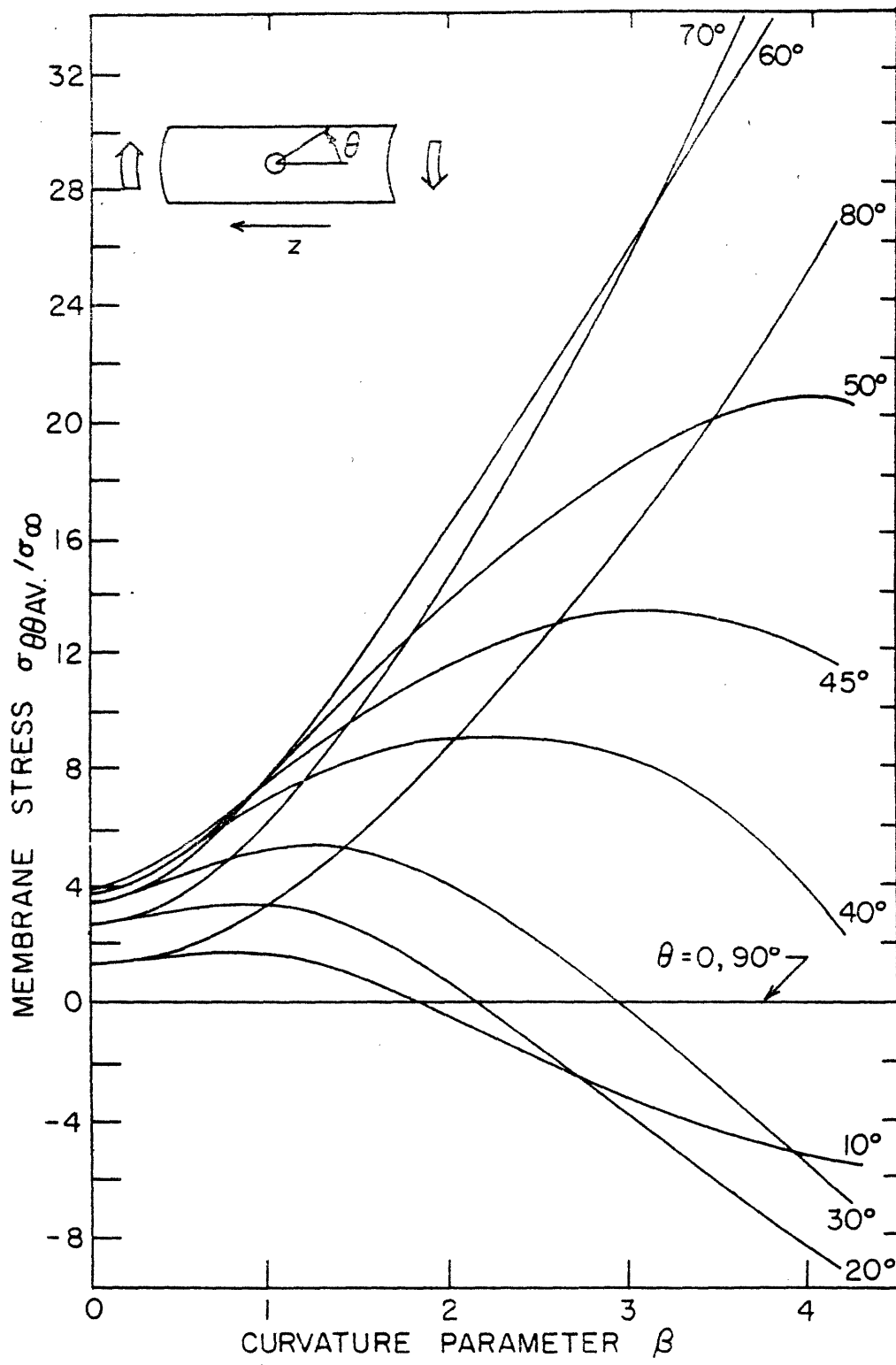


Figure 7.34 $\sigma_{\theta\theta AV} / \sigma_{\infty}$ AT THE HOLE - TORSION
(Van Dyke)

Table 7.4 Data for the Cylinder with a Hole

test1 gauge data, self interactions		
gauge no.	normal stress	tangential stress
1	0.941E+03	0.133E+05
2	0.555E+03	-0.407E+04
3	0.757E+04	0.577E+04
4	0.608E+04	0.368E+04
5	-0.188E+04	-0.157E+04
6	-0.103E+04	0.325E+03
7	0.105E+04	0.105E+04

test2 gauge data, self interactions		
gauge no.	normal stress	tangential stress
1	0.572E+03	0.121E+05
2	-0.347E+03	-0.316E+04
3	0.757E+04	0.577E+04
4	0.634E+04	0.420E+04
5	-0.155E+04	0.258E+03
6	-0.140E+04	-0.948E+03
7	0.106E+04	0.133E+04

test3 gauge data, self interactions		
gauge no.	normal stress	tangential stress
1	-0.780E+02	0.956E+04
2	0.124E+04	0.192E+04
3	0.730E+04	0.476E+04
4	0.567E+04	0.358E+04
5	0.159E+04	0.368E+04

test1f gauge data, external field interactions		
gauge no.	normal stress	tangential stress
1	0.107E+05	0.213E+05
2	-0.137E+04	-0.222E+05
3	-0.425E+04	-0.605E+04
4	-0.261E+04	-0.616E+04
5	0.195E+05	0.223E+05
6	0.384E+04	0.576E+04
7	0.243E+04	0.336E+04

test2f gauge data, external field interactions		
gauge no.	normal stress	tangential stress
1	0.169E+04	0.118E+05
2	0.446E+04	-0.149E+05
3	-0.368E+04	-0.436E+04
4	-0.854E+03	-0.570E+04
5	0.144E+05	0.169E+05
6	-0.107E+04	0.411E+04
7	-0.841E+03	0.260E+04

factors from test to test is because of the sensitivity of the stresses near the hole to small changes in the support and other test conditions.

Gauge set 5 is also at 45°. This rosette gives repeatable results which have about the same peaking factor as set 2. but shows a much larger normal component.

Referring to gauge sets 3 and 4, the tangential stress actually increases going away from the hole. At the same time, the normal stresses and the shear stress (Table 5.7) drop considerably. This may be caused entirely by a misalignment of the gauges. It is also worthwhile to point out that the test cylinder is not *exactly* centered in the external field coil. This means that the loading is not precisely symmetric. Even if it was, the experimental condition of a smoothly varying torsional pressure is not the same as the end loaded torque applied in the analytic study, so one should not expect an exact correlation between theory and experiment. In general the tendencies of the experimental data are similar to the theory, but not in any exact sense.

7.4.3. Comparison with the Continuous Shell

For the continuous shell, both the cases of self interactions and external field interactions were analyzed with FASTEDDY. An analytic solution of stresses and strains was considered highly impractical (although possible if the structural equations could be simplified and Fourier decomposed similar to the currents in Appendix C). Therefore PAFEC was relied upon for the numerical comparison with the experiment. The results with self interactions were very complex. The fields near the cylinder ends deviate from symmetry strongly. The resulting pressures are so nonsymmetric that analysis with PAFEC was not attempted. Instead, the simpler case with the axisymmetric external field is presented here. This case also had the best data experimentally due to the fact that the strains were larger. The clarity of the data and the numerical results for the external field interactions makes a simpler and more meaningful comparison possible.

7.4.3.1. Description of FASTEDDY Results

The same size mesh was used for this test case as for the test with the hole. The filaments in this case are composed of two helical filament sets which simulate a 2/1 helical current distribution in a tokamak. They are pictured in Fig. 7.35. Fig. 7.36 shows the cylindrical shell together with the filaments to give a better sense of the experimental geometry.

The resulting streamlines at 2.6 msec are drawn in Fig. 7.37. There is one subtle result in the space opposite the gaps in the filament. The currents appear to want to become axial away from the strong influence of the helical filaments. As with the hole tests, it is suspected that this is a result of the extremely strong coupling of the two shells. It may also reflect the difference in inductance between axially and circumferentially circulating flows. Fig. 7.38 shows the induced

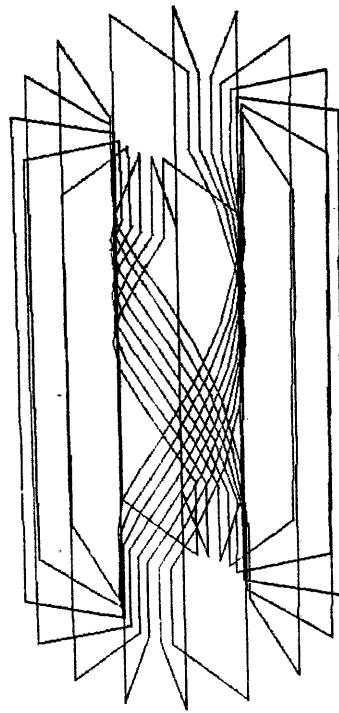


Figure 7.35 Illustration of the Helical Filaments

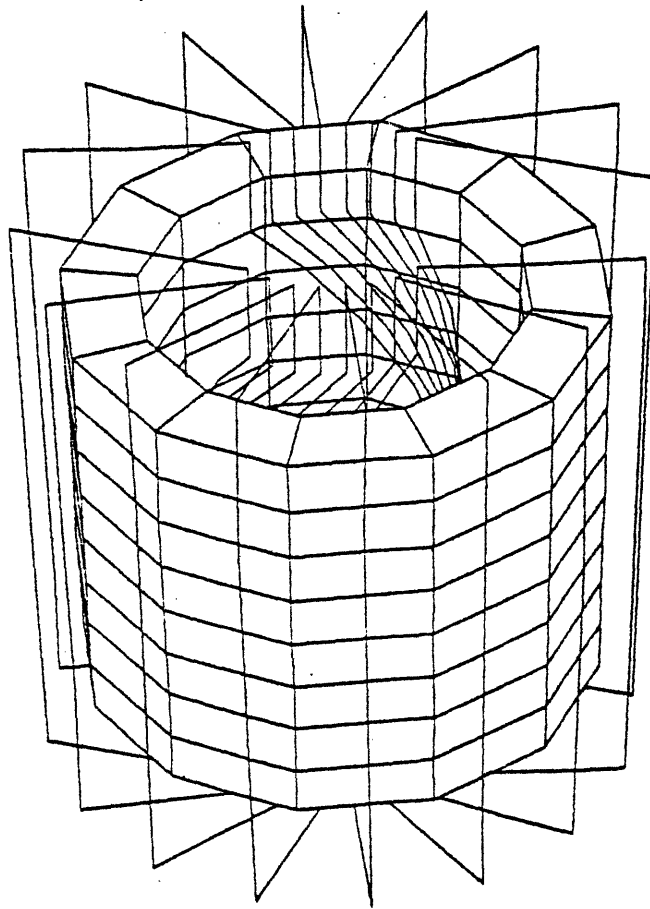


Figure 7.36 Illustration of 12x18 Continuous
Cylinder with Filaments

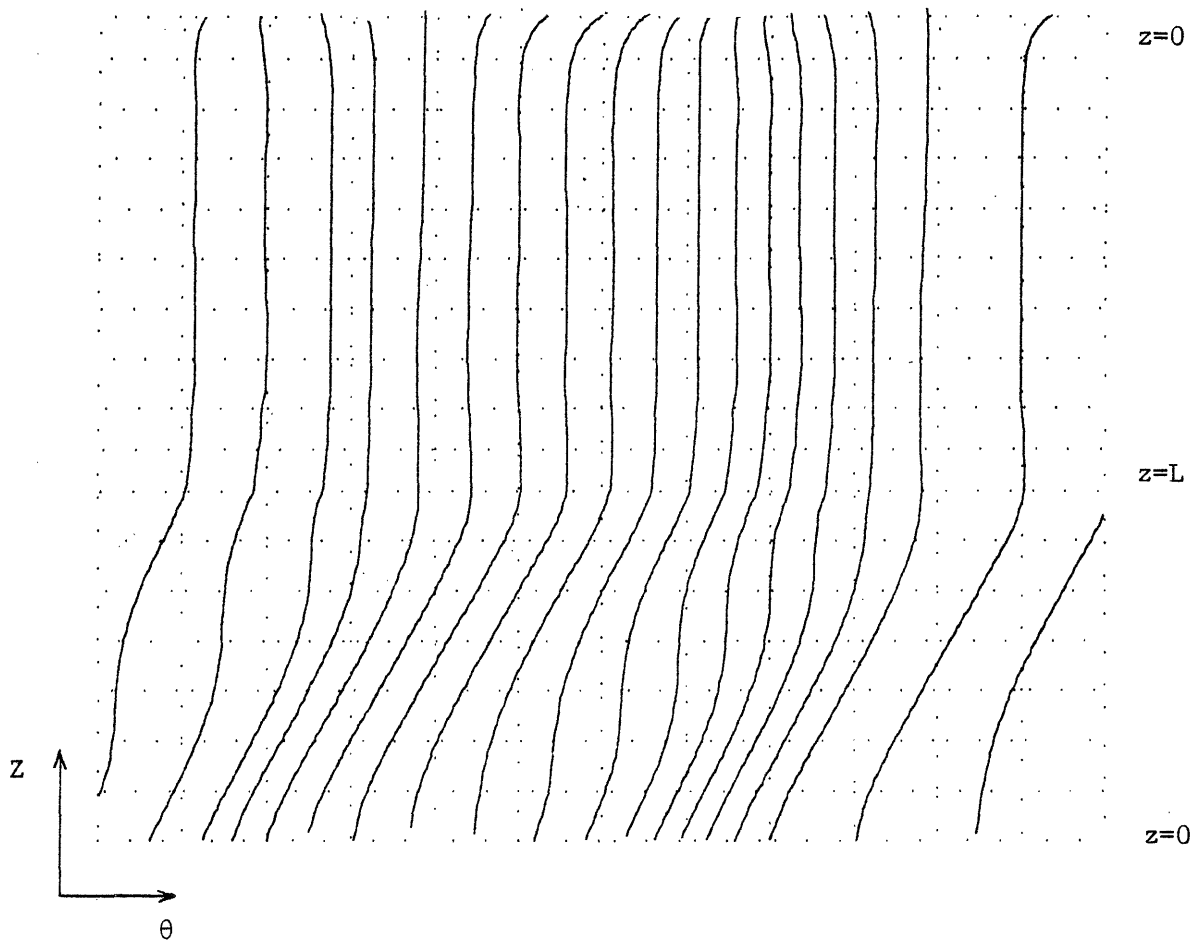


Figure 7.37 Current Streamlines for
Continuous Cylinder Test

current magnitude for this test case. Notice that the average value in the inner shell is larger than in the outer shell because of the smaller radius and also because the outer shell contains only the axial circulating component of the total current.

Figs. 7.39-7.41 show the pressures induced. An important point not borne out by the unscaled figures is that, for this example, the magnitudes of the three pressure components are approximately equal. This shows up clearly on the displacement plots shown later. The forces can be thought to consist of torsion, radial pressure, and axial compression terms which all have a constant plus a $\cos(2\theta + 2\pi z/L)$ component.

7.4.3.2. PAFEC Results and Comparison with Data

Since the mesh is now uniform, flat shell elements could be used in the structural code without much difficulty. Trouble with proper application of constant distributed loading vectors for 8-noded elements led to the use of 4-noded elements with bending and both in-plane and out-of-plane effects included.

The structural results from PAFEC are presented in two parts: the displacements and the principal stresses. Figs. 7.42-7.43 are the side view and top view of the deformed structure with the displacements exaggerated. In Fig. 7.43 the undeformed cylinder is drawn with a heavy line. In Fig. 4.42 it is clear by inspection where the undeformed shell should lie, since the narrow section at the cylinder bottom (left side of figure) is completely constrained from movement. The actual peak radial displacement is 9×10^{-7} m. From the figures it is clear that both radial and circumferential displacements are present in approximately equal proportions. The radial displacement follows the induced currents

$$p_r = p_{r0} \cos 2\theta \quad (7.17)$$

The circumferential displacements also appear to follow the currents

$$p_\theta = p_{\theta0} \cos(2\pi z/L) \quad (7.18)$$

The peak displacements are seen to occur at the thick top flange. This was an unexpected result, since the flange has a much larger stiffness than the shell. The reason for the large displacement is that bending dominates the movement rather than flexure. The bending stiffness of the thin shell is extremely small, so it is expected that the top flange supports most of the net bending force.

To obtain an order of magnitude estimate of the expected flange movement, an analytic expression was used for the displacement of a ring due to opposing point loads. The formula used is

$$\delta = 1.42 \frac{F r^3}{EI} \quad (7.19)$$

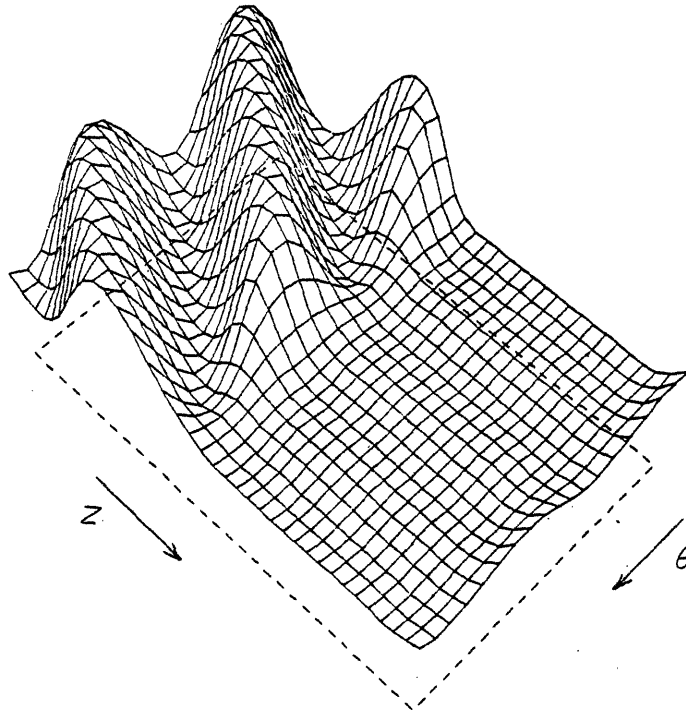


Figure 7.38 Current Magnitude for Continuous Cylinder Test

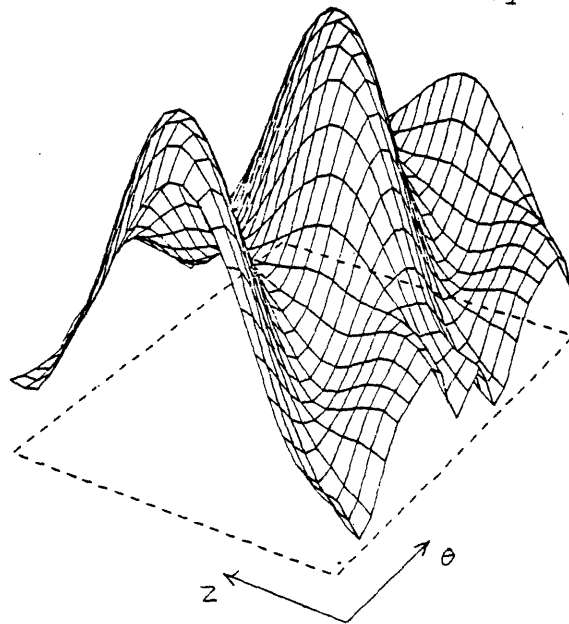


Figure 7.39 Radial Pressure - External Field Interaction

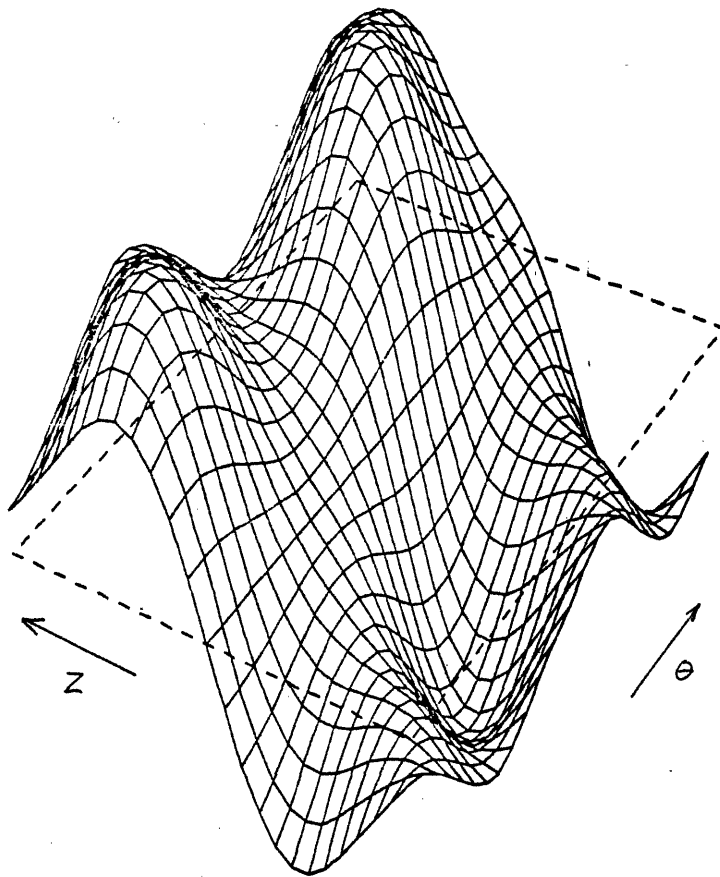


Figure 7.40 Axial Pressure - External Field Interaction

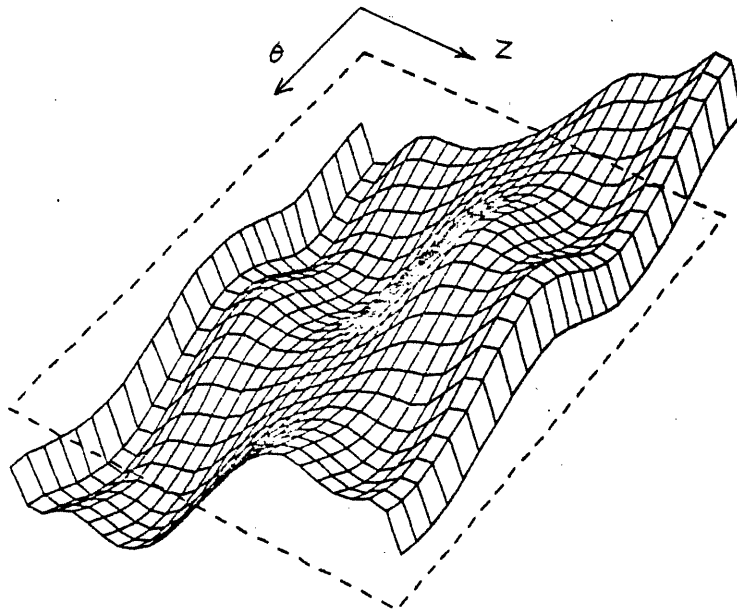


Figure 7.41 Toroidal Pressure - External Field Interaction

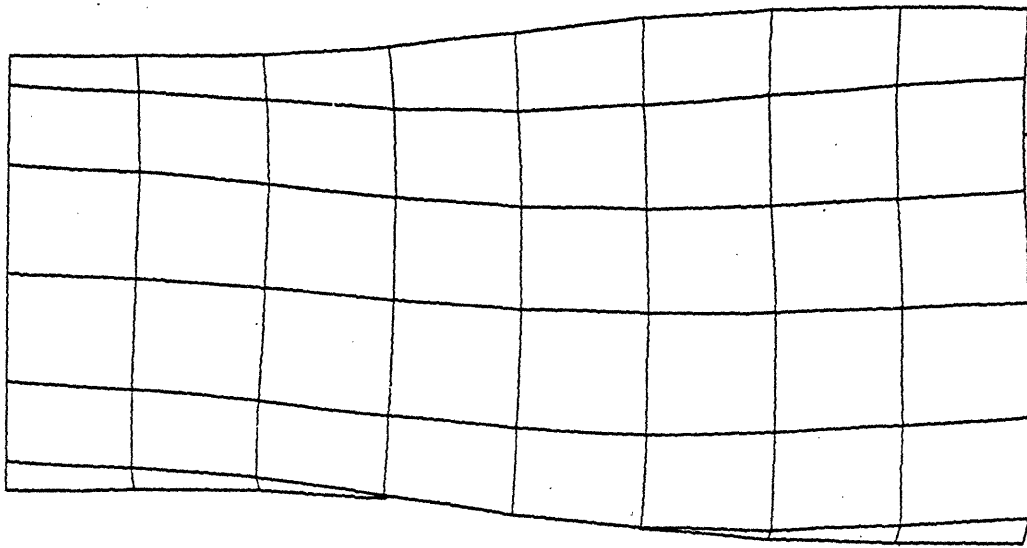


Figure 7.42 PAFEC displacements - Side View

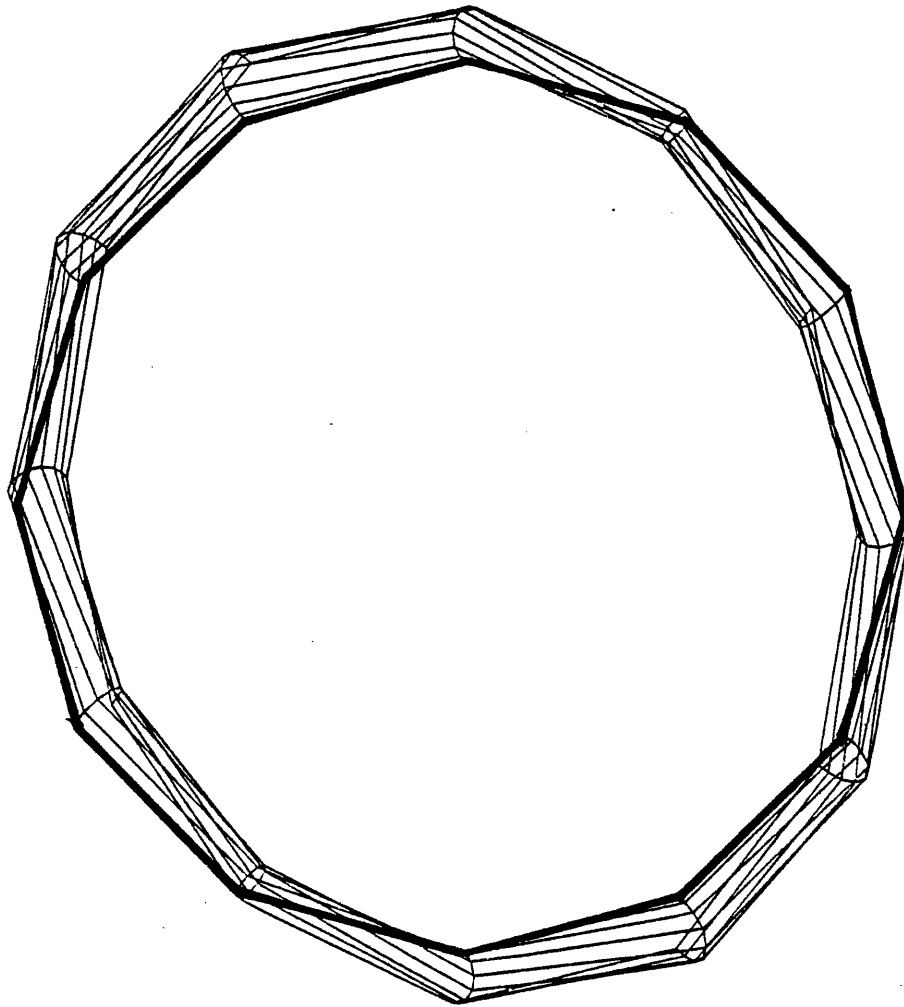


Figure 7.43 PAFEC Displacements - Top View

where δ is the displacement at the point where the force is applied, and I is the area moment of inertia of the ring. With a peak pressure of ~ 0.9 Pa on the 0.12 m^2 surface, if the total force was supported by the flange then the expected movement would be 3.5×10^{-6} . This indicates that the observed displacement quoted above is within the bounds explained by the effects of bending.

The principal stresses are obtained in PAFEC from the displacements. It is important to note that the stress function is not necessarily continuous across element boundaries ^(7.9). The finite element formulation is set up to provide for continuity of the displacements at the node points. The stress functions within an element depend upon the values of the nodal displacements in a fairly complicated way. If there is a substantial variation of the stresses across elements, then one can expect a substantial discontinuity in the stress at element interfaces.

Figs. 7.44-7.45 are to be compared with the data presented in Chapter 5. A brief glance confirms that the sinusoidal dependence on theta is correctly predicted, and in addition the magnitudes of the strains are within the expected error of the measurements. For the center gauge set, the difference between FASTEDDY/PAFEC and the data is 20-30%. For the upper gauge set there is somewhat larger variation. The estimate for a uniform current under torsion from Section 7.4.1 was 8400 Pa. Although the simple case of pure torsion cannot be used to compare directly, the numerical value is in the right ballpark.

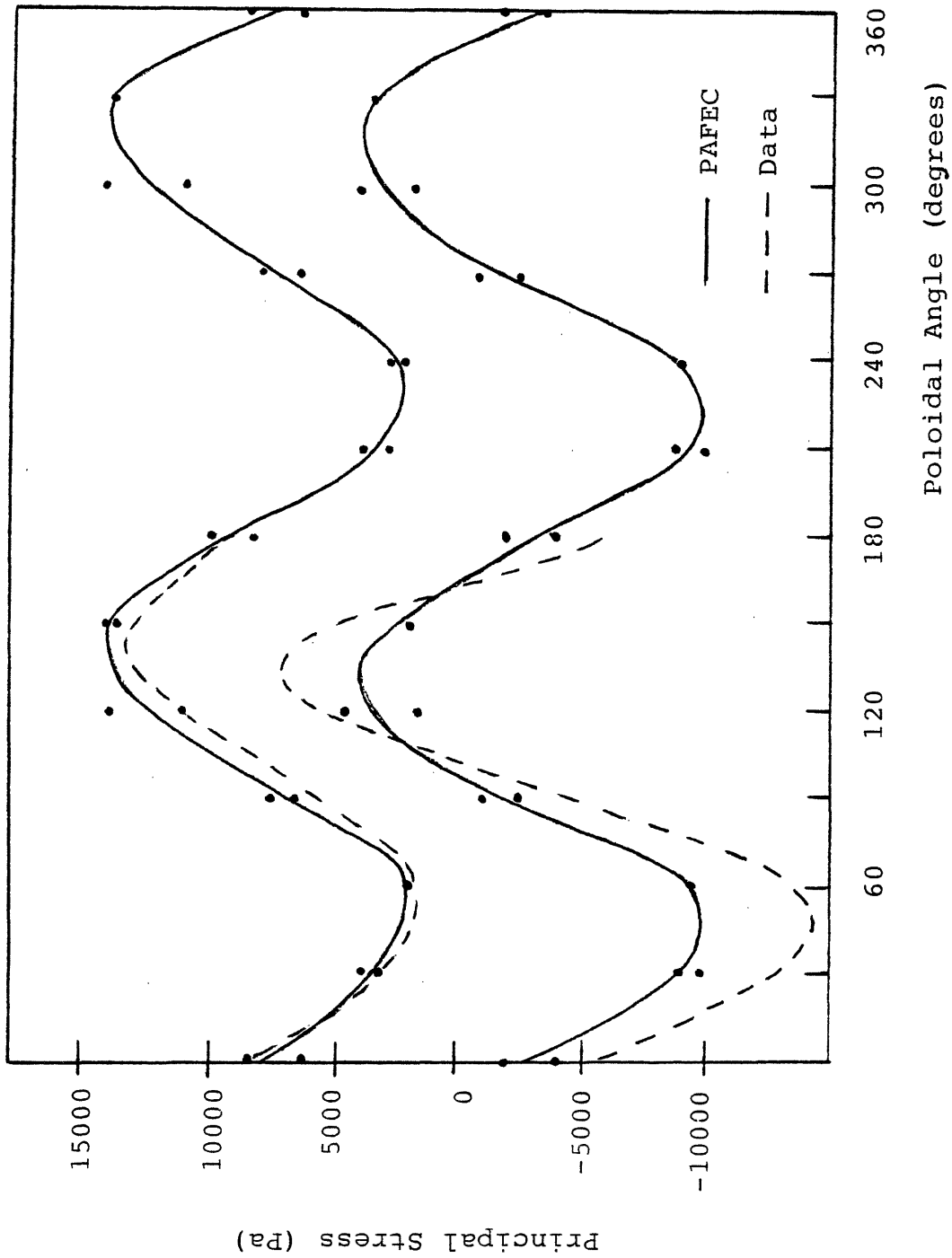


Figure 7.44 PAFEC Principal Stresses at 6 inches

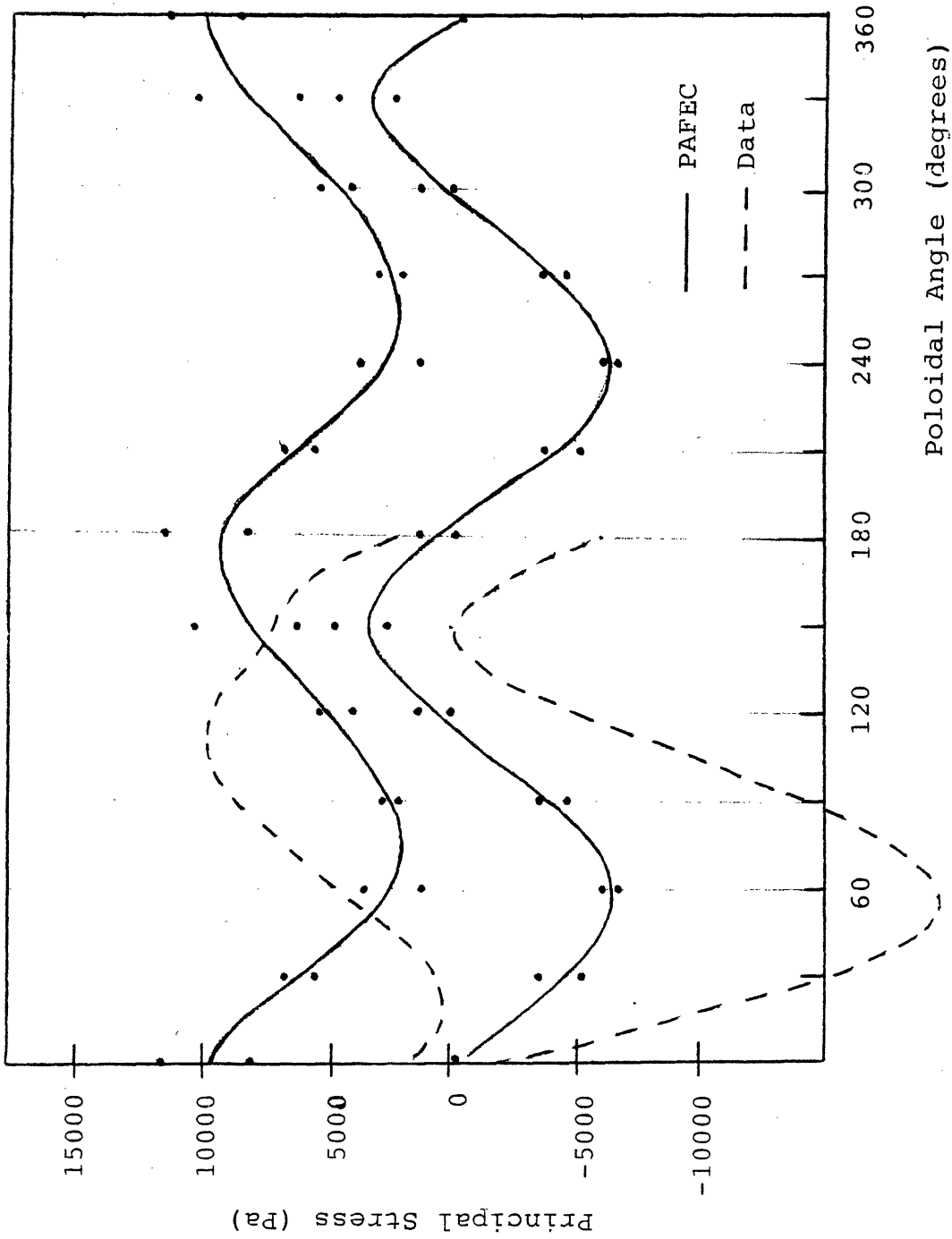


Figure 7.45 PAFEC Principal Stresses at 9 inches

References

- 7.1 C. J. Carpenter, "*Computation of Magnetic Fields and Eddy Currents*," Proceedings of the Fifth Int. Conf. on Magnet Technology, Rome, pp.147-158, 1975.
- 7.2 R. J. Lari, "Existing Eddy Current Computer Programs, List 2," 1981 Conference on the Computation of Magnetic Fields, IEEE Transactions on Magnetics, vol. MAG-18, no. 2, Chicago, March 1982.'
- 7.3 F.W. Grover, Inductance Calculation, Working Formulas and Tables, Dover Publications, Inc., New York, 1946.
- 7.4 R. J. Thome and J. M. Tarrh. MHD and Fusion Magnets: Field and Force Design Concepts, Wiley, New York, 1982.
- 7.5 R.D. Pillsbury, Jr., "NMLMAP - A Two Dimensional Finite Element Program for Transient or Static, Linear or Nonlinear Magnetic Field Problems," IEEE Transactions on Magnetics vol MAG-18, no 2, March 1982. (COMPUMAG Chicago)
- 7.6 Peter Van Dyke, "Stresses About a Circular Hole in a Cylindrical Shell," Technical Report no. 21, Harvard University Division of Engineering, Sept. 1964.
- 7.7 PAFEC Theory and Data Preparation Manuals, PAFEC Ltd., Nottingham England.
- 7.8 F. D. Baker, "Structural Analysis of the Support Rings for a Torsatron Fusion Reactor," MIT Dept. of Nuc. Eng. S.B. Thesis, 1983.
- 7.9 K. Bathe, "Numerical Methods in Finite Element Analysis," Prentice-Hall, 1976, p 102.

Conclusions

Plasma disruptions have different, sometimes severe effects on tokamak structures. These include thermal effects, first wall erosion, arcing, and electromagnetic loading. In this thesis, electromagnetic effects were singled out and examined both experimentally and numerically. Particular focus is given to effects of distributed loading in the structures including induced pressures, stresses, and strains. Local effects near discontinuities are studied and compared to uniform axisymmetric results.

A small simulation experiment was performed to explore these effects. A complete set of measurements would include currents, fields, and strains. Considering the limited resources available, this work includes measurement of the strains alone. The successful measurement of strains suggests that similar techniques may be adapted for use in tokamak experiments.

As a result of the operation of the experiments, several unexpected effects were observed to be dominant concerns. One of these is resonant behavior. Rather than being isolated peaks, for the test apparatus there are an abundance of resonances which form a continuum over some regions of frequency space. Another observation is that details in the structural response tend to have a more pronounced effect on the strains than details in the eddy current response. This is most clearly documented in the experiments with a hole where the pressures varied by less than 50%, but the stresses varied by over an order of magnitude.

In addition to the experimental measurement of strains, analytic and numerical solution techniques were examined and performed. The solution involves both induced eddy currents which result in pressure loads, and the structural response to these loads. In most practical cases an analytic solution is intractable. Nevertheless, as an approximate solution, analytic techniques can be used to illuminate the general behaviors. The work in this thesis has relied more heavily on numerical solutions. Rather than being a well established field, eddy current analysis is still in a research state of development. This resulted in the need to develop a special code for application to the connected shell structures studied. The 3-D code was used for all of the comparisons made

with the experimental results.

An axisymmetric analysis for reactor scale tokamaks indicated that for uniform loading with continuous structures, the resulting distributed stresses and strains are below the threshold for serious damage by 1-2 orders of magnitude. It is concluded that the more important cases to study involve nonuniformities in either the loading or the structures. A 3-D analysis was performed and verified with the experiments done in cylindrical geometry. The results of this work indicate that nonuniformities in the structure can easily increase the local strains by over an order of magnitude. It is noted that the largest peaking factors are likely to come from structural nonuniformities and *not* loading nonuniformities.

8.1. Experimental Results

1. The experiments have clearly shown the ability to measure strains in an electromagnetically noisy environment using synchronous detection techniques. Experiments with mechanical loading supplied by an electromagnet were able to track strains down to 10^{-9} . Experiments with electromagnetic loading were able to measure strains approaching $\sim 10^{-8}$ in the presence of strong noise fields. This was accomplished by modulating the source current and the signal detection electronics at different frequencies. The signals were then detected at the sum frequency with a lock-in amplifier.
2. The experiments have demonstrated the importance of resonant behavior and other structural effects. The resonant behavior was verified both analytically using the theory of Arnold and Warburton, and numerically using a commercial finite element structural code. In addition to resonances, other complications were observed in some cases to dominate the structural response. This includes sensitivity to the exact nature of the support, and to the existence of holes and flanges.

8.2. Numerical Results

1. A set of codes was written to study eddy current and structural response of tokamak first walls in a toroidal axisymmetric geometry. The application to a STARFIRE test case showed peak poloidal strains of 5×10^{-4} and peak bending stresses of .7MPa with a central current. A 25% outward shift caused a peak bending stress of 10 MPa and peak strain of 6×10^{-4} in the toroidal, rather than poloidal direction. Other moderate changes to the base case resulted in strains which varied by less than a factor of two.
2. A 3-D shell eddy current code was developed based on a circuit network analog method. The code was extensively benchmarked with 2-D and axisymmetric test cases, and applied

to simple example problems. It was then applied to the analysis of the experiments done as part of the thesis.

3. Using the 3-D code on the test cases with a hole, it was observed that structural irregularities cause only minor, local perturbations in the induced pressures, but larger effects result from the structural response. It is concluded that emphasis should be placed on an accurate structural solution. For the test cases with a continuous shell, the stresses were close in magnitude to the axisymmetric estimates and exhibit spatial dependence which directly reflects the spatial dependence of the source currents.

8.3. Recommendations:

1. This thesis has demonstrated the use of strain gauges in an electrically noisy environment. The next logical step is to develop similar diagnostics which could be used to instrument a real tokamak experiment such as TFTR, DCT, etc. Semiconductor strain gauges can be used for discrete measurements away from the plasma. For surfaces in contact with plasma or for measurements which require imaging a large area, optical techniques might be explored. In addition to the first wall stress, the measurements could include magnet and blanket stresses.
2. An efficient method has been developed to compute forces and structural responses due to disruptions in a simple axisymmetric geometry. There are several ways in which this method could be further applied and upgraded. Presently the code treats only circular toroidal shells. It could be extended to: (a) Compute forces on coils. (b) Treat noncircular shells, limiters, complicated driving current distributions, etc. (c) Do a 2-D treatment using 2-D basis functions. (d) Because the axisymmetric codes are so efficient, they are good candidates for initiating studies into the feedback mechanisms between the plasma currents, induced currents, and structural response.
3. An eddy current code based on an integral approach was designed specifically for application to connected shell problems. There is much room for improvements, including the addition of symmetry conditions and exploration of large, nonuniform mesh effects. There are also many potential problems which could be analyzed using the code.
4. The structural part of the problem of computing stresses has been identified as dominant in many cases, yet the amount of structural analysis done here is extremely limited. Several commercial finite element codes already exist for multi-dimensional structural analysis, such as PAFEC, NASTRAN, and SAP4. There are a number of interesting problems which remain to be explored; some of them could be fairly small and easy to run. This includes more work on toroidal structures and resonant behavior. Larger 2-dimensional shell and full 3-dimensional problems could be set up to analyze a specific reactor design.

Analytic Methods in Cylindrical Geometry

A certain amount of headway can be made with an analytic description beyond the simple central axial current problem. If the source current distribution is periodic in the axial direction (it *must* be periodic in θ) then the problem can be Fourier analyzed. If a full period is included, then each harmonic couples only to itself and can therefore be analyzed separately. This is indeed the case for the helical currents used in the EST. In addition, it is assumed that currents are contained in constant radius surfaces and that $J_r = 0$.

A.1. Scalar Potential Harmonic Expansion

There are two ways the problem can be solved by Fourier decomposition: using a scalar potential formulation or using a vector potential formulation. In toroidal coordinates Maxwell's equations are not separable and the vector potential formulation is required. In cylindrical geometry, for localized current distributions, we can write a scalar potential in regions of zero current

$$\mathbf{B} = -\nabla\Psi \quad (\text{A.1})$$

This follows from Maxwell's equation

$$\nabla \times \mathbf{B} = \mu_0 \mathbf{J} = 0 \quad (\text{A.2})$$

Including $\nabla \cdot \mathbf{B} = 0$, we obtain

$$\nabla^2 \Psi = 0 \quad (\text{A.3})$$

This equation separates into the solution

$$\Psi = \sum_n \sum_m R(r) e^{i(\beta_m z - n\theta)} \quad (\text{A.4})$$

The radial function, R , is a combination of the modified Bessel functions $I(\beta_m r)$ and $K(\beta_m r)$. The Fourier coefficients are obtained by applying the boundary conditions at the current-carrying

surfaces

$$\Psi = \text{finite}$$

$$\hat{r} \cdot (H_2 - H_1) = 0 \quad (\text{A.5})$$

$$\hat{r} \times (H_2 - H_1) = K$$

This method is particularly simple when the currents are known and the magnetic field B is required. In order to obtain induced currents from the fields, the problem must include a calculation of the areas which link the fluxes. In effect, mutual inductances are computed for each harmonic using

$$\Phi = \int B \cdot dS \quad (\text{A.6})$$

Once the induced currents are found, pressures may be formed. These are not linear in current, therefore there is mixing between the fourier components. This turns into a very complicated situation to analyze without the aid of a computer.

Example Problem

In order to demonstrate the technique, one component will be solved for a sample problem. It is important to note that the zero harmonic is a special case and must be analyzed separately.

For the experimental apparatus, the source current is given approximately by

$$\frac{K}{K_0} = \left[\frac{l\hat{z} + \pi r_1 \hat{\theta}}{(l^2 + \pi^2 r_1^2)^{1/2}} \right] \left\{ \frac{1}{2} + \frac{2}{\pi} \cos\left(\frac{2\pi z}{l} - 2\theta\right) - \frac{2}{3\pi} \cos 3\left(\frac{2\pi z}{l} - 2\theta\right) + \dots \right\} \quad (\text{A.7})$$

where $K = J\delta(r_1)$ is the surface current density and r_1 is the radius of the source current. This distribution gives the correct vector dependence and identically satisfies $\nabla \cdot K = 0$.

For the complete solution of the induced current, ultimately we must solve the equation

$$IR + L \frac{dI}{dt} + \frac{d\Phi}{dt} = 0 \quad (\text{A.8})$$

Therefore, it is necessary to compute R , L , and Φ for the first harmonic (the one with $\frac{2}{\pi}$ in front of it). R is easily obtained by inspection

$$R = \frac{\eta l}{\pi r_2 \delta} \quad (\text{A.9})$$

The inductances are obtained by integrating the fields over the associated areas. Since the associated areas are constant radius surfaces, the radial component of field is the only one needed.

The solution for B_r due to the source current is: (A.1)

$$B_r = \frac{2}{\pi} \mu_o K_o \frac{\beta r_1}{(4 + \beta^2 r_1^2)^{1/2}} \left[\frac{I'_n(\beta r_1) K'_n(\beta r_2)}{I_n(\beta r_1) K'_n(\beta r_1) - K_n(\beta r_1) I'_n(\beta r_1)} \right] \sin(\beta z - 2\theta) \quad (A.10)$$

$$\equiv A \sin(\beta z - 2\theta)$$

where $n = 1$ and $\beta = \frac{2\pi}{l}$. Similarly, the field due to the induced current, used in the self inductance calculation, is given by the same equation with r_2 substituted for r_1 .

The area to integrate for inductances can be obtained by imagining that the shell is composed of a collection of helical wires with a turns density N ,

$$N \propto \cos(\beta z - 2\theta) \quad (A.11)$$

The flux may be evaluated for one wire, and then a current weighted average is performed for the net flux. The flux for one wire is:

$$\int B \cdot dA = \int_0^l \int_{\phi+\pi z/l}^{\phi+\pi z/l+\pi/2} r_2 d\theta dz A \sin(\beta z - 2\theta) \quad (A.12)$$

where ϕ is the angle of the wire being integrated. The flux Φ is:

$$\Phi(\phi) = -Alr_2 \cos 2\phi \quad (A.13)$$

The weighted average is:

$$\Phi_{net} = \frac{\int_{-\pi/4}^{\pi/4} \Phi(\phi) \cos 2\phi d\phi}{\int_{-\pi/4}^{\pi/4} \cos 2\phi d\phi} \quad (A.14)$$

$$= -\frac{\pi}{4} \frac{Alr_2}{2}$$

Inductances are simply flux per unit current.

This procedure can be followed to obtain any number of harmonics of the induced currents. Then, as stated above, the pressures are computed by multiplying together currents and fields. The result must include spatial mixing terms. Then in order to solve the structural equations, these pressures are entered as inputs. It is possible to solve the membrane equations for a cylinder by direct integration of the pressures. This procedure is not presented here; the derivation may be found in various texts, including Timoshenko.^(A.2) For a full bending theory solution, it is probably most wise to use a finite element numerical solution.

A.2. Green's Function and Vector Methods

An alternative to the scalar potential formulation avoids the computation of mutual inductances and the solution of the circuit differential equations by solving directly for the current density. The

derivation given here is a bit unusual. It is more customary to solve for the vector potential using

$$\nabla^2 A = -\mu_0 J \quad (\text{A.15})$$

The nonseparability of the equations results in the need to transform to Cartesian coordinates.

Due to the simple current densities assumed for our problem, we can avoid some of the problems with the vector potential formulation by solving instead the two fundamental equations:

$$E = \eta J = -\frac{dA}{dt} \quad (\text{A.16})$$

$$A(x) = \frac{\mu_0}{4\pi} \int \frac{J(x') dx'}{|x - x'|} \quad (\text{A.17})$$

The usage of primes denotes source points, no prime indicates a field point. Combining these, we get

$$J(x) = -\frac{\sigma\mu_0}{4\pi} \frac{\partial}{\partial t} \left[\int \frac{J(x') dx'}{|x - x'|} + \int \frac{J_0(x') dx'}{|x - x'|} \right] \quad (\text{A.18})$$

where the source current is from the start separated out as a known function. The unknown to be solved for is J . The method is to write both J and $\frac{1}{|x-x'|}$ in cylindrical harmonics, leaving a simple ordinary differential equation for each harmonic. This is entirely analogous to the solution of the scalar potential.

First we express the source current as

$$|J_0(x)| = \sum_m \sum_n C_{mn}^0 e^{i(n\theta + \beta_m z)} \delta(r - r_0) \quad (\text{A.19})$$

and assume for the form of J a helically symmetric solution which solves the differential equation

$$|J(x)| = \sum_m \sum_n \left[A_{mn} e^{i(n\theta + \beta_m z)} I_n(\beta_m r) + B_{mn} e^{i(n\theta + \beta_m z)} K_n(\beta_m r) \right] \quad (\text{A.20})$$

The solution could proceed from here with an arbitrary radial dependence, but the fact that J appears only at discrete radial surfaces will simplify the integrals considerably. We will use

$$|J(x)| = \sum_m \sum_n C_{mn} e^{i(n\theta + \beta_m z)} \delta(r - r_1) \quad (\text{A.21})$$

If currents appear at several surfaces, then the term $C_{mn} \delta(r - r_1)$ will be replaced with a sum $\sum_k C_{mnk} \delta(r - r_k)$. For this solution we take only one surface current.

The vector nature of the problem has been omitted for simplicity. It is a constant inside the integrals and can be inferred from the exponential term by setting

$$\beta_m + n\theta = \text{constant} \quad (\text{A.22})$$

$$J = |J| \left(\frac{(r_k/n)\hat{\theta} - (1/\beta_m)\hat{z}}{r_k^2/n^2 + 1/\beta_m^2} \right) \quad (\text{A.23})$$

Substitution of J this into this expression readily yields $\nabla \cdot J = 0$ as expected.

The Green's function is expressed in the usual fashion as an expansion in the harmonic functions which are known solutions to the separated equations. In cylindrical geometry this results in: (A.3)

$$\frac{1}{|\mathbf{x} - \mathbf{x}'|} = \frac{1}{\pi} \sum_m \sum_n e^{in(\theta - \theta')} e^{i\beta_m(z - z')} I_n(\beta_m r_<) K_n(\beta_m r_>) \quad (\text{A.24})$$

The solution then proceeds by combining the Green's function with the assumed forms for the currents. One Fourier term is selected with the sums being implicit.

$$C_{mn} \delta(r - r_1) e^{i(n\theta + \beta_m z)} = -\frac{\sigma \mu_0 \partial}{4\pi^2 \partial t} \left(\int r' dr' d\theta' dz' (C_{mn} \delta(r - r_1) + C_{mn}^o \delta(r - r_o)) \right. \\ \left. \cdot e^{i(n\theta' + \beta_m z')} \sum_p \sum_q e^{iq(\theta - \theta')} e^{i\beta_p(z - z')} I_q(\beta_p r_<) K_q(\beta_p r_>) \right) \quad (\text{A.25})$$

where

$$r_< = \text{smaller of } (r, r') \\ r_> = \text{larger of } (r, r')$$

With the help of the delta functions, all of the integrals can be performed, leaving

$$C_{mn} \delta(r - r_1) = \frac{4\pi n}{\beta_m} [r_o C_{mn}^o I_n(\beta_m r_o) K_n(\beta_m r_o) + r_1 C_{mn} I_n(\beta_m r_1) K_n(\beta_m r_1)] \quad (\text{A.26})$$

The surface conductivity is defined by

$$\sigma(r) = \zeta \delta(r - r_1) \quad (\text{A.27})$$

which leaves us finally with a single ordinary differential equation for C_{mn}

$$C_{mn} = -\frac{\zeta \mu_0 n}{\beta_m} \frac{\partial}{\partial t} \{r_1 C_{mn} I_n(\beta_m r_1) K_n(\beta_m r_1) + r_o C_{mn}^o I_n(\beta_m r_o) K_n(\beta_m r_o)\} \quad (\text{A.28})$$

The solution is easily obtained for a sinusoidal source current. In order to obtain the pressures induced, the fields must be obtained from the two surface currents. The solution in terms of the scalar potential is obviously much simpler in cylindrical geometry. The advantage of the Green's function solution is that it can be extended to toroidal geometry, where the expansion becomes: (A.4-A.5)

$$\frac{1}{|\mathbf{x} - \mathbf{x}'|} = \frac{1}{a\pi} [(\cosh \eta - \cos \theta)]^{1/2} \\ \cdot \sum_n \sum_m \epsilon_m \epsilon_n (-1)^m \cos(m(\phi - \phi')) \cos(n(\theta - \theta')) P_{n-1/2}^{-m}(\cosh \eta') Q_{n-1/2}^m(\cosh \eta) \quad (\text{A.29})$$

where

$$\epsilon_k = 1, k = 0 \\ \epsilon_k = 2, k \neq 0$$

References:

- A.1 S. D. Umans et al., "Three Dimensional Transient Analysis of Superconducting Generators," Electric Power Systems Engineering Laboratory, MIT.
- A.2 S. Timoshenko and S. Woinowsky-Krieger. Theory of Plates and Shells, Mc-Graw-Hill, New York, 1959.
- A.3 J. D. Jackson. Classical Electrodynamics, John Wiley and Sons, New York, 1975.
- A.4 A. A. Mirin et al., "An Analytic Representation of Fields Resulting from Currents on a Torus," UCRL-52069, May 1976.
- A.5 Dilip Bhadra, "Field due to Current in Toroidal Geometry," Review of Scientific Instruments, vol. 39, no. 10, Oct. 1968.

Description of FASTEDDY

This appendix describes the procedures carried out by FASTEDDY. Since the code is still in a developmental phase, actual code usage is deemphasized. The description concentrates on methods of solution, explanations for the choice of the various techniques and parameters, and helpful hints on avoiding trouble with the codes. It is not intended that this guide will sufficiently explain the codes without reference to the source files.

Execution of FASTEDDY occurs in separate phases which are linked through their input/output files. This description is similarly organized. There are three main solution steps and a post-processor routine for data analysis. They are:

1. FASTMESH for mesh generation
2. FASTCOFF for computation of the input matrices and matrix inversion
3. FASTTIME for time integration through the problem
4. FASTPLOT to convert line currents to current densities and plot streamlines

The main output files are given in Table B.1. These are the files which are required by succeeding phases. In addition, each phase may create other output files which are principally diagnostic.

B.1. Overview

As discussed in Chapter 6, FASTEDDY is modeled after EDDYNET ^(B.1) which uses an electric circuit analog. The continuous structure is reduced to a set of lines connected in such a way as to form quadrilateral loops. By setting up loop voltage equations, a tremendous savings is made on the number of unknowns, since all of Kirchoff's node current equations are implicitly satisfied. This is seen dramatically by comparison to a line formulation of the same problem. When a line formulation is used, there are voltage equations associated with each line segment and unknown electric scalar potentials associated with the nodes. The potentials are important to transmit the effects of the boundaries throughout the structure. One of the values of scalar potential is arbitrary,

Table B.1 Summary of Data File Contents

<u>name</u>	<u>generating phase</u>	<u>contents</u>
file21	1	mesh generation results, x,y,z,rho
file22	2	centroids, areas, and resistances
file23	2	inverted matrix $(M + R\Delta t)^{-1} = G_{inv}$
file24	3	line currents for subsequent fitting and powers
file25	4	current densities at the centroids

Figure B.1 Example Mesh

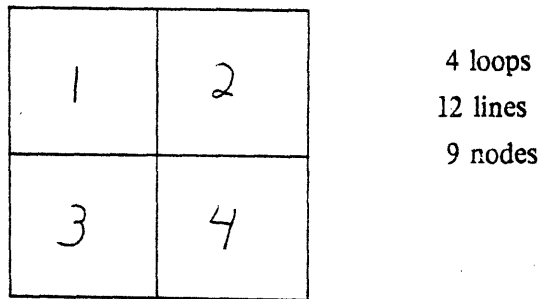


Table B.2 Mesh Sizing Parameters

icoord=	1	2	3	4
x1	xmin	xmin	Rin	a0
x2	xmax	xmax	Rout	R0
y1	ymin	ymin	zmin	unused
y2	ymax	ymax	zmax	unused

but this is consistent with the fact that the number of independent node equations is one less than the number of nodes.

As an illustrative example of these statements, consider the 4x4 mesh of figure B.1. There is a minimum of 4 equations which must be solved, since there are 4 unknown imposed fluxes. In the loop formulation each equation sums the voltage drops around one of the loops. In the line formulation there are 12 unknown line currents and 8 unknown node potentials. 12 line voltage equations are used together with 8 node current equations. Since the size of the problem scales as the square of the number of equations, there is an extreme incentive to keep the loop formulation, even at the expense of some added complexity in the description of the problem.

The solution begins by modeling the shell with these loops. FASTMESH does this in addition to allowing an efficient method for relaxing the nodes around discontinuities.

The second step is to compute the resistances and inductances for the loops to be used in solving the problem. The algorithm also requires inversion of the mutual inductance matrix. These tasks are accomplished in FASTCOFF.

The time dependent solution is generated in the third step, FASTTIME. It consists primarily of a loop which computes dI/dt by doing a matrix multiplication and then advancing the current vector. The output is expressed both as loop currents and line currents, where the line currents are simply summed from the loops which are neighbors to the line.

For presentation of the results, the final step is FASTPLOT. It computes current densities at the centroids, pressure loading, and plots various quantities such as current streamlines.

B.2. FASTMESH

FASTMESH sets up the mesh for FASTEDDY. This includes definition of the logical coordinates (numbering of loops), the real coordinates (x,y,z Cartesian coordinates), and the resistivities and other electrical properties. It also includes a rather lengthy section which does a mesh relaxation. The mesh relaxation allows discontinuities in the structure to be meshed in a semi-automatic fashion. Its principal usefulness is in computing the node positions near discontinuities in such a way that the average size of a loop is relatively constant within a relaxation region. Since most problems require fairly coarse meshes, it is important to efficiently use all of the loops included in the problem. If large and small loops are interspersed, then the accuracy is limited by the larger loops.

The method used for mesh relaxation is to iteratively locate each node at the centroid of the quadrilateral defined by the node's four neighbors. This results in a solution which minimizes

the total length of the lines connecting the nodes, and therefore also the stretching energy if the structure is assumed to be a uniform elastic material under deformation.

The quadrilateral loops of the mesh are connected in one of 4 coordinate system types. They are:

icoord=1	2-D plane
icoord=2	curved, simply connected shell with specified $z(x,y)$
icoord=3	toroidal with 2 cylindrical shells composing the torus (for use with the experiment)
icoord=4	toroidal with relaxation in theta and phi

There are really only two general types of shell — either simply connected or multiply connected, such as the topological torus. At this time, the two options have been separated into two different codes which treat specifically one type of geometry.

The logical mesh is continuous in two directions. This means that on the surface each loop is connected to the loops which are numbered one less and one more than itself. The last node may reconnect to the first one in connected coordinate systems. This is explicitly assumed in the code. The logical continuity is a significant feature. It severely limits the flexibility of the code in treating unusual problems, but makes the treatment of the standard toroidal shell problem much simpler.

The FASTMESH phase has 6 parts:

- 1) read the input data
- 2) relax the regions
- 3) plot the relaxed logical mesh
- 4) assign real coordinates
- 5) plot the relaxed real mesh with hidden lines
- 6) write output

B.2.1. Mesh Relaxation

Mesh relaxation takes place depending upon certain flags given. The region flag (irel) determines whether or not a particular region should be relaxed. The node flags determine how a particular node should be constrained. Note, if iprop= 0 is used, the region is assumed to already have properties defined and is used only for relaxation.

krel= 1	fixed in x-direction
krel= 0	float in x-direction
krel= -1	float in x-direction with k-neighbors only
lrel= 1	fixed in y-direction
lrel= 0	float in y-direction
lrel= -1	float in y-direction with l-neighbors only
irel= 1	relax, but region edges only float with nodes inside the region
irel= 0	no relaxation of this region
irel= -1	allow edges of region to float with outside nodes

The user should be aware of the following: when defining regions, the region boundaries can be used for both resistivity definition and relaxation information. The resistivity data is loop data - this means that the data extends from the node point outwards in both k and l to the next node points. The relaxation data refers directly to the point in question.

In the different coordinate systems it is assumed that the user is interested in different conditions on the relaxation. User intervention is required to override these.

icoord=1 or 2

For unconnected meshes, the relaxation is restricted to stay on the edges at the edge nodes. The x,y space is initially chopped into equal size regions in a quadrilateral space defined by the inputs x1,x2,y1,y2 (see Table B.2).

icoord=3

For the 2-shell torus, the two shells are fixed in z at the top and bottom edge of each shell ($l = 1, l = nl/2, l = nl/2 + 1, l = nl$). The two shells are separated by a single loop at the top and bottom, since the region of interest for the experiment we are modeling is away from these edges. At the edges the angle coordinate is free to relax. The points (1,1) and (1, nl) are fixed in θ (ie, k). Relaxation takes place across the boundary $\theta = 2\pi$. Extra nodes (as with icoord= 4) are defined at the end of the logical mesh, $k=nk+1$ which wrap around from $\theta = 0$ to $\theta = \pi$. These nodes are located in real space at exactly the same points as the $k= 1$ nodes.

icoord= 4

For the torus, the relaxation default is to fix the node $k=1, l=1$ only. Because of the connectedness of the structure this is sufficient for stability. $k=nk$ is connected to $k=1$ and $l=nl$ is connected to $l=1$. Coordinates are evenly spaced in θ and ϕ and are defined at $nl+1$ and $nk+1$ for plotting and for use in later solution steps (their value is 2π greater than $l=1$ and $k=1$).

B.2.2. Sample Input Deck

The mesh generator was written with an effort to make data entry very easy. At the same time, it was desirable to maintain compatibility with the local VAX 11/780 and the MFE Cray machines. The need to conform to the restrictions of multiple machine usage contradicts the desire for simplicity.

Following is a sample input deck, where precise location within format fields is important. The data is organized in modules which are identified by the keywords MESH, PROP, REGI, and NODE. The order of the modules is arbitrary. Comments can be included before any module, but not between data records in the same module. The first deck gives the variable names which can be found in Table B.3; the second deck gives actual sample values.

mesh

icoord	nk	n1	nsym	dt	w
x1	x2	y1	y2		

properties

nprop

i	eta	h	irel
j	eta	h	irel

nodes

nnode

i1	j1	xk	y1	krel	lrel
i2	j2	xk	y1	krel	lrel
i3	j3	xk	y1	krel	lrel

regions

nregi

i	iprop	k1	k2	11	12
j	iprop	k1	k2	11	12

stop

this is an actual file used to generate a symmetric torus

there is only one region

regions

1

1 1 1 6 1 4

all nodes are automatically generated

nodes

0

properties

1

1 1.67e-08 .001 0

mesh	nzfct	nk	nl	dt	w	epsilon	
4	2	6	4 99	3	.0001	.001	1.0e-05
	1.0	3.0	0.	7.			

stop

Table B.3 Description of Variables used in FASTMESH

nk	number of nodes in the logical k direction
nl	number of nodes in the logical l direction
icoord	coordinate system identifier
eta(i)	resistivity of property set i
h(i)	thickness of property set i
irel(i)	mesh relaxation flag for property set i, 0=no relaxation
irxmax	maximum iterations for mesh relaxation, normally 20
istab	relaxation stability parameter; normally 3
eps	termination criterion for mesh convergence; normally .001
nsym	type of symmetry of problem (see FASTCOFF description)
nzfct	function identifier for surface and driving function definition
dt	default time step in phase 4
w	thickness of shell for resistance calculations
x1	mesh sizing parameters...
x2	real coordinates in specified coordinate system:
y1	bounds of the internally generated mesh
y2	(toroidal c.s. has a0 in xkmin and r0 in xkmax)
xk(i,j)	logical k coordinate of node ij
yl(i,j)	logical l coordinate of node ij
krel(i,j)	type of k-freedom in mesh relaxation
lrel(i,j)	type of l-freedom in mesh relaxation
iprop(i)	property set used for region i
k1(i)	
k2(i)	logical coordinates used to specify bounds
l1(i)	of the region to be relaxed
l2(i)	
diffx	used to test convergence of mesh relaxation using
diffy	dsx and dsy

B.3. FASTCOFF

B.3.1. Evaluating the Inductance Matrix and its Inverse

FASTCOFF sets up arrays for solution of the matrix circuit equation in 2 dimensions. The basic equation to be solved is,

$$RI + M \frac{dI}{dt} + \frac{d\Phi}{dt} = 0 \quad (B.1)$$

where I is the loop current vector and M is the mutual inductance matrix. Since loop currents share resistive elements, the resistance is also a matrix. However, the mutual resistance matrix is very sparse, so instead of storing it as a full matrix, the individual elements are computed when needed. The result is that there is only one large matrix in the entire problem for any given phase. When the matrix is inverted, a space saving solution is used and the inverse is returned in place. This allows for the largest possible problem to be solved without excessive paging of the executable out of core.

Backward differencing of eqn. B.1 results in the time advancing formula:

$$\Delta I = -(M + R\Delta t)^{-1}(\Delta\Phi + R\Delta t I) \quad (B.2)$$

The corresponding forward differencing formula would be:

$$\Delta I = -M^{-1}(\Delta\Phi + R\Delta t I) \quad (B.3)$$

Back differencing is more stable, but it requires a constant time step in the time integration step, since Δt is contained in the inverted matrix. In problems with large resistivity variations on the surface, numerical stability becomes the dominant problem and a fixed time step is tolerated. The primary task of FASTCOFF is then to form and invert the matrix

$$G \equiv (M + R\Delta t) \quad (B.4)$$

In order to increase the accuracy and the size of the time step, 4th order Runge-Kutta is employed using the backward differencing form of the derivative. This is described in more detail in the following section.

The vector potential formulation is used to compute mutual inductances. Loop fluxes are computed by integrating

$$\Phi = \int A \cdot dl \quad (B.5)$$

around the loop.

Table B.4 Flux Through Special Loops Due to Special Loops:

$g(1, 1)$	self inductance of $k = 1$ loop
$g(imax, imax)$	self inductance of $l = 1$ loop
$g(1, imax)$	mutual flux through $k = 1$ loop due to $l = 1$ loop
$g(imax, 1)$	mutual flux through $l = 1$ loop due to $k = 1$ loop

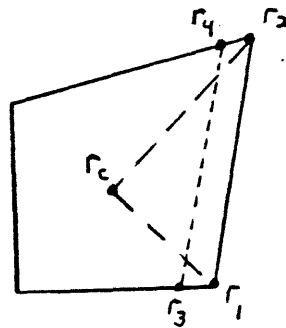


Figure B.2 Stick Self-Inductance Model

The vector potential formulation gives greatly increased accuracy as compared to the old technique of evaluating B at the loop centroid and multiplying by the loop area, as is done in EDDYNET. For multiply-connected coordinate systems this was found to be especially important. On the average, the loops are closer together in connected systems and their orientations tend to be less flat. This can result in significant (as much as 50%) differences between the two forms.

The expressions for A and B are obtained by integrating exactly

$$A = \frac{\mu_0}{4\pi} \int \frac{Idl}{r} \quad B = \frac{\mu_0}{4\pi} \int \frac{Idl \times r}{r^3} \quad (B.6)$$

The result is then written in terms of relative vectors from the observation point to the wire. If b is the displacement vector from the observation point to the start of the wire, and c is the corresponding vector to the end of the wire, we can define $a = c - b$ in the direction of the current. Then

$$A = \frac{\mu_0 I}{4\pi} \log \left(\frac{a \cdot c + |a||c|}{a \cdot b + |a||b|} \right) \frac{a}{|a|} \quad (B.7)$$

and

$$B = \frac{\mu_0 I}{4\pi} a \cdot \left(\frac{c}{|c|} - \frac{b}{|b|} \right) \frac{c \times a}{|c \times a|^2} \quad (B.8)$$

The evaluation of $\int A \cdot dl$ is done with a variable node quadrature formula ^(B.2). Three point quadrature is attempted first. If the required accuracy is not achieved, then more points are interlaced between those already evaluated, up to a maximum of 255 points.

The matrix inversion is performed using a standard IMSL routine, LINV3F. The inverter is modular and certain users may wish to optimize by using a different one. LINV3F is the reduced storage mode full inverter. The matrix is symmetric, but this feature is not exploited. The level of symmetry in the result then allows a measure of the accuracy.

B.3.2. Treatment of Special Loops

In connected systems there are two added loops covering the "holes", and one normal loop is eliminated because the structure is a closed surface. If a loop is not eliminated, then the system is overdetermined due to the applicability of Gauss' Law, $\sum \Phi = 0$. This results in a total of $n_k \times n_l + 1 = i_{max}$ loops. The special loops are not in general quadrilaterals, so the coding associated with them is kept separate. As shown in Table B.4, the first loop is replaced by the poloidally circulating loop and the toroidally circulating loop is placed in the last position, i_{max} .

B.3.3. Description of Selected Subroutines

There are several key subroutines used by FASTCOFF. These are reviewed very briefly below.

Subroutine LOOPS and functions DRES, AREAX, AREAY, and AREAZ compute the areas, centroids, and resistances of all of the loops and lines. Special circulating loops are not computed since the lines are already defined by existing loops. If icoord= 3 or 4, then the nk and nl elements are important.

Function BDOTDA(k1,11,k2,12,k3,13) finds flux through loop (k3,13) due to line from (k1,11) to (k2,12) with unit current. The field is approximated to be uniform through the loop and is evaluated at the centroid. This formulation is no longer utilized.

Functions ADOTDL(k1,11,k2,12,k3,13,k4,14) and STICK take the place of BDOTDA. The result is flux per unit current. ADOTDL is the contribution due to the line segment (k1,11) to (k2,12) for the piece of the special loop (k3,14) to (k4,14). It must be called once for each line of the special loop. The 16 pieces are added up in AINTDL(k1,11,k2,12) which relates any two loops. Variable order quadrature is used with the accuracy as input. If low order estimates do not converge, then more points are interlaced with the existing ones to save on computation (subroutine QUAD). There is no problem with lines which touch at their ends, but the result is singular when the same line is used as source and field. There is a special case section of code which accounts for this by assigning new field coordinates away from the line by a fraction of the height of a triangle formed from the line end points and the centroid of the quadrilateral loop associated with the line (see Fig. B.2). The exact placement of the source line is not critical for the accuracy of the solution. The value $e^{-1.5}$ is used for this fraction. This is the geometric mean distance for a flat current sheet. (see Grover, Ref. B.3)

The equations used to find the new field line segment defined by (r_3, r_4) given the old line segment (r_1, r_2) and the centroid r_c are as follows:

$$r_4 - r_3 = r_2 - r_1 \quad (B.9)$$

$$\frac{r_4 + r_3}{2} \equiv r_p = \alpha r_c + (1 - \alpha) \frac{r_2 + r_1}{2} \quad (B.10)$$

The first equation guarantees that the two line segments are parallel and equal in length. The second defines a point at the center of the new line segment which is a fraction α of the distance from the old line segment to the centroid of the quadrilateral associated with the line segment. The value of α is $e^{-1.5}$.

B.4. FASTTIME

FASTTIME is the final step in the solution. It advances the problem with a simple time integration algorithm. Various algorithms were tried, including fixed time step backward differencing and 4th order Runge-Kutta. The current method of choice combines backward

difference for stability to define the derivative dI/dt and Runge-Kutta for better accuracy at a given time step. Runge-Kutta requires four function evaluations per time step, but results in orders of magnitude improvement in accuracy. The algorithm proceeds by evaluating four derivatives of the current vector

$$\frac{dI}{dt} = f(t, I) \quad (B.11)$$

These derivatives are given by

$$f_1 = f(t, I(t)) \quad (12)$$

$$f_2 = f(t + \Delta t/2, I(t) + f_1 \Delta t/2) \quad (13)$$

$$f_3 = f(t + \Delta t/2, I(t) + f_2 \Delta t/2) \quad (14)$$

$$f_4 = f(t + \Delta t, I(t) + f_3 \Delta t) \quad (15)$$

The result is

$$I(t + \Delta t) - I(t) = \frac{\Delta t}{6}(f_1 + 2f_2 + 2f_3 + f_4) \quad (B.16)$$

At output times, the loop currents are properly added to form the line currents and the total power dissipated in the structure is computed.

A key part of this phase is computing the external driving currents and associated flux linkages in the structure. The user must include functions which define the driving term. These are linked together with the FASTTIME executable. They return the flux through the loops due to the external driving term. Generally it is most efficient to separate the spacial and temporal parts of the driving current unless they both vary continuously throughout the problem.

A different function is generally needed for the normal loops and for the special loops. One of the important results of benchmarking as described in Chapter 6 is the need to model this driving term in a manner consistent with the modeling of the structure. This generally requires that the driving current is composed of sticks in the same way that the structure is.

B.5. FASTPLOT

As often occurs in engineering analysis, proper presentation of the output is one of the more difficult parts of the problem. In this particular problem there are many quantities of interest, including current densities, fields, and pressures. All of these are three dimensional vector quantities, and are therefore difficult to present in a single plot. The post-solution analysis includes computation of current density, field, and pressure vectors at the centroids. Function plots of any component or the magnitude of current, field, and pressure are available. In addition, current

density streamlines may be viewed. All of these are plotted on the mesh laid out on a plane surface at any time step for which output line currents exist. Also available are time histories for the external current or induced total resistive power.

The current densities are computed by first forming the equivalent current densities of the scalar line currents. There are four current density vectors associated with the line currents nearest each centroid. These are averaged to arrive at a single current density vector at the centroids.

The next step is to fit the pointwise data with an approximating function so that interpolation can be done. Cubic B-splines are employed with periodic boundary conditions. Once the solution is given by a spacially continuous fitting function, the streamlines may be followed by choosing a starting point and moving always in the direction of the current vectors.

$$\frac{dr}{dl} = j \quad (B.17)$$

This is an initial value problem and, as with FASTTIME, a 4th order Runge-Kutta algorithm is used.

The time histories of current and power are simply obtained from a data file generated by FASTTIME.

The remaining plots are all done using software specific to the PFC VAX. The function to be plotted is first fitted with cubic B-splines. Then a 3-D surface is generated by evaluating the function across the entire mesh and plotting the values of the function with lines connecting them. A hidden line algorithm helps to visualize the function as a smooth, continuous surface.

B.6. Problems and Recommendations

The FASTEDDY set of routines is still very much in the development stage. There are certain improvements which are essential if the code is ever to be used for further research. One of these is symmetry. Symmetry has been considered an important feature, but was never implemented due to time and manpower restrictions.

When the problem exhibits symmetry in both the structure and the driving currents, there is much to be gained by explicitly accounting for the symmetry and reducing the problem size. Each plane of symmetry reduces the size of the numerical problem by a factor of four. Several kinds of symmetry might be considered, including symmetry about a point, symmetry about a plane, multiple symmetry (for example modeling 1/4 of the toroidal angle), and others.

There are two considerations which must be addressed:

- a) The current along a line of symmetry is zero. Since the equations being solved are voltage equations, this is implemented by setting to zero the resistance at the symmetry edges. This

requires changes in both FASTCOFF and FASITIME where resistive voltage drops are computed.

- b) The flux through any given loop must be summed with any "fictitious" loops which represent reflections of "real" loops through the axes of symmetry. This is taken care of in FASTCOFF when fluxes are computed.

Another possible improvement is the elimination of full matrix storage. Since the matrix is always symmetric ($M_{ij} = M_{ji}$), there is no need to store all of the elements. In addition to saving on storage, execution will be more efficient since only half as many coefficients will need to be found and a symmetric matrix inverter is more efficient. Before changing the code, studies should demonstrate that the matrix truly *is* symmetric and routine tests could be included in normal execution.

Two significant limitations have been found in the VAX implementation of FASTEDDY. These will certainly require more inspection. First, as the problem becomes very large, certain problems inevitably develop. For one thing, accuracy becomes more critical in a larger problem since a large number of small quantities dominate the solution. Another problem is inherent to the fact that FASTEDDY has the two special loops which are not treated in a completely consistent fashion. As the mesh gets larger the inductance of the special loops increases relative to the others, but logarithmically.

The other limitation is in the area of nonuniform meshes. There is clearly a dependence of the solution accuracy on the level of nonuniformity in the mesh, but the exact behavior has not been explored. This is an important concern for large meshes where a finer mesh is required near a structural discontinuity.

References

- B.1 L. R. Turner, R. J. Lari, and G. L. Sandy, "*Eddy Current Simulation in Prisms, Plates, and Shells with the Program EDDYNET*," Symposium on Eddy Current Characterizations of Materials and Structures, Gaithersburg MD, 1979.
- B.2 T.N.L. Patterson, "*Algorithm for Automatic Numerical Integration Over a Finite Interval*," Communications of the ACM, vol 16, no 11, Nov. 1973.
- B.3 F.W. Grover, Inductance Calculation, Working Formulas and Tables, Dover Publications, Inc., New York, 1946.